



**HAL**  
open science

# Rhodium based mono-and bi-metallic nanoparticles : synthesis, characterization and application in catalysis

Mahmoud Ibrahim

► **To cite this version:**

Mahmoud Ibrahim. Rhodium based mono-and bi-metallic nanoparticles : synthesis, characterization and application in catalysis. Catalysis. Université Paul Sabatier - Toulouse III, 2016. English. NNT : 2016TOU30063 . tel-01405805

**HAL Id: tel-01405805**

**<https://theses.hal.science/tel-01405805>**

Submitted on 30 Nov 2016

**HAL** is a multi-disciplinary open access archive for the deposit and dissemination of scientific research documents, whether they are published or not. The documents may come from teaching and research institutions in France or abroad, or from public or private research centers.

L'archive ouverte pluridisciplinaire **HAL**, est destinée au dépôt et à la diffusion de documents scientifiques de niveau recherche, publiés ou non, émanant des établissements d'enseignement et de recherche français ou étrangers, des laboratoires publics ou privés.



Université  
de Toulouse

# THÈSE

En vue de l'obtention du

## DOCTORAT DE L'UNIVERSITÉ DE TOULOUSE

Délivré par :

Université Toulouse 3 Paul Sabatier (UT3 Paul Sabatier)

---

**Présentée et soutenue par :**

**Mahmoud IBRAHIM**

Le Jeudi 12 mai 2016

**Titre :**

Rhodium Based Mono- and Bi-Metallic Nanoparticles: Synthesis,  
Characterization and Application in Catalysis

---

ED SDM : Chimie organométallique de coordination - CO 043

**Unité de recherche :**

Laboratoire de Chimie de Coordination (LCC) - CNRS

**Directeur(s) de Thèse :**

Dr. Karine PHILIPPOT, Directrice de Recherche, LCC - CNRS

**Rapporteurs :**

Prof. Alain ROUCOUX, Professeur ENSC - Rennes  
Dr. Eric MARCEAU, Maître de Conférences, Université Lille 1

**Autre(s) membre(s) du jury :**

Prof. Romuald Poteau, Professeur Université Toulouse III - LPCNO (Président)  
Dr. David SEMERIL, Chargé de Recherche au CNRS - Strasbourg









# Acknowledgements

I would like to thank warmly Prof. Alain Roucoux and Dr. Eric Marceau for accepting to act as referees for this thesis work, as well as, Prof. Romuald Poteau and Dr David Semeril for accepting to examine my Ph.D results. Their participation to my thesis jury is an honor for me.

Foremost, I would like to express my sincere gratitude and appreciation to my advisor Dr. Karine Philippot for the continuous support during my Ph.D, for her patience, motivation, enthusiasm, and knowledge. Her guidance helped me in all the time of research and writing of this thesis manuscript. I could not have imagined having a better advisor and mentor for my Ph.D study.

The University Paul Sabatier is acknowledged for a MESR scholarship, as well as CNRS for the financial support.

I would like to thank Pr. L. Rossi who hosted me for one month in her group at the “*Laboratory of Nanomaterials and Catalysis*” (University of Sao Paulo, Brasil) under the framework of a CAPES-COFECUB project, and Pr. N. Yan for hosting me twice at the “*Laboratory of Green Catalysis*” (NUS, Singapore) under the framework of a MERLION project.

All current and former members of the team in particular, Prof Catherine Amiens, Dr. Diana Ciuculescu-Pradines, Dr. Pierre Fau, Dr. Myrtil Kahn, Dr. Katia Fajerweg and Lea Godard are also acknowledged for their scientific discussions and also kindness towards me from the beginning till the end of my Ph.D.

I would like to express my gratitude to Dr. Pierre Lecante for the WAXS analysis, Vincent Collière for the electron microscopy experiments, Dr. Yannick Coppel and Christian Bijani for nuclear magnetic resonance experiments and for their valuable scientific discussions, and also Alain Moreau for the elemental analysis.

## Acknowledgements

Special thanks are directed to my current and previous teammates and friends, Dr. Tugce Ayvali, Dr. Marlene, Dr. Luis-Miguel Martinez-Prieto, Dr. Pascal Lignier, Dr. Natalia Jesus Costa, Dr. Lucas Vono, Dr. Solen Kinayyigit, Dr. Eric Bonnefille, Dr. Miguel Guerrero, Dr. Samuel Drouet, Roberto Gonzalez-Gomez, Laize Zaramello, Jordi Creus, Kais Gharbi, Johnathan De Tovar, also other colleagues from the LCC, Audrey, Carlos, Guangha, Muh-Mei, Nuria, Katie, you were more than just colleagues, you were my friends, thanks for the endless encouragements, ideas, jokes and happy moments. Without these valuable people, the journey would have been very difficult, your presence made me always feel at home in France.

Thanks to all the CNRS, UPS and LCC employees, Nataly Aulier, Isabelle Boutonnet, Mélanie Bégué, Gaëtan Havet, Patricia Fouquereau, Florence Di Clemente, Fabrice Candau, Philippe Prono, Michel and Brigitte Griessinger for their always warm welcoming and help in administrative tasks.

Special thanks go to my precious friends Mouin, Amar, Housein, Bouchra, Ali, Raghda, Rana, Mariam, Ramona, Khadija... and every single one who helped me feeling home, being around you feels like being with the family I am away from, thanks for all the surprises, the laughs, the encouragements, and the support.

Last, but not least, my greatest gratitude and thankfulness is dedicated to my family, especially my father Youssef Ibrahim, my mother Samira Roummieh. Thank you for the unlimited love, support and care, it is all dedicated for you, you made me reach here.



---

# **General Introduction**

---



# General Introduction

Over the last 25 years, the field of metal nanoparticles (MNPs) witnessed an evolution of interest by the scientific community that was illustrated by the extensive studies performed on their synthesis, characterization and the evaluation of their potentials for various applications. This interest evolved given the unusual properties they possess, as the result of their position at the boundary between molecular and bulk metals.<sup>1-2</sup> Applications of MNPs cover a wide range of fields including health and medicine,<sup>3</sup> magnetism,<sup>4-5</sup> electrochemistry,<sup>6</sup> energy, etc... One particular application of MNPs is in catalysis,<sup>2,7-9</sup> where it bridges the gap of differences between homogeneous and heterogeneous catalysis.<sup>2</sup> However, MNP catalytic performance is highly dependent on their physical and chemical properties, that is why the development of innovative synthesis methods is essential for manipulating and better understanding their catalytic behavior.

This work deals with the preparation of mono- and bimetallic rhodium-based Rhodium nanoparticles, their characterization and their application in nanocatalysis. The method employed to synthesize the particles is the organometallic approach. As a main advantage, this method does not require harsh reaction conditions, and allows to obtain well-defined NPs in the presence of chosen stabilizers that may be polymers or coordinating ligands. Moreover, by a careful choice of the metal precursor, one can avoid surface contamination which is an essential factor to study precisely their surface properties and catalytic activity.  $[\text{Rh}(\eta^3\text{-C}_3\text{H}_5)_3]$  organometallic complex was used as the source of rhodium in combination with a suitable stabilizing agent. This precursor is very interesting for the elaboration of Rh NPs, since it decomposes easily under low temperature and dihydrogen pressure in organic solvents, leading to the release of Rh atoms, and propane as the only by-product. This results in small, well-controlled NPs in terms of size, morphology and dispersion and “clean” metal surface that can be functionalized by a ligand. Various stabilizing agents have been used all over this work to study their ability to stabilize Rh NPs that are active in catalysis. Bimetallic NPs were also prepared using similar synthesis tools through a one pot synthesis, by co-decomposition of the  $[\text{Rh}(\eta^3\text{-C}_3\text{H}_5)_3]$  with another organometallic precursor in the presence of a specific stabilizer.

This work was carried out at the “*Laboratoire de Chimie de Coordination du CNRS*” in Toulouse, France, in the team “*Ingénierie des Nanoparticules Métalliques*”, under the

supervision of Dr. Karine Philippot. It was supported by a MESR grant and CNRS funding. During the thesis course, three one-month stays were performed overseas; one at the “*Laboratory of Nanomaterials and Catalysis*” (University of Sao Paulo, Brasil) under the framework of a CAPES-COFECUB project with the group of Pr. Liane M. Rossi, and two others at the “*Laboratory of Green Catalysis*” (NUS, Singapore) under the framework of a MERLION project with the group of Pr. Ning Yan.

This manuscript is divided into six chapters as follows:

Chapter I provides general information and bibliographic data about metallic nanoparticles. It describes the history timeline of MNPs and their development as well as the main areas of their applications. Then, a part is dedicated to what makes MNPs special and interesting materials. Main synthesis methods focusing on the chemical routes in solution and in particular organometallic approach, in solution, and selected characterization methods of MNPs are also reported. The last part of this chapter sheds the light on the synthesis of rhodium NPs and their application in hydrogenation and hydroformylation catalytic reactions.

In chapter II, we report the synthesis of monometallic rhodium nanoparticles and their characterization. A variety of ligands was used as stabilizers to study their influence on the characteristics of the particles. For comparison purpose, we also performed the synthesis of Rh NPs in the presence of a polymer, polyvinylpyrrolidone (PVP), considering that the NPs grow inside the 3D polymeric matrix without direct interaction between PVP and the metal surface. In the contrary, with ligands we expect a coordination at the metal surface and different effects depending on their composition. A variety of phosphorous-containing ligands was tested including phosphines (PPh<sub>3</sub>, dppb, and PTA), calix[4]arene and phosphine ferrocenes. Water-soluble carbenes were also used to obtain aqueous colloidal solutions of rhodium. Last part of this chapter is devoted to the deposition of selected Rh NPs on amino-modified magnetic silica as a support that can facilitate the recovery and recycling of the catalyst.

Bimetallic RhM NPs syntheses are described in chapter III. PVP- and HDA-stabilized RhNi and RhPd NPs were synthesized and characterized using different metal ratios. PVP-stabilized RhNiOx NPs were also prepared for their interest as selective hydrogenolysis

catalyst to cleave C-O bonds. Synthesis conditions were also tested to form PVP-stabilized RhPt and RhRu MNPs, opening the door for future investigations.

Chapter IV reports the results obtained in catalysis using mono- and bimetallic rhodium-based nanoparticles prepared during the PhD. Application in catalysis concerned mainly hydrogenation reaction, using RhPVP, RhPPh<sub>3</sub>, Rhdpbb and Rh Phosphino Ferrocene as catalysts. RhPPh<sub>3</sub> and Rh calix[4]arene nanoparticles were evaluated in hydroformylation reaction. Finally, RhNiO<sub>x</sub> bimetallic NPs were applied in the hydrogenolysis of 1-benzoxy-2-methoxy-benzene, a model substrate of lignin, in comparison with RhPVP and NiPVP systems.

Conclusions, general remarks and perspectives for the work are presented in chapter V, and the last chapter of this manuscript is devoted to the experimental part.



---

# Index

---





# Table of Contents

Acknowledgements.....	5
General Introduction .....	9
Table of Contents .....	15
Table of Figures .....	19
Table of Tables.....	24
Table of Schemes .....	25
I. Bibliographic Introduction on Metal Nanoparticles.....	29
I.1 Generalities .....	29
I.1.1 Definition and Timeline .....	29
I.1.2 Interests of Metal Nanoparticles .....	31
I.2 Synthesis of Metal Nanoparticles .....	34
I.2.1 Nucleation and Growth of Metal Nanoparticles in Solution.....	36
I.2.2 Chemical Reduction .....	38
I.2.3 Organometallic Approach .....	39
I.3 Characterization Methods of Metal Nanoparticles .....	41
1.3.1 Transmission Electron Microscopy (TEM) and Energy-dispersive X-ray spectroscopy (EDX) .....	41
1.3.2 Wide Angle X-Ray Scattering (WAXS) .....	42
1.3.3 Nuclear Magnetic Resonance (NMR) Spectroscopy.....	43
1.3.4 Infrared Spectroscopy (IR) .....	44
1.3.5 X-Ray Absorption techniques .....	44
I.4 Applications of Metal Nanoparticles .....	45
I.4.1 Medicine, Biotechnology, Food and Personal Care.....	46
I.4.2 Energy and Electronics.....	46
I.4.3 Manufacturing and Materials .....	47
I.4.4 Environment .....	47
I.4.5 Catalysis and Energy .....	48
I.5 Rhodium Nanoparticles in Catalysis.....	49
I.5.1 Hydrogenation Reactions .....	50

1.5.1.1 Polymers and Macromolecules as Stabilizers .....	50
1.5.1.2 Ligands and Surfactants as Stabilizers .....	57
I.5.2 Hydroformylation Reactions .....	63
II. Monometallic Rhodium Nanoparticles.....	73
II.1 Introduction .....	73
II.2 PVP-Stabilized Rhodium NPs .....	77
II.2.1 Electron Microscopy Analysis .....	78
II.2.2 Wide Angle X-ray Scattering Analysis.....	80
II.2.3 X-Ray photoelectron Spectroscopy Analysis .....	81
II.2.4 CO Adsorption Study.....	82
II.3 PPh <sub>3</sub> -Stabilized Rhodium NPs.....	87
II.3.1 Electron Microscopy Analysis .....	87
II.3.2 Wide Angle X-ray Scattering Analysis.....	90
II.3.3 NMR Study .....	90
II.3.4 CO Adsorption Study.....	92
II.4 dppb-Stabilized Rhodium NPs .....	93
II.4.1 Electron Microscopy Analysis .....	94
II.4.2 Wide Angle X-ray Scattering Analysis.....	98
II.4.3 CO Adsorption Study.....	98
II.5 PTA-Stabilized Rhodium NPs .....	100
II.5.1 Electron Microscopy Analysis .....	101
II.5.2 Wide angle X-ray Scattering Analysis.....	103
II.5.3 CO Adsorption Study.....	104
II.6 Phosphino-Ferrocene ligand Stabilized Rhodium NPs .....	106
II.6.1 High Resolution Electron Microscopy Analysis.....	110
II.6.2 CO Adsorption Study.....	111
II.7 Calixarene-biphosphite ligand-Stabilized Rhodium NPs:.....	114
II.8 N-Heterocyclic Carbene-Stabilized Rhodium NPs .....	116
II.9 Deposition of Rhodium NPs on Amino Modified Magnetic Support.....	122
II.9.1 Synthesis of Magnetic Silica Particles .....	123
II.9.2 Functionalization of the surface of silica magnetic particles.....	125
II.9.3 Deposition of Rh NPs on the modified silica support.....	127

II.10 Conclusion.....	128
III. Bimetallic Rhodium Nanoparticles .....	133
III.1 Introduction.....	133
III.2 RhNi Bimetallic Nanoparticles .....	137
III.2.1 Monometallic Systems .....	139
III.2.1.1 PVP-stabilized Ni NPs.....	139
III.2.1.2 HDA-stabilized Rh NPs.....	142
III.2.1.3 HDA-stabilized Ni NPs .....	145
III.2.2 Bimetallic RhNi Systems .....	148
III.2.2.1 PVP-stabilized RhNi NPs .....	149
III.2.2.2 HDA-stabilized RhNi NPs.....	150
III.2.3 PVP-stabilized RhNiO <sub>x</sub> NPs .....	153
III.2.3.1 XPS Analysis .....	158
III.2.3.2 XAS Analysis .....	159
III.2.3.3 Magnetic Measurements.....	162
III.2.3.4 Conclusion .....	164
III.3 RhM Bimetallic Nanoparticles (M=Pd, Pt, Ru).....	166
III.3.1 RhPd System .....	167
III.3.1.1 PVP-stabilized Pd NPs .....	168
III.3.1.2 HDA-stabilized Pd NPs .....	169
III.3.1.3 PVP-stabilized RhPd NPs.....	172
III.3.1.4 HDA-stabilized RhPd NPs .....	175
III.3.2 RhPt System .....	177
III.3.3 RhRu System.....	182
III.4 Conclusion and Perspective .....	186
IV: Application in Catalysis .....	189
IV.I Introduction .....	189
IV.2 Hydrogenation Reaction .....	191
IV.2.1 Non-Supported and Supported Rh NPs in Hydrogenation Reaction .....	191
IV.2.1.1 Hydrogenation of Cyclohexene with Non-Supported Rh NPs.....	193
IV.2.1.2 Hydrogenation of Cyclohexene with Supported Rh NPs.....	194
IV.2.1.3 Hydrogenation of Arenes with Supported Rh NPs .....	196

IV.2.2 PVP-Stabilized Rh NPs in Hydrogenation of Benzoic acid, its Derivatives and Levulinic acid.....	197
IV.2.2.1 Optimization of Reaction Parameters.....	198
IV.2.2.2 Hydrogenation of Levulinic Acid (LA) and its Methyl Ester Derivative. ....	201
IV.2.3 Hydrogenation of Styrene with Ferrocenyl Phosphine-stabilized Rh NPs.....	202
IV.3 Hydroformylation Reaction.....	205
IV.3.1 Hydroformylation of Oct-1-ene and Styrene with PPh <sub>3</sub> - and TOAB-stabilized Rh NPs. ....	205
IV.3.1 Hydroformylation of Styrene with CXP-stabilized Rh NPs. ....	212
IV.4 Hydrogenolysis Reaction.....	215
IV.5 Conclusion.....	218
References.....	228
VI Experimental Part.....	247
VI.1 Generals and Materials.....	247
VI.2 Characterization Techniques.....	248
VI.2.1 Transmission Electron Microscopy.....	248
VI.2.2 Wide Angle X-ray Scattering.....	248
VI.2.3 Infrared Spectroscopy.....	249
VI.2.4 Elemental Analysis.....	250
VI.2.5 Nuclear Magnetic Resonance Spectroscopy.....	250
VI.2.6 X-Ray Absorption Spectroscopy.....	250
VI.2.7 Magnetic Properties Analysis.....	251
VI.2.8 X-Ray Photoelectron Spectroscopy.....	251
VI.3 Synthesis Procedures.....	251
VI.3.1 [Rh( $\eta^3$ -C <sub>3</sub> H <sub>5</sub> ) <sub>3</sub> ] complex.....	251
VI.3.2 PVP-stabilized Rh NPs.....	252
VI.3.3 PPh <sub>3</sub> -stabilized Rh NPs.....	252
VI.3.4 dppb-stabilized Rh NPs.....	253
VI.3.5 PTA-stabilized Rh NPs.....	253
VI.3.6 Phosphine Ferrocene ligands-stabilized Rh NPs.....	254
VI.3.7 CXP-stabilized Rh NPs.....	254
VI.3.8 N-Heterocyclic Carbene-stabilized Rh NPs.....	255

VI.3.2.9 Bimetallic NPs.....	255
VI.3.10 of magnetic silica support.....	255
VI.3.11 Deposition NPs onto silica support .....	255
VI.4 Catalytic Reactions .....	256
VI.4.1 Hydrogenation of cyclohexene with Supported and Non-Supported Rh NPs: .....	256
VI.4.2 Hydrogenation of benzoic acid and derivatives with Rh PVP NPs .....	257
VI.4.3 Hydrogenation of styrene with Ferrocenyl Phosphine-stabilized Rh NPs .....	257
VI.4.4 Hydroformylation of 1-octene and styrene with Rh-PPh <sub>3</sub> and Rh-TOAB NPs ..	258
VI.4.5 Hydroformylation of styrene with CXP-stabilized Rh NPs. ....	258
VI.4.6 Hydrogenolysis of 1-benzyloxy-2-methoxy benzene.....	259
VI.5 Calculations on NPs .....	260
VI.5.1 Number of Atoms .....	260
VI.5.2 Percentage of Surface Atoms .....	261

## Table of Figures

<i>Figure 1.1: Number of publications dealing with metal nanoparticles (1990–2014). (Source: SciFinder Scholar. Keywords: Metal nanoparticles) .....</i>	32
<i>Figure 1.2: Different colors for colloidal solutions of gold and silver nanoparticles depending on their size and shape.<sup>45</sup> .....</i>	33
<i>Figure 1.3: Representation of the electronic state in (a) bulk metal, (b) nanoparticles and (c) small molecular clusters. ....</i>	34
<i>Figure 1.4: General approaches for the synthesis of metal NPs.( Top down=physical, and Bottom Up=Chemical).....</i>	35
<i>Figure 1.5: Different methods for the preparation of metal nanoparticles (adapted from: Microwaves in Nanoparticle Synthesis<sup>47</sup>).....</i>	36
<i>Figure 1.6: WAXS analysis of Rh NPs embedded in PVP polymer. Comparison between (a) the experimental measurement of Rh/PVP NPs and (b) the theoretically calculated RDF of Rh NPs with fcc structure and a 2.5 nm size.<sup>85</sup> .....</i>	43
<i>Figure 1.7: Representation of full-shell metal clusters with “magic numbers” of atoms, which are built upon the densest sphere packing (adapted from reference<sup>109</sup>).....</i>	49
<i>Figure 1.8: Schematic representation of steric stabilization of colloidal metal particles.<sup>69</sup> ...</i>	51

Figure 1.9: PVP polymer and modified structures. <sup>141</sup> .....	54
Figure 1.10: poly(mono-( $\beta$ -cyclodextrin-2-yl)-maleate-alt-maleate-alt-methylvinylether) used to stabilize Rh NPs. <sup>147</sup> .....	56
Figure 1.11: 1,3-diphosphite ligands used to stabilize RhNPs. <sup>151</sup> .....	58
Figure 1.12: Fluorinated phosphine ligands used to stabilize Rh NPs. <sup>152</sup> .....	58
Figure 1.13: Rhodium Bis(imino)pyridine Complexes. <sup>153</sup> .....	59
Figure 1.14: Selected sulfonated water-soluble phosphine ligands. <sup>157</sup> .....	61
Figure 1.15: Optically active ammonium surfactants as protective agents of Rh(0) NPs. N-dodecyl-N-methylephedrium (NMeEph12) <sup>+</sup> salt, N-hexadecylN-methyl-L-prolinolinium (NMeProl16) <sup>+</sup> salt, N-hexadecyl-quicorinium (QC116) <sup>+</sup> salt, N-hexadecyl-quicoridinium (QCD16) <sup>+</sup> salt. <sup>165-166</sup> .....	63
Figure 1.16: Chiral diphosphite ligands used as stabilizers of Rh NPs. ....	65
Figure 1.17: General principle of hydroformylation in an aqueous/ 1-butanol biphasic system using Ph <sub>2</sub> P(CH <sub>2</sub> CH <sub>2</sub> O) <sub>16</sub> CH <sub>3</sub> -stabilized rhodium nanoparticles as catalyst. <sup>177</sup> .....	67
Figure 2.18: (a) <sup>1</sup> H NMR spectrum of [Rh] and PPh <sub>3</sub> mixture in THF-D <sub>8</sub> , (b) <sup>1</sup> H NMR spectrum of [Rh] and PPh <sub>3</sub> mixture in THF-D <sub>8</sub> after 1 h of heating at 70 °C under H <sub>2</sub> pressure, (c) [Rh] and PPh <sub>3</sub> mixture after 3h of heating under H <sub>2</sub> pressure. ....	76
Figure 2.19: (a) TEM image of Rh NPs stabilized with PVP polymer. (b) Corresponding size distribution histogram (d <sub>m</sub> = 2.2 ± 0.9 nm; >215 particles). ....	78
Figure 2.20: (a) HRTEM image showing the lattice interplanar spacing, (b) Fast Fourier Transformation (FFT), and (c) EDX analysis of Rh PVP NPs. ....	79
Figure 2.21: (a) WAXS measurements for Rh PVP NPS in reciprocal space (red line) with theoretically calculated Rh fcc structure (green line). (b) WAXS measurements for Rh PVP NPs in real space (solid line) and theoretically calculated (dotted line). ....	80
Figure 2.22: (a) X-Ray photoelectron spectra of RhPVP NPs elemental survey. (b) Zoomed in area of Cl 2p level. (c) 3d core level X-Ray photoelectron spectra of RhPVP NPs. ....	81
Figure 2.23: FT-IR spectrum recorded after reaction of CO with Rh NPs at r.t. (D: gem-dicarbonyl (2093 cm <sup>-1</sup> , 2030 cm <sup>-1</sup> ), M: linear monocarbonyl (2060 cm <sup>-1</sup> ), B: bridged-bonded CO (broad band 1910 cm <sup>-1</sup> ), and C: carbonate-type species). <sup>210</sup> .....	82
Figure 2.24: (a) FT-IR of purified Rh-PVP NPs, (b) FT-IR of RhPVP NPs after reaction with 1bar of CO at RT for 24h. ....	83
Figure 2.25: Solid state <sup>13</sup> C{ <sup>1</sup> H} NMR of (a) RhPVP NPs, (b) RhPVP NPs under 1 bar of CO over 20h, (c) RhPVP NPs under 3 bar of CO over 48h. ....	85
Figure 2.26: CP MAS <sup>13</sup> C{ <sup>1</sup> H} NMR spectrum of RhPVP NPs after CO adsorption (1bar, 20h). ....	86
Figure 2.27: TEM images of RhPPh <sub>3</sub> NPs ([L]/[Rh]=0.2 eq.) at two different magnifications. ....	88

Figure 2.28: TEM images of RhPPh <sub>3</sub> NPs ([L]/[Rh]=0.5 eq.) at two different magnifications. ....	88
Figure 2.29: (a) TEM image of the RhPPh <sub>3</sub> NPs ([PPh <sub>3</sub> ]/[Rh]= 1). (b) Corresponding size distribution of RhPPh <sub>3</sub> NPs. ....	89
Figure 2.30: (a) HRTEM images of the RhPPh <sub>3</sub> NPs ([PPh <sub>3</sub> ]/[Rh]= 1) and (b) corresponding EDX analysis. ....	89
Figure 2.31: (a) WAXS measurements (solid line) in reciprocal space and (b) in real space, for RhPPh <sub>3</sub> NPs in comparison with calculated data for Rh in manganese-β structures (dashed line). ....	90
Figure 2.32: (a) [Rh(C <sub>3</sub> H <sub>5</sub> ) <sub>3</sub> ]complex + PPh <sub>3</sub> in THF-D8 at -80°C, (b) [Rh(C <sub>3</sub> H <sub>5</sub> ) <sub>3</sub> ]complex + PPh <sub>3</sub> in THF-D8 at r.t., (c) [Rh(C <sub>3</sub> H <sub>5</sub> ) <sub>3</sub> ]complex + PPh <sub>3</sub> +H <sub>2</sub> at 40°C (d) [Rh(C <sub>3</sub> H <sub>5</sub> ) <sub>3</sub> ]complex + PPh <sub>3</sub> +H <sub>2</sub> at 65°C. ....	91
Figure 2.33: (a) FT-IR spectrum of RhPPh <sub>3</sub> NPs after 24h of CO exposure, (b) FT-IR of purified RhPPh <sub>3</sub> NPs. ....	92
Figure 2.34: TEM images of Rh NPs obtained with 0.2 equivalent of dppb ligand in THF at two different magnifications. ....	94
Figure 2.35: TEM images of Rh NPs obtained with 0.2 equivalent of dppb ligand in toluene at two different magnifications. ....	95
Figure 2.36: (a) Picture of the Rhdppb crude colloidal solution (0.5 eq.) (b) TEM image of Rhdppb (0.5 eq.) NPs and (c) Corresponding size distribution. ....	95
Figure 2.37: (a) TEM image of Rhdppb NPs obtained at a ratio [dppb]/[Rh]=0.3, and (b) Corresponding size distribution. ....	96
Figure 2.38: HRTEM images of Rhdppb NPs (0.3 eq.) ....	97
Figure 2.39: (a) EDX spectrum of Rhdppb NPs (0.3 eq.) (b) Quantitative analysis of the chemical composition of Rh dppb NPs. ....	97
<b>Figure 2.40:</b> (a) WAXS measurements (solid line) in reciprocal space and (b) in real space, for Rhdppb NPs in comparison with calculated data for Rh in manganese-β structures (dashed line). ....	98
Figure 2.41: (a) FT-IR of Rhdppb NPs (0.3 eq.), (b) FT-IR of Rhdppb NPs after 24h reaction with CO. ....	99
Figure 2.42: 1,3,5-triaza-7-phosphaadamantane (PTA). ....	100
Figure 2.43: (a) TEM image of RhPTA <sub>0.5</sub> NPs, (b) with the corresponding size histogram, and (c) TEM image of the particles after dispersion in water. ....	102
Figure 2.44: (a) TEM image of RhPTA <sub>0.8</sub> NPs, (b) with the corresponding size histogram, and (c) TEM image of the particles after dispersion in water. ....	102
Figure 2.45: (a), (b) and (c) HRTEM images of RhPTA <sub>0.8</sub> NPs at different magnifications, (d) STEM-HAADF on bright mode and (e) with Z-contrast, (f) EDX analysis spectrum. ....	103

<i>Figure 2.46: WAXS measurements in (a) reciprocal space and (b) in real space, for RhPTA<sub>0.8</sub> NPs.</i>	104
<i>Figure 2.47: (a) FT-IR of purified RhPTA<sub>0.8</sub> NPs and (b) FT-IR after reaction with 1bar of CO at r.t. for 24h.</i>	105
<i>Figure 2.48: (a) TEM images and corresponding size distributions of Rh NPs stabilized with L1, (b) L2, (c) L3, (d) L4, (e) L5.</i>	109
<i>Figure 2.49: HRTEM images of L2-stabilized Rh NPs (0.2 eq) at different magnifications.</i>	110
<i>Figure 2.50: HRTEM images of L5-stabilized Rh NPs at different magnifications.</i>	111
<i>Figure 2.51: (a) FT-IR spectrum of purified L2-stabilized Rh NPs (b) FT-IR spectrum of L2-stabilized Rh NPs after 48h under CO atmosphere.</i>	112
<i>Figure 2.52: (a) FT-IR spectrum of L5-stabilized Rh NPs (b) FT-IR spectrum of L5-stabilized Rh NPs after 48h under of CO atmosphere.</i>	113
<i>Figure 2.53: TEM images of Rh NPs prepared with 0.2 molar eq. ([L]/[Rh]) of CXP ligand in THF at r.t.</i>	115
<i>Figure 2.54: TEM images of Rh NPs prepared with 0.2 molar eq. ([L]/[Rh]) of CXP ligand in Toluene at 65 °C.</i>	115
<i>Figure 2.55: TEM images of (a) PrIPr-H (b) PrIMes-H (c) MPr-H stabilized Rh NPs after the synthesis in DMSO.</i>	118
<i>Figure 2.56: TEM images of PrIMes-H stabilized Rh NPs in THF (a) before dialysis (b) after dialysis.</i>	119
<i>Figure 2.57: TEM images of MPr-H stabilized Rh NPs in THF (a) before dialysis (b) after dialysis.</i>	119
<i>Figure 2.58: TEM images of PrIPr-H stabilized Rh NPs in THF at 65 °C before dialysis with the corresponding size distribution.</i>	120
<i>Figure 2.59: TEM images of PrIPr-H stabilized Rh NPs in THF at 65 °C after dialysis.</i>	121
<i>Figure 2.60: TEM image of PrIMes-H stabilized Rh NPs in THF at 65 °C before dialysis with the corresponding size distribution.</i>	121
<i>Figure 2.61: TEM images of PrIMes-H stabilized Rh NPs in THF at 65 °C after dialysis.</i>	121
<i>Figure 2.62: Concentration of paramagnetic support upon magnet exposure and redispersion after removal of the magnet.</i>	123
<i>Figure 2.63: (a)TEM image of iron-core silica support. (b) Size distribution of the magnetic silica particles.</i>	125
<b>Figure 2.64:</b> XPS spectrum of N 1 s region of the amino-modified catalyst support (Fe <sub>3</sub> O <sub>4</sub> @SiO <sub>2</sub> -NH <sub>2</sub> ). (Adapted from reference <sup>247</sup> ).	126
<b>Figure 2.65:</b> TEM images of the RhPVP NPs attached to the surface of the magnetic silica support at two magnifications.	128



<i>Figure 3.66: Main types of structures encountered for bimetallic nanoparticles.</i>	133
<i>Figure 3.67: (a) TEM image of PVP-stabilized Ni NPs (b) corresponding size distribution histogram.</i>	140
<i>Figure 3.68:(a)HRTEM images of Ni PVP NPs at different magnifications (b)STEM-HAADF image (c) EDX analysis spectrum.</i>	141
<i>Figure 3.69: TEM image of Rh NPs stabilized with 1 eq. of HDA ligand in THF, with the corresponding size distribution histogram.</i>	144
<i>Figure 3.70: TEM image of Rh NPs stabilized with 2 eq. of HDA ligand in THF, with the corresponding size distribution histogram.</i>	144
<i>Figure 3.71: TEM image of Rh NPs stabilized with 5 eq. of HDA ligand in THF, with the corresponding size distribution histogram.</i>	145
<i>Figure 3.72: (a) TEM images and (b) Size distribution histogram of HDA-stabilized Ni NPs (5 eq.).</i>	146
<i>Figure 3.73: (a) HRTEM images and (b) EDX analysis spectrum of HDA-stabilized Ni NPs (5 eq.).</i>	147
<i>Figure 3.74: TEM images of PVP-stabilized (a) Rh<sub>2</sub>Ni<sub>8</sub> (b) Rh<sub>5</sub>Ni<sub>5</sub> (c) Rh<sub>8</sub>Ni<sub>2</sub>, with their corresponding size distribution histograms (a') (b') (c').</i>	150
<i>Figure 3.75: TEM images of HDA-stabilized (a) Rh<sub>2</sub>Ni<sub>8</sub> (b) Rh<sub>5</sub>Ni<sub>5</sub> (c) Rh<sub>8</sub>Ni<sub>2</sub>, with their corresponding size distribution histograms (a') (b') (c').</i>	152
<i>Figure 3.76: Selective hydrogenolysis of C–O bond over arene hydrogenation of 1-benzyloxy-2-methoxy-benzene.<sup>85</sup></i>	154
<i>Figure 3.77: Oxidation of the PVP-stabilized Rh<sub>5</sub>Ni<sub>5</sub> NPs to obtain NiO<sub>x</sub> islands on Rh cores .</i>	155
<i>Figure 3.78: STEM images of NiO<sub>x</sub>/Rh NPs with four randomly selected particles, and their corresponding EDX spectra, where Ni/Rh atomic ratios are shown.</i>	156
<i>Figure 3.79: TEM and HRTEM analysis of Rh/NiO<sub>x</sub> NPs with the corresponding size distribution histogram.</i>	157
<i>Figure 3.80: XPS spectra of (a) NiO<sub>x</sub>/Rh and (b) Ni NPs at Ni 2p region; (c) NiO<sub>x</sub>/Rh and (d) Rh NPs at Rh 3d region.</i>	158
<i>Figure 3.81: (a) Ni and (b) Rh K-edge XANES spectra of NiO<sub>x</sub>/Rh, Ni, and Rh NPs. Fourier transformed (c) Ni and (d) Rh K-edge EXAFS spectra of NiO<sub>x</sub>/Rh, Ni and Rh NPs. The spectra of Ni foil, Rh foil, NiO, and Rh<sub>2</sub>O<sub>3</sub> are included as references.</i>	160
<i>Figure 3.82: (a) Magnetization curve M–H of NiO<sub>x</sub>/Rh and Ni NPs measured at 2 K (inset: enlargement of low field). ZFC-FC curves for (b) Ni and (c) NiO<sub>x</sub>/Rh NPs.</i>	163
<i>Figure 3.83: TEM images of PVP-stabilized Pd NPs and their corresponding size distribution histogram.</i>	168
<i>Figure 3.84: HRTEM images of PVP-stabilized Pd NPs.</i>	169

<i>Figure 3.85: TEM images of Pd NPs stabilized with (a) 1, (b) 2, (c) 5, and (d) 10 molar equivalents of HDA.</i> .....	170
<i>Figure 3.86: HRTEM images of Pd NPs stabilized with 5 eq. of HDA.</i> .....	171
<i>Figure 3.87: TEM images of PVP-stabilized (a) Rh<sub>2</sub>Pd<sub>8</sub>, (b) Rh<sub>5</sub>Pd<sub>5</sub>, and (c) Rh<sub>8</sub>Pd<sub>2</sub> with their corresponding size distribution histograms.</i> .....	173
<i>Figure 3.88: STEM-HAADF images, EDX and metal contents of PVP-stabilized Rh<sub>5</sub>Pd<sub>5</sub>.</i> ..	174
<i>Figure 3.89: TEM images of HDA (5 eq.) stabilized (a) Rh<sub>2</sub>Pd<sub>8</sub>, (b) Rh<sub>5</sub>Pd<sub>5</sub>, and (c) Rh<sub>8</sub>Pd<sub>2</sub> with their corresponding size distribution histograms.</i> .....	175
<i>Figure 3.90: TEM image of PVP-stabilized Pt NPs with the corresponding size histogram.</i> .....	177
<i>Figure 3.91: (a) TEM, (b) HRTEM, (c) and HAADF-STEM images of PVP-stabilized Rh<sub>50</sub>Pt<sub>50</sub> NPs with (d) the corresponding size histogram.</i> .....	179
<i>Figure 3.92: EDX analysis of PVP-stabilized Rh<sub>50</sub>Pt<sub>50</sub> NPs with quantitative metal ratios.</i>	181
<i>Figure 3.93: TEM, and HRTEM HAADF-STEM images of PVP-stabilized Rh<sub>50</sub>Ru<sub>50</sub> NPs with the corresponding size histogram.</i> .....	183
<i>Figure 3.94: EDX analysis of PVP-stabilized Rh<sub>50</sub>Ru<sub>50</sub> NPs with quantitative metal ratios.</i>	185
<i>Figure 4.95: (a) Expected benefits of nanocatalysis; and (b) catalyst market by end-use.<sup>2</sup></i>	189
<i>Figure 4.96: Catalyst recycling test expressed as TOF (h<sup>-1</sup>, corrected for exposed Rh atoms) of Rhdppb@FFSiNH<sub>2</sub> (square), RhPPh<sub>3</sub>@FFSiNH<sub>2</sub> (circle) and RhPVP @FFSiNH<sub>2</sub> (triangle) for successive hydrogenations of cyclohexene.</i> .....	196

## Table of Tables

<i>Table 1.1: Hydrogenation of Arenes Using Rh-PFA System.<sup>135</sup></i> .....	52
<i>Table 1.2: Hydrogenation of olefinic acids by the colloidal RhCl<sub>3</sub>/TPPTS system in the presence of β-cyclodextrins<sup>a</sup> (adapted from ref 155)</i> .....	60
<i>Table 1.3: Hydrogenation of 1-hexene and benzene at 20 °C using rhodium clusters of varying size as catalysts.<sup>156</sup></i> .....	60
<i>Table 2.4: N-heterocyclic carbenes-stabilized Rh NPs.</i> .....	108
<i>Table 2.5: Summary of the characteristics of the prepared monometallic Rh NPs.</i> .....	130
<i>Table 3.6: Summary of synthesized Rh, Ni and RhNi NPs with their corresponding average sizes, and the Rh and Ni metal content in each system.</i> .....	153
<i>Table 3.7: Structure parameters by curve fitting of FT-EXAFS<sup>a</sup></i> .....	161
<i>Table 3.8: Summary of synthesized Rh, Pd and RhPd BMNPs with their corresponding average sizes, and the Rh and Pd metal content in each system.</i> .....	176

<i>Table 4.9: Hydrogenation of cyclohexene with non-supported RhNPs.<sup>a</sup></i> .....	193
<i>Table 4.10: Hydrogenation of cyclohexene with supported Rh NPs.<sup>a</sup></i> .....	194
<i>Table 4.11: Hydrogenation of arenes with RhPVP@FFSiNH<sub>2</sub> NPs.<sup>a</sup></i> .....	196
<i>Table 4.12: Solvent effect on the BM hydrogenation to CCM over Rh@PVP NPs.</i> .....	198
<i>Table 4.13: Substrates scope on the hydrogenation of aromatics with RhPVPNPs.</i> .....	199
<i>Table 4.14: Styrene and ethyl-benzene hydrogenation using L2- and L5-stabilized Rh NPs. Reaction conditions: iso-propanol solvent, 30 bar H<sub>2</sub>, r.t, 24h</i> .....	203
<i>Table 4.15: Hydroformylation of oct-1-ene and styrene catalyzed by Rh-PPh<sub>3</sub>.<sup>a</sup></i> .....	206
<i>Table 4.16: Hydroformylation of oct-1-ene and styrene by RhTOAB NPs with and without addition of an external PPh<sub>3</sub>.<sup>a</sup></i> .....	208
<i>Table 4.17: CS<sub>2</sub> addition at the beginning of the oct-1-ene hydroformylation reaction for RhTOAB and RhPPh<sub>3</sub> NPs.<sup>a</sup></i> .....	211
<i>Table 4.18: Hydrogenation of Styrene with RhCXP and RhPVP NPs.<sup>a</sup></i> .....	213
<i>Table 4.19: Hydrogenolysis of 1-benzoxy-2-methoxy-benzene compounds using NiOx /Rh, Rh, and Ni NPs stabilized by PVP as catalysts.</i> .....	216

## Table of Schemes

<i>Scheme 1.1: Formation of nanostructured metal colloid by the ‘salt reduction’ method, (adapted from reference <sup>55</sup>).</i> .....	37
<i>Scheme 1.2: Schematic representation of the organometallic approach for the synthesis of metal nanostructures. (adapted from reference <sup>75</sup>).</i> .....	40
<i>Scheme 1.3: Schematic illustration of an X-ray absorption edge.</i> .....	45
<i>Scheme 1.4: P-donor ligands used to stabilize the Rh NPs.</i> .....	62
<i>Scheme 1.5: Rh NPs formation on graphene oxide.</i> .....	69
<i>Scheme 2.6: Synthesis of [Rh(<math>\eta^3</math>-C<sub>3</sub>H<sub>5</sub>)<sub>3</sub>] complex.</i> .....	74
<i>Scheme 2.7: Decomposition of [Rh(<math>\eta^3</math>-C<sub>3</sub>H<sub>5</sub>)<sub>3</sub>] complex releasing only propane as byproduct.</i> .....	75
<i>Scheme 2.8: Polyvinylpyrrolidone (PVP) polymer.</i> .....	77
<i>Scheme 2.9: 1,4-Bis(diphenylphosphino)butane (dppb) ligand.</i> .....	93
<i>Scheme 2.10: Different ferrocenyl phosphine ligands used for the synthesis of Rh NPs.</i> .....	107
<i>Scheme 2.11: Calixarene-biphosphite ligand (CXP) used to prepare Rh NPs.</i> .....	114
<i>Scheme 2.12: General Formula of N-heterocyclic carbenes (NHCs)</i> .....	116

<i>Scheme 2.13: Structure of NHC ligands used in stabilizing Rh NPs.</i> .....	118
<i>Scheme 2.14: Dispersion of magnetic iron particles in the presence of oleic acid.</i> .....	124
<i>Scheme 2.15: Dispersion of magnetic Fe<sub>2</sub>O<sub>3</sub> particles followed by silica condensation coating.</i> .....	125
<i>Scheme 2.16: Deposition of Rh NPs on the amino modified silica support.</i> .....	127
<i>Scheme 3.17: Structure of bis(cyclooctadiene)-nickel(0) [Ni(cod)<sub>2</sub>] complex.</i> .....	138
<i>Scheme 3.18: Decomposition of [Ni(cod)<sub>2</sub>] precursor following the organometallic approach.</i> .....	138
<i>Scheme 3.19: Formula of hexadecylamine (HDA).</i> .....	142
<i>Scheme 3.20: Possible ways of coordination of hexadecylamine (HDA) on nanoparticles as a function of amine concentration.<sup>71</sup></i> .....	142
<i>Scheme 3.21: Schematic presentation of the decomposition of [Rh(<math>\eta^3</math>-C<sub>3</sub>H<sub>5</sub>)<sub>3</sub>] and [Ni(cod)<sub>2</sub>] complexes following the organometallic approach</i> .....	148
<i>Scheme 3.22: Structures of [Pd<sub>2</sub>(dba)<sub>3</sub>], [Ru(cod)(cot)] and [Pt(nor)<sub>3</sub>] complexes.</i> .....	166
<i>Scheme 3.23: Decomposition of tris(dibenzylideneacetone)dipalladium(0) [Pd<sub>2</sub>(dba)<sub>3</sub>] complex following the organometallic approach.</i> .....	167
<i>Scheme 4.24: Synthesis of Rh NPs following the organometallic approach using [Rh(<math>\eta^3</math>-C<sub>3</sub>H<sub>5</sub>)<sub>3</sub>] complex.</i> .....	190
<i>Scheme 4.25: Schematic presentation of the hydrogenation monitoring system.</i> .....	192
<i>Scheme 4.26: Ferrocenyl phosphine ligands used for the synthesis of Rh NPs for styrene hydrogenation reaction.</i> .....	202
<i>Scheme 4.27: Rh complex with the L2 ligand.</i> .....	202
<i>Scheme 4.28: Hydroformylation of oct-1-ene (1) and styrene (4) and the corresponding linear (2, 5) and branched (3, 6) aldehyde products, respectively.</i> .....	206

---

# **Chapter I: Bibliographic Introduction**

---



# I. Bibliographic Introduction on Metal Nanoparticles

This chapter introduces the concepts of nanotechnologies and metal nanoparticles (MNPs) from the chemistry point of view. It describes first the discovery and the main uses of MNPs through history till nowadays. Then, a part is dedicated to the interests of MNPs, in summary, what makes them special and interesting materials. Main chemical synthesis and selected characterization methods of MNPs are also reported as well as their main applications. The end of the chapter focuses on NPs of rhodium because this metal is the center of this PhD work, especially with examples of their applications in hydrogenation and hydroformylation catalytic reactions.

## I.1 Generalities

### I.1.1 Definition and Timeline

In definition, according to the National Nanotechnology Initiative (NNI), nanotechnology is referred to the field of science that is dedicated to synthesis, engineering and formation of materials and functional systems at the nanometer scale in the size range of 1 to 100 nm. The lower limit is restricted by size of individual atoms, knowing that at the molecular scale, atoms are the building blocks of materials, whereas the higher limit is more or less unrestrained with the 100 nm value, but is rather the size at which the specific phenomena obtained from nanomaterials are not observed anymore.<sup>10</sup> The prefix “nano” is derived from the Greek *νᾶνος* or the Latin word *nannus*, meaning "dwarf". It has been adopted as an official SI prefix, meaning  $10^{-9}$  of an SI base unit at the 11<sup>th</sup> Conférence Générale des Poids et Mesures (CGPM) in 1960.<sup>11</sup>

Despite the absence of the term “nano-technology” till 1974 where it was introduced by Norio Taniguchi,<sup>12</sup> who was inspired by the famous talk of Richard Feynman “There's Plenty of Room at the Bottom”,<sup>13-14</sup> the use of nanomaterials and nanoparticles belongs to a much older era. For instance, the red glasses of the late Bronze Age (1200-1000 BCE) from Frattesina di Rovigo (Italy) were colored through the excitation of copper nanoparticles on their surfaces.<sup>15</sup> On the other hand, one of the earliest uses of gold and silver nanosized particles goes back to the 4<sup>th</sup> century with the “Lycurgus Cup” manufactured by the Roman Empire.<sup>16</sup> Moreover, metallic luster decoration of glazed ceramics appeared in Mesopotamia

during the 9<sup>th</sup> century,<sup>17</sup> where these materials were mainly used for their outstanding optical properties. Again, during the Renaissance Period in Italy (15<sup>th</sup> and 16<sup>th</sup> centuries) different iridescent or metallic glazed ceramics were found in the potteries of Deruta (Umbria). They achieved these effects by using particles of copper and silver (between 5 and 100 nm) in their glazes. This caused the light to bounce off their surface at different wavelengths, thus giving it the “iridescent” look. Furthermore, over a thousand years ago, the Chinese people were known to use gold nanoparticles as an “inorganic dye” to create a red color in their ceramic porcelains.<sup>18</sup>

Although nanoparticles and nanomaterials have been widely used given their unique properties, and different “recipes” have been developed for their preparation throughout history (mainly during the 15<sup>th</sup> and 16<sup>th</sup> centuries),<sup>19</sup> the first scientifically described synthesis of nanoparticles was published in 1857 by Michael Faraday,<sup>20</sup> who reported the formation of a deep red solution of colloidal gold through the reduction of chloroaurate ( $\text{AuCl}_4^-$ ) using white phosphorous in  $\text{CS}_2$ . Faraday also investigated the interest of the obtained dried colloids in optics after observing change in color from the deep red-bluish into green upon pressurizing. Later on, Thomas Graham in his discussion about the liquid diffusion in 1861,<sup>21</sup> proposed the use of the term colloid (coming from the French word “*colle*”) for the first time. Further, the field attracted a higher number of researchers and numerous developments took place with different milestones. As an illustrative example, one can cite the discovery of Surface Plasmon Resonance (SPR) in 1902 by R.W. Wood,<sup>22-23</sup> who in addition to the work of Gustav Mie in 1908 on the scattering and absorption of electromagnetic fields by a nanosphere, explained the color change of particles (studies on gold) with the change of size.<sup>24</sup> This was followed by a huge advancement that finally overcame the barrier to a higher resolution microscopy through the invention of the transmission electron microscope in 1931 by Max Knoll and Ernst Ruska. This latter was awarded with the Nobel prize for this work in 1936.<sup>25</sup> Couple of years later, Manfred von Ardenne developed the scanning electron microscope in 1937.<sup>26</sup> This brings us back again to the talk of Richard Feynman “There's Plenty of Room at the Bottom” at the American Physical Society meeting at Caltech in 1959,<sup>13-14</sup> where he invited the research community into the new field of manipulating at the atomic scale, this field which was later called “nanotechnology” by Norio Taniguchi in 1974.<sup>12</sup>



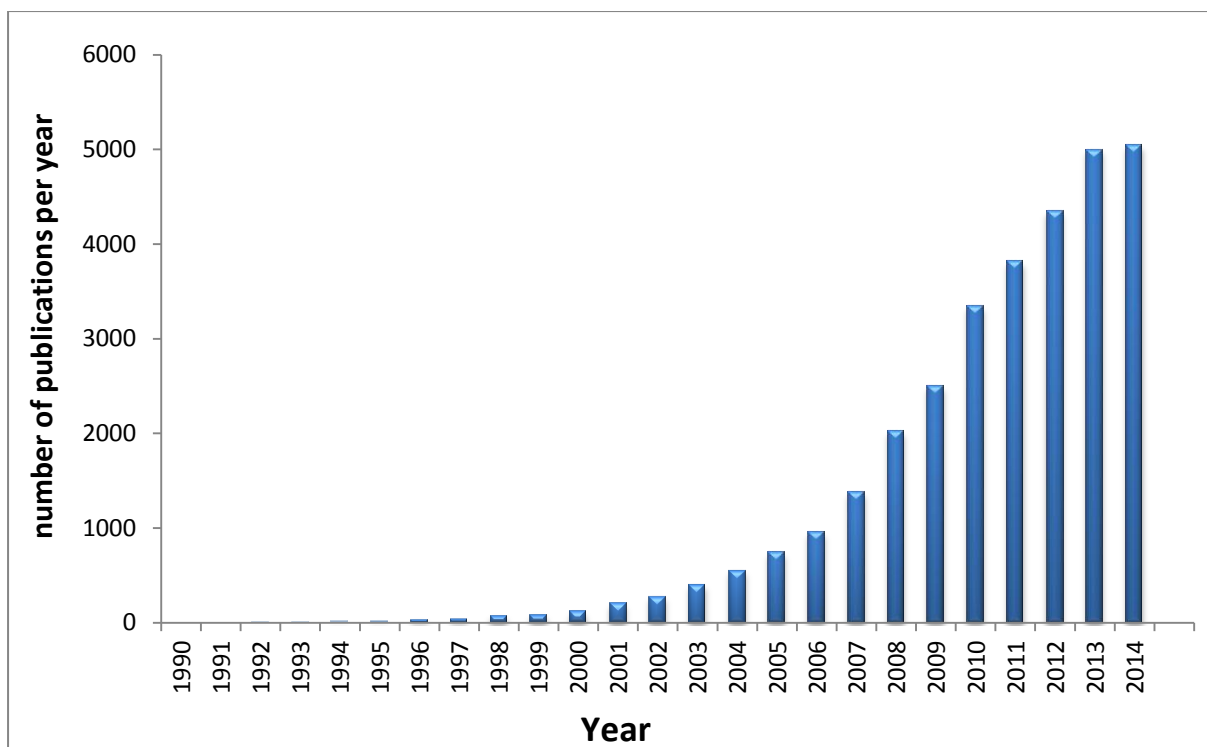
These advances opened the door for different research domains at the nanoscale, such as the discovery of carbon nanofibers by Morinobu Endo<sup>27-28</sup> and of the amorphous silicon solar cells by Carlson<sup>29</sup> in 1976. Subsequently, the Nobel Prize was awarded to the work of Klaus von Klitzing on the quantum hall effect in 1980.<sup>30</sup> This is in addition to the evolution of new techniques of characterization and manipulation of metal particles, like the Scanning Tunneling Microscope (STM) in 1982<sup>31</sup> (Nobel Prize 1986) and the Atomic Force Microscopy (AFM) in 1986<sup>32</sup> by Gerd Binnig and Heinrich Rohrer.

All these advances and developments led to the discovery of novel applications for the nano-sized particles. For example, in 1987 Masatake Haruta *et al.*<sup>33</sup> showed that the so believed chemically inert gold metal is not inert anymore when it is at the nanoscale (<5nm) and can be a very effective catalyst in the oxidation of carbon monoxide. The fact that particles at the nanoscale showed unique catalytic properties initiated a huge research concerning both the explanation of this quite unexpected effect and the search for chemical reactions that can be catalyzed by nanoparticles in general.<sup>34</sup>

With the interesting and unique properties of metal nanoparticles and the recent evolution of novel nanomaterials (carbon nanotubes,<sup>35</sup> graphene<sup>36</sup>...), different national and international initiatives have been launched to develop and advance this field including Japan's National Project on Ultimate Manipulation of Atoms and Molecules (1992), National Nanotechnology Initiative NNI, USA (2000), 21<sup>st</sup> Century Nanotechnology Research and Development Act, USA (2003), Nanosciences and Nanotechnologies: An action plan, Europe (2005).

### I.1.2 Interests of Metal Nanoparticles

Over the last few years, scientific and engineering communities witnessed an evolution of interest and investments in the fields of nanoscience and nanotechnology.<sup>37</sup> This evolution was evident through the exponentially increasing number of publications in the literature concerning this topic during the last 2 decades (Figure 1.1), reaching over 5000 publications in 2014. One of the key driving forces for this rapidly developing field is the high potential of nanoparticles, especially the metallic ones, in different scientific fields including chemistry,<sup>38</sup> physics,<sup>39</sup> biology,<sup>3</sup> medicine,<sup>3</sup> electronics,<sup>40</sup> material science<sup>41</sup> and others.

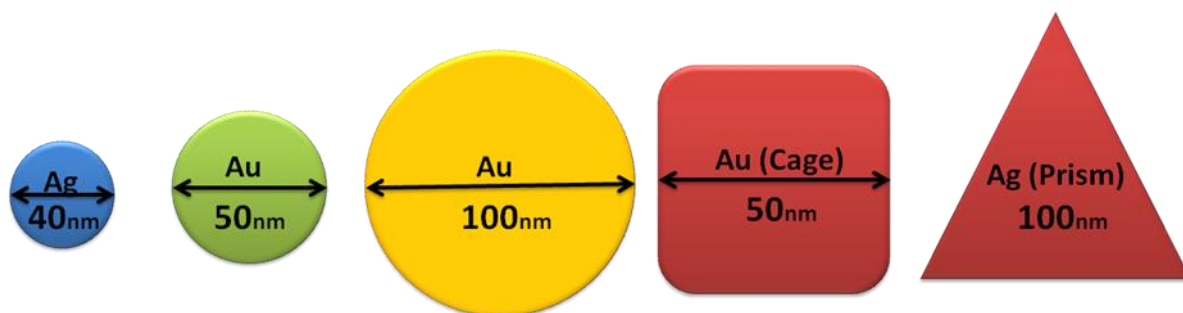


**Figure 1.1:** Number of publications dealing with metal nanoparticles (1990–2014). (Source: SciFinder Scholar. Keywords: Metal nanoparticles)

The interests of metallic nanoparticles also called “nanoclusters” mainly come from their state of matter that is positioned on the border between their molecular and bulk counterparts.<sup>42</sup> They are larger than individual atoms and molecules but are small enough to not be considered as bulk solid; hence they obey neither absolute quantum chemistry nor laws of classical physics and have properties that differ markedly from those expected.

Concerning electrical and optical properties, colloidal solutions of MNPs, of gold and silver especially, display very attractive properties, due to different interactions with light in the visible to near-infrared (NIR) regions (Figure 1.2),<sup>43</sup> in addition to unpredicted conductivity behavior. These properties were found to be very shape and size-dependent, unlike their respective bulk state. For instance, spheres of gold with diameters of 1 m, 1cm and 1 mm will all be shiny and gold colored, and will exhibit metallic properties such as malleability and conductivity. At the macroscale, all of these properties remain the same. However, when spheres of gold become very small, those properties change. At the

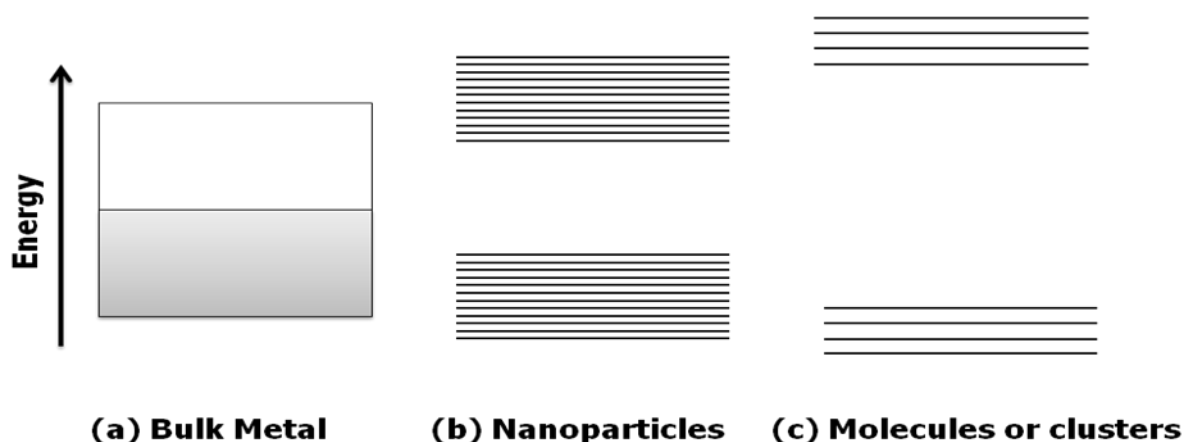
nanoscale, the color of gold particles becomes very sensitive to the size. Gold spheres with a diameter of 13 nm suspended in solution (a colloidal solution) afford a red color. At sizes less than 10 nm, gold loses its metallic properties and is no longer able to conduct electricity. Therefore, studying a variety of size-dependent phenomenon where finite size effects take place becomes important.<sup>44</sup>



**Figure 1.2:** Different colors for colloidal solutions of gold and silver nanoparticles depending on their size and shape.<sup>45</sup>

Comparing electronic properties (like conductivity, magnetism, etc.) of a metal nanoparticle with its corresponding bulk metal, the density of states in the valence band and the conductivity band decreases respectively with the reduction of size (tens to hundreds of atoms) to such an extent that the electronic properties change dramatically (Figure 1.3).

According to Günter Schmid<sup>46</sup> this quantum size effect can be demonstrated as follows: on the way from an electronically three-dimensional (bulk system) to a zero-dimensional system (quantum dots) the density of states will continuously decrease. In practice, a nanoparticle has a dimension of a particle containing hundreds or thousands of atoms. It is of great importance that electrons trapped in such a particle must have discrete energy levels that replace the quasi-continuous density of states.<sup>46</sup>

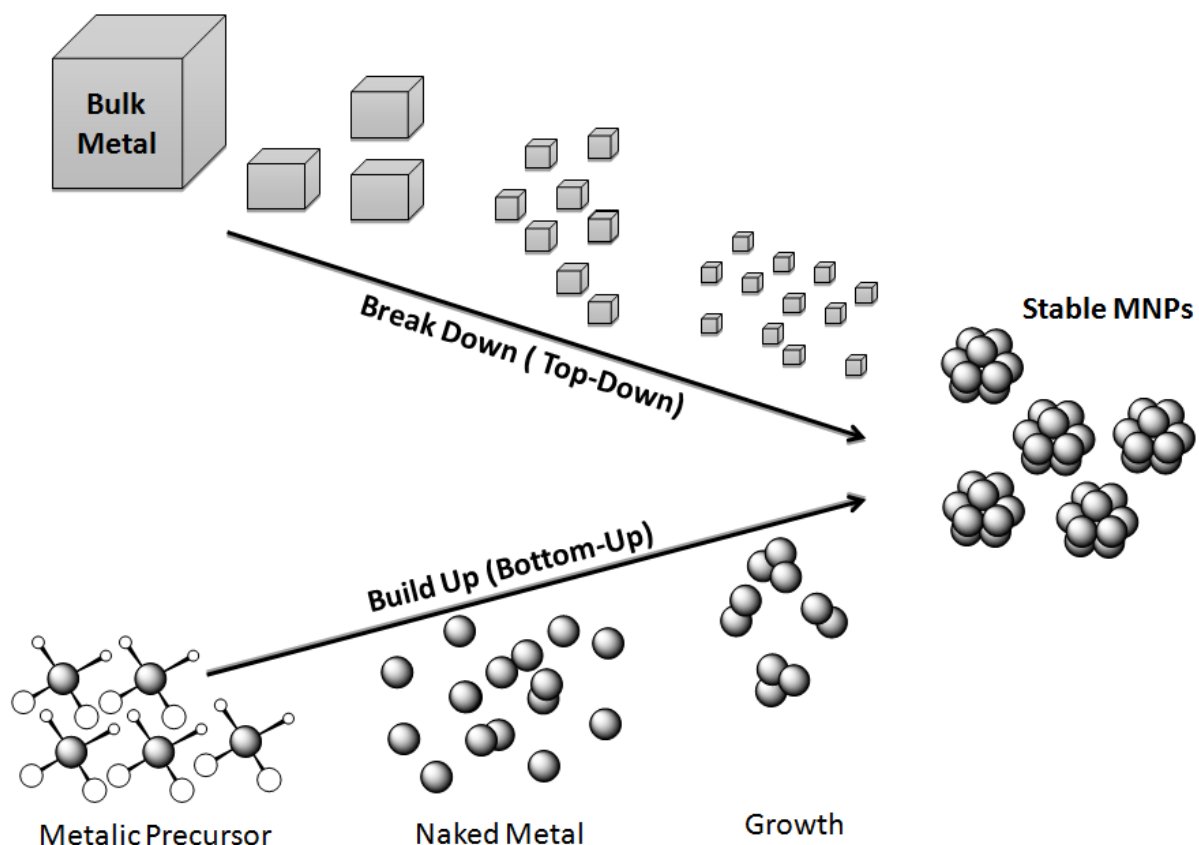


**Figure 1.3:** Representation of the electronic state in (a) bulk metal, (b) nanoparticles and (c) small molecular clusters.

## I.2 Synthesis of Metal Nanoparticles

In literature, different techniques have been reported for the preparation of metal nanoparticles from old times till nowadays. For a method to be considered as effective it should fulfill several conditions, mainly control of size, shape, and crystal structure, stable chemical and physical properties. It should also control the aggregation rate, achieve the lowest possible impurities presence, and make it possible of scaling up and reproducibility with the lowest costs.

According to Satoshi Horikoshi and Nick Serpone,<sup>47</sup> the different synthesis techniques can be divided into two main approaches; the first is the breakdown (top-down) method by which an external force is applied to a solid that leads to its break-up into smaller particles. The second is the build-up (bottom-up) method that produces nanoparticles starting from atoms of gas or liquids based on atomic transformations or molecular condensations (Figure 1.4).<sup>47</sup>

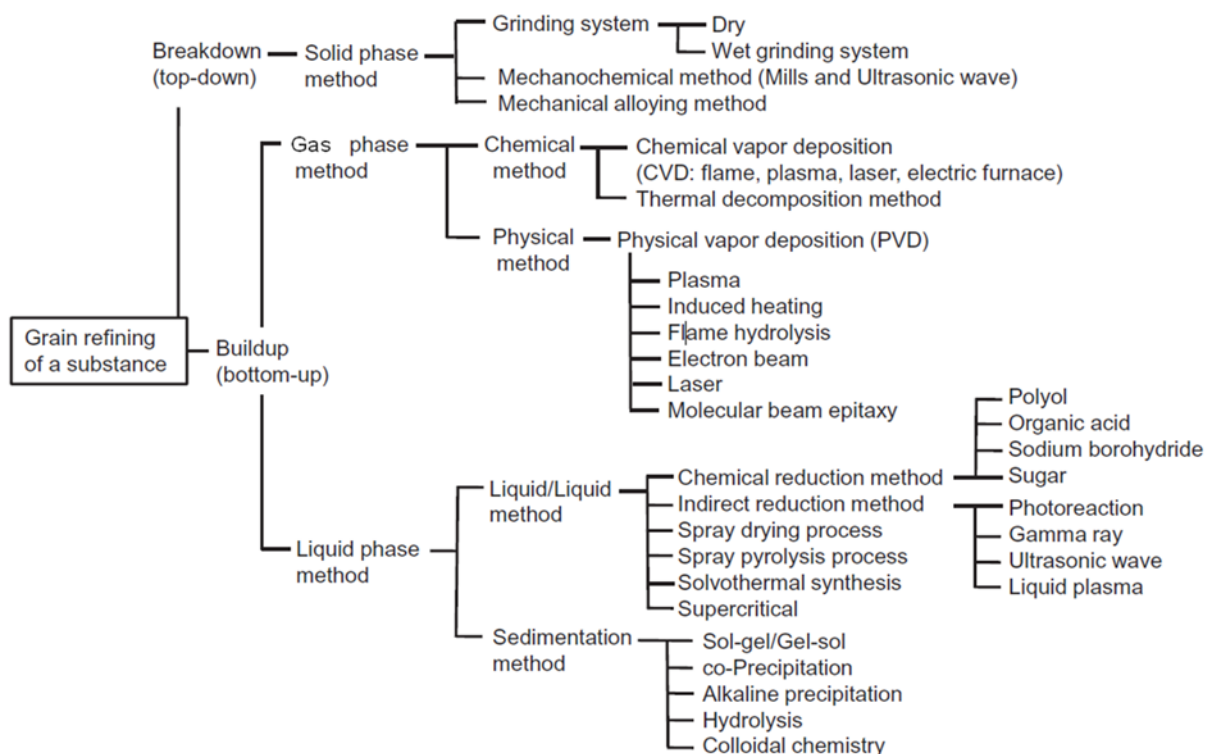


**Figure 1.4:** General approaches for the synthesis of metal NPs. (Top down=physical, and Bottom Up=Chemical)

The top-down approach is based on breaking up a bulk solid material into fine and ultra fine particles. In general, it is a dry or wet physical grinding method where bulk matter put under shock, compression, or friction. The drawback of this approach is that it is difficult to obtain highly dispersed particles due to simultaneous condensation of small particles that takes place with the pulverization (grinding) step. Wet grinding could partially overcome this obstacle by decreasing condensation phase.<sup>48</sup>

On the other hand, the bottom-up approach is roughly divided into gaseous phase methods and liquid phase ones (Figure 1.5). For the former (gaseous), although these methods minimize the occurrence of organic impurities in the particles compared to the liquid phase methods, they necessitate the use of complicated vacuum equipment whose disadvantages are the high costs involved and low productivity. Liquid phase methods are the major preparation routes to obtain nanoparticles, and a wide range of different ways exist (Figure 1.5). For example, chemical reduction method is the most commonly used one in fine chemistry, as a principal advantage the possibility to obtain particles of various sizes and

shapes, such as nanorods, nanowires, nanoprisms, nanoplates, and hollow nanoparticles. Using this method, it is possible to tune the morphology and size of the nanoparticles by manipulating different variables such as the metal source, the reducing agent,<sup>49-50</sup> the stabilizer,<sup>51</sup> the solvent,<sup>52</sup> the reaction time and the temperature.<sup>53</sup>

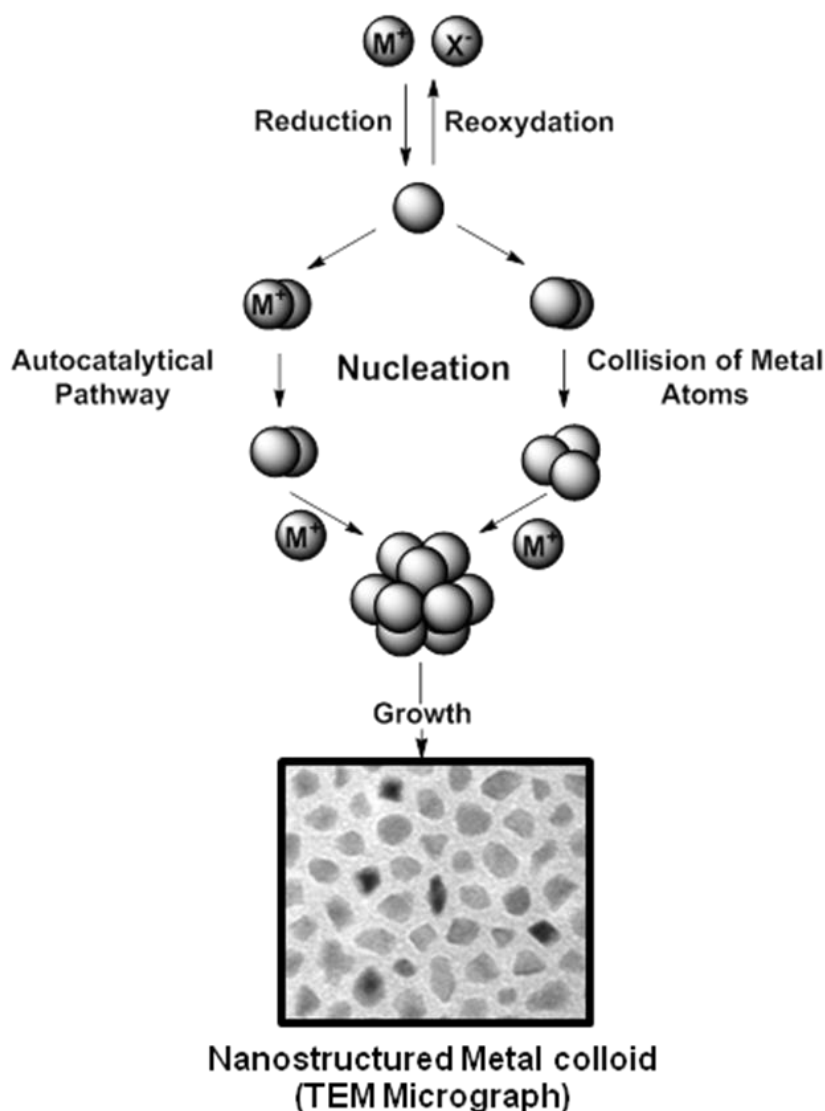


**Figure 1.5:** Different methods for the preparation of metal nanoparticles (adapted from: *Microwaves in Nanoparticle Synthesis*<sup>47</sup>)

### I.2.1 Nucleation and Growth of Metal Nanoparticles in Solution

In 1970, John Turkevich published the first standard reproducible protocol for the preparation of metal colloids (20 nm gold by reducing  $[\text{AuCl}_4]_2$  with sodium citrate).<sup>54</sup> He also proposed a mechanism for the stepwise formation of nanoclusters based on nucleation, growth, and agglomeration, which in essence is still valid. Data from modern analytical

techniques and more recent thermodynamic and kinetic results have been used to refine this model, as illustrated in Scheme 1.1.



***Scheme 1.1:*** Formation of nanostructured metal colloid by the ‘salt reduction’ method, (adapted from reference<sup>55</sup>)

Nucleation is known to be the key step and the very first stage of the synthesis of metal nanoparticles. Despite the scientific importance of this phenomenon and the tremendous efforts that have been devoted to this subject, attempts to examine, understand, and control this process have met with limited success,<sup>56</sup> due to the absence of suitable techniques for capturing the nuclei evolution. It is also difficult (if not impossible) to follow the formation of nuclei directly in real space and time. Since, by the time a particle is visible using an electron microscope, it has already grown beyond the nucleation stage.

In a primary step of the nucleation process, the metal salt is reduced to give zerovalent metal atoms (naked atoms),<sup>57</sup> which collides with other atoms, or small clusters, to form the first irreversible “seeds” of stable metal nuclei. The diameter of the “seeds” can be well below 1 nm depending on the strength of the metal-metal bonds and the difference between the redox potentials of the metal salt and the reducing agent applied.<sup>58</sup>

### I.2.2 Chemical Reduction

In 1857, Faraday published the first chemical reduction of transition metal salts in the presence of stabilizing agents in order to generate stable zerovalent metals in aqueous or organic media.<sup>20</sup> This approach has become one of the most common and powerful synthetic methods of nanoparticles in this field.

The reduction method allows controlling the size and the shape of the transition metal nanoparticles that are formed, these characteristics being very important for their properties towards applications. The different reduction methods that have been developed to synthesize colloidal transition metal nanoparticles for catalysis are summarized below.

- Chemical reduction of transition metal salts is the most widely known method for synthesizing metal nanoparticles in colloidal solution mainly, for applications in catalysis. The reduction of a metal salt in solution can be performed using various reducing agents like alcohols, dihydrogen, sodium borohydrate, silanes, etc. Zerovalent metal nanoparticles can also be obtained after reduction of metal-organic complexes, mainly under H<sub>2</sub> atmosphere or using NaBH<sub>4</sub>.
- Thermal,<sup>59</sup> photochemical,<sup>60</sup> or sonochemical<sup>61</sup> reduction of transition metal salts have been also developed.
- Ligand reduction or their displacement from organometallic precursors.<sup>62</sup>
- Electrochemical reduction of transition metal salts.<sup>61</sup>
- Metal vapor synthesis.<sup>63</sup>

Stabilization of nanoparticles in the solution is necessary in order to prevent their agglomeration and aggregation. For catalytic applications, the choice of the stabilizer plays an important role in determining the reactivity of MNPs.

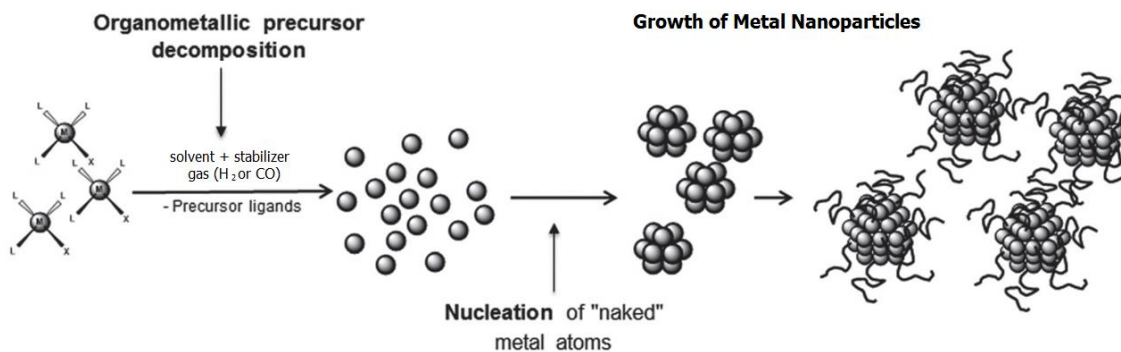


### I.2.3 Organometallic Approach

Physical and chemical properties of nanostructures, which are at the origin of their various applications, may vary dramatically with the variation of their size, shape and surface state. Thus, development of efficient methods that allow controlling the characteristics of metal nanoparticles in a reproducible manner is a fundamental objective in modern nanosciences. The use of organometallic chemistry techniques was found to be an efficient mean for achieving this and inspiring the formation of well-controlled nanostructures. The organometallic approach for the synthesis of metal nanoparticles is based on using an organometallic complex as the source of metal in combination with a suitable stabilizing agent which might be various functional organic molecules,<sup>64</sup> surfactants,<sup>65</sup> polymers,<sup>66</sup> dendrimers,<sup>67</sup> ionic liquids,<sup>68</sup> etc. In liquid solutions, the metal nanoparticles are close enough to each other to be affected by van der Waals forces. If there isn't anything to oppose these forces, then the nanoparticles will aggregate, which will lead to a change of size and properties, for example, in activity by lowering the active surface area.<sup>69</sup> So, the choice of the stabilizer is fundamental as it will influence the growth, stability and surface chemistry of the nanostructures, in addition to its potential role for any target application.

The choice of organometallic precursors is governed by their ability to be decomposed in mild reaction conditions. Their decomposition is generally performed using a gas that can be H<sub>2</sub> or CO to give the naked zero-valent metal atoms.<sup>1</sup> Both H<sub>2</sub> or CO are reducing gases. They can thus decompose or reduce the metal precursors when they are not in the zerovalent oxidation state or displace the ligands present in the coordination sphere of the metal center by simple substitution for CO (leading to unstable intermediate) or by reduction for H<sub>2</sub>.

Treatment of the organometallic complexes under H<sub>2</sub> or CO releases naked and free metal atoms in solution. These atoms will tend to associate together to form the irreversible seeds, that are the center of growth of the particles. The stabilizers will interact chemically with the surface of the growing particles or make a steric barrier around them, thus controlling their size by preventing them from excessive agglomeration (Scheme 1.2). Size control of the particles can derive from electrostatic forces (chemical bonding) when employing coordinating ligands,<sup>70-71</sup> or from sterical hindrance which limits the growth of the particles, when using polymers<sup>72-73</sup> or dendrimers.<sup>74</sup>



**Scheme 1.2:** Schematic representation of the organometallic approach for the synthesis of metal nanostructures. (adapted from reference <sup>75</sup>).

Ideally, olefinic and allylic complexes are the most attractive type of metal precursors since under dihydrogen pressure in mild reaction conditions, the unsaturated ligands give rise to alkanes which are innocent to the surface of the nanoparticles. For example,  $[\text{Rh}(\text{C}_3\text{H}_5)_3]$ ,<sup>76-77</sup>  $[\text{Ni}(\text{cod})_2]$  (cod = 1,5-Cyclooctadiene),<sup>4</sup>  $[\text{Ru}(\text{cod})(\text{cot})]$  (cot = 1,3,5,7-Cyclooctatetraene),<sup>71</sup>  $[\text{Re}_2(\text{C}_3\text{H}_5)_4]$ ,<sup>78</sup>... all decompose easily under low pressure of dihydrogen, resulting in a very good metal source for nanoparticles synthesis. In addition to this type of precursors, mixed complexes are also interesting when they also decompose in mild conditions but they release potential stabilizing molecules for the particles. For example, complexes such as  $[\text{Rh}(\text{acac})(\text{C}_8\text{H}_{12})]$ <sup>79</sup> (acac =  $(\text{CH}_3\text{CO})_2\text{CH}$ ) or  $\text{CpCu}^t\text{BuNC}$ <sup>80</sup> (Cp =  $\text{C}_5\text{H}_5$ ), that release acacH and  $\text{CpH}^t\text{BuNC}$  respectively.

Although the use of carbonyl complexes resulted in well-stabilized NPs with several complexes including  $\text{Co}_2(\text{CO})_8$ ,  $\text{Rh}_6(\text{CO})_{16}$  and  $\text{Ir}_4(\text{CO})_{12}$  and else,<sup>81-82</sup> but a major drawback is the necessity of the high temperature to decompose the precursors, in addition, to the release of the CO molecules which is well-known to coordinate to the surface of metal NPs, blocking the active sites in different application mainly catalysis.

### **I.3 Characterization Methods of Metal Nanoparticles**

Since nanoparticles are considered to be special materials given their very small size, different techniques are required to characterize their properties and to understand their chemical/physical behavior. The most effective and used methods include the basic transmission electron microscopy (TEM) and the high resolution one (HR-TEM), elemental analysis and Energy-Dispersive X-ray Spectroscopy (EDS), Dynamic Light Scattering (DLS), UV-visible spectroscopy, Infrared Spectroscopy (IR), Nuclear Magnetic Resonance (NMR) Spectroscopy in different states, Wide Angle X-ray Scattering (WAXS), Extended X-ray Absorption Fine Structure (EXAFS), X-ray Absorption Near Edge Structure (XANES), X-ray Photoelectron Spectroscopy (XPS), Atomic Force Microscopy (AFM), X-ray Diffraction (XRD), among other techniques.

In the following sections a brief description of the different characterization techniques used in this PhD work is given.

#### **1.3.1 Transmission Electron Microscopy (TEM) and Energy-dispersive X-ray spectroscopy (EDX)**

Transmission Electron Microscopy (TEM) is a very useful characterization tool for directly imaging nanomaterials and obtain quantitative measures of particle and/or grain size, size distribution, as well as morphology. It is a microscopy technique in which a beam of electrons is transmitted through an ultra-thin specimen, interacting with the specimen as it passes through. An image is formed from the interaction of the electrons transmitted through the specimen; the image is magnified and focused onto an imaging device, such as a fluorescent screen, a layer of photographic film, or to be detected by a sensor such as a CCD camera. However, because electrons are used rather than light to illuminate the sample, TEM imaging has significantly higher resolution (by a factor of about 1000!) than light-based imaging techniques. Although, TEM might present some limitations such as only black and white images, high cost, sensitivity toward magnetic particles, and structural rearrangement and agglomeration, but it is almost always the first method used to determine the size and size distribution of nanoparticle samples.<sup>83</sup>

Energy-dispersive X-ray spectroscopy (EDS, EDX, or XEDS) systems are typically integrated into electron microscopy instruments. It is an analytical technique used for the elemental analysis or chemical characterization of a sample. It separates the characteristic x-rays of the different elements present in the sample that are emitted due to the interaction of the electron beam and the sample, and transfer them into an energy spectrum. By this way, the abundance of specific elements (qualitatively and quantitatively) in a given sample can be determined.

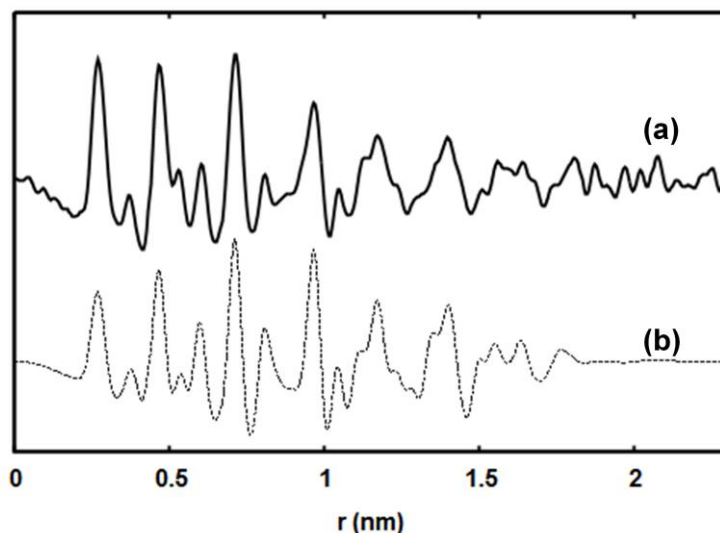
### 1.3.2 Wide Angle X-Ray Scattering (WAXS)

Wide angle X-ray scattering(WAXS) is a non-destructive analytical technique which reveals information about the crystal structure, chemical composition, and physical properties of materials and thin films. This technique specifically refers to the analysis of Bragg peaks scattered to wide angles, which (by Bragg's law) implies that they are caused by sub-nanometer-sized structures.<sup>84</sup>

Well-dispersed metal nanoparticles with a size smaller than 4 nm can be treated as an amorphous material, since the long range crystalline order disappears in such size range. Therefore, typical X-Ray diffraction techniques are not effective. In contrast, diffusion signal remains. The irradiation of metal nanoparticle samples with an X-Ray of sufficiently short wavelength (e.g. molybdenum or silver  $K\alpha$  radiation) induces a secondary emission of radiation scattering rays in all directions of the space.

The samples are generally measured in solid state inside Lindemann thin capillary tubes. After subtraction of the tube and the atmospheric contributions, subtraction of the contribution of the matrix, ligand or polymer, in which the NPs are embedded, correction for absorption and polarisation of incident radiation, the obtained corrected intensity is the result of 3 data: chemical composition and structure of the particles and the interaction between them. Samples in concentrated solutions can be measured also.

Finally, to ease the interpretation of the obtained intensity peaks, conversion of the powder diagram into direct space and thus access to the Radial Distribution Function (RDF) is achieved by means of a simple Fourier transformation (Figure 1.6). Comparison with the theoretical data obtained by modeling, helps in determining the crystalline structure of the particles (position and intensity of the peaks are compared), as well as the coherence length (longest metal-metal distance).



**Figure 1.6:** WAXS analysis of Rh NPs embedded in PVP polymer. Comparison between (a) the experimental measurement of Rh/PVP NPs and (b) the theoretically calculated RDF of Rh NPs with fcc structure and a 2.5 nm size.<sup>85</sup>

### 1.3.3 Nuclear Magnetic Resonance (NMR) Spectroscopy

Nuclear magnetic resonance (NMR) spectroscopy is a powerful technique to address the gap formed by different characterization techniques of solid inorganic materials and solution phase molecular species. It facilitates routine, direct, molecular scale analysis of nanoparticle formation and morphology in situ, in both the solution and the solid phase.<sup>86</sup>

Application of NMR in surface chemistry studies of nanoparticles is particularly interesting, since MNPs prepared by wet chemical techniques are often capped with organic molecules. By combining the unique impact of metal conduction electrons on ligand nuclei with traditional NMR spectroscopy techniques, NMR investigation of these capping ligands can provide detailed insight into properties of the particle core (e.g., electronic structure, atomic composition, or compositional architecture) as well as important aspects of the ligand shell including ligand identity, arrangement, and dynamics.<sup>73</sup>

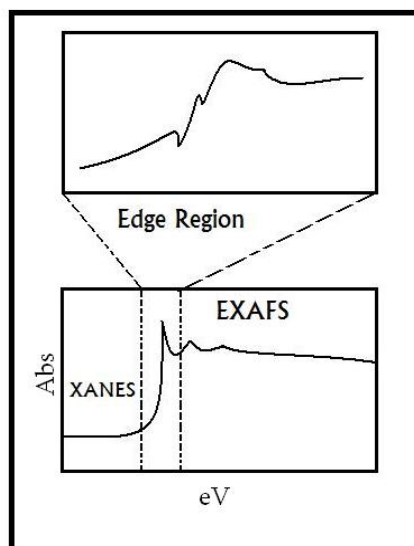
Another useful information of NMR spectroscopy in MNPs characterization is the Knight Shift which helps in understanding the electronic environment of metallic atoms inside the particles by the unusual displacement of broadened chemical shifts generated by the free electrons.<sup>87</sup>

### 1.3.4 Infrared Spectroscopy (IR)

Infrared (IR) spectroscopy techniques are very helpful in studying the surface state of the nanoparticles, especially the coordination of chemical compounds at their surface. Carbon monoxide can be used as a probe molecule to investigate the surface of the NPs. From CO vibrational frequencies we can analyze its coordination modes (terminal or bridging), that gives in turn valuable information on the surface state of the particles.<sup>73</sup>

### 1.3.5 X-Ray Absorption techniques

X-Ray absorption techniques including both Extended X-Ray Absorption Fine Structure (EXAFS) and X-ray Absorption Near Edge Structure (XANES), are widely used techniques for determining the local geometric and/or electronic structure of matter. The experiment is usually performed at synchrotron radiation sources, which provide intense and tunable X-ray beams.<sup>85</sup> EXAFS corresponds to the oscillating part of the spectrum to the right of the absorption edge (appearing as a sudden, sharp peak), starting at roughly 50 eV and extending to about 1000 eV above the edge (Scheme 1.3). Through mathematical analysis of this region, one can obtain local structural information for the atom in question, in particular the geometric analysis of amorphous crystalline solids.<sup>88</sup> XANES which corresponds to the left of the absorption edge (within ~50eV) in the spectrum (Scheme 1.3), it can give details about the electronic structure and the local arrangement of atoms around the absorbing atom, in addition to the ability of determining the chemical state of elements which are present in bulk.<sup>89</sup>



***Scheme 1.3:*** Schematic illustration of an X-ray absorption edge.

X-ray photoelectron spectroscopy (XPS), also known as Electron Spectroscopy for Chemical Analysis (ESCA) is a surface-sensitive quantitative spectroscopic technique that measures the elemental composition usually employed to investigate the electronic state and surface content of the NPs. It can be applied to a broad range of materials and provides valuable quantitative and chemical state information from the surface of the material being studied.<sup>85</sup> XPS is typically accomplished by exciting a sample surface with mono-energetic Al  $K\alpha$  x-rays causing photoelectrons to be emitted from the sample surface. An electron energy analyzer is used to measure the energy of the emitted photoelectrons. From the binding energy and intensity of a photoelectron peak, the elemental identity, chemical state, and quantity of a detected element can be determined.

#### **I.4 Applications of Metal Nanoparticles**

In the past history, people were using nanoparticles without understanding precisely their properties and behavior, mainly for optical applications.<sup>16-18</sup> Since the last century, with the evolution of nanosciences and nanotechnologies, metal nanoparticles received a great deal of attention due to their extraordinary properties which opened the doors for deep studies in

order to better understand them. Most of nanoparticle properties arise from their large surface-area-to-volume ratio and the spatial confinement of electrons, phonons, and electric fields in and around these particles. Their applications are helping to considerably improve, even revolutionize, many sciences, technology and industry sectors such as material science, information technology, energy, environmental science, medicine, food safety, and transportation, among many others, as briefly reported hereafter.

### **I.4.1 Medicine, Biotechnology, Food and Personal Care**

During the recent decades, metal nanoparticles emerged as an important domain in modern medicine, knowing that the nanoscale level is where most of the biology occurs. For instance, NPs of different noble metals such as gold,<sup>90</sup> silver,<sup>91</sup> platinum<sup>92</sup> have been widely used in cancer treatment to achieve highly sensitive diagnostic assays,<sup>93</sup> thermal ablation, and radiotherapy enhancement, as well as non-toxic carriers for drug and gene delivery.<sup>94</sup> Other metal nanoparticles like cerium oxide (nanoceria) have shown promise as catalytic antioxidants, to remove oxygen free radicals that are present in a patient's bloodstream following a traumatic injury. The nanoparticles absorb the oxygen free radicals and then release the oxygen in a less dangerous state, freeing up the nanoparticles to absorb more free radicals.<sup>95</sup>

Recently, different metal nanoparticles have been used in food industries, mainly silver<sup>96</sup> and titanium<sup>97</sup> particles as a new generation of antimicrobials. Also, NPs of titanium dioxide are commonly used as additive in many foods, personal care, and other consumer products used by people.

### **I.4.2 Energy and Electronics**

The unique properties of metal nanoparticles make them also capable to serve the field of electronics. Synthesis and fabrication of electrically conductive nanopatterns has become a necessity to advance the field, especially in the area of low cost or large area electronics on flexible substrates. Metal nanoparticles based Ink-jet direct writing has emerged as an attractive direct patterning technique,<sup>98-99</sup> which can be used in various applications such as photovoltaic cells, light-emitting diodes (LEDs), organic thin film



transistors, displays, radio-frequency identification devices (RFIDs), smart clothing and sensors.

### I.4.3 Manufacturing and Materials

In the industrial fields of technology and material manufacturing, several metal nanoparticles found to be of great interest to develop new approaches and novel materials. For instance, the use of a composite material made of nickel nanoparticles and a polymer, led to the production of a synthetic skin, which may be used in prosthetics. This nanomaterial has been demonstrated with both self healing capability and the ability to sense pressure by taking profit of the electrical resistance of the material which changes with pressure, giving it a sense ability like touch.<sup>41</sup> Another interest of metal nanoparticles in synthetic materials is found in the use of silver nanoparticles in the production of SmartSilver durable textiles. The integration of Ag NPs offers an effective protection against odor-causing bacteria, fungus, and mold in a variety of textiles, health care, and industrial products.<sup>100</sup> The use of zinc oxide nanoparticles as UV-absorbers in industrial coatings, plastics, and textiles is another example.<sup>101</sup> Iron nanoparticles are widely employed right now as additive in construction materials and coatings for their particular interest as a coloring and anti-corrosion agent.<sup>102</sup> Titanium dioxide nanoparticles are known for their ability to break down dirt or pollution when exposed to UV light and thus allowing to wash off by rainwater on different surfaces like tiles, glass and sanitarywares.<sup>103</sup>

### I.4.4 Environment

Although the excessive and uncontrolled use of metal nanoparticles in industrial and household applications might lead to the release of such materials into the environment, and consequently increase the environmental and health risks,<sup>104</sup> some metal nanoparticles were also found to be at the same time very powerful candidates to help solving big environmental issues. Iron nanoparticles, for instance, are one of the most extensively applied nanomaterials for groundwater and hazardous waste treatment by degrading a wide variety of common contaminants such as chlorinated and brominated methanes, trihalomethanes, chlorinated ethenes, chlorinated benzenes, other polychlorinated hydrocarbons, pesticides and dyes.<sup>105</sup> Gold nanoparticles embedded in a porous manganese oxide are successfully used as a room temperature catalyst to breakdown volatile organic pollutants in air.<sup>106</sup> Also metal

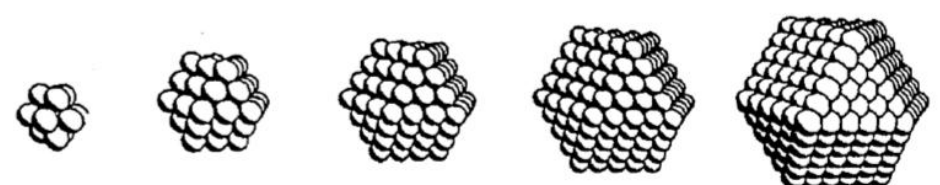
nanoparticles with nanocatalysis appears as a great solution in solving environmental issues, such as the evolution of biofuel from industrial wastes (lignin<sup>107</sup>, cellulose<sup>108</sup>...).

### I.4.5 Catalysis and Energy

Chemistry of the last century could not have been developed to its present state without catalysis, where approximately 85–90 % of the products of chemical industry are made by catalytic processes. Therefore, catalysts are of high importance in chemistry and without them, many reactions that are common in the chemical industry would not be possible, as well as many other processes would not be economical. These catalysts can be divided into two types: homogeneous and heterogeneous. Homogeneous catalysts are present in the same phase (gas or liquid) as the reactants and thus allow greater interaction with the reaction mixture. In the opposite, heterogeneous catalysts occupy a different phase. Typically, heterogeneous catalysts are solid materials placed in a liquid reaction mixture, thus leading to two different phases.

Heterogeneous catalysis benefits from easy removal of catalytic materials and possible use of high temperatures, but it suffers from lack of selectivity and understanding of the mechanistic aspects that are indispensable for parameter improvements. At the same time, homogeneous catalysis that overcomes the obstacle of selectivity and high efficiency, suffers from the difficulty or the impossibility of catalyst recovering of from the reaction media and most often limited thermal stability. That is why development of new catalysts that are able to combine the beneficial properties of both homogeneous and heterogeneous catalysts is essential. In this context, metal nanoparticles proved to be strong candidates to bridge the gap of differences between the two types,<sup>8</sup> owing to their unique large surface-to-volume ratios, electronic behavior, and quantum-size effects.

Given their colloidal specificity nanoparticles become “soluble” and should be available for homogeneous reactions. A colloidal catalyst may indeed be seen as a “heterogeneous catalysis in solution” due to the outer shell of stabilizers around NPs that is responsible for their solubility properties.<sup>46</sup> Therefore, nanocatalysts often combine higher reactivity and selectivity. This is induced by their large surface area, and consequently the large percentage of catalyst’s metal atoms that are available to react with the substrates (Figure 1.7).



Full-shell “magic number” clusters	1	2	3	4	5
Number of shells	1	2	3	4	5
Number of atoms in cluster	13	55	147	309	561
Percentage of surface atoms	92	76	63	52	45

**Figure 1.7:** Representation of full-shell metal clusters with “magic numbers” of atoms, which are built upon the densest sphere packing (adapted from reference<sup>109</sup>)

## I.5 Rhodium Nanoparticles in Catalysis

Since the discovery of Rhodium metal in 1803 by William Hyde Wollaston<sup>110</sup> it appeared that the scientific community showed little interest in this metal. This is mainly due to its low abundance and for being one of the most costly metals, until its essential role in catalysis was discovered.<sup>111-114</sup> Especially in the catalytic reactions of hydrogenation, hydroformylation, and oxidation reactions.

Rhodium based catalysts are found in literature as supported heterogeneous catalysts and dispersed homogeneous ones, as well as “pseudo-homogeneous” or “semi-

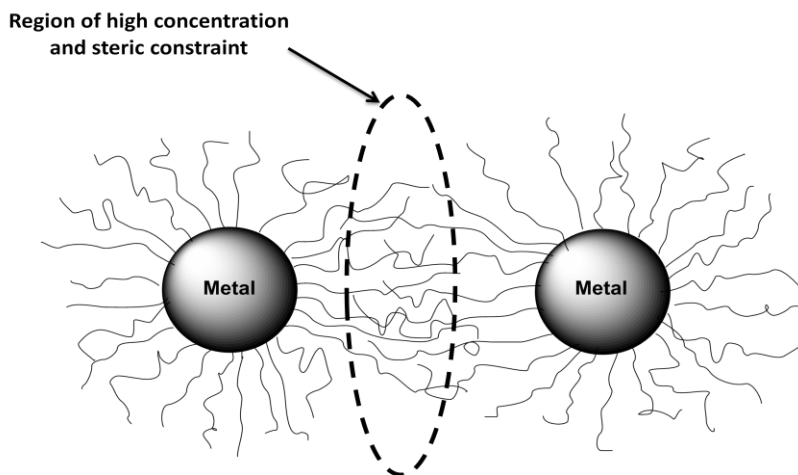
heterogeneous” nanocatalysts, also often called colloids, nanoclusters or nanoparticles.<sup>112</sup> These rhodium nanoparticles, as we mentioned before, combine the benefits of both homogeneous and the heterogeneous catalysts. In literature, nanocatalysts of rhodium deal with several catalytic reactions like carbon coupling,<sup>115-118</sup> oxidation,<sup>119-121</sup> and carbonylation reactions.<sup>122-123</sup> In addition, their uses in the energy field, being very active in the catalytic water splitting reactions,<sup>124-126</sup> they are also used as supported catalysts in fuel cells.<sup>127-129</sup> But the most cited catalytic applications of rhodium nanoparticles in catalysis are the hydrogenation and hydroformylation reactions. Focus on these two last reactions derives from their importance in industry, research, and many other different fields. The activity of rhodium metal in catalyzing these reactions is remarkable, as it will be illustrated here after.

### 1.5.1 Hydrogenation Reactions

Rhodium nanoparticles are considered to be among the most active hydrogenation catalysts covering a wide range of reactants and functional groups. That is why most of the publications dealing with rhodium nanoparticles in solution are dedicated to their application in hydrogenation reactions. We will discuss in the first part of this section the most recent and significant reports about Rh NP systems that are stabilized with polymers and macromolecules (especially PVP and cyclodextrins), while the second part will be dedicated to Rh NPs that are stabilized by ligands (mainly phosphines and surfactants), and their catalytic behavior in hydrogenation reactions.

#### 1.5.1.1 Polymers and Macromolecules as Stabilizers

One of the most efficient means for stabilizing rhodium nanoparticles by which metal colloids can be prevented from aggregating is to use macromolecules such as polymers or oligomers.<sup>130-131</sup> These organic polymers provide steric stabilization, where by the adsorption or the embedding of the metal into the polymer matrix, a protective layer around the metal surface is established, preventing the approach and aggregation of other colloids (Figure 1.8).



**Figure 1.8:** Schematic representation of steric stabilization of colloidal metal particles.<sup>69</sup>



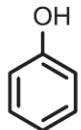

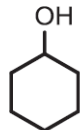
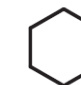
Using different types of polymers such as polyvinyl alcohol (PVA), poly(methyl vinyl ether) (PMVE) or polyvinylpyrrolidone (PVP), Hirai and coworkers published several papers describing the synthesis of noble metal nanoparticles obtained by refluxing the metal salts with the polymer in alcohols (like methanol, and ethanol) or in a mixture of alcohol and water. For instance, reflux of a solution of rhodium(III) chloride and poly(vinyl alcohol) (PVA) in a methanol-water mixed solvent under argon or air for 4 h gave rise to a homogeneous colloidal dispersion of rhodium particles (Rh-PVA-MeOH/H<sub>2</sub>O) with a particle size in the range of 3-7 nm. The same reaction using PVP in ethanol yielded in the formation of Rh-PVP-EtOH with a size of *ca.* 2.2 nm. These NPs were proven to be efficient in the hydrogenation of olefins and dienes at 30°C under an atmospheric hydrogen pressure.<sup>132</sup> Using the same synthesis approach, Delmas *et al.* performed extensive kinetic studies with RhPVP NPs in the hydrogenation of benzene or phenylacetylene in a biphasic mixture at 30 °C and under 7 bar of H<sub>2</sub>. The complete benzene conversion with a substrate/catalyst ratio of 2000 was observed after 8h, giving rise to a TOF (turn over frequency) of 250 h<sup>-1</sup>. No influence of the amount of water on the catalytic activity was observed.<sup>133</sup>

Choukroun, Philippot and Chaudret,<sup>134</sup> also used PVP to stabilize Rh NPs. This time, the nanoparticles were synthesized from the organometallic dimer complex [RhCl(C<sub>2</sub>H<sub>4</sub>)<sub>2</sub>]<sub>2</sub> in THF that was reduced by adding 2 equivalents of Cp<sub>2</sub>V in the presence of the PVP

polymer. The obtained Rh NPs were used as a heterogeneous catalyst or as a soluble heterogeneous catalyst in biphasic conditions (liquid/liquid) when the catalyst was dissolved in water. Hydrogenation of different arenes at 80 °C under 20 or 40 bar H<sub>2</sub> was achieved in with [catalyst]/[C<sub>6</sub>H<sub>6</sub>] ratio of 1/34000.

In 2004, Wai *et al.*<sup>135</sup> published a new approach for catalytic hydrogenation by using rhodium nanoparticles stabilized in plastics in supercritical CO<sub>2</sub>. Plastics in supercritical CO<sub>2</sub> conditions swelled allowing the metal precursors dissolved in the fluid phase to penetrate into the formed structures of the plastics. Then, the rhodium precursor (Rh(III) acetylacetonate ; [Rh(acac)<sub>3</sub>]) got reduced by dihydrogen pressure resulting in metallic nanoparticles trapped in the nano chambers of the swelled plastics similar to NPs stabilized in a polymer matrix. During catalytic hydrogenation, because of the hydrodynamic diameters of the obtained Rh nanoparticles was much larger than that of substrates (such as benzene and phenol), the plastic structures allowed the reactants to diffuse into the interior but not metal nanoparticles. After reaction, the hydrogenation products could be easily separated from the plastic catalysts by rapid expansion of CO<sub>2</sub>. These NPs were shown very active in arene hydrogenation. For instance, hydrogenation of benzene using high density polyethylene (HDPE) granules and fluoropolymer (PFA) as the plastic stabilizer of Rh was almost completed (99%) within 10 min at 50°C with 10 bar H<sub>2</sub> and 100 atm H<sub>2</sub>. Furthermore, phenol hydrogenation mostly yielded the cyclohexanone product with high selectivity (Table 1.1).

**Table 1.1:** Hydrogenation of Arenes Using Rh-PFA System.<sup>135</sup>

$[\text{Rh}(\text{acac})_3] \xrightarrow[\text{scCO}_2]{\text{PFA}} \text{Rh NPs (4-5 nm)}$			
Entry	Substrate	Conversion (%)	Products
1		>99	
2		60 / 33 / 3	  

<sup>a</sup> hydrogenation conditions: 50°C; 100 atm H<sub>2</sub>,

Kou, Evans and Mu<sup>136</sup> synthesized PVP-stabilized Rh NPs through ethanolic reduction of  $[\text{RhCl}_3 \cdot 3\text{H}_2\text{O}]$ , followed by their immobilization into ionic liquid of 1-n-butyl-3-methylimidazolium hexafluorophosphate ( $[\text{BMI}][\text{PF}_6]$ ). This approach resulted in 3 nm particles displaying high catalytic activity in hydrogenation of cyclohexene and benzene; 100% conversion was reached for both substrates at 1 bar and 40 °C in a reaction time of 2 and 10 h respectively, but TOF values appeared to be moderate with  $125 \text{ h}^{-1}$  for cyclohexene and  $25 \text{ h}^{-1}$  for benzene.

Matsumura and coworkers<sup>137</sup> also performed the synthesis of Rh PVP nanoparticles in an ethanolic solution, followed by their encapsulation in a hollow porous carbon shell. Obtained nanomaterials exhibited excellent catalytic activity for hydrogenation of aromatic and heterocyclic rings in aqueous media, with full conversion of *t*-butylbenzene into *t*-butylcyclohexane under 5 bar and 80 °C, against 27% conversion using pure Rh/PVP NPs under the same reaction conditions in 2 h reaction. They attributed this difference in catalysis to the porous wall structure of the hollow porous carbon shell that provides channels for efficient mass-transfer of species into the hydrophobic void space where active Rh nanoparticles are present.

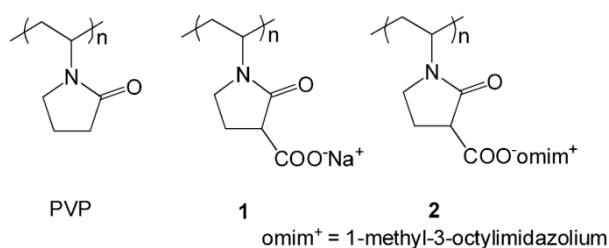
Dyson *et al.*<sup>138</sup> published the first direct combination of hydroxyl-functionalized ionic liquids and PVP as media for stabilizing Rh nanoparticles. This approach provided an effective and highly stable catalytic system for biphasic hydrogenation reactions. Comparisons to non functionalized ILs demonstrated the superiority of this system (full conversion of styrene under 50 bar of  $\text{H}_2$  at 40 °C for 2 h) with respect to activity, stability, leaching, and consequently recyclability.

Following also the ethanolic reduction of  $\text{RhCl}_3$  salt in the presence of PVP polymer, 2 nm rhodium particles were obtained by Lin and his group<sup>139</sup> to study the influence of their surface modification. In fact, the surface of these Rh NPs was modified by their partial encapsulation and distribution throughout a framework of mesoporous silica nanoparticles which were functionalized with thiol groups to get a chiral environment. That acted as a linker for the following tethering of (-)-cinchonidine (CD) chiral molecule. Enantioselective hydrogenation of ethyl pyruvate using free and immobilized Rh nanoparticles onto mesoporous silica nanoparticles without losing the reactivity and enantioselectivity of the catalyst (TOF =  $60 \text{ min}^{-1}$ , ee = 58%). The catalyst could be recycled or reused with the same

reactivity and selectivity as the fresh catalyst without any supplemental chiral reagent (TOF =  $60 \text{ min}^{-1}$ , ee = 58%).

Hensen *et al.*<sup>140</sup> evaluated the effect of the size of Rh PVP NPs (3.5 to 11.4 nm) on their performance as catalysts in the hydrogenation of phenylacetylene and 1-octene. Catalytic results showed that activity increased with Rh particle size in the hydrogenation of phenylacetylene (3.5 nm particles TOF=  $250 \text{ h}^{-1}$  ; 11.4 nm particles TOF=  $650 \text{ h}^{-1}$ ) , whereas the activity in 1-octene hydrogenation did not depend on particle size. This behavior was attributed to the difference in the adsorption site requirement (large surface ensemble for phenyl adsorption) and to the difference in rate limiting step. For phenylacetylene hydrogenation, the activation of the unsaturated bond is the rate limiting step, which is the formation of the C–H -bond for 1-octene. The substituent group attached to the unsaturated bond is suspected to have influence on the rate limiting step.

Yan, Yuan, and Dyson modified the structure of PVP polymer to enhance its stability and activity (Figure 1.9).<sup>141</sup> Rh NPs were synthesized either in water by reduction of  $\text{RhCl}_3$  salt using  $\text{NaBH}_4$  in the presence of the polymer, or by direct coating of preformed (naked) Rh NPs, synthesized in glycol, with the polymer. Whatever the method, the size and shape of Rh NPs for the two samples were the same. The obtained NPs were tested in the catalytic hydrogenation of arenes in water at  $60 \text{ }^\circ\text{C}$  under 20 bar of  $\text{H}_2$ . These catalysts were recycled and reused without loss of activity. Rh NPs stabilized by carboxylate modified PVP polymer (Figure 1.9, 1) were found to exhibit superior thermal and catalytic stability than PVP-stabilized ones (93% conversion modified PVP-stabilized Rh ; <70% of PVP-stabilized Rh). They attributed the enhanced stability to the presence of the carboxylate groups that may weakly coordinate to the NP surface and provide an electrical double-layer that helps to prevent aggregation.



**Figure 1.9:** PVP polymer and modified structures.<sup>141</sup>



Hanguli and Bhorali<sup>142</sup> recently performed the deposition of 3-4 nm Rh/PVP NPs, that were previously synthesized by NaBH<sub>4</sub> reduction of RhCl<sub>3</sub> salt, on mesoporous silica SBA-15. The obtained supported rhodium nanocatalysts showed high activity for hydrogenation of various unsaturated hydrocarbons and could be reused for several times without significant loss of activity.

Rossi *et al.*<sup>143</sup> performed the synthesis and the comparison, in catalytic hydrogenation of cyclohexene and different arenes, between polyvinyl alcohol (PVA) polymer stabilized Rh NPs and tetraoctylammonium bromide (TOAB) surfactant stabilized Rh NPs in both solution and magnetic silica supported state. Both catalysts showed considerably reproducible hydrogenation activity of mono- and di-substituted arenes at temperatures below 60 °C and H<sub>2</sub> pressures below 15 bar. Product separation was immediate due to the magnetic property of the nanomaterials, allowing facile recycling.

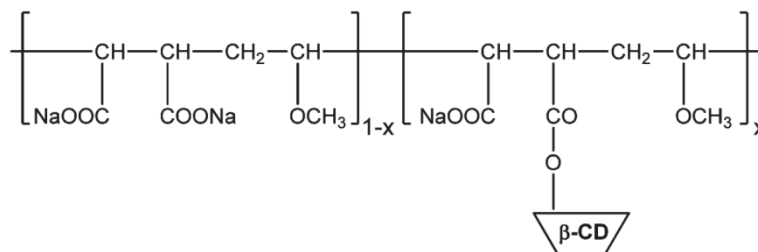
Very recently, Claver, Godard and Barbaro<sup>144</sup> described a clean route for the preparation of supported rhodium nanoparticle (3.0 ± 0.7 nm) catalysts onto commercial ion-exchange resins. This work was based on the use of [Rh(NBD)<sub>2</sub>]BF<sub>4</sub> as precursor which was reduced on the resin by either NaBH<sub>4</sub> or H<sub>2</sub> gas flow. The so prepared supported Rh NPs have been shown to be efficient catalysts in the hydrogenation reaction of diverse carbon-carbon double bonds under very undemanding conditions (full conversion of styrene into ethyl cyclohexane, P(H<sub>2</sub>)= 1 bar, r.t., TOF= 36 h<sup>-1</sup>), as well as to be easily recovered with neither activity loss nor metal leaching in solution upon reuse.

Use of macromolecules such as cyclodextrins (CDs) as protective agents in NPs synthesis has become increasingly common in the past few years. These compounds are generally considered as steric stabilizers, allowing particles entrapment, displaying weak interactions at the particle surface. Few papers describe the combination of Rh NPs and cyclodextrins in hydrogenation reaction.<sup>145</sup>

In 1983, Komitama and Hirai<sup>146</sup> have prepared rhodium colloids by the reduction of RhCl<sub>3</sub> salt with ethanol in the presence of α or β-CDs. Highly dispersed rhodium nanospecies were observed with an average diameter of 2.8 nm. They proposed that the particle surface is mostly covered with several CDs, avoiding NPs aggregation. These rhodium nanospecies

effectively catalyzed the hydrogenation of various olefins (3-buten-2-one; 3-methyl-3-buten-2-one; 3,4-dimethyl-3-penten-2-one) under 1 bar  $H_2$  and 30 °C.

Monflier and coworkers<sup>147</sup> stabilized Rh(0) NPs by a polymer containing carboxylate and  $\beta$ -cyclodextrin (Figure 1.10) moieties which resulted in a narrow size distribution centered around 2.5 nm, with high stability and catalytic activity for aqueous hydrogenation reactions of olefins and aromatic substrates reaching highest TOF of 2000  $h^{-1}$  under 10 bar of  $H_2$  at 303 K for 1-tetradecene, and a TOF of 250  $h^{-1}$  for styrene under the same conditions. This behavior was attributed to the conjugated steric interactions (polymeric structure and CD moiety) and electrostatic (carboxylate groups) interactions within the same macromolecules.



**Figure 1.10:** poly(mono-( $\beta$ -cyclodextrin-2-yl)-maleate-alt-maleate-alt-methylvinylether) used to stabilize Rh NPs.<sup>147</sup>

Very recently Kharakhanov and his group<sup>148</sup> evaluated the effect of cyclodextrins on the activity and selectivity of a catalytic system based on preformed rhodium nanoparticles stabilized by polyacrylic acid (PAA) in the hydrogenation of phenol in aqueous solution and ionic liquid. They found out that the activity and selectivity were significantly affected by the CDs, this was attributed to the ability of cyclodextrins to form host-guest inclusion complexes with both the initial phenol and the intermediately formed cyclohexenol, which isomerized to cyclohexanone later with yields up to 100% under relatively mild conditions (1 h; T = 80 °C, P( $H_2$ ) = 10–40 bars).

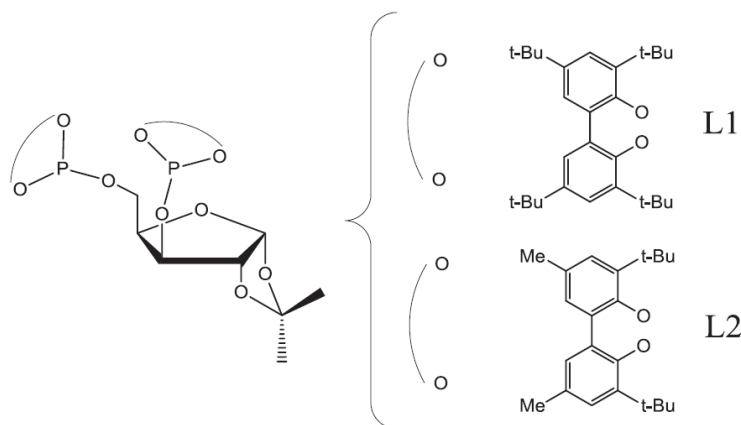
### 1.5.1.2 Ligands and Surfactants as Stabilizers

In addition to polymers and macromolecules, stabilization of metal NPs with ligands is today more and more investigated owing to their potentialities to tune the particle surface properties by the sterical and/or electronic influence of the ligand.<sup>149</sup> Another advantage of using ligands as stabilizers for nanoparticles in solution is their possible asymmetric character giving access to enantioselective catalysis. Nevertheless, it is necessary to find ligands giving rise to sufficiently stable but also active nanocatalysts.

In 1994, Lemaire et al.<sup>150</sup> used a chiral amine to stabilize Rh nanoparticles prepared under phase transfer catalysis conditions, catalytic hydrogenation of *o*-methylanisole and derivatives with the formation of *cis*-diastereomer with selectivity up to 97%. However, low ee values were observed back then.

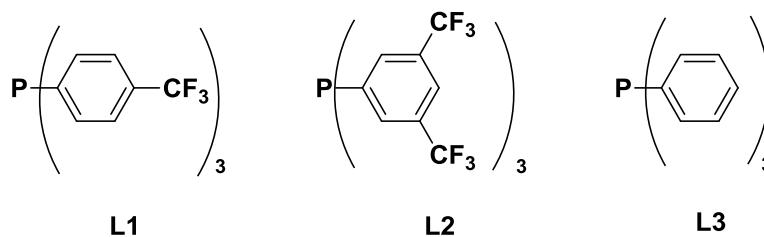
Philippot, Roucoux and Claver<sup>151</sup> reported the use of 1,3-diphosphite ligands derived from carbohydrates for stabilizing Rh NPs. These ligands were selected because of their successful enantioselective discrimination in several catalytic processes. Rh NPs were synthesized following the organometallic approach using  $[\text{Rh}(\eta^3\text{-C}_3\text{H}_5)_3]$  as the metal source under dihydrogen pressure. Colloidal ultra small NPs were obtained with 0.2 molar equivalent of the ligand with a size of 1.3 nm for ligand L1 and 2.4 nm for ligand L2 (Figure 1.11).

In the catalytic hydrogenation of *o*- and *m*-methylanisoles, in pentane and at room temperature, the Rh nanoparticles showed interesting catalytic activity. In all cases, total selectivity for the *cis*-product in the hydrogenation of *o*-methylanisole, however, the ee of the product was always less than 6%. A maximum of 81% *cis*-selectivity was obtained for the hydrogenation of *m*-methylanisole, however, no asymmetric induction was observed. Also, no effect was observed on the *cis/trans*-selectivity from H<sub>2</sub> pressure (2 vs. 40 bar H<sub>2</sub>). Moreover, all these results confirmed the positive effect of the alkyl chain of the ligand structure on the catalytic activity of the system (ee).



**Figure 1.11:** 1,3-diphosphite ligands used to stabilize RhNPs.<sup>151</sup>

Gómez and Masdeu-Bultó<sup>152</sup> used monophosphine ligands containing fluorinated groups (Figure 1.12) to control the growth and stabilize Rh NPs starting from the  $[\text{Rh}(m\text{-OMe})(\text{COD})]_2$  precursor resulting in particles in a size range of 1.7-2.5 nm.



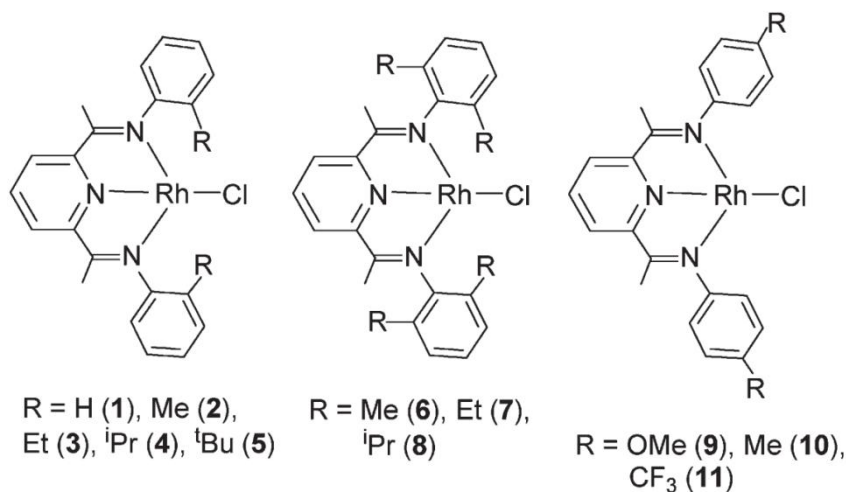
**Figure 1.12:** Fluorinated phosphine ligands used to stabilize Rh NPs.<sup>152</sup>

Obtained NPs were tested in the hydrogenation reactions of arenes derivatives in organic solvent (THF) and in supercritical carbon dioxide ( $\text{scCO}_2$ ). Results showed that NPs were less active in  $\text{scCO}_2$  than in THF (100% conversion of styrene with  $\text{RhNPs}_{\text{THF}}$ , 40% conversion of styrene with  $\text{RhNPs}_{\text{scCO}_2}$  under same reaction conditions  $T = 50\text{ }^\circ\text{C}$ ;  $t = 24\text{ h}$ ,  $P(\text{H}_2) = 20\text{ bar}$ ). This difference was attributed to the lower solubilities of the MNPs in  $\text{scCO}_2$  compared to THF even for the ligands containing fluorinated groups. For instance, different rhodium systems were able to hydrogenate the styrene totally in both solvents. But only in THF, the product corresponding to the full hydrogenated compound was formed (ethylcyclohexane), while, the major product was ethylbenzene in  $\text{scCO}_2$  medium.

In 2010, Vallribera and coworkers<sup>153</sup> published the synthesis of Rh NPs generated from a series of different rhodium Bis(imino)pyridine complexes (Figure 1.13)

(decomposition under 1 bar of hydrogen, in 2 propanol as solvent, at 60°C, and in the presence of KtBuO). No excess ligands were added to stabilize the particles, since these complexes are stabilized by the partially hydrogenated ligand. The resulting nanoparticles had a mean diameter of 1.5 nm.

Different arenes including benzene, toluene, p-xylene, styrene, aniline, phenol, pyridine and other derivatives were efficiently hydrogenated under hydrogen atmosphere and at 60 °C. Mercury poisoning test showed that arene hydrogenation is a heterogeneous process, highlighting the role of the Rh NPs in this reaction.



**Figure 1.13:** Rhodium Bis(imino)pyridine Complexes.<sup>153</sup>

Patin and coworkers<sup>154</sup> proposed the first amphiphilic colloidal Rh NPs, based on trisulfonated triphenylphosphine (TPPTS), in which the sulfonated phosphine acted both as the reducing agent and capping agent. They also widely investigated this system in catalytic hydrogenation of olefins. Later, using the same system Arzoumanian and Nuel<sup>155</sup> reported the influence of the addition of native ( $\beta$ -CD) or ionic ammonium ( $\beta$ -CD<sup>+</sup>) cyclodextrins in the reduction of olefinic acid derivatives. They found out that the addition of cyclodextrin increased the rate of the reaction and brought a high selectivity through its ability of formation of host-guest complexes *via* the olefinic function (Table 1.2). High selectivity was attained only in the presence of sulfonate ions which probably helped to stabilize the catalytic species.

**Table 1.2:** Hydrogenation of olefinic acids by the colloidal RhCl<sub>3</sub>/TPPTS system in the presence of β-cyclodextrins<sup>a</sup> (adapted from ref 155)

Entry	Acid	β-cyclodextrins <sup>b</sup>	Time (h)	Yield (%)
1	Acrylic acid	Ionic ammonium	24	100
2	Acrylic acid	Native	24	70
3	Acrylic acid	--	114	100
4	Methacrylic acid	Ionic ammonium	24	78
5	Methacrylic acid	Native	24	86
6	Methacrylic acid	--	80	100
7	Crotonic acid	Ionic ammonium	24	13
8	Crotonic acid	Native	48	16
9	Crotonic acid	--	48	100

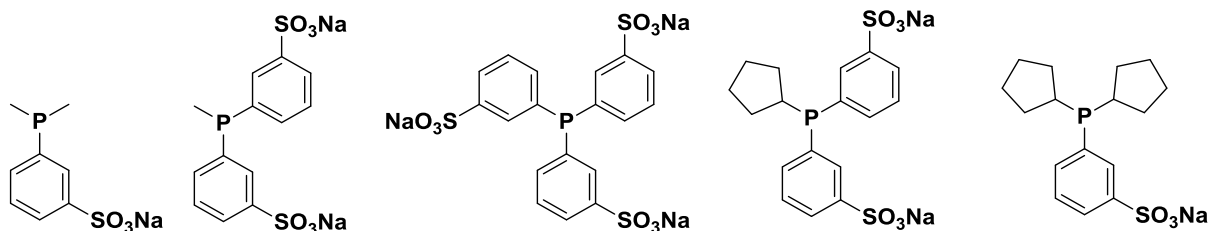
<sup>a</sup> Hydrogenation conditions: RhCl<sub>3</sub>·3H<sub>2</sub>O + 3TPPTS (0.5 mol%), CD (1 mol%), 5 mL H<sub>2</sub>O, 1 mmol of acid, 1 bar H<sub>2</sub>; <sup>b</sup> β-CD+ is a cationic CD modified by addition of an ammonium group (with an average substitution of one ammonium per cyclodextrin).

W. Kläui<sup>156</sup> introduced a phosphonate substituent (PO<sub>3</sub><sup>2-</sup>) to increase the solubility of the phosphane ligand Na<sub>2</sub>[Ph<sub>2</sub>PCH<sub>2</sub>CH<sub>2</sub>PO<sub>3</sub>]. Their corresponding water-soluble rhodium(I) complex was reduced by dihydrogen, providing isolated and dispersible rhodium nanoclusters given the electrostatic repulsion of the covering double negative charge of the phosphonate ligands in water. The mean diameter of the Rh NPs was 6 nm under atmospheric pressure, 3 nm and 2.5 nm at 30 bar and 60 bar H<sub>2</sub>, respectively. Catalytic hydrogenation of 1-hexene and benzene showed that under the same conditions smaller clusters exhibited significantly higher catalytic activity than larger ones (Table 1.3).

**Table 1.3:** Hydrogenation of 1-hexene and benzene at 20 °C using rhodium clusters of varying size as catalysts.<sup>156</sup>

Cluster size [nm]	1-Hexene		Benzene	
	H <sub>2</sub> pressure [bar]	TOF [h <sup>-1</sup> ]	H <sub>2</sub> pressure [bar]	TOF [h <sup>-1</sup> ]
6.2	20	2100	20	1
3.1	20	3600	20	50
2.0	20	5700	20	80

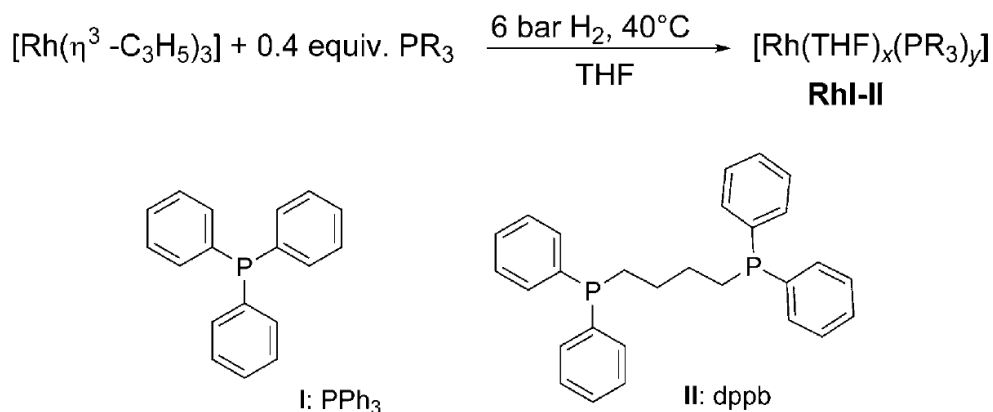
Dyson and coworkers<sup>157</sup> investigated PVP-stabilized Rh nanoparticles dispersed in water with phosphine ligand additives with different steric and electronic properties and polarities in hydrogenation catalysis (Figure 1.14).



**Figure 1.14:** Selected sulfonated water-soluble phosphine ligands.<sup>157</sup>

They observed catalytic chemoselective hydrogenation of phenylacetone to cyclohexylacetone under 30 bar of H<sub>2</sub> in water. Selective reduction of the aromatic ring increased from 70 to 92%, by using phosphine ligands with different steric and electronic properties and with differing polarities, which modified the properties of the nanoparticle surface and consequently influenced their catalytic behavior.

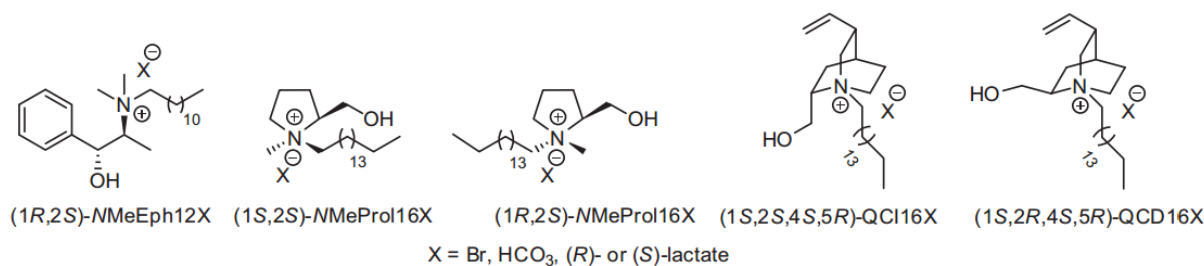
Claver, Chaudret and Godard<sup>158</sup> recently published the use of triphenylphosphine (PPh<sub>3</sub>) and diphenylphosphinobutane (dppb) to synthesize well-dispersed Rh NPs following the organometallic approach under 6 bar H<sub>2</sub> at 40 °C (Scheme 1.4). With both ligands, NPs had a size of 1.5 nm. Obtained particles were tested in the catalytic hydrogenation reaction of alkenes and substituted arenes. A comparative study of the reduction of aryl ketones using these NPs was also performed. This showed that the coordination of the arene dominates the interaction of the substrate with the NP, whereas the coordination of the ketone group with the NP was not evidenced. For alkyl ketones and aromatic compounds that contain a carbonyl group far from the ring, the carbonyl remained unaltered and only the aromatic ring was reduced. Whereas the case of acetophenone derivatives was unique, as although coordination to the NP takes place through the aromatic ring, the carbonyl group remains in a position very favorable for its reduction, in such a way that it is hydrogenated faster than the arene moiety.



**Scheme 1.4:** *P-donor ligands used to stabilize the Rh NPs.*

Roucoux *et al.* carried out an extensive work on surfactant-stabilized rhodium nanoparticles and their application in hydrogenation reaction.<sup>159</sup> Synthesis of the particles was mainly performed by reducing the RhCl<sub>3</sub> salt using sodium borohydride in presence of highly water-soluble surfactants such as N-alkyl-N-(2-hydroxyethyl)ammonium salts (HEA-Cn).<sup>160</sup> High hydrogenation catalytic activity of different benzene derivatives was achieved by manipulating the surfactant concentration<sup>161</sup> and the counter ion.<sup>162</sup> Also, impregnation of these NPs on silica support<sup>163</sup> and magnetic silica support<sup>164</sup> was tested, followed by elimination of the surfactant stabilizer. The obtained “heterogeneous” catalysts displayed good activities for the hydrogenation of mono-, dialkylsubstituted and/or functionalized aromatic derivatives in water under mild conditions, in addition to good recycling properties without any significant loss in catalytic activity. In addition to that, Roucoux and co-workers developed a series of water-soluble and optically active ammonium salts possessing polar heads, derived from N-methylephedrine, N-methylprolinol or cinchona derivatives, in combination with different counter-ions, such as Br<sup>-</sup>, HCO<sub>3</sub><sup>-</sup>, (S)- or (R)-lactate (Figure 1.15).<sup>165-166</sup> These surfactants proved to be efficient stabilizers for spherical rhodium(0) nanospecies with a mean size range between 0.8 and 2.5 nm. They were tested in the enantioselective reduction of ethyl pyruvate as well as the diastereoselective hydrogenation of prochiral 3-methylanisole as a challenging reaction.





**Figure 1.15:** Optically active ammonium surfactants as protective agents of Rh(0) NPs. *N*-dodecyl-*N*-methylphedrium (NMeEph12)<sup>+</sup> salt, *N*-hexadecyl-*N*-methyl-*L*-prolinolinium (NMeProl16)<sup>+</sup> salt, *N*-hexadecyl-*quicorinium* (QCI16)<sup>+</sup> salt, *N*-hexadecyl-*quicoridinium* (QCD16)<sup>+</sup> salt.<sup>165-166</sup>

Finally, Roucoux, Philippot, Chaudret and Hemati investigated the hydrogenation activity of model arenes, using silica-supported rhodium nanoparticles, which were synthesized by wet impregnation from a surfactant-stabilized aqueous colloidal suspension. No significant effect of silica grain size in hydrogenation results was obtained. Recycling of the catalyst in several successive runs was achieved.<sup>167</sup>

To conclude, hydrogenation reactions are the most often cited reactions for which rhodium nanoparticles are applied. Different routes of synthesis have been followed by the scientific community for the development of novel rhodium-based nanocatalysts. Although this metal is considered to be one of the rarest and the most expensive, its high activity and robustness in catalyzing this reaction make it of high interest to investigate more and try to discover more performant systems. The presented examples are not comprehensive but provide a view of the main methods used to synthesize rhodium nanoparticles for hydrogenation reactions.

## 1.5.2 Hydroformylation Reactions

Hydroformylation, called also “oxo process” is the addition of synthesis gas (“syngas”), a mixture of CO and H<sub>2</sub>, to olefins promoted by a catalyst under the formation of aldehydes.<sup>168</sup> It is a very important industrialized transition metal-catalyzed reaction mainly by homogeneous cobalt and rhodium catalysts. It appears that only a few works investigated

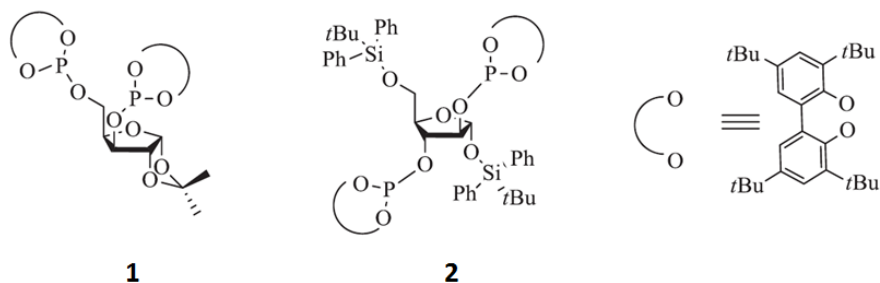
this reaction using Rh nanoparticles which might be due to the dramatic reaction conditions (high pressure and temperature), which cause the deformation or destruction of the particles.<sup>112</sup> In many cases, there is no evidence on the nature of the real active species in this reaction whether they are nanoparticles or homogeneous complexes due to metal leaching.<sup>169</sup>

The first reported use of rhodium nanoparticles in hydroformylation goes back to 1981, by Thomas W. Smith,<sup>170</sup> who patented the synthesis of Rh NPs prepared using copoly(styrene/butadiene) as a stabilizer in diethylene glycol dimethyl ether. Obtained particles were between 8 and 12 nm in diameter. Their catalytic performance was evaluated in 1-hexene hydroformylation at 100 °C under 42 bar syngas. 95% 1-hexene was converted into aldehydes with a l/b ratio of 2.

Mecking and coworkers<sup>171</sup> reported the synthesis of Rh-NPs stabilized by poly(ethylene imine)-amide in toluene through the chemical reduction of Rh(I) complex  $[\text{Rh}(\text{acac})(\text{C}_2\text{H}_4)_2]$  using either  $\text{H}_2$  gas or hydride salts as a reducing agent. Obtained NPs were found to have a high colloidal stability with a size range of  $2 \pm 0.5$  nm. Previous studies of this group have clearly shown that well dispersion of NPs is due to unimolecular inverted micelles formed by the polymer in aromatic solvents.<sup>172</sup> These NPs were found to be very active in the hydroformylation of 1-hexene at 120 °C under 50 bar of a 1:1  $\text{H}_2/\text{CO}$  mixture. At lower pressure (30 bar and less), hydrogenation and isomerization products of 1-hexene were formed preferentially rather than hydroformylation ones. Also at lower temperature (80 °C) about one-third of the substrate is converted to byproducts from hydrogenation and isomerization, while at 120 °C byproducts accounted for only 3%. Whereas, Dupont and coworkers,<sup>173</sup> used either unmodified or ligand-modified Rh(0) NPs with the size of 5 nm prepared by simple hydrogen reduction of  $\text{RhCl}_3 \cdot n\text{H}_2\text{O}$  dissolved in 1-n-butyl-3-methylimidazolium tetrafluoroborate ( $\text{BMI} \cdot \text{BF}_4$ ) ionic liquid, these catalysts were active in a solventless hydroformylation reaction of different linear alkenes. But, most of the obtained data are indicative of nanoparticle degradation under the reaction conditions into soluble mononuclear Rh-carbonyl catalytically active species having similar activity to pre-tested Rh-carbonyl molecular clusters in the same catalytic reactions.<sup>174</sup>

Philippot *et al.*<sup>77</sup> investigated the synthesis of metallic Rh nanoparticles stabilized by chiral diphosphite ligands (Figure 1.16) following the organometallic approach. Two different metallic precursors  $[\text{Rh}(\eta^3\text{-C}_3\text{H}_5)_3]$ <sup>76</sup> and  $[\text{Rh}(\mu\text{-OMe})(\text{cod})_2]$ <sup>175</sup> were decomposed

under  $H_2$  pressure in THF. Obtained NPs were size and shape dependent on the precursor used for the synthesis.  $[Rh(\eta^3-C_3H_5)_3]$  led to small rhodium nanoparticles, whereas sponge-like structures were obtained with  $[Rh(\mu-OMe)(cod)]_2$ . This difference could be explained by taking into account the byproducts resulting from decomposition of each precursor. Indeed, the decomposition of the olefinic precursor  $[Rh(\eta^3-C_3H_5)_3]$  only leads to the production of propane, which does not interact with the growing metal surface. In contrast, the decomposition of the rhodium  $[Rh(\mu-OMe)(cod)]_2$  complex produces cyclooctane and methanol, which remain in solution. Rhodium-catalyzed asymmetric hydroformylation of styrene using these NPs, showed interesting activity and selectivity under 20 bar syngas at 80 °C. In order to understand the catalytic species responsible for the activity, several setups including diluted experiments, poisoning tests and *in situ* HP NMR under hydroformylation conditions were performed and revealed the formation of molecular species that probably were the ones active in the studied reaction. This work showed thus that such colloids could be considered as a reservoir for molecular catalysts.

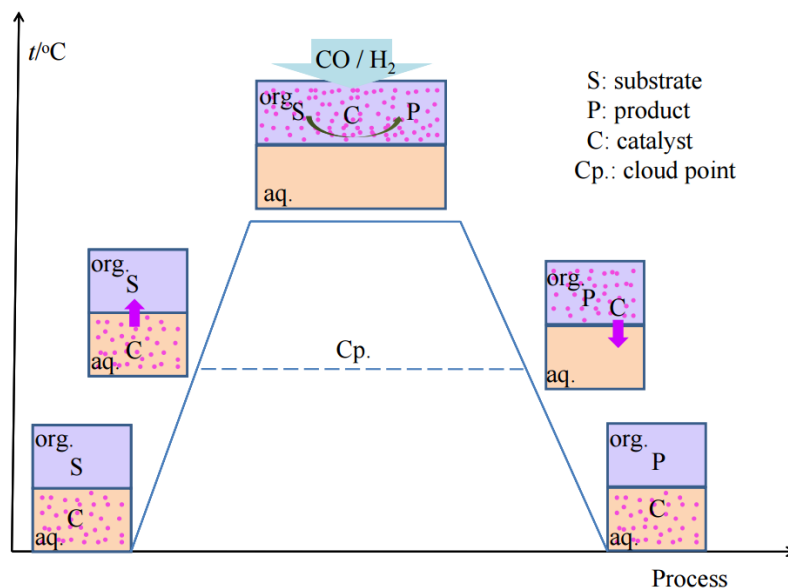


**Figure 1.16:** Chiral diphosphite ligands used as stabilizers of Rh NPs.

Li *et al.*<sup>176</sup> obtained highly dispersed rhodium nanoparticles, presenting small and narrowly distributed core sizes (1.5–2.0 nm), by one-pot chemical reduction of aqueous rhodium chloride ( $RhCl_3 \cdot 3H_2O$ ) dispersed in toluene solution in the presence of amphiphilic tetraoctylammonium bromide (TOAB) and chiral (R)-BINAP at ambient conditions. These rhodium nanoparticles catalyzed the asymmetric hydroformylation of olefins under mild conditions and exhibited high regioselectivity and chiral inductivities (92:8 b/n, 26% ee for styrene and 99:1 b/n, 59% ee for vinyl acetate, respectively). The achieved chirality was attributed to the chiral environment on the rhodium nanoparticles formed due to the strong

coordination interaction of (R)-BINAP adsorbed onto rhodium surface sites, which was studied by  $^{31}\text{P}$  MAS NMR and CO-IR. Also, they performed the impregnation of the chiral nanocatalysts on silica which yielded in higher activity in the hydroformylation of styrene ( $12\text{ h}^{-1}$  for not supported vs.  $22\text{ h}^{-1}$  for supported system), and in several recycling possibilities by addition of extra (R)-BINAP to insure its continuity.

Wang, Jin and coworkers<sup>177</sup> took profit of a thermoregulated phase-transfer ligand [ $\text{Ph}_2\text{P}(\text{CH}_2\text{CH}_2\text{O})_{16}\text{CH}_3$ ] that exhibits an inverse-temperature-dependent solubility in water, to stabilize Rh NPs synthesized by reducing  $\text{RhCl}_3 \cdot 3\text{H}_2\text{O}$  in water/butanol mixture under  $\text{H}_2$  pressure.<sup>178</sup> Aqueous solutions of  $\text{Ph}_2\text{P}(\text{CH}_2\text{CH}_2\text{O})_{16}\text{CH}_3$  thermoregulated ligand undergo a phase separation on heating to Cloud point (Cp) while become homogeneous again on cooling to a temperature lower than the Cp. The coordination interaction between the ligand and the rhodium nanoparticles was shown by  $^{31}\text{P}$  NMR spectroscopy, and appeared to be the driving force for transferring the ligand thermo properties to the Rh NPs. Hydroformylation of several long chain alkenes using these nanocatalysts under 50 bar pressure and  $70\text{ }^\circ\text{C}$  achieved with high conversions and in high yields in aldehydes. Also, recycling of the NPs was investigated by taking profit of their thermo-regulation properties. After catalytic reaction, the upper organic phase was separated from the lower catalyst-containing aqueous phase by phase separation. The aqueous phase was directly used in the next reaction run (Figure 1.17). The catalyst could be reused for three runs without evident loss in activity. However, after every catalyst recycling run, the Rh nanoparticles increased in size as seen by TEM analysis.



**Figure 1.17:** General principle of hydroformylation in an aqueous/ 1-butanol biphasic system using  $\text{Ph}_2\text{P}(\text{CH}_2\text{CH}_2\text{O})_{16}\text{CH}_3$ -stabilized rhodium nanoparticles as catalyst.<sup>177</sup>

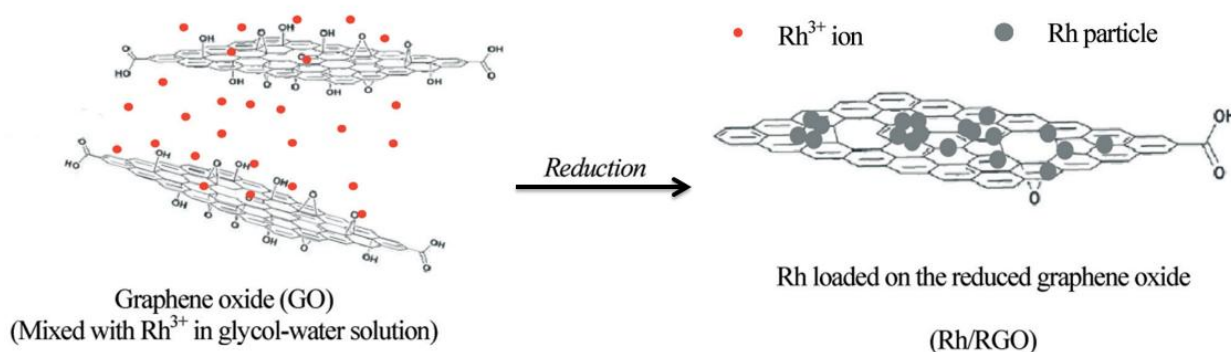
Similarly, the group of Behr<sup>179</sup> described the synthesis of Rh-NPs dispersed and recycled in a free-ligand thermomorphic solvent system (TMS), a system developed using solvents of variable polarity.<sup>180</sup> The synthesis of the rhodium nanoparticles was performed under dihydrogen pressure ( $p = 10$  bar) and increased temperature ( $T = 80$  °C), after dissolving a rhodium precursor ( $\text{Rh}(\text{acac})(\text{CO})_2$  or  $\text{Rh}_2(\text{AcO})_4$ ) in a polar solvent such as dimethylformamide or propylene carbonate. Hydroformylation of 1-dodecene under 30 bar of syngas and 110°C with these Rh NPs, resulted in a yield of 97% aldehyde and a relatively high n/iso ratio of 70:30. Addition of phosphine ligands (biphephos) in the reaction mixture increased regioselectivity reaching n/iso ratio up to 96:4 but negatively affected the aldehyde conversion. Catalyst recycling and reusing was feasible giving two-phase reaction medium after cooling down the reaction taking profit of the TMS system.

Zilin and coworkers published the use of rhodium thermoregulated ionic liquid/organic biphasic systems by using either  $[\text{CH}_3(\text{OCH}_2\text{CH}_2)_{16}\text{N}^+\text{Et}_3][\text{CH}_3\text{SO}_3^-]$  ( $\text{IL}_{\text{PEG750}}$ ),<sup>181</sup> and an organic solvent or N,N-dimethyl-N-(2-(2-methoxyethoxy)ethyl)-N-(2-(2-octyloxyethoxy)ethyl) ammonium methanesulfonate and cyclohexane.<sup>182</sup> NPs were prepared by mixing the ionic liquid with the  $[\text{RhCl}_3 \cdot \text{H}_2\text{O}]$  salt that was reduced under dihydrogen (40 bar) at 70 °C for 2 h. The obtained nanoparticles were found to be an active,

stable, and recyclable catalyst for olefin hydroformylation. The catalyst could be recovered readily by simple phase separation thanks to a thermoregulated ionic liquid/organic biphasic system and reused, without evident loss of activity until eight catalytic cycles.

The incorporation of Rh nanoparticles into a hypercross-linked polystyrene matrix was developed by Davankov and his team.<sup>183</sup> This work is based on the reduction of  $[\text{RhCl}_3 \cdot \text{H}_2\text{O}]$  using excess of  $\text{NaBH}_4$  in the presence of a biporous hypercross-linked polystyrene/divinylbenzene copolymer bearing non-coordinating tertiary amine moieties. TEM images showed small nanoparticles in a size range 2-4 nm. Catalytic hydroformylation performed with several olefins in supercritical  $\text{CO}_2$  conditions showed high activity, with increasing aldehyde ratio when increasing the pressure and the temperature of the reaction. Reuse of the catalyst up to six times was performed without any noticeable decrease in the activity and with constant selectivity. Gubin *et al.*<sup>184</sup> performed surface modification of graphene oxide into a methylated graphene oxide which was used as a support for the formation of rhodium nanoparticles (2-3 nm). Using  $[\text{RhCl}_3 \cdot \text{H}_2\text{O}]$  and  $\text{NaBH}_4$ . The prepared catalyst showed moderate and high substrate conversion as well as regioselectivity in the hydroformylation of various olefins mainly in the "green" medium of  $\text{scCO}_2$ .

Very recently, Tsubaki *et al.*<sup>185</sup> used graphene to get supported Rh NPs by mixing graphene oxide (GO) with  $\text{Rh}^{3+}$  ions generated from  $\text{Rh}(\text{NO}_3)_3$  followed by ultrasonic treatment for 2 h, and heating the solution at  $105^\circ\text{C}$  for 10 h while refluxing (Scheme 1.5). Particles with a large size of 40–60 nm were obtained, that correspond to cluster-like structure comprising dozens of smaller Rh nanoparticles with individual particle size of 6 nm. These supported Rh NPs were applied in hydroformylation of 1-hexene at different reaction temperatures and times. Surprisingly, in comparison to examples from literature,<sup>183</sup> low reaction temperature could effectively promote the 1-hexene hydroformylation to form n-heptanal, while high reaction temperature enhanced side reactions like 1-hexene isomerization and hydrogenation, generating internal hexene and hexane.<sup>185</sup>



***Scheme 1.5:*** Rh NPs formation on graphene oxide

In 2015, Rossi and her team,<sup>169</sup> published the preparation of a hydroformylation nanocatalyst through the immobilization of air-stable Rh NPs onto a magnetic silica support functionalized with chelating phosphine ligands. In this work colloidal Rh NPs were first synthesized following the method of Brust *et al.*<sup>49</sup> and then deposited on the magnetic silica support previously modified on the surface with amine or diphenylphosphine ligands,<sup>186</sup> leading to an easily recoverable, and reusable catalyst for the hydroformylation of styrene and 1-octene. These supported Rh nanocatalysts were active for successive reactions even after air exposure during the recycling runs that was easy to perform through magnetic separation. But, Raman analysis before and after catalytic reactions suggested that the rhodium NPs act as precursors of active molecular species formed *in situ*, probably due to the drastic reaction conditions applied.

In conclusion, various rhodium nanoparticle systems have shown activities and selectivities in catalytic hydroformylation as good as homogeneous catalysts, with advantages of easy recovery and recycling in some cases. Although, the nature of the real active species in this reaction remains often unsolved, the need of more robust catalytic systems with strong stabilizing agents without blocking the activity is a need to obtain more applications of Rh NPS in hydroformylation.





# **Chapter II :**

# **Monometallic**

# **Nanoparticles**

---



## II. Monometallic Rhodium Nanoparticles

### II.1 Introduction

The synthesis of metallic nanostructures through the organometallic approach allows taking benefit from the concepts of coordination and organometallic chemistry. Metal complexes (organometallic or metal organic complexes) are used as metal sources and polymers (steric barriers) or ligands (coordination at the metal surface) as stabilizing agents. This approach proved to be a powerful and versatile way to develop efficient synthesis tools that provide in a reproducible manner controlled nanosystems with reproducible physical or chemical properties.

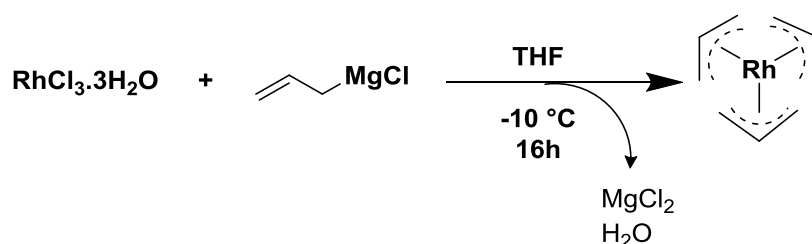
Several factors may influence the formation of MNPs and this can be seen through their different characteristics like the size, shape, structure, composition, etc... The main factors can be summarized by the nature of precursors used as metal sources,<sup>187</sup> the stabilizing agents used to control the growth of the particles and the reaction conditions (solvent, temperature, gas pressure).<sup>188</sup>

Many classes of metallic complexes have been investigated for the elaboration of MNPs; they can be thermally decomposed or reduced in the presence of a reducing gas. The main classes include carbonyl complexes,<sup>189</sup> non-carbonyl organometallic complexes,<sup>190</sup> carboxylate complexes,<sup>191</sup> acetylacetonate complexes,<sup>192</sup> amido complexes<sup>193</sup> and amidinate complexes.<sup>194</sup> Olefinic allyl complexes are of particular interest for the synthesis of MNPs because of their facile decomposition under mild reaction conditions, the clean metal surface that can be obtained and functionalized, and the wide diversity of metal nanostructures that can be synthesized.

Before this PhD work, the synthesis of Rh NPs was explored in the team using different organometallic precursors. During her PhD, Esther Ramirez-Meneses<sup>195</sup> evaluated the potential of  $[\text{Rh}(\text{acac})(1,5\text{-C}_8\text{H}_{12})]$ ,  $[\text{Rh}(\eta\text{-Cl})(1,5\text{-C}_8\text{H}_{12})]_2$  and  $[\text{Rh}(\eta^3\text{-C}_3\text{H}_5)_3]$  in forming well-dispersed NPs stabilized by either hexadecylamine or an alkyl-N-(2-hydroxyethyl)ammonium salts like HEA-Cl-16 surfactant. The few obtained results starting from the allylic  $[\text{Rh}(\eta^3\text{-C}_3\text{H}_5)_3]$  complex showed that the NPs synthesized from this precursor

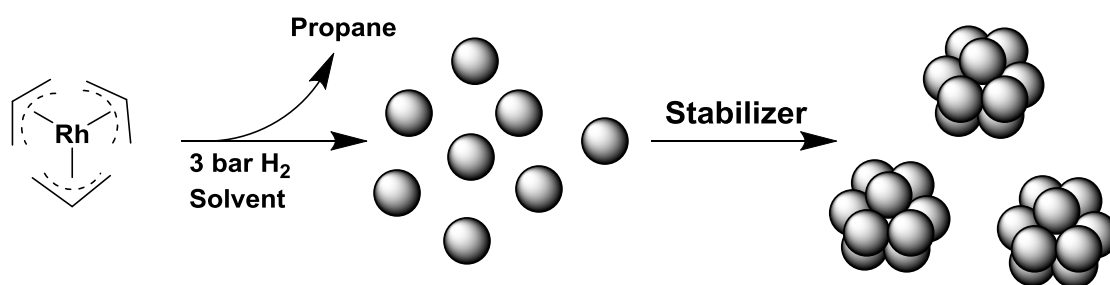
were well-dispersed, in general small in size and stable in solution. This is the reason why this organometallic complex was chosen as starting point for all the syntheses of Rh NPs reported in this manuscript.

Thus, the first step of the PhD work was the synthesis of the rhodium source,  $[\text{Rh}(\eta^3\text{-C}_3\text{H}_5)_3]$ . For this purpose, we took inspiration from the work of Powel *et al.*<sup>196-197</sup> and Becconsall *et al.*<sup>198-199</sup> who described how to synthesize allylic precursors of palladium and rhodium. The preparation of the  $[\text{Rh}(\eta^3\text{-C}_3\text{H}_5)_3]$  complex was performed by reacting hydrated rhodium trichloride salt with allylmagnesium chloride in THF at  $-10\text{ }^\circ\text{C}$  overnight, followed by several purification steps including first dissolving cold pentane, then purification over celite column and finally by sublimation at  $40\text{ }^\circ\text{C}$ . Final yield of 65% was attained. (Scheme 2.6)



**Scheme 2.6:** Synthesis of  $[\text{Rh}(\eta^3\text{-C}_3\text{H}_5)_3]$  complex.

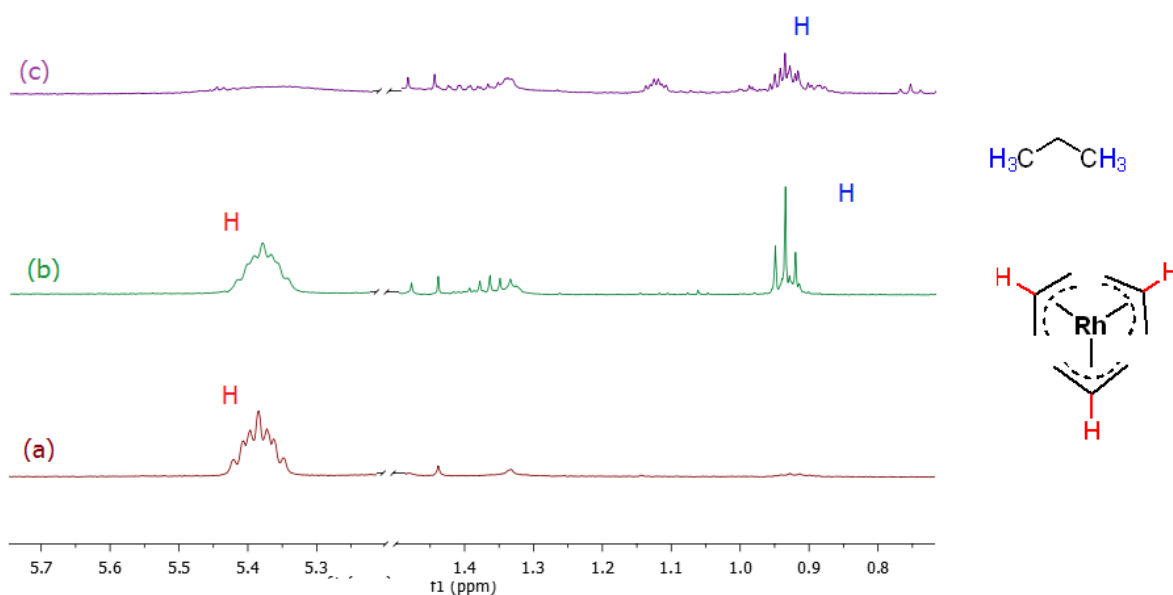
The effectiveness of this precursor for the synthesis of Rh NPs derives from the allyl propene ligands it bears. When this complex is treated with  $\text{H}_2$  atmosphere, the allyl propene ligands are reduced resulting in propane gas as the only byproduct (Scheme 2.7). Propane is inert and does not interfere with stabilizer coordination at the surface of the particles and is easily eliminated under vacuum. As a blank test it has been shown that the decomposition of this complex at room temperature in THF as a solvent, without addition of any stabilizer resulted in the formation of bulk rhodium.



**Scheme 2.7:** Decomposition of  $[\text{Rh}(\eta^3\text{-C}_3\text{H}_5)_3]$  complex releasing only propane as byproduct.

To study the decomposition process of the  $[\text{Rh}(\eta^3\text{-C}_3\text{H}_5)_3]$  complex and the release of propane, mimicking of the NP synthesis reaction was performed inside a NMR tube. The Rh complex, triphenylphosphine as a stabilizer and deuterated THF were introduced in the NMR tube. Then the tube was pressurized under 3 bar of dihydrogen and heated up to 70 °C. The reaction was followed by  $^1\text{H}$  NMR till black colloidal solution of NPs appeared. A characteristic peak of the  $[\text{Rh}(\eta^3\text{-C}_3\text{H}_5)_3]$  complex at 5.4 ppm corresponding to the hydrogen of the allyl ( $\text{CH}_2\text{CHCH}_2$ ) group in middle position was taken as a reference to follow the evolution of the reaction. Its disappearance was followed and the emergence of new peaks at 0.5 and 1.5 ppm was observed, as the result of formation of propane (Scheme 2.7).

Figure 2.18a shows the  $^1\text{H}$  NMR spectrum recorded for the crude reaction mixture at room temperature without pressurizing with  $\text{H}_2$ . The reference peak of the allyl groups of the starting complex is clearly observed at 5.4 ppm, while only very weak peaks are present in the alkane region of the spectrum. Figure 2.18b corresponds to the  $^1\text{H}$  NMR spectrum of the reaction mixture after 1h under dihydrogen pressure (3 bar) at 70 °C. Evolution of new peaks around 0.9 ppm reveals the presence of propane gas in the tube. We can also notice that the reaction is not yet complete as the characteristic peak of the complex at 5.4 ppm is still visible. After 3h under 3 bar  $\text{H}_2$  at 70 °C, the spectrum (Figure 28.1c) reveals the disappearance of the peak at 5.4 ppm indicating the absence of the allylic ligands and then, the total decomposition of the precursor.



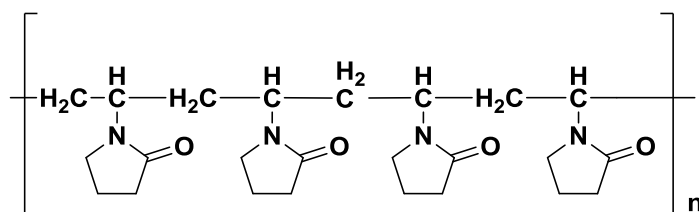
**Figure 2.18:** (a)  $^1\text{H}$  NMR spectrum of  $[\text{Rh}]$  and  $\text{PPh}_3$  mixture in  $\text{THF-D}_8$ , (b)  $^1\text{H}$  NMR spectrum of  $[\text{Rh}]$  and  $\text{PPh}_3$  mixture in  $\text{THF-D}_8$  after 1 h of heating at  $70\text{ }^\circ\text{C}$  under  $\text{H}_2$  pressure, (c)  $[\text{Rh}]$  and  $\text{PPh}_3$  mixture after 3 h of heating under  $\text{H}_2$  pressure.

Having in hands a convenient metal precursor for the liberation of Rh metal atoms in mild reaction conditions, we wanted to explore the influence of various stabilizing agents in the synthesis of Rh NPs. Our main objective was to develop new synthesis tools for providing a variety of Rh NPs displaying different surface properties for application in catalysis. Thus, polyvinylpyrrolidone polymer (PVP), phosphines ( $\text{PPh}_3$ , dppb, PTA), phosphino ferrocenes, N-Heterocyclic carbenes ... etc, were tested as stabilizers. The obtained Rh NPs were analyzed by different techniques including TEM/HRTEM, WAXS, ICP-AES, IR, NMR, XPS and others. In addition, some of the NPs were deposited onto amino-functionalized magnetic silica support for investigation in supported catalysis conditions.

This first part of the thesis is thus dedicated to the synthesis of different monometallic systems of Rh NPs, and their characterization for a better understanding of their surface state, morphology, and composition.

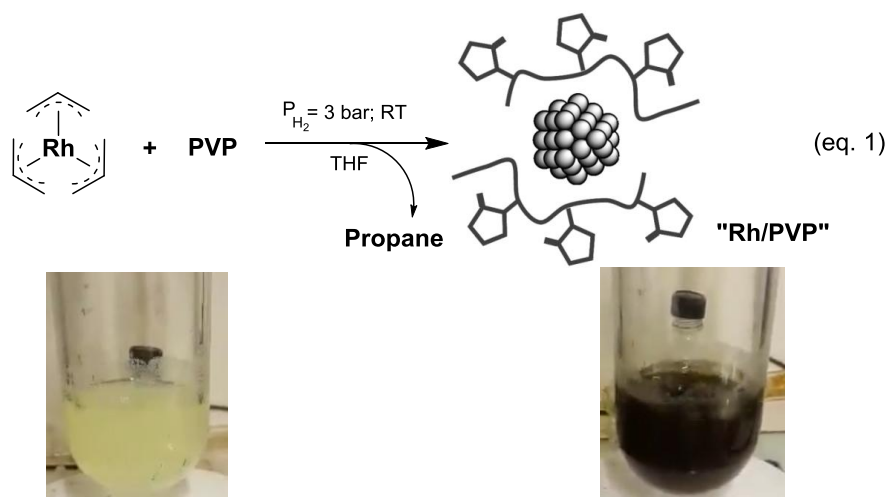
## II.2 PVP-Stabilized Rhodium NPs

Literature reports many good results obtained by the employment of polymers for the stabilization of MNPs. Thanks to the steric effect they generate, polymers allow to control the particle growth while assuring accessible path to the active sites of the particles. Polyvinylpyrrolidone polymer (PVP) in particular, being a bulky, non-toxic, non-ionic polymer with both a strongly hydrophilic character (the pyrrolidone group, Scheme 2.8) and a considerable hydrophobic character (the alkyl chain, Scheme 8), is recognized as an efficient stabilizer for various MNPs. PVP wraps the particles and prevents their aggregation *via* the repulsive forces that arise from its hydrophobic carbon chains that extend into solvents and interact with each others (steric hindrance effect).<sup>200</sup>



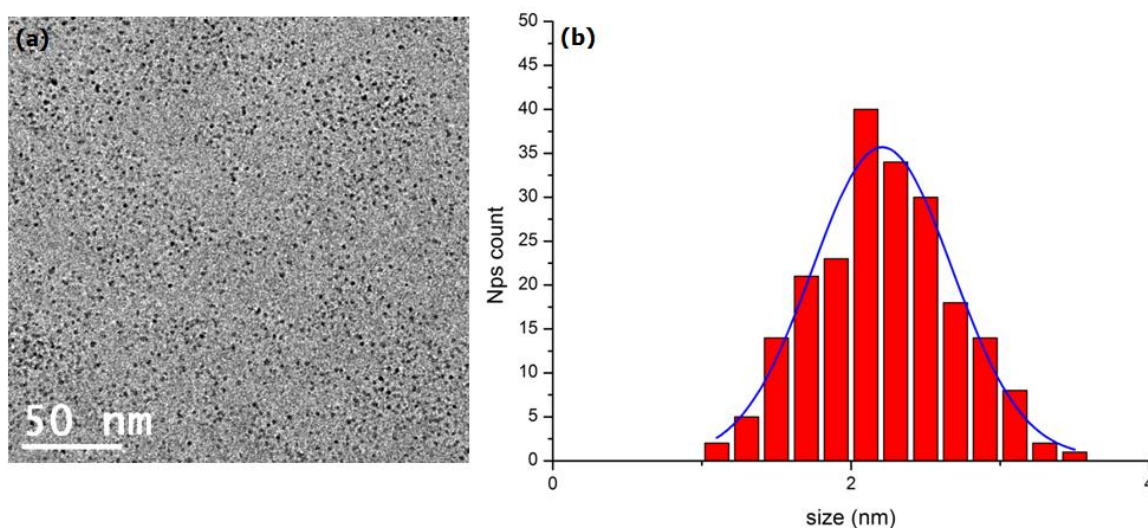
**Scheme 2.8:** Polyvinylpyrrolidone (PVP) polymer.

The decomposition of  $[\text{Rh}(\eta^3\text{-C}_3\text{H}_5)_3]$  complex was carried out at room temperature (r.t.) in THF solution under 3 bar of dihydrogen in the presence of the polyvinylpyrrolidone polymer (PVP M.W. 40000) ( $[\text{Rh}]/[\text{PVP}]$ , 10 wt. %) (eq. 1) as the stabilizer. The yellow reaction mixture turned into a stable black colloidal solution within 15 minutes. Nevertheless, to insure full decomposition of the precursor, reaction time was extended to 16 h (overnight), as usually applied in the team. The black colloidal solution was found to be stable for over 3 weeks. Resulting RhPVP NPs were easily isolated under the form of a dark grey powder by pentane precipitation, showing a metal content of 14.9% as measured by ICP-AES analysis.



### II.2.1 Electron Microscopy Analysis

Transmission electron microscopy analysis of the colloid, after putting a drop of the fresh colloidal solution on a carbon coated copper grid, revealed the presence of well-dispersed and spherical Rh NPs with average diameter size of  $2.2 \pm 0.9$  nm (Figure 2.19) (the error range corresponds to  $2\sigma$  which covers 95.5% accuracy of the data). To estimate the number of Rh atoms contained in a Rh NP, we considered close packing 2.2 nm spheres, where the Rh atoms occupy approximately 74% of the volume of the spheres.<sup>201</sup> Knowing that the diameter of a single Rh atom is 0.267 nm, we could estimate that 400 Rh atoms are present in a 2.2 nm spherical Rh NP.

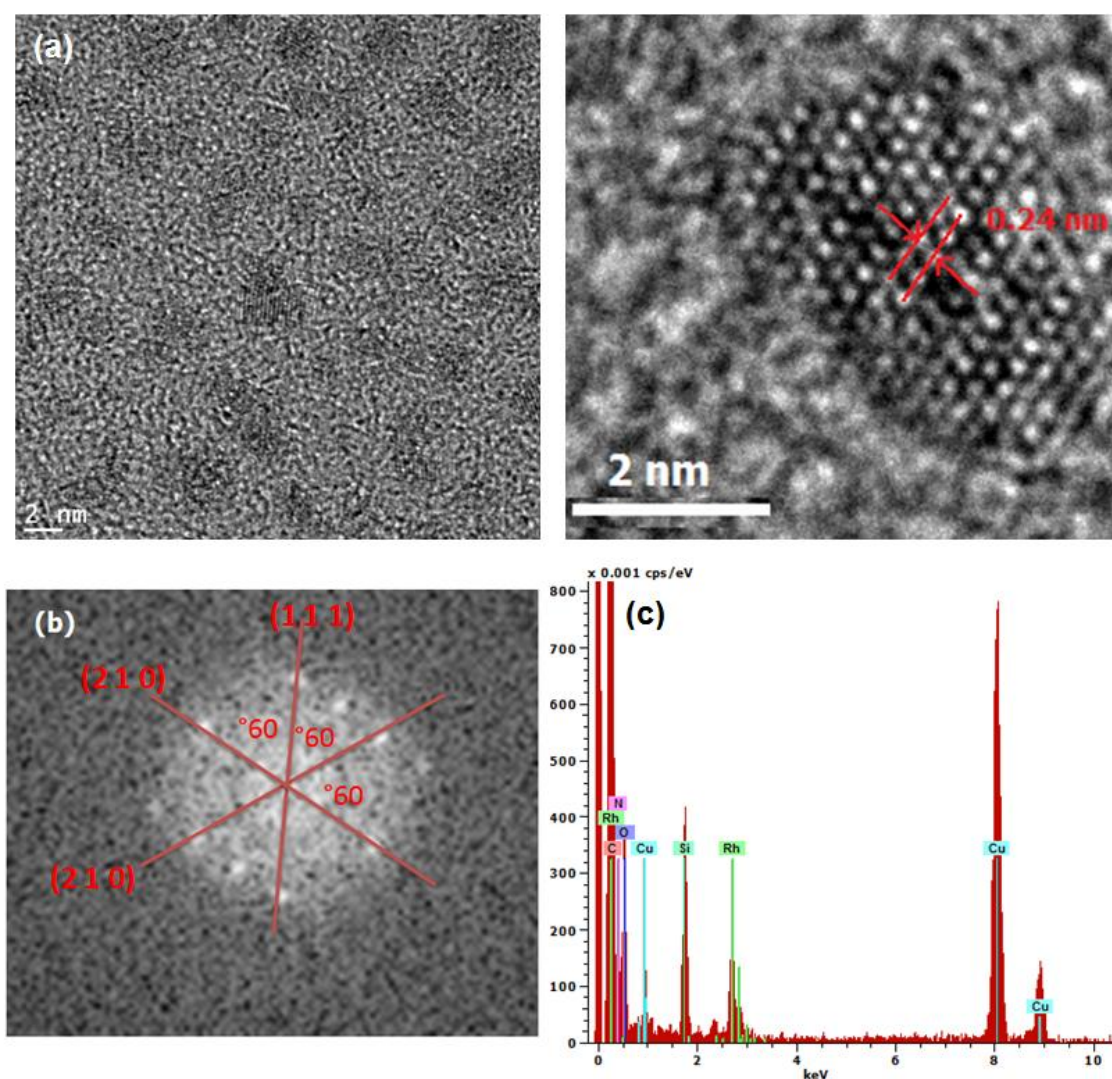


**Figure 2.19:** (a) TEM image of Rh NPs stabilized with PVP polymer. (b) Corresponding size distribution histogram ( $d_m = 2.2 \pm 0.9$  nm; >215 particles).

In order to obtain more information on their shape and crystallinity, the RhPVP NPs were analyzed by High Resolution Transmission Electron Microscopy (HRTEM). HRTEM



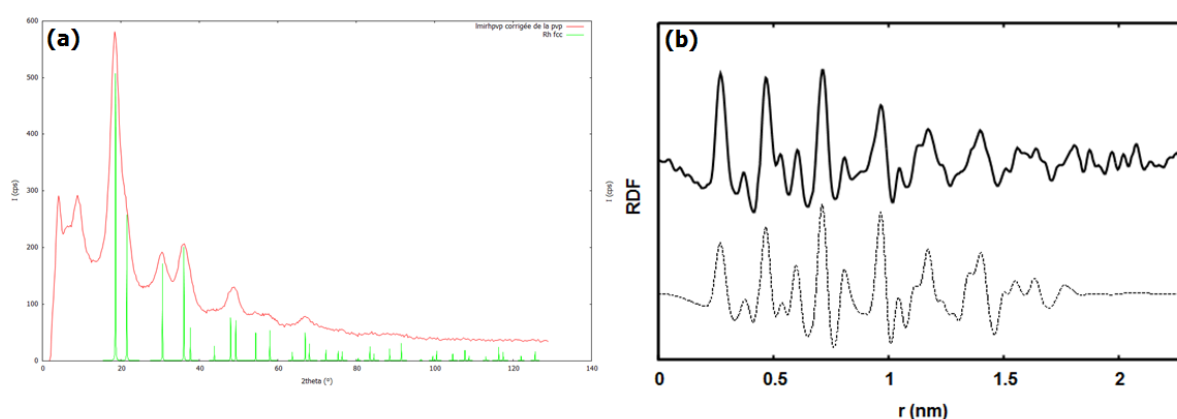
allowed us to study selected individual nano-objects and provided size, morphology and crystallographic evidences, including structural defects diffracting samples. On Figure 2.20, it can be clearly observed that the NPs are in well crystalline form. Rh atoms are clearly observed with one interplanar spacing of 0.24 nm found, corresponding to  $(11\bar{1})$  spacing of typical fcc Rh. By EDX analysis, a clear peak of elemental Rh was detected as well as well-identified peaks for C and N resulting from the PVP polymer that embeds the particles (Figure 2.20c).



**Figure 2.20:** (a) HRTEM image showing the lattice interplanar spacing, (b) Fast Fourier Transformation (FFT), and (c) EDX analysis of Rh PVP NPs.

## II.2.2 Wide Angle X-ray Scattering Analysis

Wide Angle X-ray Scattering (WAXS) is a powerful technique developed by P. Lecante at CEMES-Toulouse that provides a set of accurate interatomic distances which always define a characteristic signature and gives access to three-dimensional structure. The Radial Distribution Function (RDF) is obtained by applying Fourier Transform to WAXS diffraction pattern. The fcc crystalline structure of the purified RhPVP NPs could be easily confirmed by WAXS analysis. Indeed, the measurements in reciprocal space after elimination of the polymer showed that the obtained NPs (in red, Figure 2.21a) are very coherent with the theoretical calculated peaks of fcc Rh NPs (in green, Figure 2.21a). However, measurements in real space (Figure 2.21b) showed particles with a coherence length of *ca.* 2.2 nm (solid line) that is in very good agreement with the mean diameter measured by TEM, in addition to total accordance with theoretically calculated real space measurements of such NPs. Such agreement also indicates that these NPs are single crystalline.

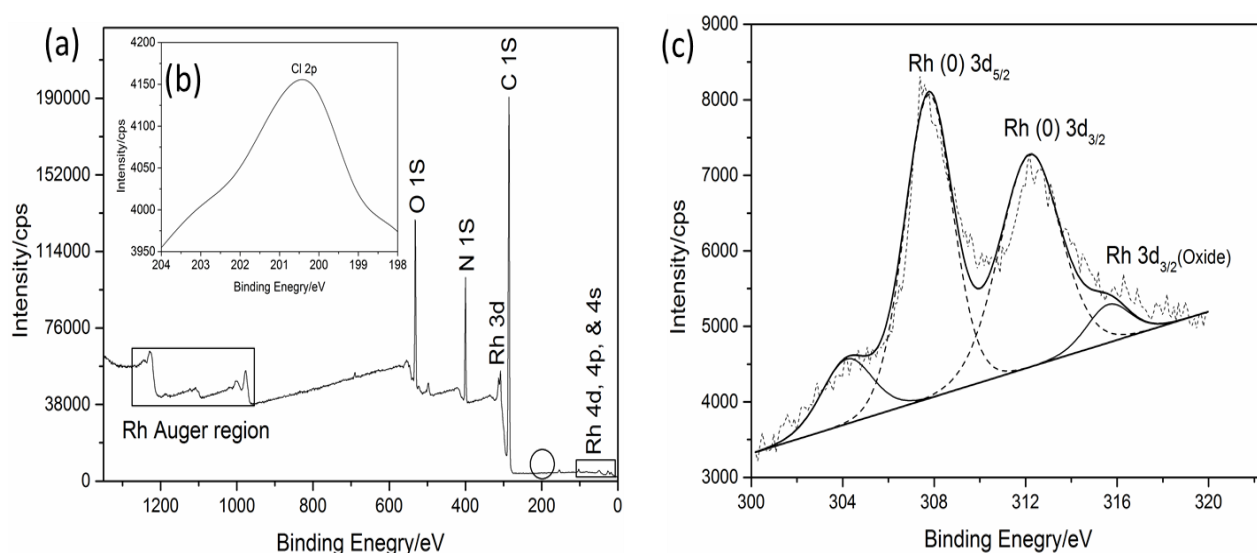


**Figure 2.21:** (a) WAXS measurements for Rh PVP NPs in reciprocal space (red line) with theoretically calculated Rh fcc structure (green line). (b) WAXS measurements for Rh PVP NPs in real space (solid line) and theoretically calculated (dotted line).

### II.2.3 X-Ray photoelectron Spectroscopy Analysis

X-ray photoelectron spectroscopy allows identifying elements, and to know their surrounding chemical environment and oxidation state. Measurements of RhPVP NPs illustrated in Figure 2.22 were performed at room temperature using Al-K $\alpha$  radiation (1484.6 eV) as the excitation X-ray source at the Technical University of Denmark. Figure 2.22a shows photopeaks corresponding to the constituent atoms of PVP (carbon, oxygen, and nitrogen) and Rh (elemental survey). It is found that remnant chlorine derived from the Rh salt (RhCl<sub>3</sub>) used in the synthesis of the [Rh( $\eta^3$ -C<sub>3</sub>H<sub>5</sub>)<sub>3</sub>] complex, or perhaps from the contamination appeared at its 2p binding energy level as shown in the inset (b). However, it is quite insignificant and about 0.13% in terms of intensity with respect to the C1s level peak.

2.22c shows the 3d core level photopeak of RhPVP NPs. The lower binding energy peaks at 307.8 (3d<sub>5/2</sub>) and at about 311.9 eV (3d<sub>3/2</sub>) confirm the metallic state of Rh/PVP. The higher binding energy peak between 313 and 315 eV (3d<sub>3/2</sub>) suggests the presence of oxidized rhodium species. Subsequent comparisons with earlier investigations are in agreement with the Rh<sup>3+</sup> species suggesting Rh<sub>2</sub>O<sub>3</sub> formation.<sup>202-203</sup> Partial oxidation of Rh during sample preparation and/or sample introduction to the spectrometer is likely and could be a substantial reason for oxidic rhodium peaks. Surprisingly, a small peak at a lower end of the binding energy (304 eV) can possibly be attributed to the 3d level with different chemical environment on the surface. At high binding energies, electrons due to Auger process can also be seen from Figure 2.22a.

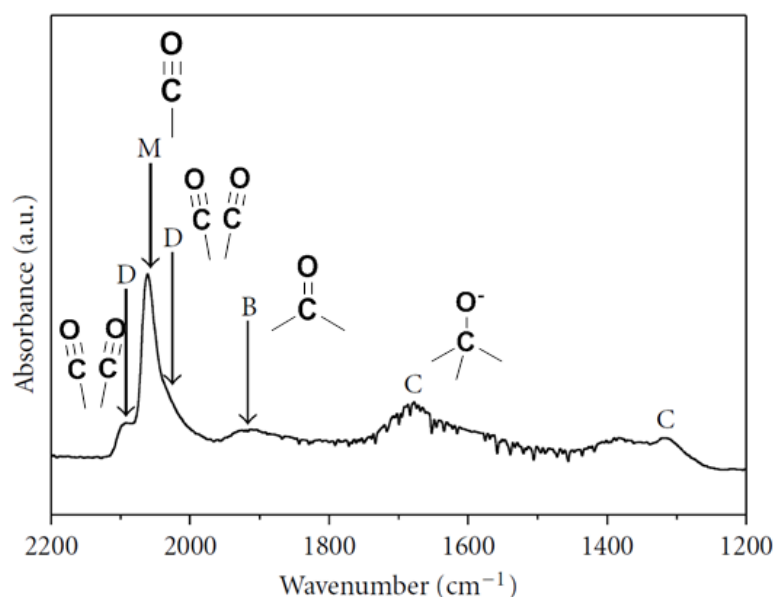


**Figure 2.22:** (a) X-Ray photoelectron spectra of RhPVP NPs elemental survey. (b) Zoomed in area of Cl 2p level. (c) 3d core level X-Ray photoelectron spectra of RhPVP NPs.

## II.2.4 CO Adsorption Study

Adsorption of CO on the surface of MNPs showed to be a very useful technique for studying the surface state of the particles. Adsorbed CO molecules serve as an active probe molecule for the determination of coordination sites on metal surfaces in both infrared and NMR studies.<sup>73,204-205</sup> Bradley *et al.*<sup>206-208</sup> showed that CO molecules first coordinate on metal NPs surface in bridging mode on the extended faces and later adopt the terminal mode on the edges and the apexes. This approach was previously used in the team, in particular for Ru<sup>209</sup> and Re<sup>78</sup> NPs.

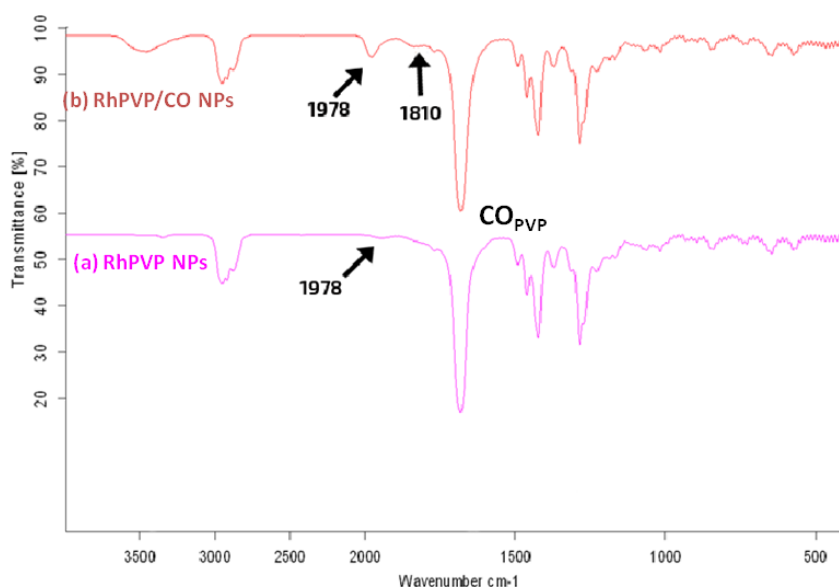
Moreover, Vaccari *et al.*<sup>210</sup> performed extensive studies on the CO adsorption on Rh NPs. Results obtained (Figure 2.23) show the different CO peaks which correspond to the different CO coordination types on the surface of the particles. From the results they obtained, a correlation between the vibrational energy and the electron density on the C=O bond could be concluded; the more electron dense C=O bond have less vibrational frequency which is translated in higher wavelength, and the opposite is true for less electron dense C=O bond that have higher vibrational frequency shown in lower wavelength values.



**Figure 2.23:** FT-IR spectrum recorded after reaction of CO with Rh NPs at r.t. (D: gem-dicarbonyl ( $2093\text{ cm}^{-1}$ ,  $2030\text{ cm}^{-1}$ ), M: linear monocarbonyl ( $2060\text{ cm}^{-1}$ ), B: bridged-bonded CO (broad band  $1910\text{ cm}^{-1}$ ), and C: carbonate-type species).<sup>210</sup>

In order to study the coordination mode of CO molecules at the PVP-stabilized Rh NP surface, a pellet of KBr was prepared with purified RhPVP NPs for a reference measurement by FT-IR technique. The resulted spectrum (Figure 2.24b) showed a standard spectrum of PVP stabilized particles with main sharp characteristic peak of CO carbonyl groups of PVP at  $1681\text{ cm}^{-1}$ . In addition, a wide band of very low intensity was observed around  $\sim 1970\text{ cm}^{-1}$  that may correspond to CO absorption. Presence of this peak had been previously observed with different NP systems in the team, and a recent study with N-heterocyclic carbene stabilized Ru NPs in THF,<sup>209</sup> indicated that such a presence of CO is due to THF decarbonylation *in situ* process during the synthesis of the NPs. Moreover, another recent study by Jessica Castelbo at the Rovira i Virgili University, led to the conclusion that such peaks could refer to free hydrides on the surface of the particles.<sup>211</sup> This study was inspired by the work of Worely and co-workers<sup>212</sup> who studied by FT-IR, Rh NPs deposited on alumina support.

After exposing the pellet of RhPVP NPs for 24h with 1 bar of CO pressure, the FT-IR spectrum revealed a clear absorption band at  $1978\text{ cm}^{-1}$  as expected for CO coordination in terminal mode, as well as a lower intensity band at  $\sim 1810\text{ cm}^{-1}$  that can correspond to bridging coordination mode on the surface of Rh NPs according to our reference.<sup>210</sup> The presence of this peak demonstrates the ability of the Rh PVP NPs in hosting CO molecules on their surface indicating the existence of free Rh sites.

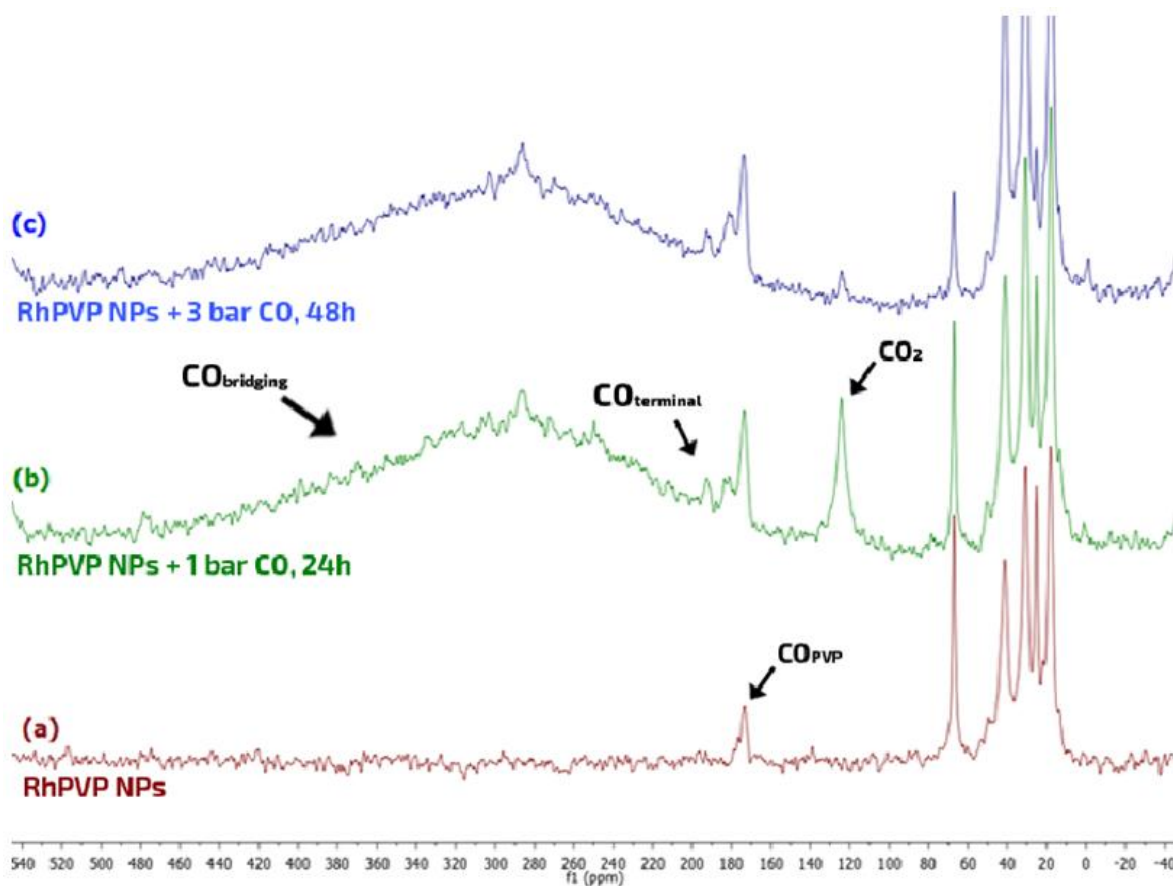


**Figure 2.24:** (a) FT-IR of purified Rh-PVP NPs, (b) FT-IR of RhPVP NPs after reaction with 1bar of CO at RT for 24h.

In order to better understand the coordination of CO on the surface of the NPs,  $^{13}\text{C}$  NMR studies in the solid state for the RhPVP NPs before and after exposure to labeled  $^{13}\text{CO}$  were performed at the magic angle spinning (MAS) mode.

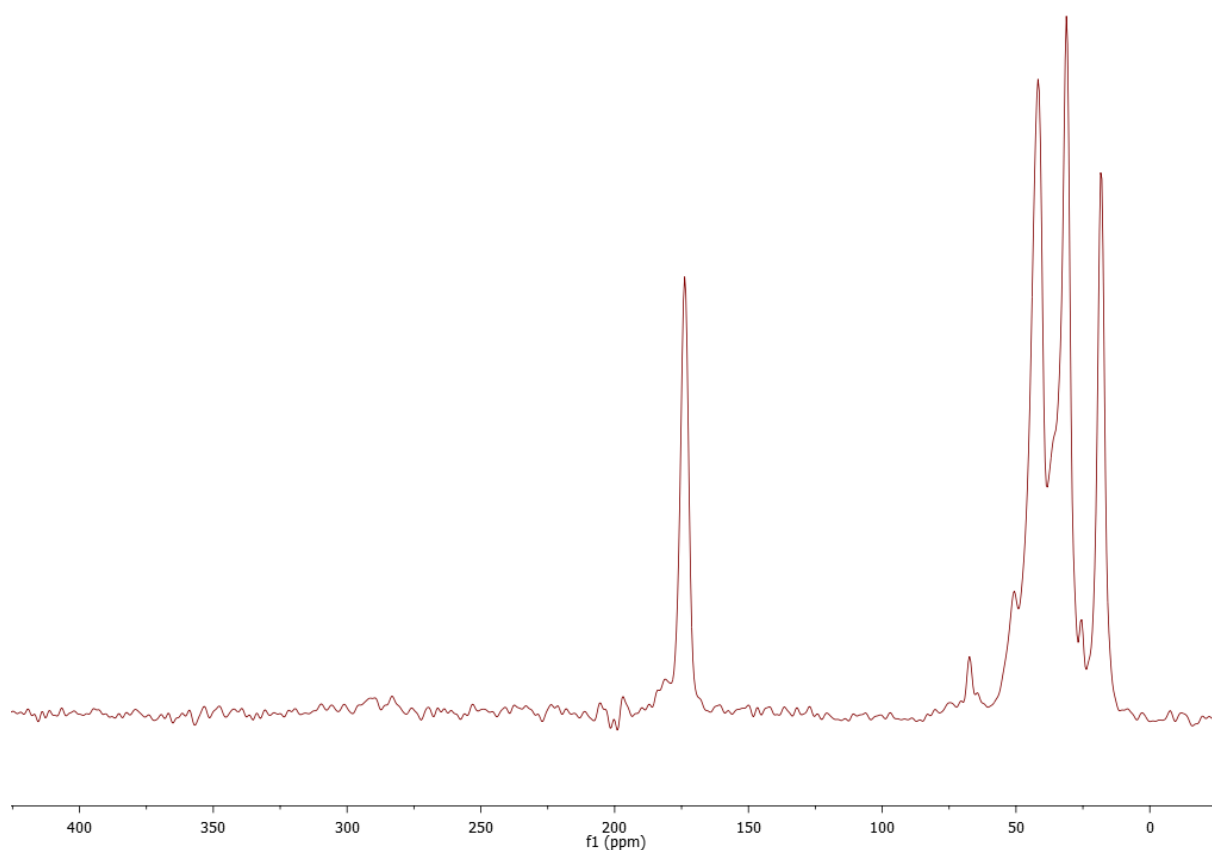
$^{13}\text{C}$  NMR measurements on RhPVP NPs (Figure 2.25a) showed a typical PVP polymer spectrum including a signal at 174 ppm for the CO coming from the PVP. Exposing the NPs to atmospheric pressure of  $^{13}\text{CO}$  over 20 h, showed appearance of a peak at 125 ppm that corresponds to carbon dioxide ( $\text{CO}_2$ ), a very wide large signal between 200 and 420 ppm, with a sharp peak in central position at *ca.* 290 ppm, and another short sharp peak at 193 ppm. The broad  $^{13}\text{CO}$  signal can be attributed to CO molecules coordinated in bridging mode. The sharp peak at *ca.* 290 ppm is difficult to attribute, probably to the geminal COs. Whereas, the sharp peak at 193 ppm can be attributed to CO molecules coordinated in terminal mode. According to literature,<sup>208</sup> and referring to previous studies in the team,<sup>73</sup> bridging CO molecules are expected to coordinate onto the faces of the NPs, whereas terminal ones onto corners and edges. The presence of both a wide peak and sharper ones evidence that bridging and terminal COs are present on the surface of the RhPVP NPs, with probably high mobility character for terminal COs but less one for bridging COs as indicated by the shapes of their corresponding signals. Indeed, the free surface of the PVP-stabilized RhNPs is expected to present different available sites on faces, edges and apexes that can accommodate different types of CO coordination with different interaction strength.

In a trial to force higher coordination of  $^{13}\text{CO}$  on the surface the NPs were treated with 3 bar of labeled carbon monoxide ( $^{13}\text{CO}$ ) over a duration of 48h. But new NMR spectrum (Figure 2.25c) showed no significant difference than the previous one, indicating that higher pressure up to 3 bar and longer reaction time are not sufficient to modify the coordination of CO on the surface of the NPs.



**Figure 2.25:** Solid state  $^{13}\text{C}\{^1\text{H}\}$  NMR of (a) RhPVP NPs, (b) RhPVP NPs under 1 bar of CO over 20h, (c) RhPVP NPs under 3 bar of CO over 48h.

Cross Polarization at Magic Angle Spinning (CP MAS)  $^{13}\text{C}\{^1\text{H}\}$  NMR spectrum revealed the disappearance of the two peaks previously observed after coordination of CO on the surface of the NPs (Figure 2.26). This signifies that CO groups attached on the surface of the NPs are not affected by cross polarization phenomenon that may be expected from close hydrogen carriers. Such results thus confirm our beliefs that CO molecules are not close to PVP and consequently that no chemical coordination of the PVP polymer takes place on the surface of the NPs. The control of the growth of the NPs takes place through steric hindrance inside the matrix of the organic polymer.

CP MAS  $^{13}\text{C}\{1\text{H}\}$ 

**Figure 2.26:** CP MAS  $^{13}\text{C}\{1\text{H}\}$  NMR spectrum of RhPVP NPs after CO adsorption (1bar, 20h).

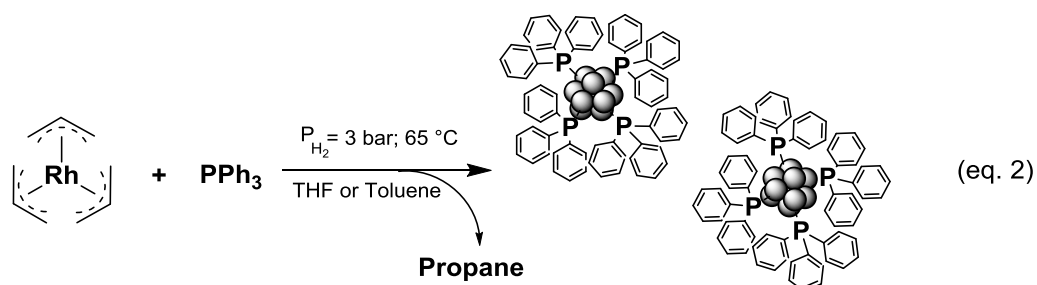
Synthesis of Rh NPs stabilized with PVP using  $[\text{Rh}(\eta^3\text{-C}_3\text{H}_5)_3]$  complex as the metal source, showed to be an effective approach to obtain small spherical NPs with a mean size of  $2.2 \pm 0.9$  nm without agglomeration. Obtained NPs are nicely crystalline with interplanar spacing of 0.24 nm, as expected for fcc rhodium typical crystalline structure. CO adsorption studies on the surface of the particles demonstrated their ability to coordinate molecules on faces, edges and apexes. This can be of high interest in different catalytic reactions. Solid state NMR studies showed that the surface of the particles is not interacting with the PVP leading to a metallic surface that is very accessible for potential reactants. These results evidence that this RhPVP NPs system is a good model to perform comparison studies with other ligand-stabilized Rh NPs, in terms of surface properties for application in catalysis.



### II.3 PPh<sub>3</sub>-Stabilized Rhodium NPs

Triphenylphosphine (PPh<sub>3</sub>) ligand was selected as stabilizer for Rh NPs synthesis owing to our experience in nanochemistry with phosphorous ligands with other metals.<sup>213</sup> Moreover, PPh<sub>3</sub> is well-known as a strong coordinating ligand with interesting electron donating effect especially for applications in catalysis.<sup>214-216</sup>

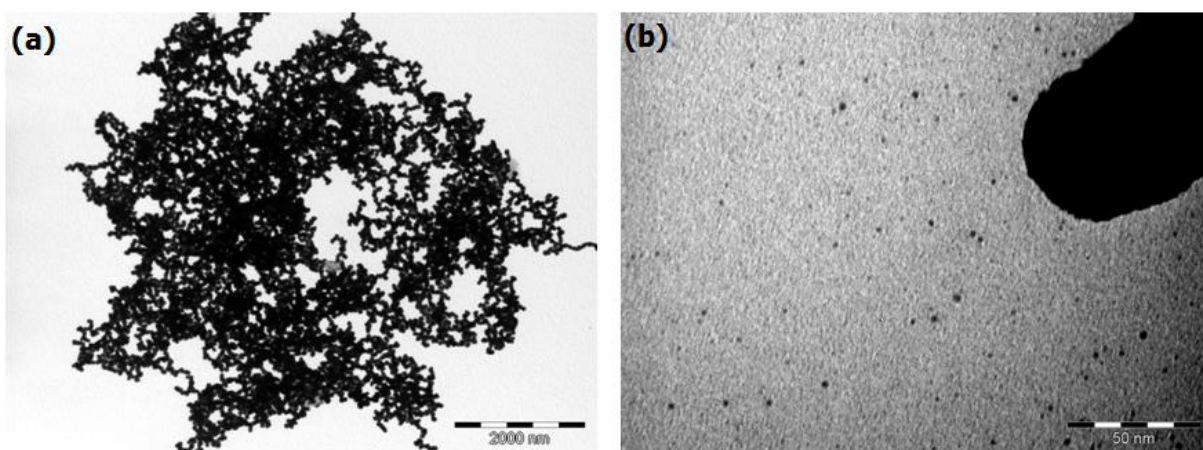
The synthesis of the particles was realized from [Rh( $\eta^3$ -C<sub>3</sub>H<sub>5</sub>)<sub>3</sub>] complex in the presence of different ratios of triphenylphosphine dispersed in either THF or toluene solution under 3 bar of dihydrogen according to eq. 2.



Performing the reaction overnight at room temperature with different ratios of PPh<sub>3</sub> (0.2, 0.5, and 1 molar eq./[Rh]) did not yield in any change of color of the starting yellow reaction mixture, indicating no formation of NPs. Whereas, heating the reaction up to 65°C allowed the solution to become dark brown within a few hours. Analysis of the colloidal solutions by TEM techniques confirmed the presence of RhNPs.

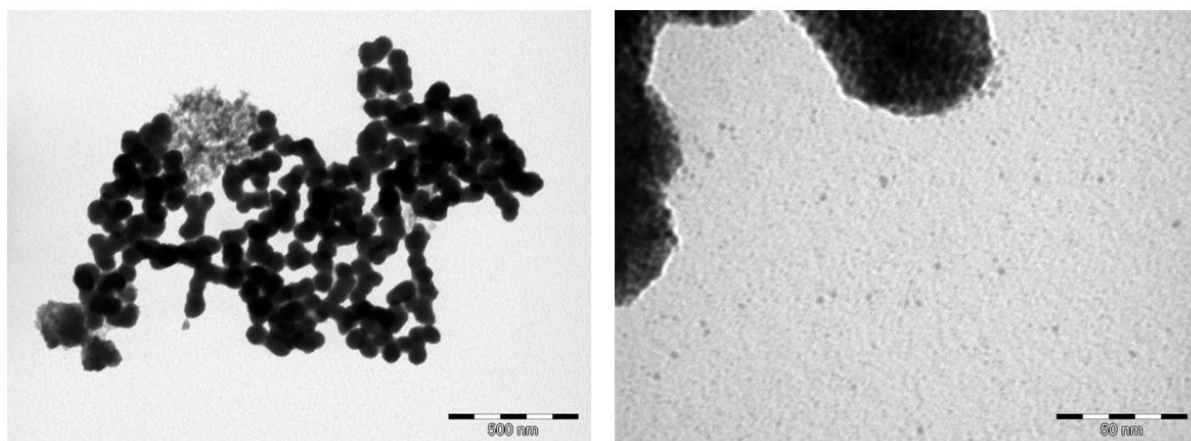
#### II.3.1 Electron Microscopy Analysis

First of all, a [PPh<sub>3</sub>]/[Rh] ratio of 0.2 eq. was tested which is a value very often applied in the team for the synthesis of ligand-stabilized MNPs. Figure 2.27 shows results collected from TEM analysis from the crude colloidal suspension obtained. The reaction was performed over 16 h to insure complete decomposition of the metal complex and the obtained black solution precipitated within 1 h after stopping the stirring. Figure 2.27a reveals very big objects. This type of formations was observed all over the grid. At higher magnification (Figure 2.27b) the bright and clear areas of the TEM grid reveal the presence of small spherical particles, in a size range between 2 and 5 nm, but most of them are agglomerated.



**Figure 2.27:** TEM images of RhPPh<sub>3</sub> NPs ( $[L]/[Rh]=0.2$  eq.) at two different magnifications.

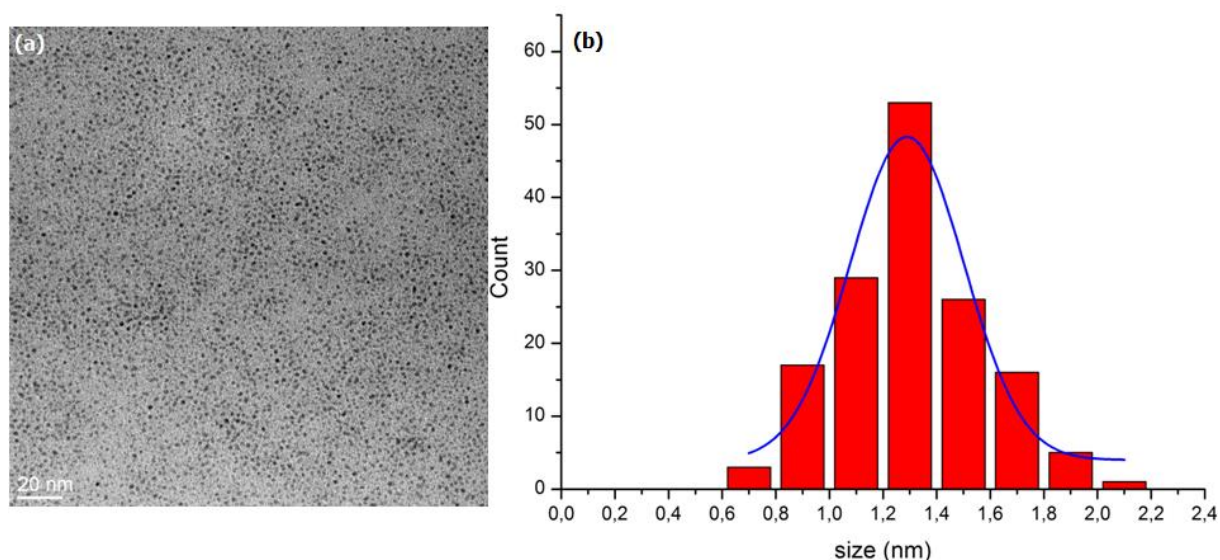
The use of 0.5 equivalent of PPh<sub>3</sub> while keeping all the parameters the same did not induce a significant change, it just took longer time for the resulted dark solution to precipitate (overnight). TEM images showed again the presence of big agglomerates of particles all over the grid (Figure 2.28a), but with smaller size than for the previous essay. At higher magnification we could observe that they are constituted of aggregated smaller particles. In the bright regions of the grid (Figure 2.28b), small NPs are visible.



**Figure 2.28:** TEM images of RhPPh<sub>3</sub> NPs ( $[L]/[Rh]=0.5$  eq.) at two different magnifications.

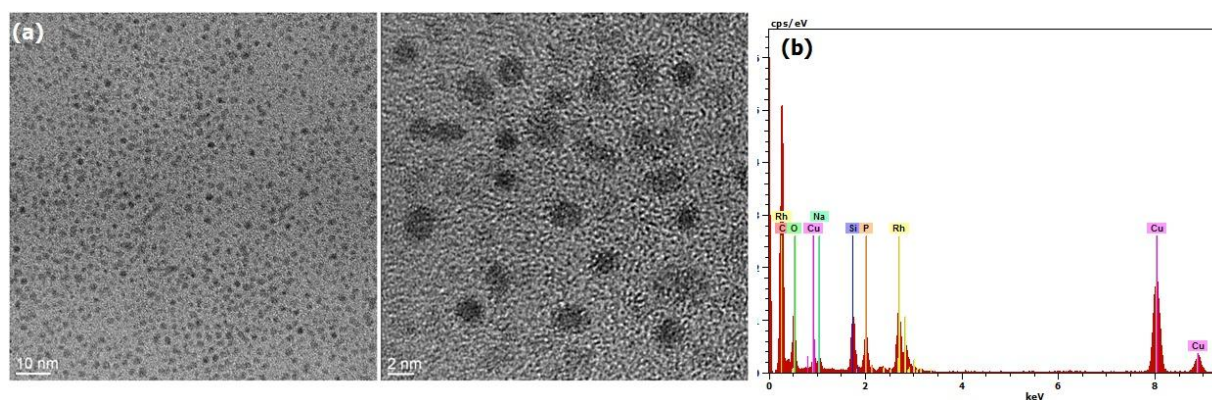
Doubling the amount of the PPh<sub>3</sub> ( $[PPh_3]/[Rh]=1$ ) under the same reaction conditions resulted in a dark brown colloidal solution that was stable for several weeks without precipitation. TEM analysis (Figure 2.29a), revealed the presence of ultra small NPs with a mean size of  $1.3 \pm 0.4$  nm. They are spherical and well-dispersed all over the grid, without any aggregation. Estimation of the number of Rh atoms to fill the closed packing structure of

a 1.3 nm spherical particle is around 83. At such a small size, a high number of Rh atoms are present at the particle surface (~50%) which may lead to a high number of potential active sites for catalysis. ICP-AES analysis after precipitation of the particles and purification by washing with cold pentane indicated a rhodium content in the sample of 66.2%.



**Figure 2.29:** (a) TEM image of the RhPPh<sub>3</sub> NPs ([PPh<sub>3</sub>]/[Rh]= 1). (b) Corresponding size distribution of RhPPh<sub>3</sub> NPs.

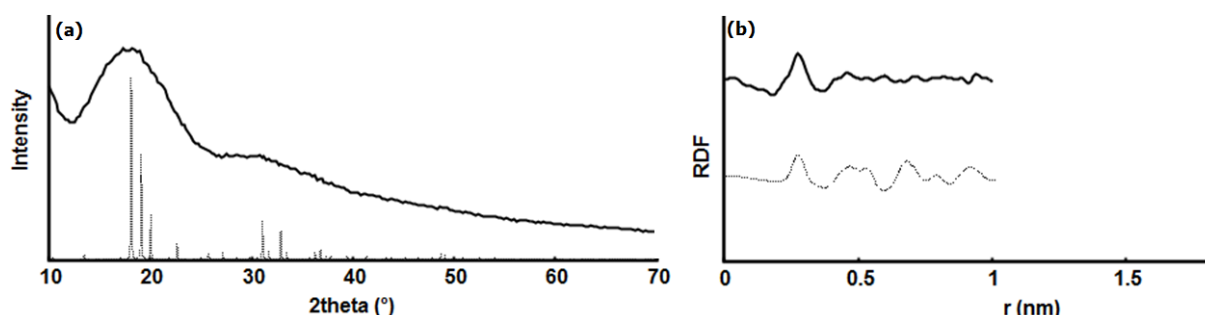
HRTEM images of the RhPPh<sub>3</sub> NPs synthesized in the presence of 1 equivalent of the phosphine before purification (Figure 2.30a), unlike the RhPVP NPs (see part II.2.1), they present an amorphous structure, but, they are in coherence with the mean size measured from regular TEM images. EDX analysis (Figure 2.30b) shows clearly the peaks that correspond to Rh and P elements.



**Figure 2.30:** (a) HRTEM images of the RhPPh<sub>3</sub> NPs ([PPh<sub>3</sub>]/[Rh]= 1) and (b) corresponding EDX analysis.

### II.3.2 Wide Angle X-ray Scattering Analysis

In order to further investigate the structure of the purified  $\text{PPh}_3$ -stabilized Rh NPs, we employed WAXS techniques (Figure 2.31) in the solid state. The measurements confirmed the small size of the  $\text{RhPPh}_3$  NPs with a coherence length of ca. 1.2 nm (close to 1.3 nm determined by TEM) but showed their poorly crystalline character. Moreover, they evidenced that these  $\text{RhPPh}_3$  NPs do not display a perfect fcc crystalline structure; longer Rh-Rh distances are observed which can result from a strong interaction of the  $\text{PPh}_3$  ligand at the metal surface as previously observed in the team with other systems of NPs.<sup>72,217</sup> From reciprocal space measurements (Figure 2.31a), a very broad pattern was observed in the reciprocal space, which cannot be safely attributed to a well-defined structure. Consistently, very few distances are observed in the related RDF. The most likely structure is highly disordered manganese beta. Coherence length can be grossly evaluated to 1 nm, and from these elements, objects can be either described as very small NPs or just metallic clusters.



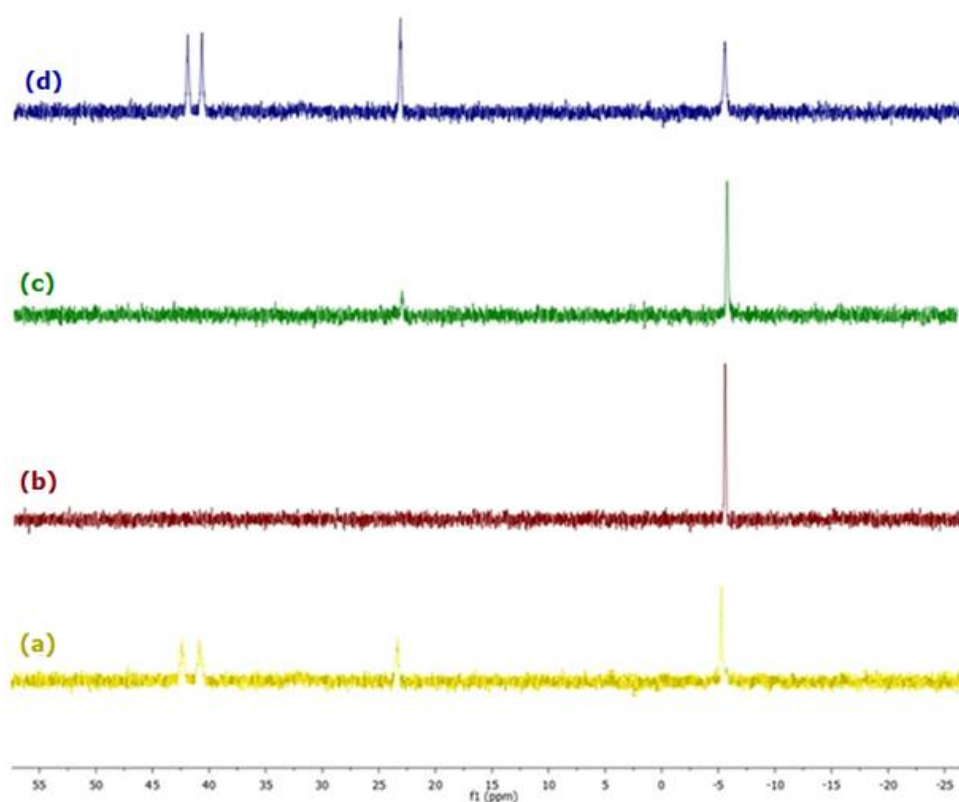
**Figure 2.31:** (a) WAXS measurements (solid line) in reciprocal space and (b) in real space, for  $\text{RhPPh}_3$  NPs in comparison with calculated data for Rh in manganese- $\beta$  structures (dashed line).

### II.3.3 NMR Study

Synthesis of phosphine-stabilized rhodium nanoparticles during the thesis did not proceed without heating the reaction mixture. Our hypothesis is that internal Rh-P species may be formed that do not decompose at r.t. Therefore, in order to understand the reason behind this, we tried to follow the behavior of a  $[\text{Rh}(\eta^3\text{-C}_3\text{H}_5)_3] + \text{PPh}_3$  mixture in deuterated THF, inside a NMR tube, by  $^{31}\text{P}$  NMR under decomposition conditions.

Figure 2.32b shows the  $^{31}\text{P}$  spectrum of the mixture recorded before pressurizing the NMR tube. This spectrum revealed a single sharp peak at -5 ppm, which corresponds to free triphenylphosphine in solution, without any detection of other peaks. But the spectrum recorded at  $-80^\circ\text{C}$  (Figure 2.32a) reveals evolution of a peak at 23 ppm that correspond to the oxide of  $\text{PPh}_3$ , in addition to two short new peaks at 40 and 42 ppm. The two new peaks, according to the studies performed by Heaton *et al.*<sup>218</sup> can be attributed to “ $\text{Rh}(\text{PPh}_3)_3$ ” complex with a planar T-shaped fragment most probably. Therefore, *in situ* formation of an intermediate rhodium-phosphine complex may explain why heating of the reaction medium is necessary to form Rh NPs.

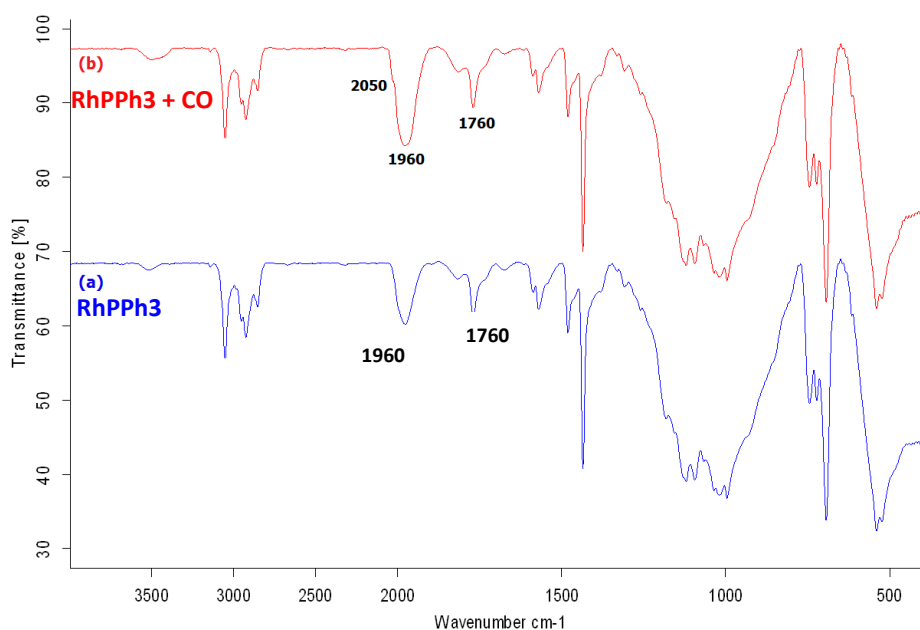
Later on, the tube was pressurized by 3 bar of dihydrogen, and the decomposition was followed by  $^{31}\text{P}$  NMR. After 6 h at  $65^\circ\text{C}$ , the 2 peaks at 40 and 42 ppm are present again with higher intensity revealing higher quantity of the ppm *in situ* formed species. Therefore, from these results we can suggest formation of an intermediate rhodium-phosphine complex that may explain why it is necessary to heat the reaction medium to form Rh NPs.



**Figure 2.32:** (a)  $[\text{Rh}(\text{C}_3\text{H}_5)_3]$  complex +  $\text{PPh}_3$  in THF-D8 at  $-80^\circ\text{C}$ , (b)  $[\text{Rh}(\text{C}_3\text{H}_5)_3]$  complex +  $\text{PPh}_3$  in THF-D8 at r.t., (c)  $[\text{Rh}(\text{C}_3\text{H}_5)_3]$  complex +  $\text{PPh}_3 + \text{H}_2$  at  $40^\circ\text{C}$  (d)  $[\text{Rh}(\text{C}_3\text{H}_5)_3]$  complex +  $\text{PPh}_3 + \text{H}_2$  at  $65^\circ\text{C}$

### II.3.4 CO Adsorption Study

The coordination of CO on the surface of the RhPPh<sub>3</sub> NPs was investigated by FT-IR technique. The FT-IR spectrum recorded with purified RhPPh<sub>3</sub> NPs before exposure to CO gas (Figure 2.33a) revealed, as in the case of RhPVP NPs, the presence of several peaks at *ca.* 1760, 1810 and 1960 cm<sup>-1</sup>, which as mentioned before can result from CO coming from decarbonylation of THF<sup>209</sup>. The strong peak at higher wavelength (1960 cm<sup>-1</sup>) may correspond to terminal CO coordination, where the others to COs in bridging modes. After 24 h of treatment of the NPs with 1 bar of CO, a new FT-IR spectrum (Figure 2.33b) showed an increase in the intensity of the peak at *ca.* 1960 cm<sup>-1</sup> that indicates coordination of more CO molecules on the surface. Besides the increased intensity of the peak, we can also observe a small shoulder on the left side of the peak at *ca.* 2050; peaks at this value range correspond to high electron dense C=O bond, attributed to gem-carbonyl mode (multicarbonyl) generally caused by excess of CO. These results show the ability of the metal surface to coordinate CO molecules in different modes and probably at different positions including faces, edges or apexes.

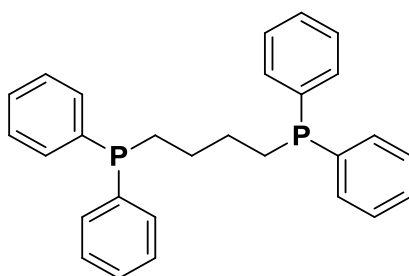


**Figure 2.33:** (a) FT-IR spectrum of RhPPh<sub>3</sub> NPs after 24h of CO exposure, (b) FT-IR of purified RhPPh<sub>3</sub> NPs.

PPh<sub>3</sub>-stabilized Rh NPs were synthesized under the form of small and well-controlled NPs. They present an amorphous surface, and their structure is not fcc but manganese- $\beta$ . The CO adsorption studies on the surface of these NPs revealed their ability to host CO in different coordination modes, which may be of great interest for catalytic reactions.

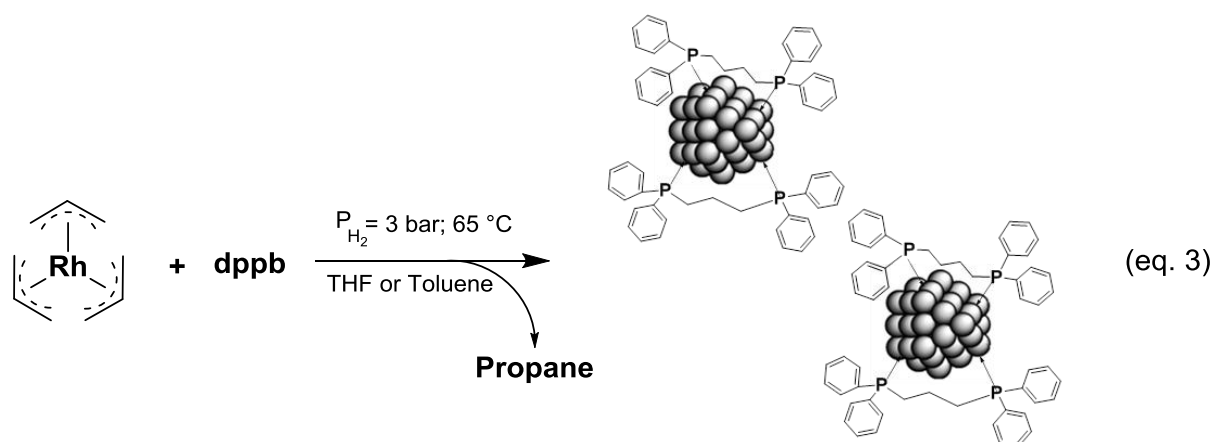
## II.4 dppb-Stabilized Rhodium NPs

1,4-Bis(diphenylphosphino)butane (dppb) is another coordinating phosphine ligand that was used in this work. dppb resembles to  $\text{PPh}_3$  ligand used in the previous part, having two phenyl groups on each phosphorous atom in addition to a C4-allyl chain connecting the two P atoms. Therefore, this type of ligand is believed to provide a bidentate coordination through the lone electron pairs of the phosphorous atoms. Such a ligand is expected to cover more the surface of MNPs.



**Scheme 2.9:** 1,4-Bis(diphenylphosphino)butane (dppb) ligand.

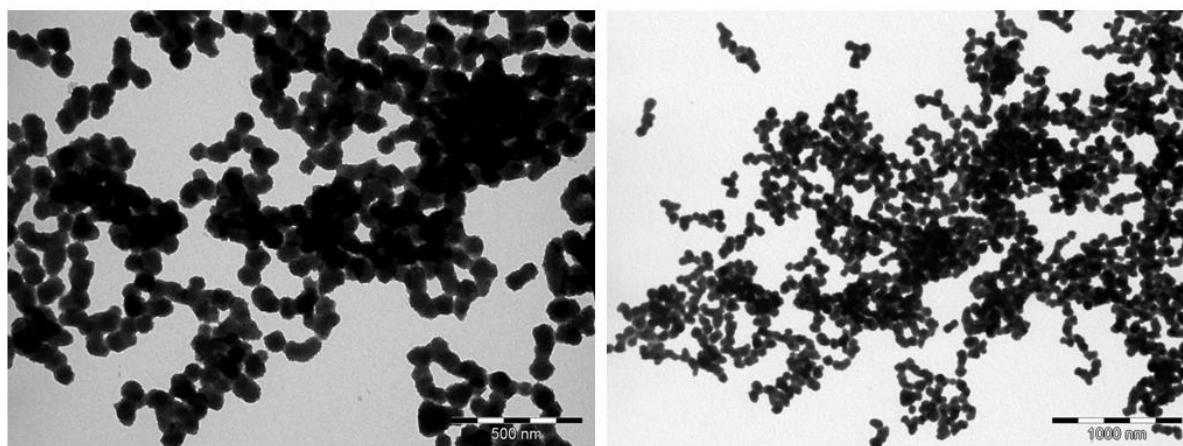
The dppb-stabilized Rh NPs were synthesized starting from  $[\text{Rh}(\eta^3\text{-C}_3\text{H}_5)_3]$  complex in the presence of different ratios of 1,4-Bis(diphenylphosphino)butane dispersed in either THF or toluene solution under 3 bar of dihydrogen at r.t. and at 65 °C according to (eq. 3).



Similarly to the RhPPh<sub>3</sub> NPs, performing the reaction overnight at r.t. with different ratios of ligand (0.2, 0.5, 0.7 and 1 molar eq./[Rh]) did not yield in any change of color of the starting yellow reaction mixture, indicating no formation of NPs. When heating the reaction up to 65°C, the reaction mixture became black within a few hours, as expected if MNPs are formed.

### II.4.1 Electron Microscopy Analysis

Using 0.2 equivalent of dppb ligand, which corresponds to 0.4 in terms of P/Rh ratio when considering the two phosphorous atoms present in the ligand, over 16 h under 3 bar of dihydrogen resulted in the formation of a black solution that precipitated fast. Figure 2.34 shows TEM images collected at different magnifications from the crude colloidal solution obtained in these conditions. Agglomerates are present all over the grid, containing large and very dark spherical particles in a size range between 50 and 100 nm connected together that appear to not be agglomerates of smaller particles (Figure 2.34).

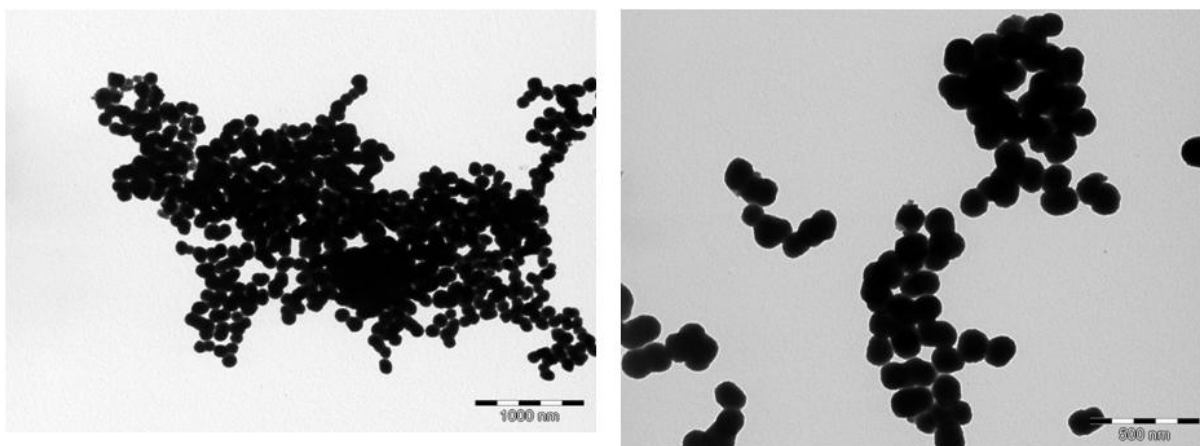


**Figure 2.34:** TEM images of Rh NPs obtained with 0.2 equivalent of dppb ligand in THF at two different magnifications.

It is worthy to mention that when the reaction was carried out in toluene instead of THF while keeping all other parameters equal, a slightly larger particle size was obtained. Figure 2.35 presents TEM images of Rh NPs stabilized with 0.2 equivalent of dppb ligand in toluene showing the formation of spherical particles having a size around 200 nm against 50-100 nm in THF. This difference can be explained by a lower or no stabilization effect of

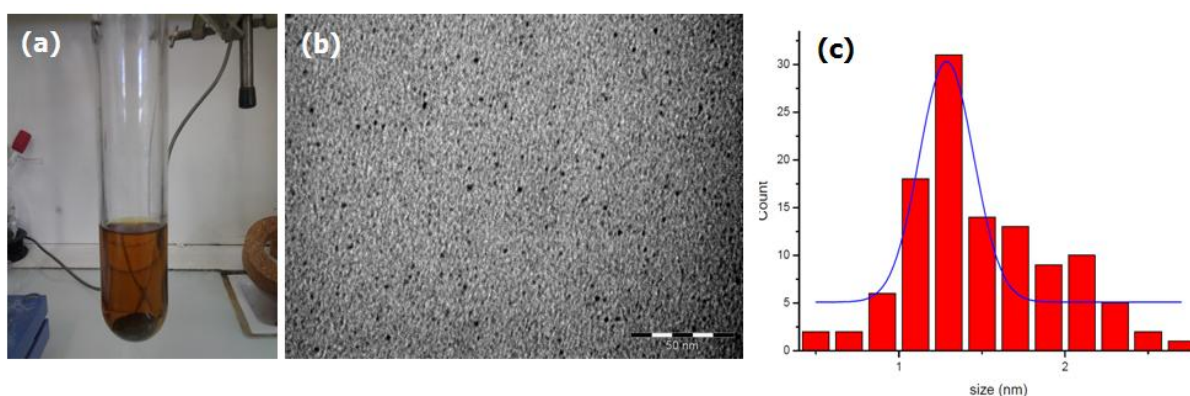


toluene compared to THF. Indeed, THF is known to be a coordinating solvent and has already been observed at the surface of MNPs.<sup>219-220</sup>



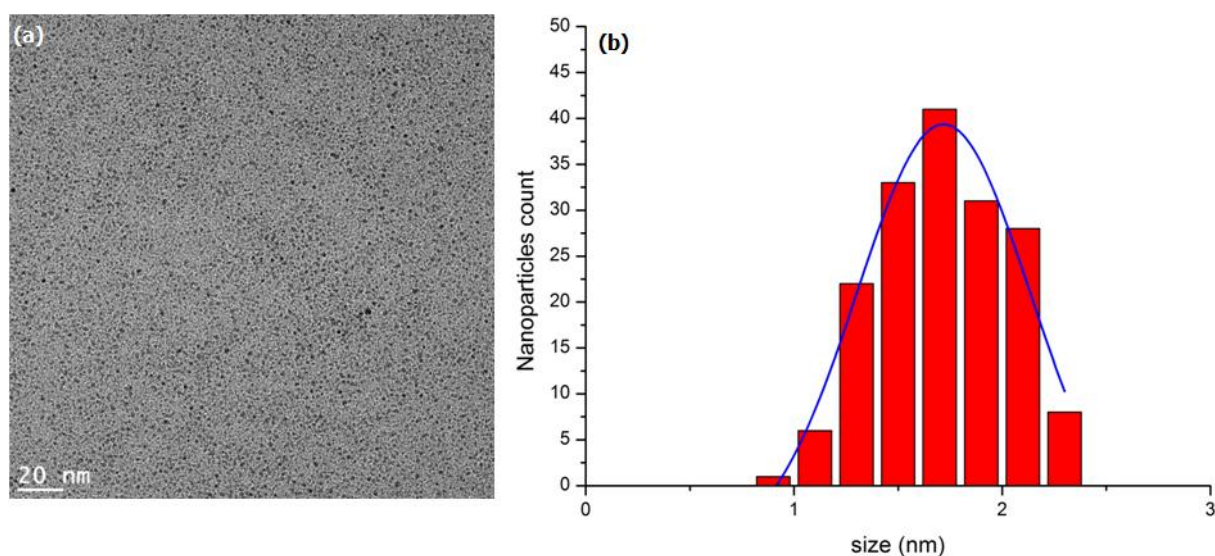
**Figure 2.35:** TEM images of Rh NPs obtained with 0.2 equivalent of dppb ligand in toluene at two different magnifications.

When using 0.5 equivalent of dppb to synthesize Rh NPs under the same reaction conditions (3 bar H<sub>2</sub>, 65 °C overnight) which corresponds to 1 in terms of P/Rh ratio when considering the two phosphorous atoms present in the ligand, a brown colloidal solution was formed (Figure 2.36a). Electron microscopy images of this crude colloid showed the presence of small spherical NPs with a mean size of  $1.3 \pm 0.3$  nm. Purification of the system by precipitation induced by cold pentane addition resulted in the separation of an orange solution and a very low NPs yield. This indicates that a stable soluble intermediate species is formed, resulting in low quantity of NPs formed.



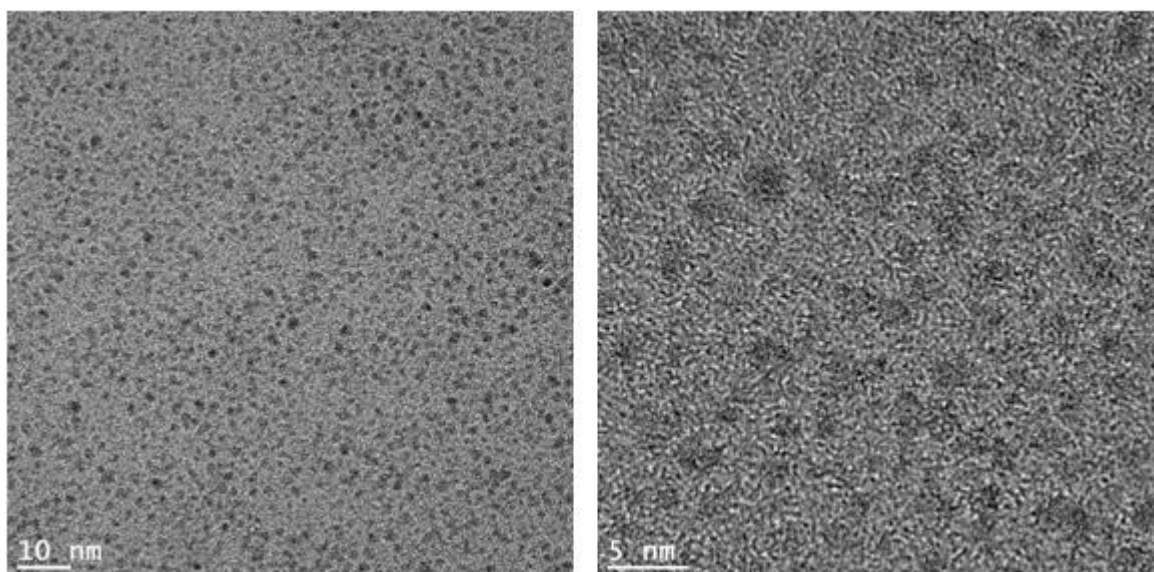
**Figure 2.36:** (a) Picture of the Rh dppb crude colloidal solution (0.5 eq.) (b) TEM image of Rh dppb (0.5 eq.) NPs and (c) Corresponding size distribution.

Given the big difference between the results obtained with 0.1 and 0.5 equivalent of dppb ligand, we decided to use an intermediate quantity of dppb that is 0.3 molar equivalent, which corresponds to 0.6 in terms of P/Rh ratio when considering the two phosphorous atoms present in the ligand. TEM images of the obtained colloidal solution (Figure 2.37a) evidenced the presence of small and well-dispersed NPs without significant agglomeration. They are spherical in shape with a mean size of  $1.7 \pm 0.8$  nm. Purification of the particles performed through precipitation in cold pentane resulted in a black powder. ICP-AES analysis indicated a Rh content of 45.6% in this sample. Estimation of the number of Rh atoms to fill the closed packing structure of a 1.7 nm spherical particle is around 185 atoms with  $\sim 40\%$  of atoms on the NP surface that is *ca.* 46 atoms.



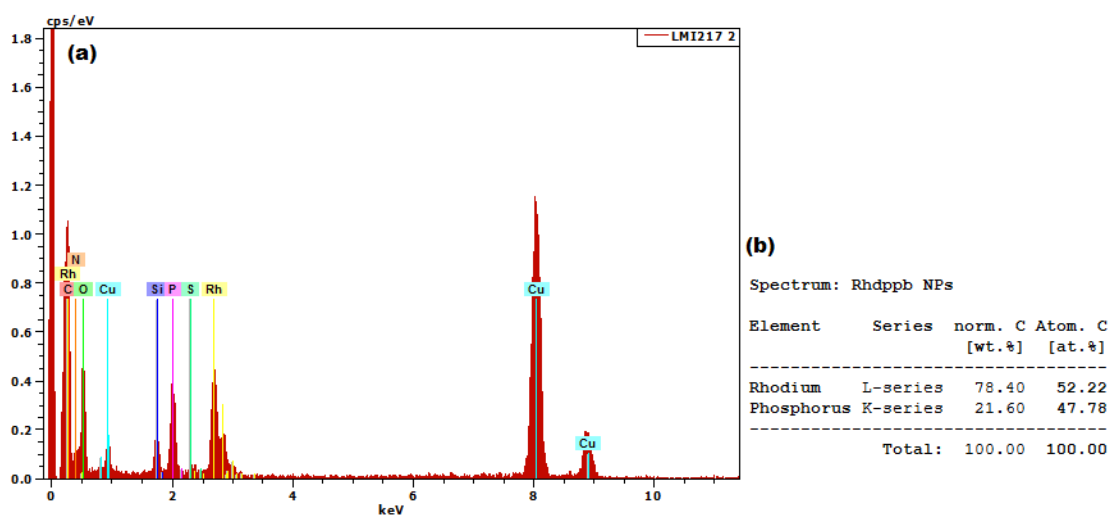
**Figure 2.37:** (a) TEM image of Rhdpbb NPs obtained at a ratio  $[dppb]/[Rh]=0.3$ , and (b) Corresponding size distribution.

Similarly to the  $PPh_3$ -stabilized Rh NPs, HRTEM images (Figure 2.38) of the dppb-stabilized Rh NPs revealed an amorphous structure with low crystallinity, but the size is in coherence with the mean size measured by regular TEM.



**Figure 2.38:** HRTEM images of Rhdppb NPs (0.3 eq.)

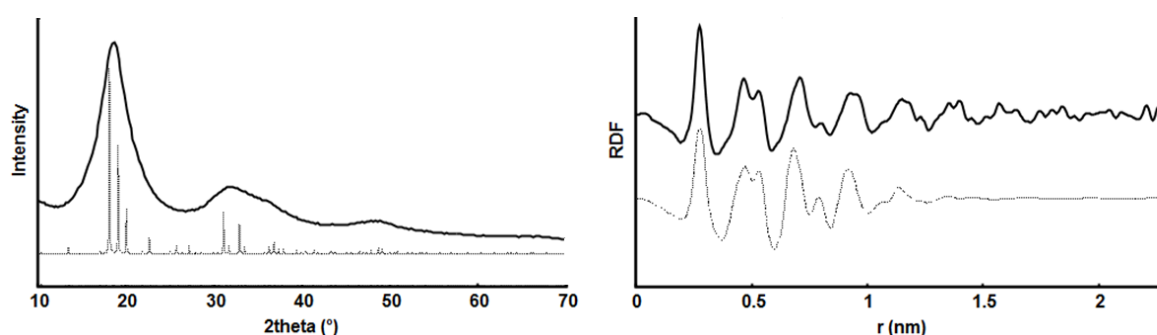
Energy Dispersive X-ray analysis (Figure 2.39a) was performed on several particles on the grid in order to determine the present elements, leading to similar results. Figure 2.39a shows an EDX spectrum as example, both Rh and phosphine are clearly present in equal global ratios. Figure 2.39b illustrates the quantitative measurements revealing a ratio of almost 1:1 (52 Rh:47 P). But considering that 40% of the Rh atoms are on the surface of the NPs, and that the phosphine coordinates only to these surface atoms, we can estimate that the number of dppb ligands coordinated to each Rh atom on the surface is equal to 0.9 dppb/Rh. Therefore, for a 1.7 nm particle having ~46 Rh atoms on the surface, 41 molecules of dppb are coordinated.



**Figure 2.39:** (a) EDX spectrum of Rhdppb NPs (0.3 eq.) (b) Quantitative analysis of the chemical composition of Rh dppb NPs.

### II.4.2 Wide Angle X-ray Scattering Analysis

WAXS analysis technique in the solid state on purified NPs was used to investigate the structure of the obtained dppb-stabilized Rh NPs (Figure 2.40). The analysis revealed metallic Rh NPs, however the pattern observed in reciprocal space doesn't match the expected fcc one. Moreover, coherence length is here also close to 2.2 nm, much larger than the size of 1.7 nm observed by TEM which is counter intuitive since crystalline domains are necessarily smaller than the overall size or equal for single crystalline NPs. Such a behavior was however previously observed for metallic NPs elaborated in solution, including Co<sup>221-222</sup> and Rh<sup>223</sup> and could be related to a structure primarily observed for the beta phase of manganese (ICSD 41775, PDF 33-887). This less compact structure doesn't include extended regular planes like the fcc or hcp ones. It is much more difficult to observe and characterize by TEM which explains the strong discrepancy between size from TEM and coherence length from WAXS.

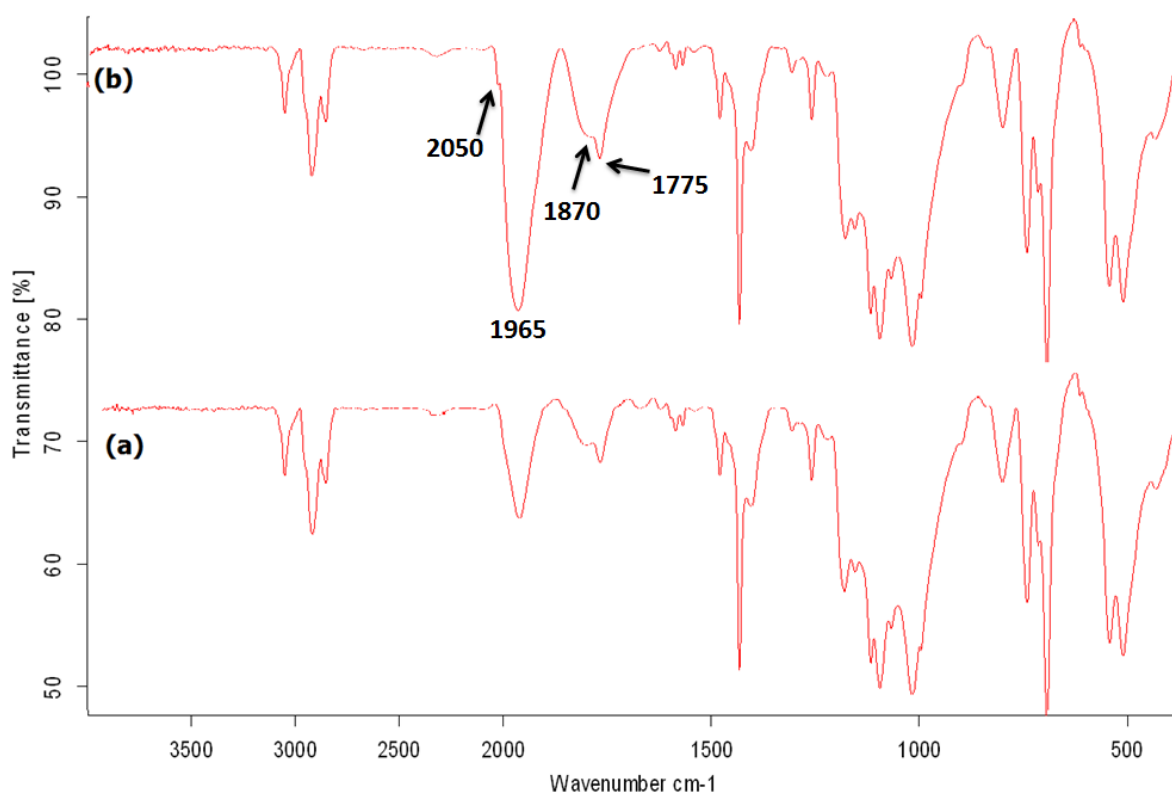


**Figure 2.40:** (a) WAXS measurements (solid line) in reciprocal space and (b) in real space, for Rh<sub>dppb</sub> NPs in comparison with calculated data for Rh in manganese-β structures (dashed line).

### II.4.3 CO Adsorption Study

The coordination of CO at the surface of the Rh<sub>dppb</sub> NPs was investigated by FT-IR spectroscopy. The FT-IR spectrum of the purified dppb<sub>0.3</sub>-stabilized NPs (Figure 2.41a) revealed, as in the previous cases, the presence of peaks at the CO region before any exposure to CO atmosphere, which may be attributed to CO resulting from decarbonylation of THF<sup>209</sup> or to hydrides on the surface,<sup>211-212</sup> as mentioned before. After 48 h of reaction under 1 bar of CO, FT-IR data showed a high increase of the CO peaks intensity indicating the coordination of more CO molecules on the surface of the particles. Peaks at 1775 and 1870 cm<sup>-1</sup>

correspond to CO molecules coordinating in bridging mode, whereas the peak at  $1965\text{ cm}^{-1}$  to a CO in a terminal mode. Moreover, we can observe a small shoulder on the left side of the peak at *ca.*  $2050\text{ cm}^{-1}$ , which can correspond to multicarbonyl species according to Vaccari *et al.*<sup>210</sup> This results highlight the potentials of this system of NPs in hosting CO molecules at their surface while having a lot of coordinating ligand.

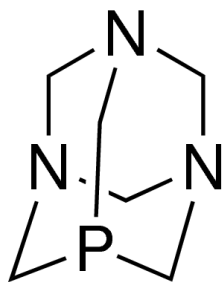


**Figure 2.41:** (a) FT-IR of Rhdpbb NPs (0.3 eq.), (b) FT-IR of Rhdpbb NPs after 24h reaction with CO.

The synthesis of small and well-controlled dppb-stabilized Rh NPs was achieved, the surface of the particles revealed to be amorphous with the unusual manganese- $\beta$  structure. Through CO adsorption studies, it was shown that substrates could be coordinated on the surface in different positions, which is of interest for different catalytic reactions.

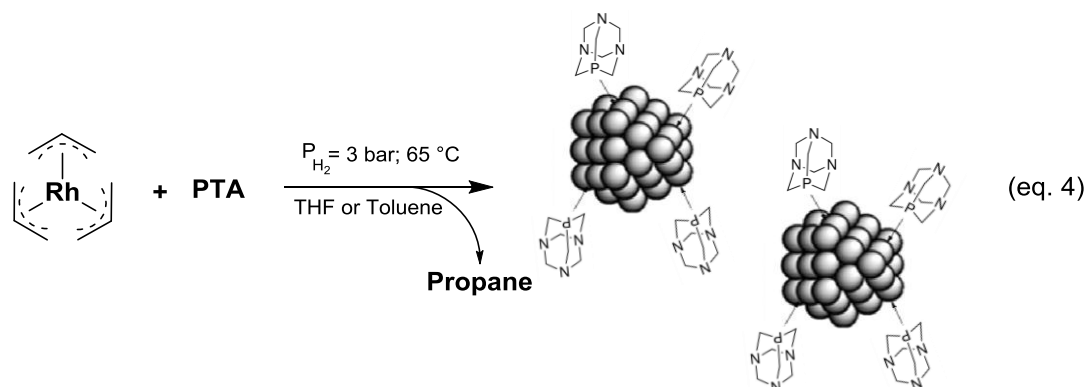
## II.5 PTA-Stabilized Rhodium NPs

In 1974, Daigle and coworkers<sup>224</sup> synthesized the water soluble phosphine 1,3,5-triaza-7-phosphaadamantane (PTA) (Figure 2.42). Since then, this ligand has been used in the development of water-soluble complexes for their application in aqueous catalysis. The use of nanocatalysts provides new opportunities and the development of water-soluble NPs offers the possibility to use them as catalysts in multiphase reaction systems like liquid/liquid biphasic systems, which insures low cost catalyst recovery. Indeed, in many industrial applications the catalyst is soluble in water whereas the substrates and products are only soluble in the organic phase, hence providing a feasible separation process.



**Figure 2.42:** 1,3,5-triaza-7-phosphaadamantane (PTA).

The preparation of water-soluble NPs following our organometallic approach necessitates to circumvent the fact that the complexes used as metal precursors are water/air sensitive. In this objective, PTA is an interesting ligand because it is both soluble in THF and water. It can thus transfer its solubility properties to MNPs. This alternative was first used in the team for ruthenium<sup>225</sup> and platinum<sup>226</sup> NPs, which gave rise to very small and well-controlled NPs. This methodology has been applied after for preparing palladium<sup>227</sup> and gold<sup>228</sup> NPs. But, to the best of our knowledge, no examples for rhodium are described in the literature. So we decided to develop the synthesis of PTA-stabilized Rh NPs starting from the same  $[\text{Rh}(\eta^3\text{-C}_3\text{H}_5)_3]$  complex in the presence of different molar ratios of 1,3,5-triaza-7-phosphaadamantane (PTA) dispersed in either THF or toluene solution under 3 bar of dihydrogen (eq. 4).

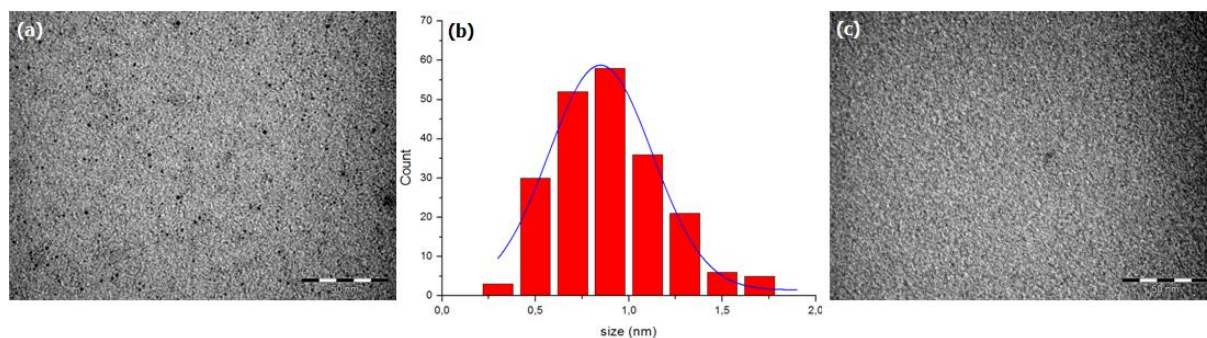


Performing the reaction overnight at room temperature with different ratios of PTA (0.5, 0.7, 0.8, 1 and 2 molar eq./[Rh]) did not yield in any change of color of the starting yellow reaction mixture, indicating no formation of NPs, also  $^{31}\text{P}$  and  $^1\text{H}$  NMR spectra showed the continuous presence of the free ligand and complex. Whereas, heating the reaction up to  $65^\circ\text{C}$  allowed the solution to become dark brown within a few hours. Analysis of the colloidal solutions par TEM confirmed the presence of RhNPs. The use of PTA in stabilizing MNPs resembles those of  $\text{PPh}_3$  and dppb ligands in terms of temperature and  $[\text{M}]/[\text{L}]$  ratio. 0.5 molar equivalents or more of PTA, and a temperature of  $65^\circ\text{C}$  are necessary to form well-dispersed NPs. Similar conditions appeared already necessary to prepare Ru NPs stabilized with this ligand.<sup>216,226</sup> The heating probably increased the solubility of PTA ligand in THF.

### II.5.1 Electron Microscopy Analysis

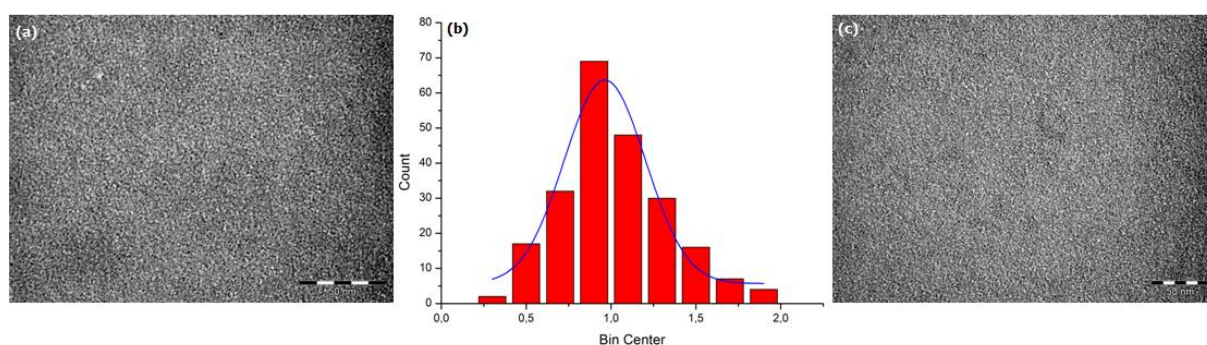
We performed the synthesis of the RhPTA NPs with  $[\text{Rh}]/[\text{PTA}]$  ratio of 0.5, 0.7, 0.8, or 1. In all the cases dark brown solutions were obtained after 2h at  $65^\circ\text{C}$ , under 3 bar of dihydrogen. Reactions were kept under  $\text{H}_2$  pressure and heating for 16h to insure full decomposition of the precursor. Then a drop of the crude colloidal solutions was dispersed over a carbon coated grid for electron microscopy analysis. In order to evaluate the behavior of the obtained NPs in water, after precipitation and purification in cold pentane, the solid powder was dissolved in ultra-pure water which yielded in a brown solution that was stable for several days. A drop of the aqueous solution of the NPs was also deposited over carbon coated grid for electron microscopy analysis in order to perform comparison studies between THF and water colloidal solutions.

Reaction with 0.5 molar equivalents of PTA resulted in a stable colloidal solution with brown color, the microscopy images of which showed the presence of well-controlled NPs with an average mean size of  $0.9 \pm 0.5$  nm (Figure 2.43). After purification, the NPs were dispersed easily in water and they presented similar stability and size range. This shows how the PTA ligand transferred its hydrophilic character to the RhNPs without change in their dispersion or size characteristics.



**Figure 2.43:** (a) TEM image of RhPTA<sub>0.5</sub> NPs, (b) with the corresponding size histogram, and (c) TEM image of the particles after dispersion in water.

Using 0.8 molar equivalents of the PTA ligand to stabilize the Rh NPs also yielded in a well-controlled system with NPs of similar size range of  $1.0 \pm 0.4$  nm. No observable changes in terms of size or shape of the NPs were observed after dispersing them in water indicating also the high stability of the system (Figure 2.44)

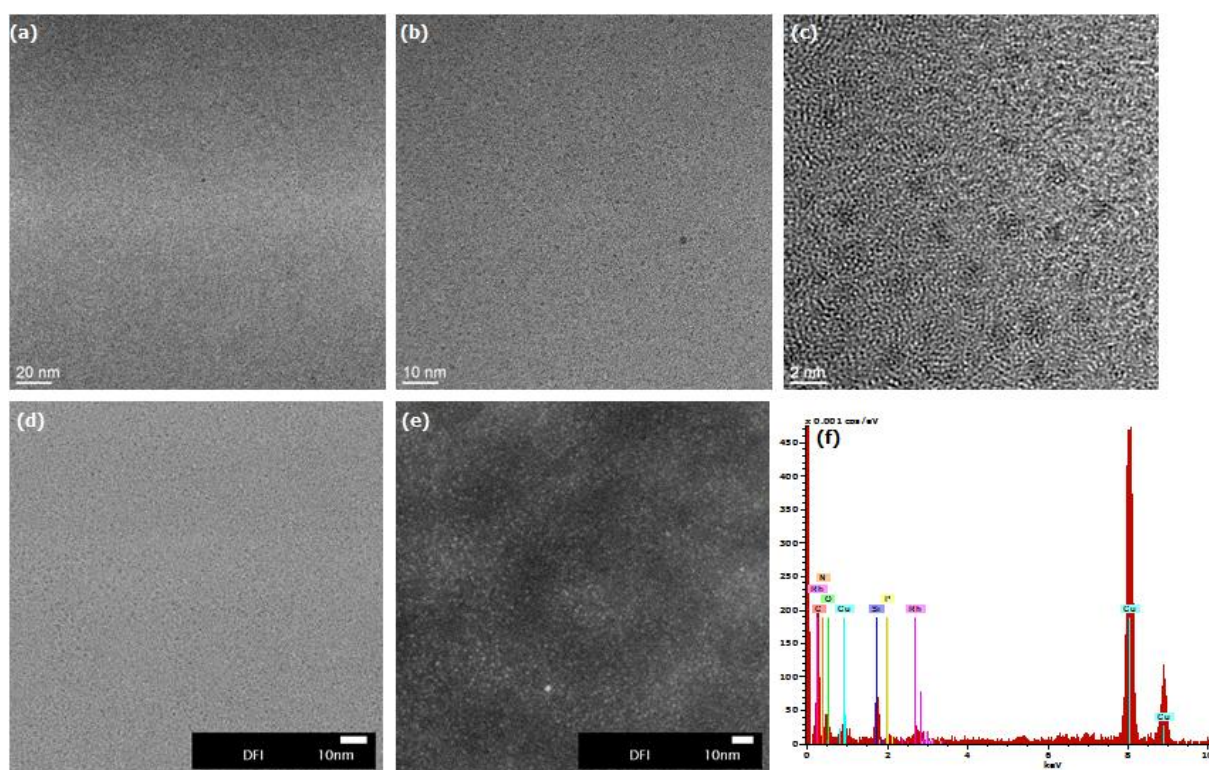


**Figure 2.44:** (a) TEM image of RhPTA<sub>0.8</sub> NPs, (b) with the corresponding size histogram, and (c) TEM image of the particles after dispersion in water.

High resolution TEM investigations were carried out on the RhPTA<sub>0.8</sub> system, (Figure 2.45a,b,c), that confirmed the size of the NPs previously determined from regular TEM. Moreover it showed that they are highly amorphous with very low crystalline regions, which



might be due to high ligand ratio on the Rh surface, or oxidation. STEM-HAADF was also applied to better identify the NPs on bright mode and with Z-contrast imaging; where metal cores of rhodium that have higher atomic number ( $Z$ ) appear more bright in color (Figure 2.45e). EDX analysis confirmed the coordination of the phosphine on the Rh, where targeting individual particles resulted in the detection of both Rh, P and N peaks.

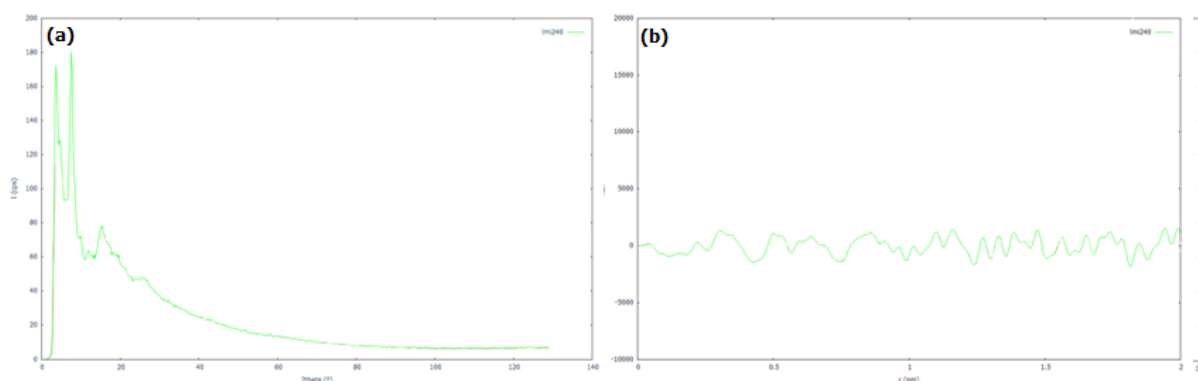


**Figure 2.45:** (a), (b) and (c) HRTEM images of RhPTA<sub>0.8</sub> NPs at different magnifications, (d) STEM-HAADF on bright mode and (e) with Z-contrast, (f) EDX analysis spectrum.

## II.5.2 Wide angle X-ray Scattering Analysis

In order to investigate the structure of the obtained RhPTA<sub>0.8</sub> NPs, WAXS analysis technique in the solid state was applied (Figure 2.46). The analysis revealed that the brownish solid clearly degraded and was actually nearly fully amorphous. The Radial Distribution Function (RDF) that is obtained by applying Fourier Transform to the WAXS diffraction pattern shows that the system is completely oxidized. Such result might be attributed to sample handling issues due to air exposure, or due to inner oxidation reaction during the synthesis of the particles. It is important to note that <sup>31</sup>P NMR spectroscopy of the purification pentane solution always showed the PTA oxide peak. This was previously

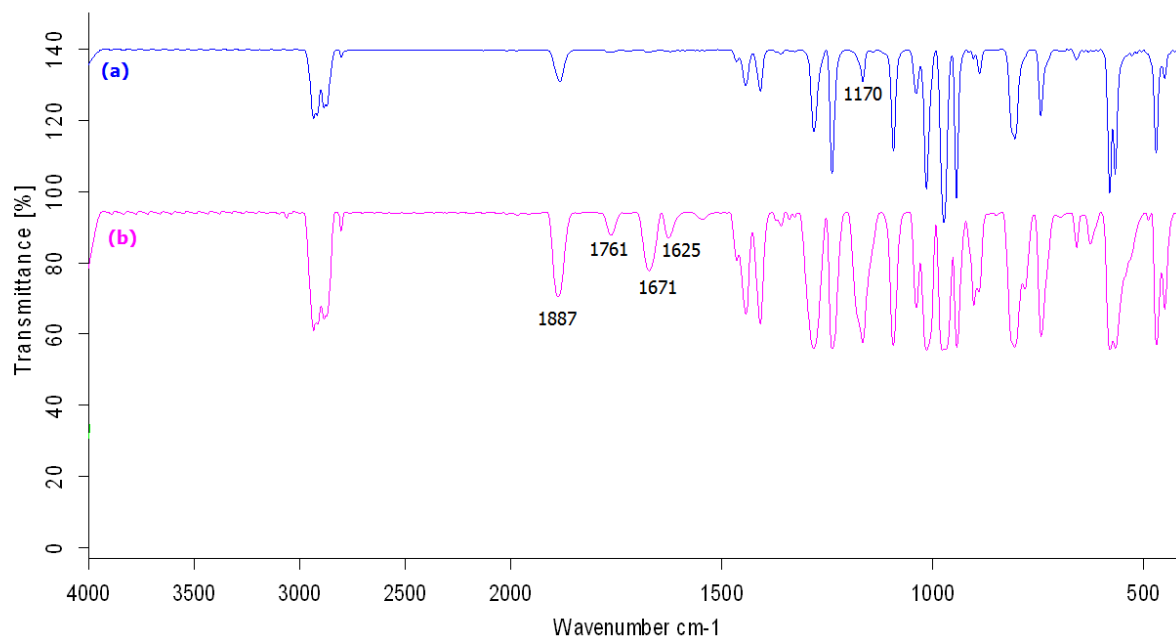
observed with Ru PTA NPs<sup>226</sup> but WAXS analysis of the RuNPs indicated Ru metallic structure. Thus, these results would necessitate to be confirmed.



**Figure 2.46:** WAXS measurements in (a) reciprocal space and (b) in real space, for RhPTA<sub>0.8</sub> NPs.

### II.5.3 CO Adsorption Study

The coordination of CO at the surface of the RhPTA<sub>0.8</sub> NPs was investigated by FT-IR spectroscopy. The FT-IR spectrum of the purified Rh NPs (Figure 2.47) shows the corresponding peak of PTA oxide at around  $\sim 1170\text{ cm}^{-1}$ . As observed with previous Rh NPs systems, a clear peak is observed before exposure to CO gas at  $1887\text{ cm}^{-1}$ ; this peak can be attributed either to CO coming from THF decarbonylation reaction or hydrides on the metal surface. Moreover, according to literature data, Rh carbonyl clusters vibrate at the same region, indicating that small clusters could be present. After exposing the RhPTA<sub>0.8</sub> NPs pellet to 1 bar of CO gas for 24 h, the FT-IR spectrum was recorded again revealing an increase in the intensity of the peak at  $1887\text{ cm}^{-1}$ , in addition to the evolution of new peaks at  $1625$ ,  $1671$  and  $1761\text{ cm}^{-1}$ . According to Vaccari *et al.* CO peaks on Rh NPs observed at less than  $1700\text{ cm}^{-1}$  correspond to carbonate-type CO. Thus vibration bonds observed here at  $1625$  and  $1671\text{ cm}^{-1}$  could correspond to carbonate species. The bonds observed at  $1887$  and  $1761\text{ cm}^{-1}$  are difficult to attribute. Given the position, the band at  $1887\text{ cm}^{-1}$  could correspond to bridging COs but this would mean that no terminal Cos are visible because no other signal is detected at upper field. Another possibility could be that the bond at  $1887\text{ cm}^{-1}$  is for terminal COs and that at  $1761\text{ cm}^{-1}$  for bridging ones. This second hypothesis would mean an important low frequency shift on the vibrational bonds compared to the other systems induced by electronic effect of PTA ligands. Additional studies are thus necessary to better understand this system.



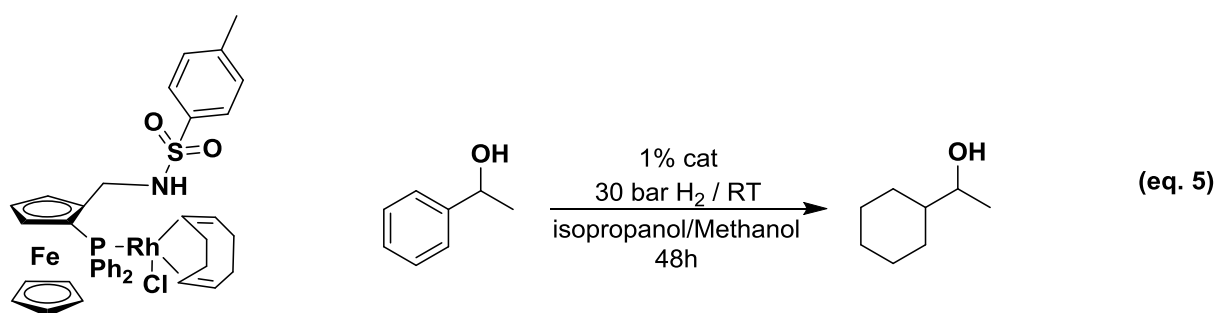
**Figure 2.47:** (a) FT-IR of purified RhPTA<sub>0.8</sub> NPs and (b) FT-IR after reaction with 1bar of CO at r.t. for 24h.

The use of PTA ligand to prepare RhNPs led to very small NPs as already observed with the Ru and Pt metals. These particles showed a strong hydrophilic character and could be dispersed easily in water, where they maintain their small mean size as in organic solvents. WAXS analysis indicated a completely oxidized surface. CO deposition studies on the surface of the particles revealed the evolution of several peaks at positions that are very different compared to other RhPPh<sub>3</sub> and Rhdppb NPs systems. The absorption bands are also narrow and could correspond to small clusters. It thus appears that PTA ligands led to NPs that would merit to be studied more deeply to understand better this new system of NPs that could be of interest for catalysis in water.

## II.6 Phosphino-Ferrocene ligand Stabilized Rhodium NPs

Ferrocenyl phosphino compounds are a family of ligands considered to be one of the highly attractive new phosphine ligands. This interest is mostly attributed to the chiral character these ligands may offer. These ligands are stable, their planar chirality is easily introduced and they possess exotic stereoelectronic properties that are assigned to the ferrocene moiety. The 1,2-disubstituted ferrocene derivatives play a major role in several contributions mostly in asymmetric catalysis. Examples of these ligands include (P,P) ligands,<sup>229</sup> (P,N),<sup>230</sup> (P,S),<sup>231-232</sup> or (P,O)<sup>232</sup>.

The inspiration of synthesizing ferrocenyl phosphine-stabilized Rh NPs came after discussing with some collaborators at the LCC, in the group of R. Poli and E. Manoury who accidentally obtained a black solution during catalytic hydrogenation of acetophenone using ferrocenyl phosphine Rh complexes (eq. 5).

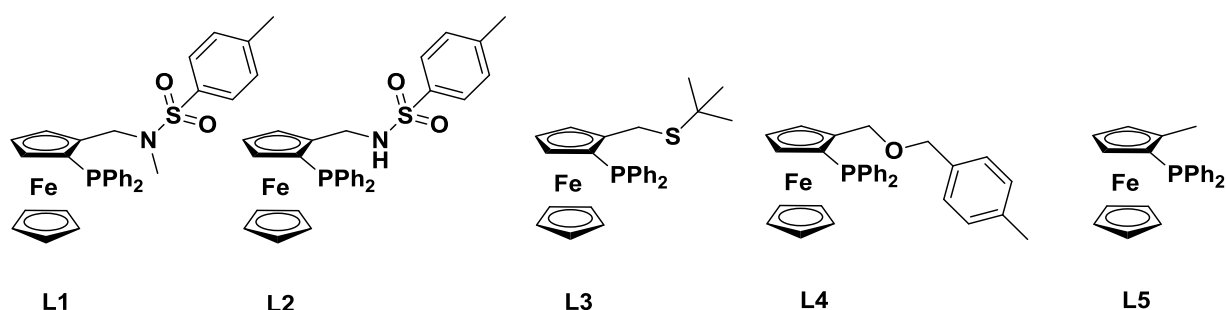


The hypothesis was that under dihydrogen pressure, the ferrocenyl complex may be decomposed due to hydrogenation of the cyclooctadiene ligand like in our organometallic approach towards MNPs. This would give rise to the formation of a colloid where NPs would be stabilized by species present in solution, mainly the ferrocenyl phosphine ligand, which contains also a nitrogen atom that can contribute in the NPs stabilization, forming a P,N bidentate coordination. TEM images of the obtained black solution, confirmed the formation of NPs during the reaction, but they were not very well-controlled in terms of size and shape, with the presence of both single particles and large agglomerates.

Thus, our aim was to take benefit of our previous results in the synthesis of phosphine-stabilized rhodium NPs achieved using the  $[\text{Rh}(\eta^3\text{-C}_3\text{H}_5)_3]$  complex with mono-

and disubstituted P ligands, and to apply the same approach to study the formation of Rh NPs using different ferrocenyl phosphine ligands as stabilizers (Scheme 2.10). Another objective was to evaluate their reactivity in hydrogenation catalysis aiming to achieve asymmetric catalysis, in comparison with both Rh complexes having the same ligands and Rh NPs formed *in situ*. To our best of knowledge, the use of such a type of ligands is a first for stabilizing MNPs.

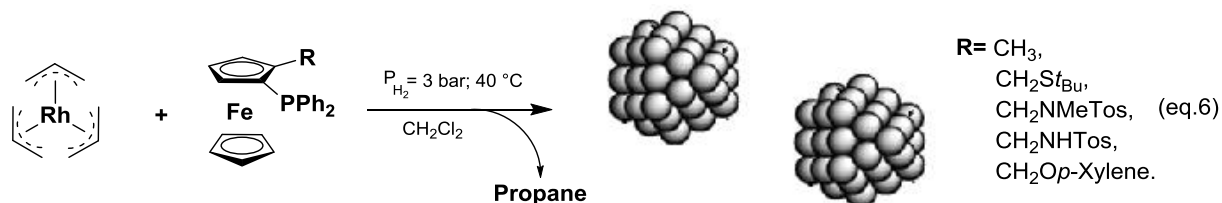
All the utilized ligands in this study (Scheme 2.10, L1-L5) have a diphenyl phosphine moiety on the position 1 of the ferrocene, and different other groups on position 2. Ligands **L1** and **L2** present almost the same moieties on position 2, a  $-\text{CH}_2$  is attached to aminotosyl group. In **L1** the amine is tertiary with extra methyl whereas **L2** presents a secondary amine with hydrogen substituent. Ligand **L3** bears a *t*Bu sulfur group attached to the  $-\text{CH}_2$  moiety. **L4** contains an ether function, an oxygen atom connects the *para*-xylene into the  $-\text{CH}_2$  of position 2. Ligand **L5** contains a simple methyl group that does not bear a second coordinating element.



**Scheme 2.10:** Different ferrocenyl phosphine ligands used for the synthesis of Rh NPs.

The synthesis of the NPs was performed in dichloromethane as the solvent ( $\text{CH}_2\text{Cl}_2$ ), to insure the solubility of both  $[\text{Rh}(\eta^3\text{-C}_3\text{H}_5)_3]$  complex and ferrocenyl phosphino ligands. The reaction was carried out under 3 bar of dihydrogen. Heating the reactor at  $40\text{ }^\circ\text{C}$  was fundamental to obtain the change of the initial yellow solution into black in shorter reaction time (eq. 6). 0.2 molar equivalent of [ligand]/[Rh] ratio was applied in the case of ligands **L1**, **L2**, **L3** and **L4**. As these ligands are bidentate, they offer an extra coordination through the

heteroatom they have, which may duplicate the ligand/metal ratio into 0.4. Whereas, in the case of ligand **L5** a ratio of 0.4 equivalent was directly applied due to absence of other coordinating heteroatom.

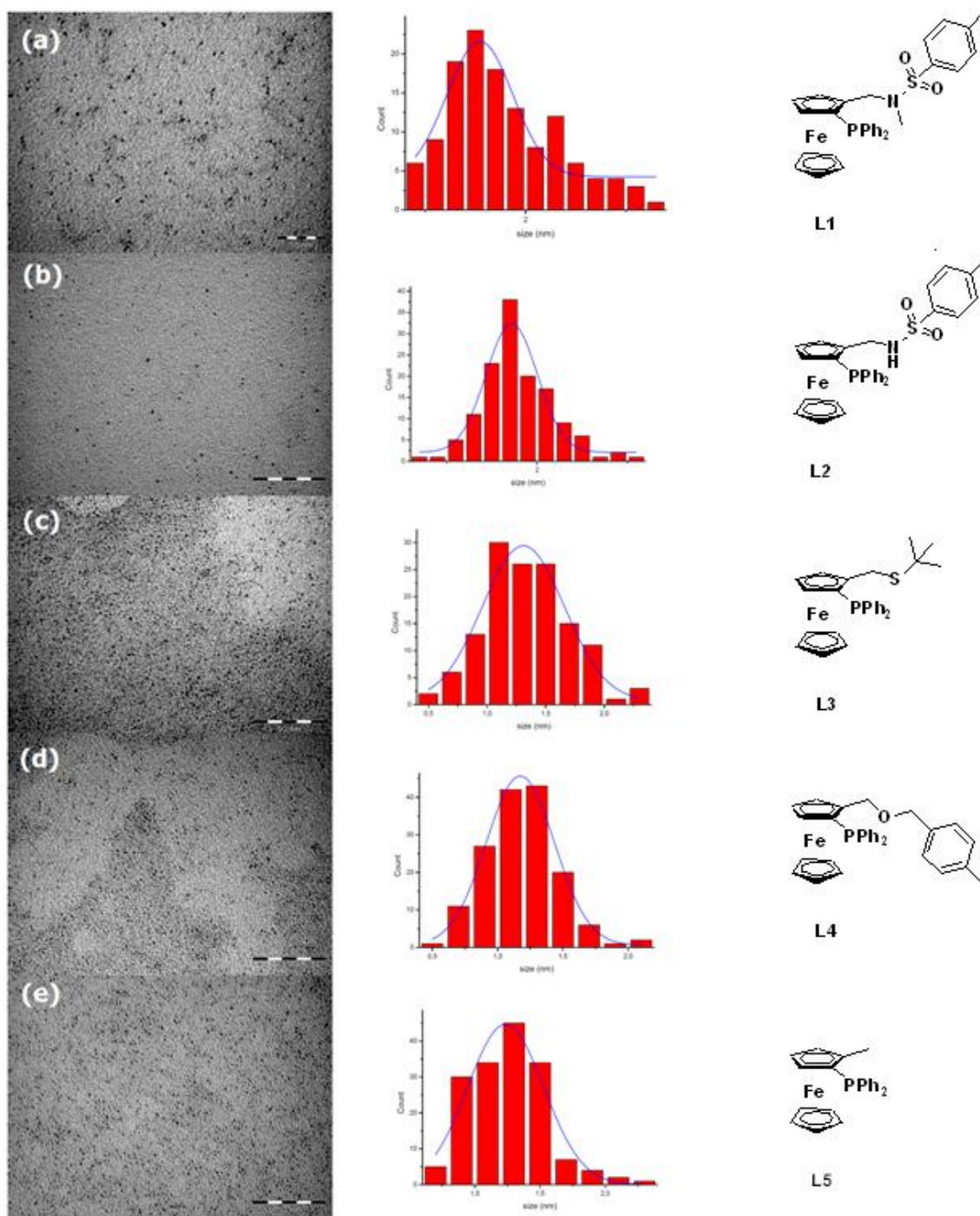


Although the change of solution color occurred within a few hours in all the cases, the reaction was kept running up to 16 h to insure the complete decomposition of the precursor. The obtained colloidal solutions in CH<sub>2</sub>Cl<sub>2</sub> appeared to be stable under argon for several weeks. TEM images obtained from crude colloidal solutions showed well-dispersed NPs for all the systems. They have a spherical shape and a quite narrow size distribution with a size range between 1 and 2 nm (Figure 2.48, Table 2.4). (L1@RhNPs = 1.5 ± 0.6 nm, L2@RhNPs = 1.7 ± 0.5 nm, L3@RhNPs = 1.3 ± 0.7 nm, L4@RhNPs = 1.1 ± 0.5 nm, L5@RhNPs = 1.2 ± 0.6 nm).

**Table 2.4:** *N-heterocyclic carbenes-stabilized Rh NPs.*

Type of Coordination	Ligand	Size (nm)	Estimated total Rh atoms number*	% of Rh atoms on the surface of the particles
Bidentate	L1	1.5 ± 0.6	127	44
	L2	1.7 ± 0.5	258	40
	L3	1.3 ± 0.7	83	50
	L4	1.1 ± 0.5	50	56
Monodentate	L5	1.2 ± 0.6	65	53

\*considering the NPs in perfect closed packing spherical shape.

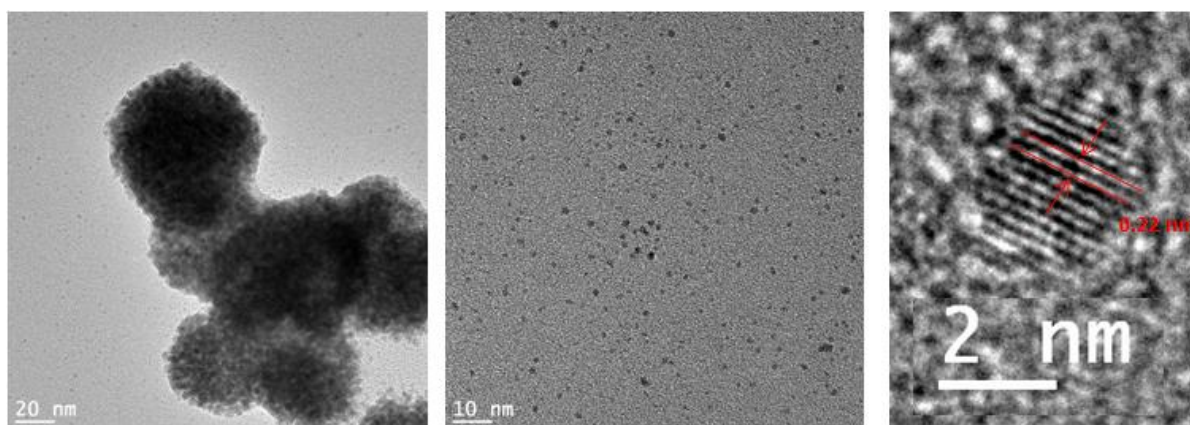


**Figure 2.48:** (a) TEM images and corresponding size distributions of Rh NPs stabilized with L1, (b) L2, (c) L3, (d) L4, (e) L5.

### II.6.1 High Resolution Electron Microscopy Analysis

NPs synthesized with Ligands **L2** and **L5** were further deeply characterized because of our interest in catalysis with these systems. This choice was supported by the idea to compare the effect in catalysis between disubstituted and monosubstituted ligands. In addition, the reactivity of the L2@RhNPs could be compared to that of the homogeneous Rh system with this ligand presented in (eq 5)

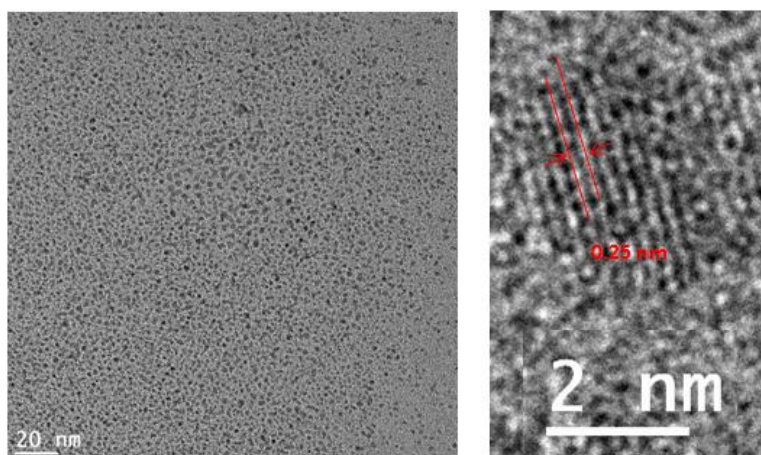
High resolution TEM images of the **L2**-stabilized Rh NPs, upon large scale synthesis, showed the presence of few large agglomerates in addition to single nanoparticles (Figure 2.49). These agglomerates appeared to be composed of smaller spherical particles that are gathered together. Otherwise, individual NPs are present all over the grid, they match the size obtained by regular TEM analysis. Particles display crystalline regions with interplanar space of 0.22 nm, that corresponds to the expected fcc structure for Rh NPs.



**Figure 2.49:** HRTEM images of **L2**-stabilized Rh NPs (0.2 eq) at different magnifications.

The HRTEM images of the **L5**-stabilized Rh NPs showed complete agreement with the regular TEM images obtained previously in terms of size and shape (Figure 2.50). The particles are well-dispersed, very small and spherical in shape. Zooming revealed a pattern of crystalline domains with interplanar space of 0.25 nm, that corresponds to the expected fcc structure.



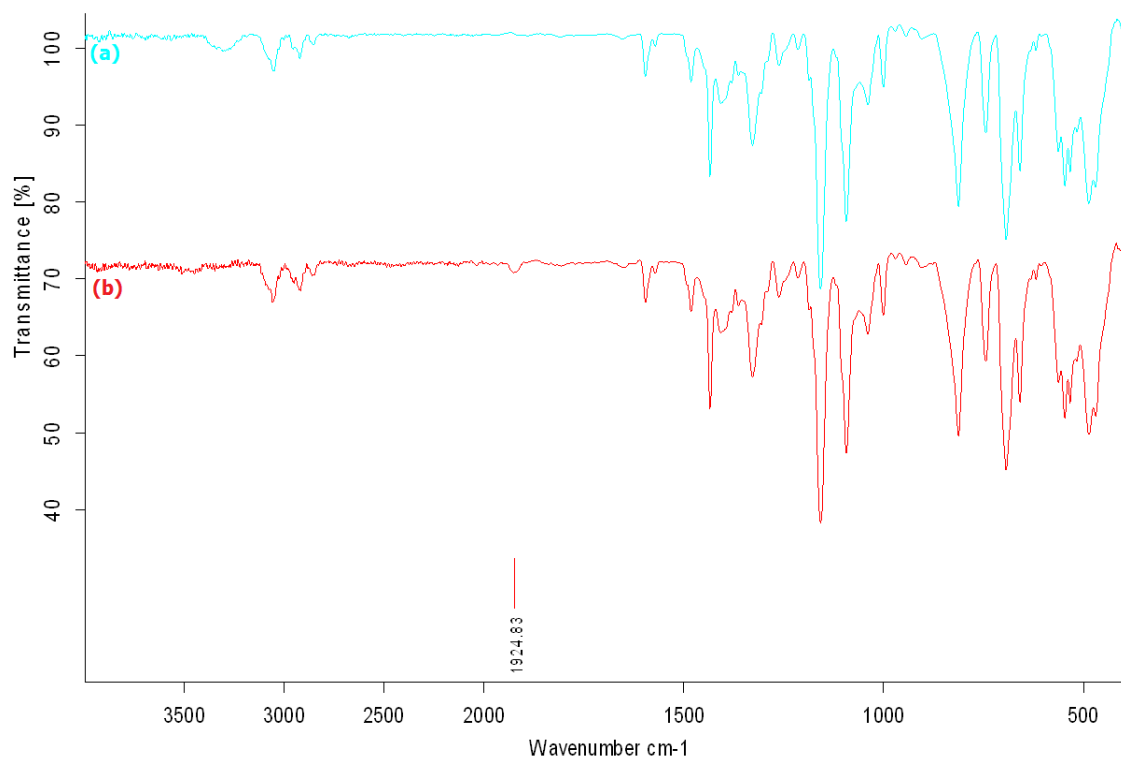


**Figure 2.50:** HRTEM images of L5-stabilized Rh NPs at different magnifications.

### II.6.2 CO Adsorption Study

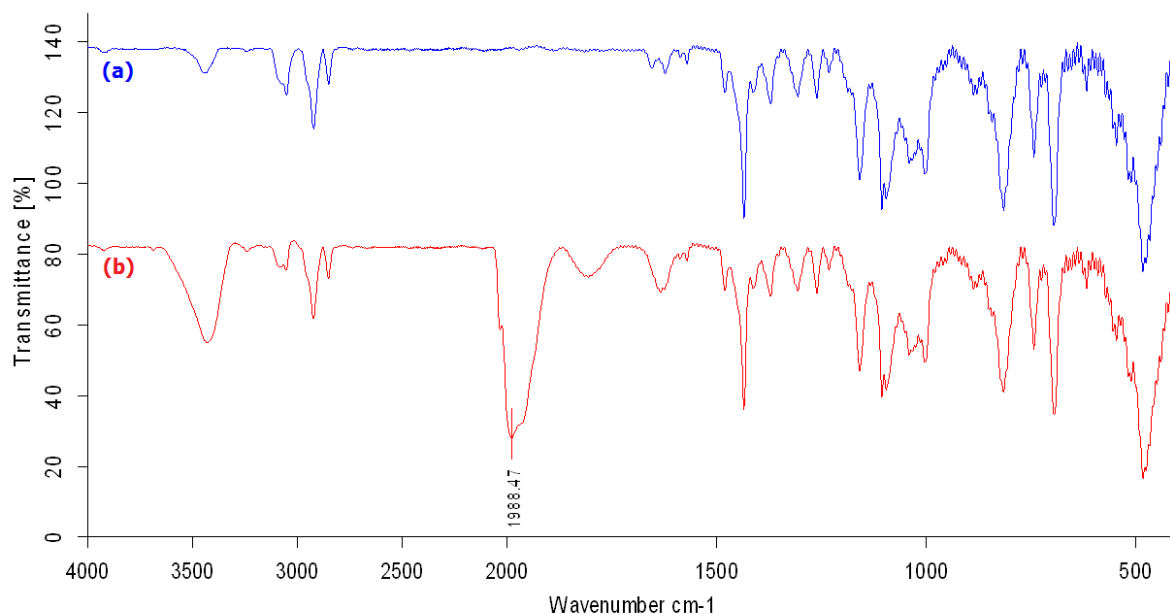
The coordination of CO on the surface of L2- and L5-stabilized RhNPs was further investigated by FT-IR spectroscopy. The spectra of the purified NPs (KBr pellet) were first recorded individually. Then, atmospheric pressure of CO gas (1 bar) was applied into the fischer porter reactor over a period of 48h, and new FT-IR spectra were recorded.

Figure 2.51a corresponds to the spectrum obtained for purified L2-stabilized RhNPs and Figure 2.51b for the same particles after reaction with CO. A peak of very low intensity is visible at  $1924\text{ cm}^{-1}$  after 48 h under 1 bar CO that can correspond to CO adsorbed at the rhodium surface. In comparison with previous phosphine-stabilized Rh NPs, it appears that CO coordination is not easy at the surface of these particles, maybe due to sterical hindrance induced by the bidentate ligand that may cover the surface of the particles.



**Figure 2.51:** (a) FT-IR spectrum of purified **L2**-stabilized Rh NPs (b) FT-IR spectrum of **L2**-stabilized Rh NPs after 48h under CO atmosphere.

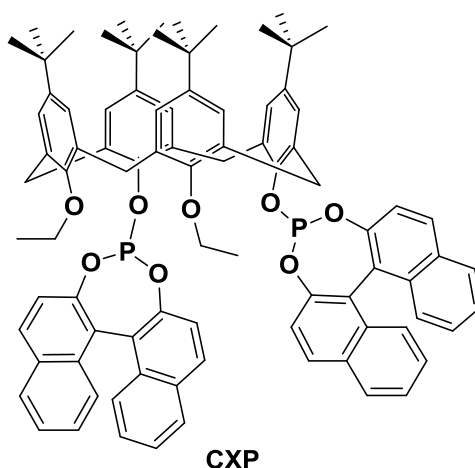
In the case of the **L5**-stabilized RhNPs, the spectrum recorded after 48 h of CO exposure revealed the appearance of 3 peaks between 1550 cm<sup>-1</sup> and 2050 cm<sup>-1</sup> (Figure 2.52b) in comparison to the spectrum obtained before the gas exposure (Figure 2.52a). The more intense peak at ~1990 cm<sup>-1</sup> can be attributed to semi-terminal CO coordination and the shoulder at around 2020 cm<sup>-1</sup> to the terminal one. The higher intensity of the peak reveals the high quantity of CO coordinated molecules in terminal mode on the surface of the NPs, which is known to attach on the edges and the corners surface sites of the particles. The peak at *ca.* 1800 cm<sup>-1</sup> refers to typical bridging CO coordination mode. And the evolution of a lower peak at around 1600 cm<sup>-1</sup> can be explained by a triple coordinating CO molecule with the lowest vibrational frequency. The bridging coordination mode is generally considered to take place on the faces of the particles.



**Figure 2.52:** (a) FT-IR spectrum of **L5**-stabilized Rh NPs (b) FT-IR spectrum of **L5**-stabilized Rh NPs after 48h under of CO atmosphere.

These results obtained with this new family of ligands, indicate that phosphine-ferrocene ligands are able to stabilize Rh NPs in a good manner. Rh NPs with a mean size comprised between 1.1 and 1.7 nm that are well-dispersed were formed. CO adsorption studies performed with monosubstituted L5 and disubstituted L2 ligands revealed that the accessibility of the metal surfaces is not the same. Indeed, coordination of CO at metal surface was possible in both bridging and terminal modes with L2 but not with L5. This may result from high coverage of the NPs surface with disubstituted L2 ligand. This difference could be of interest to orientate surface properties of NPs for catalysis application.

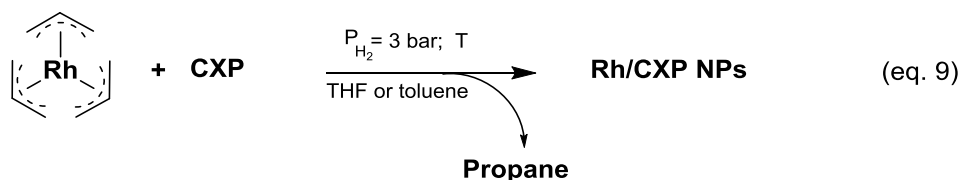
## II.7 Calixarene-biphosphite ligand-Stabilized Rhodium NPs:



**Scheme 2.11:** Calixarene-biphosphite ligand (CXP) used to prepare Rh NPs.

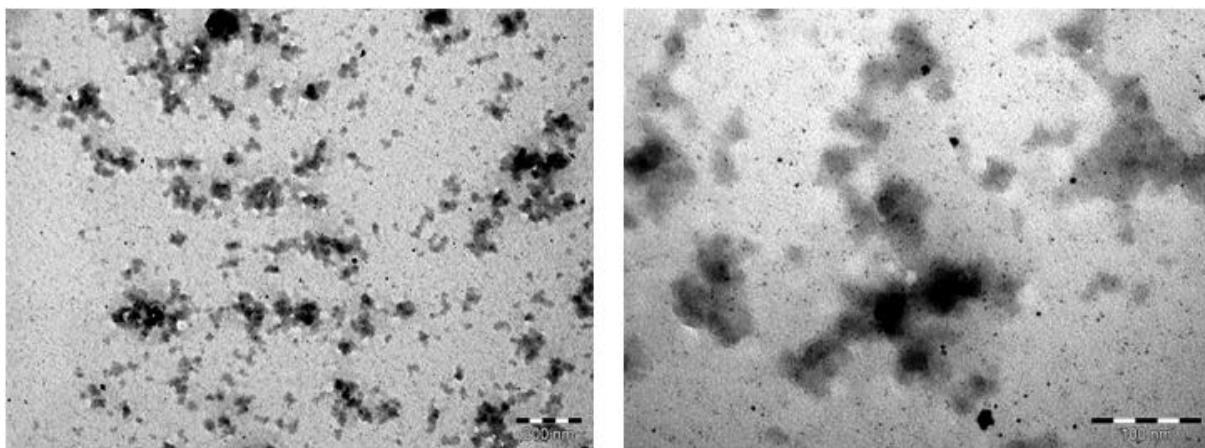
In collaboration with David Sémeril at the "Laboratoire de Chimie Inorganique Moléculaire et Catalyse" in Strasbourg, France, we aimed to investigate the ability of macromolecules such as CXP ligand (Scheme 2.11) in stabilizing rhodium nanoparticles following the organometallic approach.

CXP is a calix[4]arene macrocyclic molecule with 4 phenolic entities linked together by methylene bridges, in addition to two phosphite moieties attached to a dinaphthalene (Scheme 2.11). The stabilization of the NPs is expected to occur through the phosphorous atoms. Control of the particles growth inside the calixarene ring is possible to occur also as the result of confinement effect. Due to ligand solubility restrictions, we performed the synthesis of Rh NPs in either toluene or THF as the solvent (eq. 9)

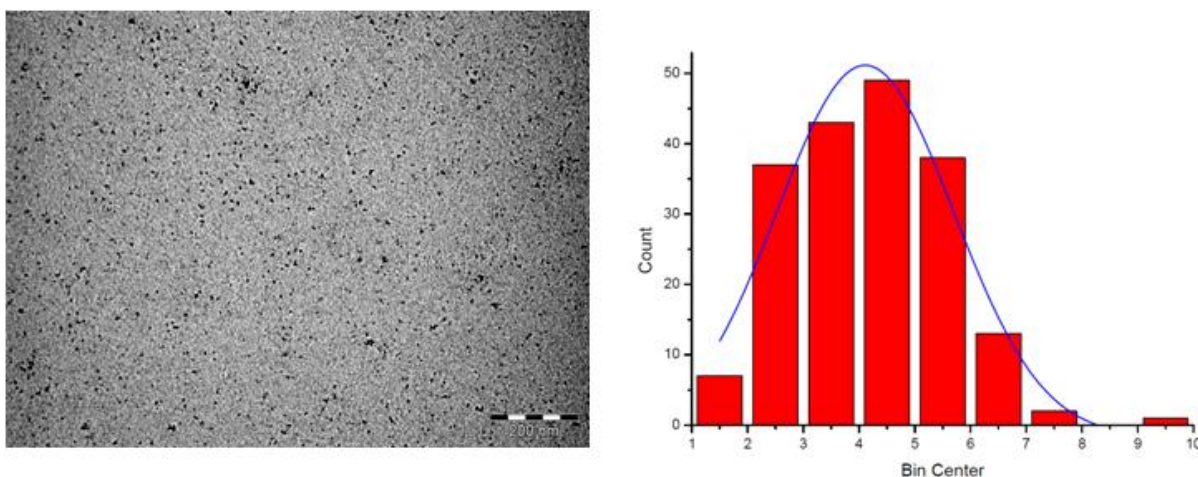


Performing the synthesis of NPs with 0.2 molar equivalent of CXP was positive at room temperature in THF, while heating the system up to 65 °C appeared essential in the case of toluene. The obtained NPs were analyzed by electron microscopy. The resulting images

showed that NPs obtained in THF are not homogeneous in size but mostly organized in large agglomerates even if small individual particles were observed (Figure 2.53). When the synthesis was performed in toluene solution at 65 °C, well-dispersed particles were detected all over the grid with a mean size of  $4.11 \pm 3.2$  nm (Figure 2.54).



**Figure 2.53:** TEM images of Rh NPs prepared with 0.2 molar eq. ( $[L]/[Rh]$ ) of CXP ligand in THF at r.t.



**Figure 2.54:** TEM images of Rh NPs prepared with 0.2 molar eq. ( $[L]/[Rh]$ ) of CXP ligand in Toluene at 65 °C.

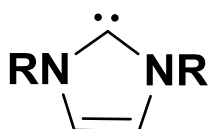
This difference can be attributed to solubility properties of the CXP ligand that is higher in Toluene than in THF. By this way interaction on phosphite groups or confinement inside the cavities of CXP may take place.

In comparison with other phosphine ligands used previously in stabilizing Rh NPs, we noticed that lower quantity of CXP ligand was sufficient to control efficiently the NPs growth but a size increase (*ca.* 4.1 nm) was obtained.

These NPs were tested in hydroformylation of styrene (chapter IV), where they showed very interesting results in terms of activity and selectivity compared to another system of Rh NPs. Further characterization for this system is essential to continue this work and to better understand the exact role of the ligands in stabilizing the nanoparticles, and the behavior of the system in catalysis.

### II.8 N-Heterocyclic Carbene-Stabilized Rhodium NPs

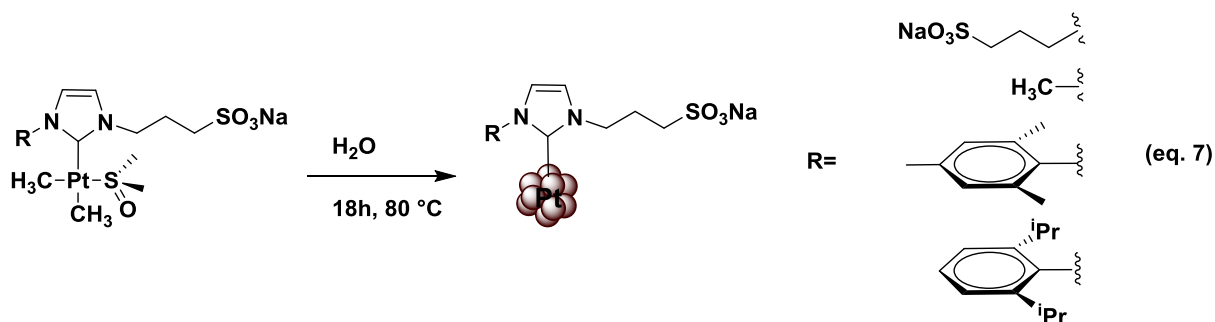
N-heterocyclic carbenes (NHCs) have been shown to form fairly robust transition-metal complexes, which are excellent candidates for a large number of homogeneous catalytic processes.<sup>233-237</sup> They are electron-rich nucleophilic species in which the divalent carbenic centre is directly bonded to at least one nitrogen atom within the heterocycle (Scheme 2.12). These neutral two-electron donor ligands show pronounced  $\sigma$ -donor ability with only little to no  $\pi$ -back-bonding. Due to their strong  $\sigma$ -electron-donating properties, NHC ligands usually form strong bonds with most metal centers and are therefore highly resistant toward decomposition.



**Scheme 2.12:** General Formula of N-heterocyclic carbenes (NHCs)

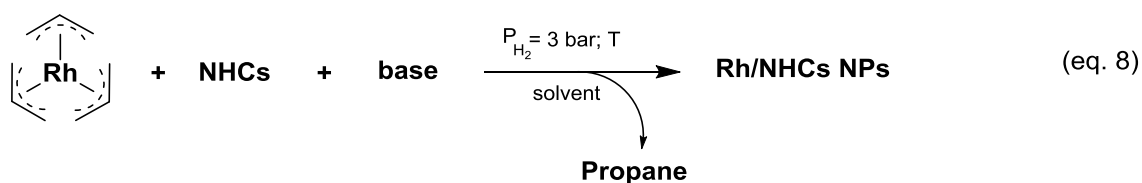
Although these strong coordinating ligands have been widely used for the development of organometallic complexes, only very few examples in literature deal with their effectiveness in the synthesis of metal nanoparticles.<sup>238-242</sup> Chaudret, Jesus and Flores<sup>243</sup> recently published the thermal decomposition of preformed molecular Pt complex containing

NHC ligands in water, resulting in NHC-stabilized Pt NPs with a small size and interesting surface properties (eq. 7).

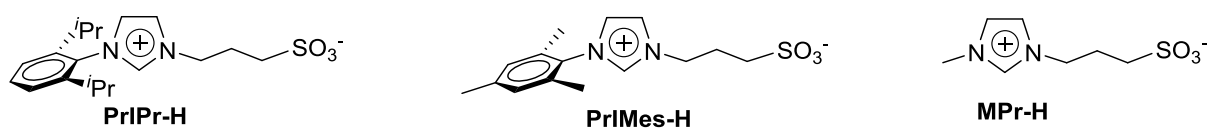


In a collaboration with the group of Ernesto de Jesús Alcañiz at the university of Alcalá (Spain), we investigated the synthesis of platinum nanoparticles stabilized with the same free carbenes, but following the organometallic approach by using  $[\text{Pt}(\text{norbornene})_3]$  complex as the metal source. This approach resulted in the formation of homogeneous and well-dispersed water-soluble NPs with a narrow size distribution (ongoing project). Thus, we decided to apply the same strategy to prepare NHC-stabilized Rh NPs from the  $[\text{Rh}(\eta^3\text{-C}_3\text{H}_5)_3]$  complex.

Since the free NHC ligands are very reactive and not stable, they should be handled with extreme care under inert conditions.<sup>209</sup> Their deprotonation was thus performed either before NP synthesis step (two steps method) or in a one pot synthesis method under the NP formation conditions. After comparison between the 2 steps synthesis and the one pot reaction synthesis of the NPs followed by a purification step (dialysis in water), we found that the one pot reaction reduces time and results in well-dispersed NPs according to (eq. 8).

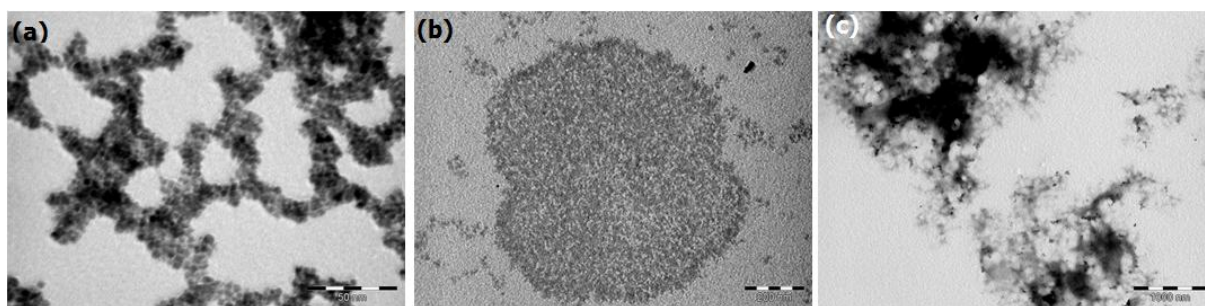


We chose a series of three N-heterocyclic carbenes (Scheme 2.13) to evaluate their ability in Rh NPs synthesis, inspired by previously obtained results with platinum. One important issue with such type of ligands is that they possess limited solubility in organic solvents, but thanks to their sulfonate groups that provide hydrophilic character, these ligands are highly soluble in water.



**Scheme 2.13:** Structure of NHC ligands used in stabilizing Rh NPs.

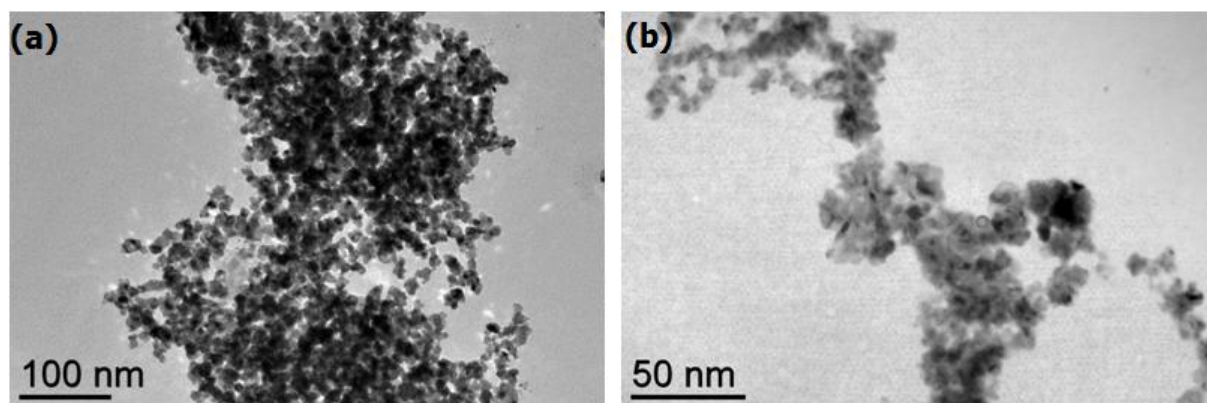
Performing the decomposition of  $[\text{Rh}(\eta^3\text{-C}_3\text{H}_5)_3]$  precursor with 3 bar of dihydrogen gas in the presence of 0.2 equivalent of the carbene and ter-butoxide as the base ( $[\text{base}]/[\text{ligand}] = 1$ ) in dimethyl sulfoxide (DMSO) at r.t. did not work with the three ligands (no change of color after 16 h). Repeating the same reactions while heating at  $65^\circ\text{C}$  resulted in decomposition of the Rh precursor, and evolution of colloidal black solutions indicating the formation of NPs. TEM analysis of the crude colloidal solutions Figure 2.55 showed that the obtained NPs are not controlled in size and shape, and that they are agglomerated all over the grid.



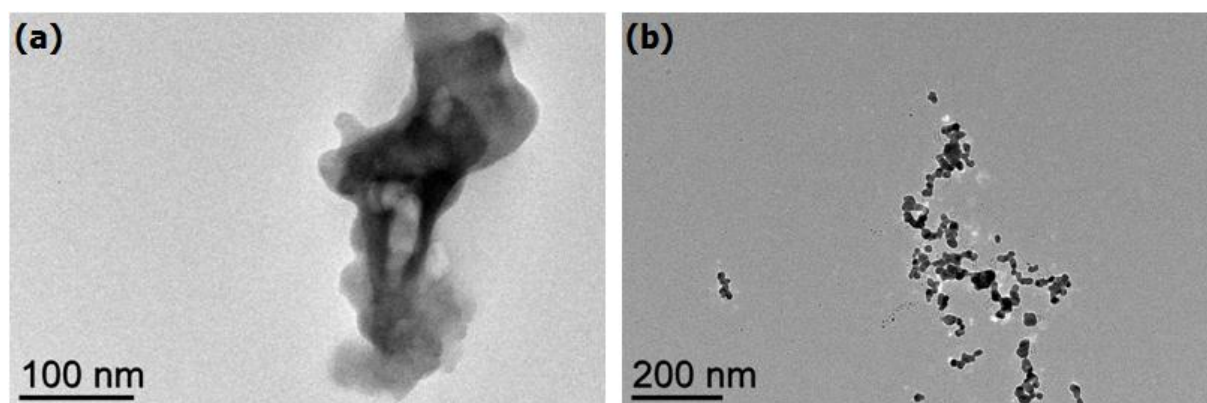
**Figure 2.55:** TEM images of (a) PrIPr-H (b) PrIMes-H (c) MPr-H stabilized Rh NPs after the synthesis in DMSO.



We thus decided to perform the same reactions in THF as the solvent, using 0.2 equivalent of carbenes (in the presence of *ter*-butoxide with  $[\text{base}]/[\text{ligand}] = 1$ ) dissolved in THF and transferred into the Rh precursor (3 bar  $\text{H}_2$  gas overnight). Reaction with PrIPr-H carbene showed no change of color and the TEM analysis revealed the absence of NPs, whereas change of color occurred in the other two cases as the results of the decomposition of the metal precursor. THF was evaporated from the reaction mixtures, and purification of the particles was performed using a cellulose dialysis bag in water. TEM images of the obtained particles after dialysis revealed that they are agglomerated, with non-uniform sizes and shapes (Figures 2.56). Reaction with the MPr-H ligand resulted in large bulk species with very few amounts of NPs. These results could be due to the lack of solubility of the NHCs and the *ter*-butoxide base in THF (Figures 2.57).



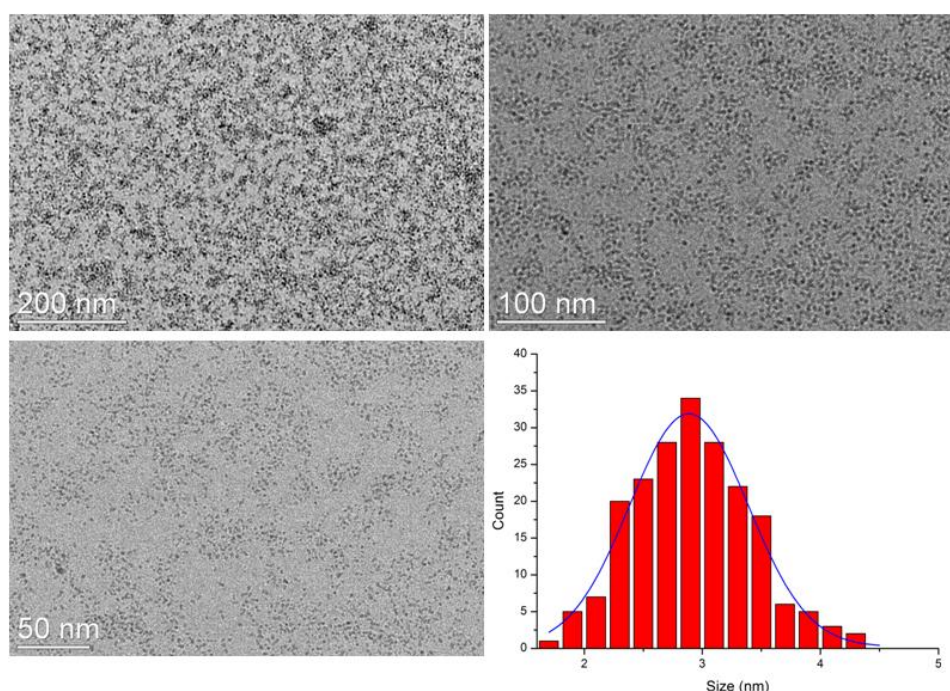
**Figure 2.56:** TEM images of PrIMes-H stabilized Rh NPs in THF (a) before dialysis (b) after dialysis.



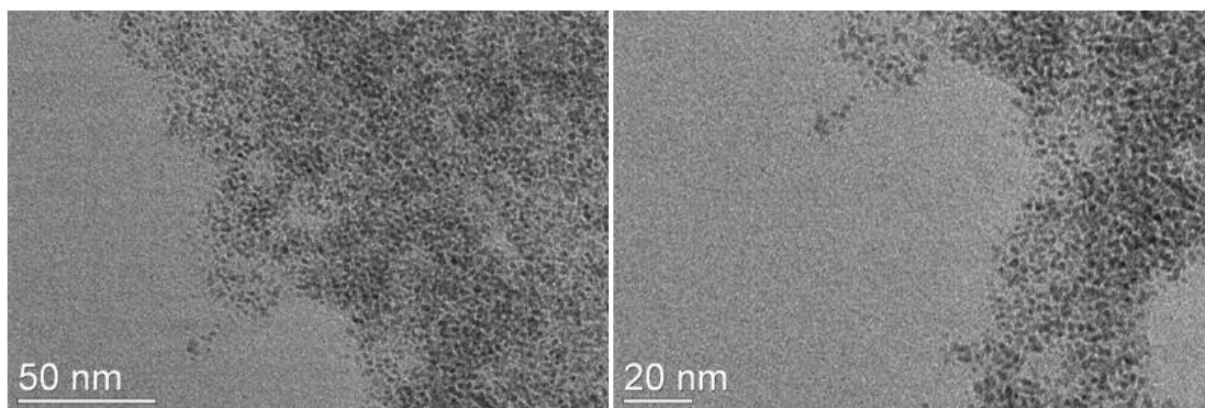
**Figure 2.57:** TEM images of MPr-H stabilized Rh NPs in THF (a) before dialysis (b) after dialysis.

In order to overcome the problem of solubility and to achieve well-controlled Rh NPs with the chosen carbene ligands, we decided to repeat the reactions at 65 °C. Heating the systems resulted in yellow clear solutions, in which changed in color was obtained after reaction with 3 bar of dihydrogen overnight. Reactions with PrIPr-H and PrIMes-H led to black colloidal solutions, whereas, the reaction with MPr-H resulted in the formation of black bulk species that precipitated rapidly, probably as the result of bulk rhodium metal.

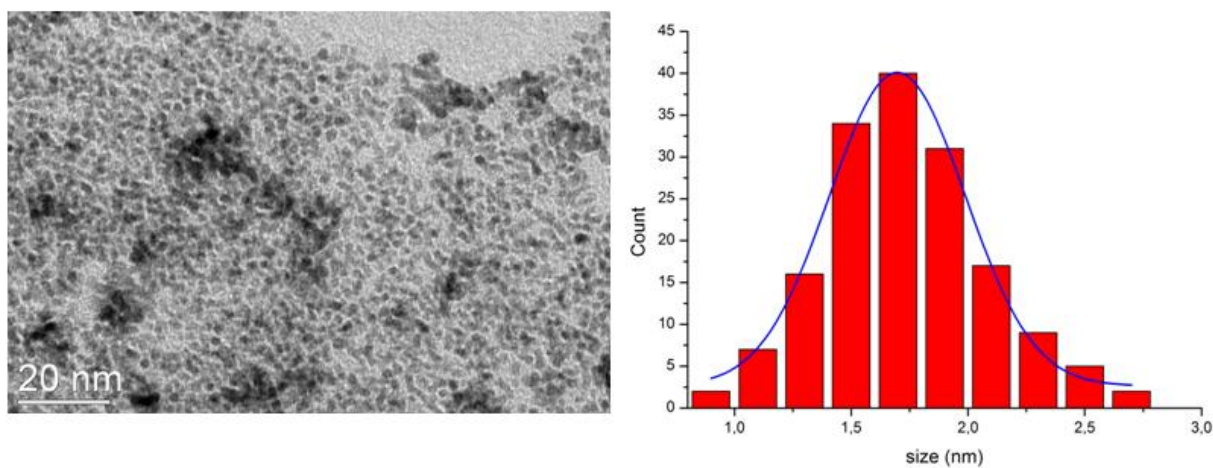
The TEM images of the crude reaction solutions of PrIPr- and PrIMes-stabilized Rh NPs in THF at 65 °C showed well-controlled NPs with spherical shape. In the case of PrIPr-H ligand, the NPs before dialysis in water were highly dispersed all over the carbon coated copper grid with a mean size of  $2.9 \pm 1$  nm (Figure 2.58). These particles maintained the same size range after purification by dialysis in water, but sets of individual agglomerated particles are also present over the grid (Figure 2.59), which can be due to low evaporation rate of water. TEM images of the PrIMes-stabilized Rh NPs in THF at 65 °C present a mean size of  $1.7 \pm 0.6$  nm (Figure 2.60) and have also a very close size range after purification in water. A few agglomerates are also visible on the TEM images obtained from aqueous colloidal solutions after purification (Figure 2.61).



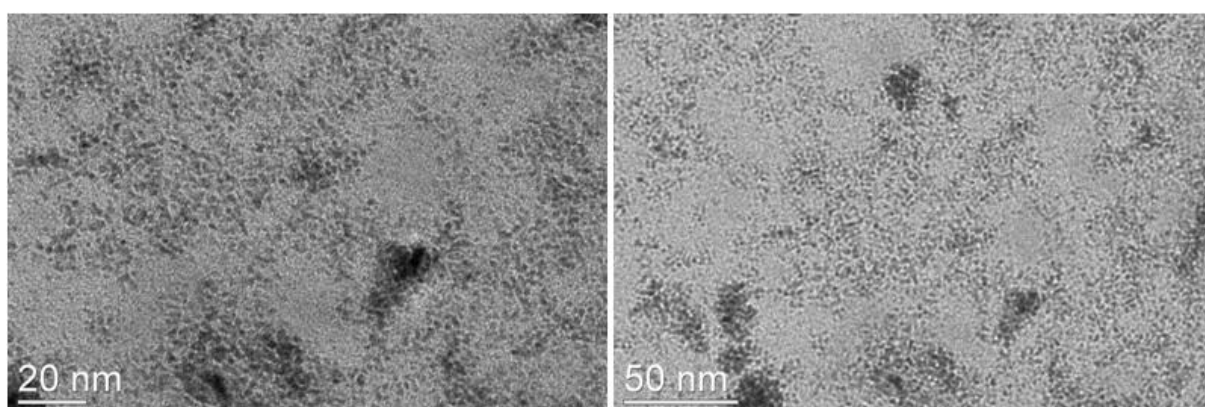
**Figure 2.58:** TEM images of PrIPr-H stabilized Rh NPs in THF at 65 °C before dialysis with the corresponding size distribution.



**Figure 2.59:** TEM images of PrIPr-H stabilized Rh NPs in THF at 65 °C after dialysis.



**Figure 2.60:** TEM image of PrIMes-H stabilized Rh NPs in THF at 65 °C before dialysis with the corresponding size distribution.



**Figure 2.61:** TEM images of PrIMes-H stabilized Rh NPs in THF at 65 °C after dialysis.

This part of the work is not finished yet, but the results obtained are very encouraging. Reaction conditions have been developed to achieve ca. 2-3 nm in size, well-dispersed Rh NPs that were easily transferred into water thanks to the hydrophilic character of the sulfonated carbene ligands used. A deep characterization of these Rh NPs is needed to complete this work.

### II.9 Deposition of Rhodium NPs on Amino Modified Magnetic Support

Development of new strategies for recovering and recycling of catalysts to boost their lifetime can result in considerable economical and environmental benefits. Ongoing research activities in this area include the use of metal nanoparticles (MNPs) in catalysis.<sup>244</sup> We already discussed the importance of the MNPs in catalysis. They are expected to be very active catalysts because of their high surface area and high ratio of atoms present at the surface, that are available for the chemical transformation of substrates.<sup>186</sup> But, the application of liquid suspensions of metal nanoparticles in catalysis is limited, mainly because the separation of the catalyst from the products and its recycling in colloidal catalytic systems are not simply achieved.<sup>69</sup> Therefore, the immobilization of such materials on a solid support seems to be an interesting alternative to facilitate the catalyst recovery by simple separation techniques.

Several immobilization methods and several supports have been investigated in the literature for the immobilization of metal colloids. The immobilization of catalysts on magnetically separable solid supports appears as an attractive way to give better handling properties to homogeneous and MNPs catalysts.<sup>5,245</sup> The magnetic properties of a support where the NPs can be deposited will result in a simple separation by application of a magnet, without requirement of filtration, decantation, centrifugation, or any other separation technique thereby, overcoming traditional time and solvent consuming procedures. This method can thus be considered as a “greener” approach.

In this context, SiO<sub>2</sub>-coated magnetic nanoparticles have been widely studied due to their superparamagnetic properties and biocompatibility.<sup>186,245-246</sup> Nanometric iron oxide magnetic cores of a silica support respond to an external magnetic field but do not remain magnetized when the magnetic field is removed. Therefore, with the help of a magnet, the paramagnetic materials can be easily concentrated from the solution, and re-dispersed after

taking away the magnet (Figure 2.62). We were thus interested in using such an approach to be able to improve the catalyst recycling of the Rh NPs during catalytic studies.

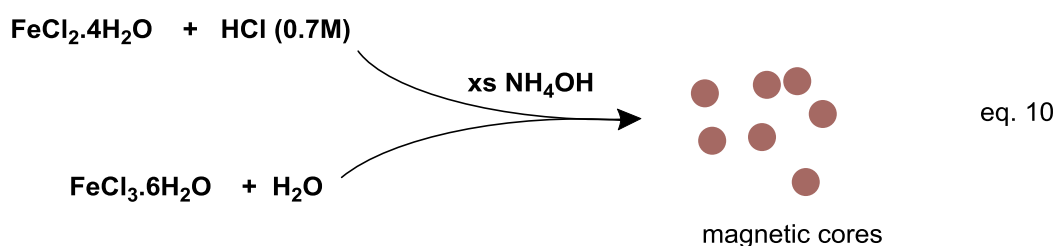


**Figure 2.62:** Concentration of paramagnetic support upon magnet exposure and redispersion after removal of the magnet.

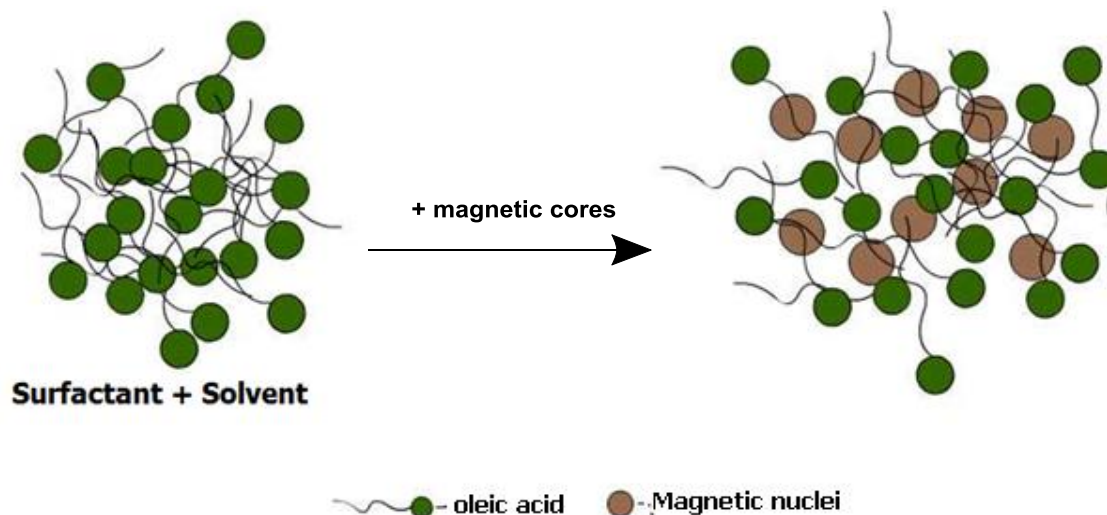
### II.9.1 Synthesis of Magnetic Silica Particles

Synthesis of the silica-coated magnetic particles was performed during a stay at the Laboratory of Nanomaterials and Catalysis (University of Sao Paulo, Brasil) under the framework of CAPES-COFECUB project (N°695/10) with the group of Pr. Liane M. Rossi.

The support was prepared through the procedure described by Philipse *et al.*<sup>246</sup> A first step consists in magnetic cores preparation that is performed by coprecipitation of  $\text{Fe}^{2+}/\text{Fe}^{3+}$  ions under alkaline conditions under the following reaction conditions (eq. 10):

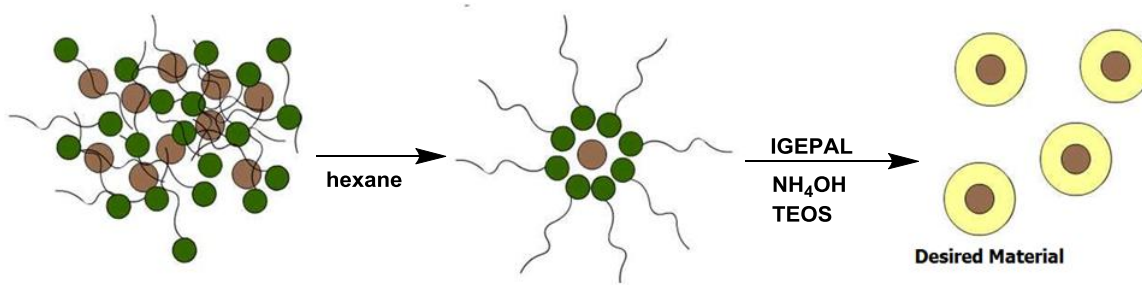


The coprecipitation step is followed by stabilization of the nanometric iron cores with oleic acid, which is essential to improve the solubility of the magnetic particles in hexane solution, that is used in the following step to grow the silica layer. (Scheme 2.14)



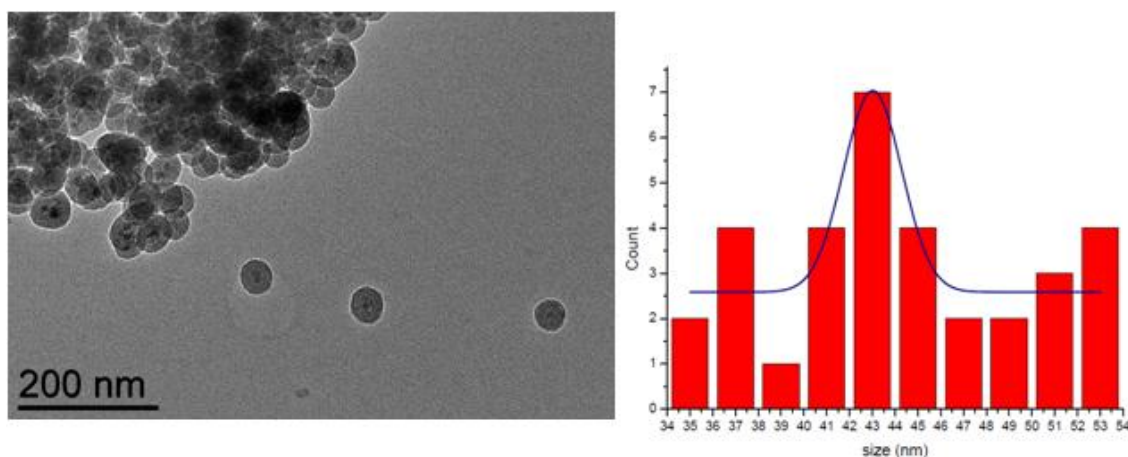
***Scheme 2.14:*** Dispersion of magnetic iron particles in the presence of oleic acid.

After dispersing the magnetic iron nanoparticles with the oleic acid in hexane solution, coating of the surface of these particles with soluble silicate, and subsequent growth of a silica layer by condensation of tetraethylorthosilicate (TEOS) in ammonia solution were performed under stable stirring rate (Scheme 2.15). The silica layer coating is a time dependant process; the longer the reaction time the thicker the silica layer is, but at the same time, very high silica concentration may lead to merging of individual particles together forming unwanted agglomerates.



**Scheme 2.15:** Dispersion of magnetic  $Fe_2O_3$  particles followed by silica condensation coating.

Coating the iron core magnetite with silica for 16 h yielded in individual spherical particles with mean size of  $43 \pm 2.5$  nm (Figure 2.63)



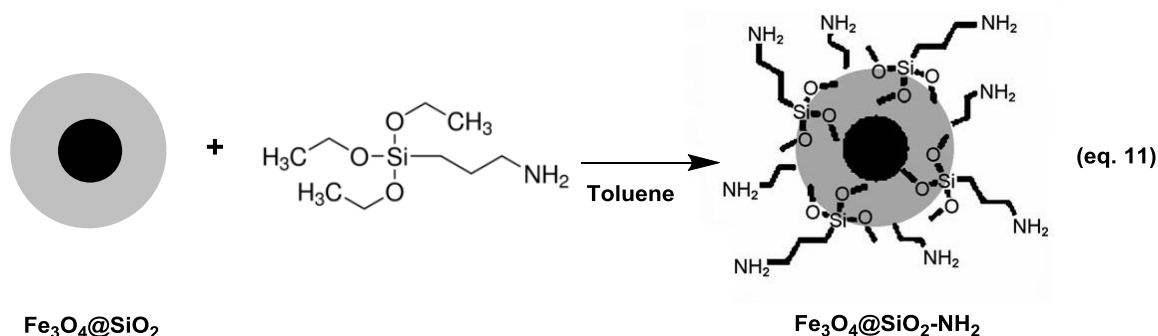
**Figure 2.63:** (a) TEM image of iron-core silica support. (b) Size distribution of the magnetic silica particles.

## II.9.2 Functionalization of the surface of silica magnetic particles

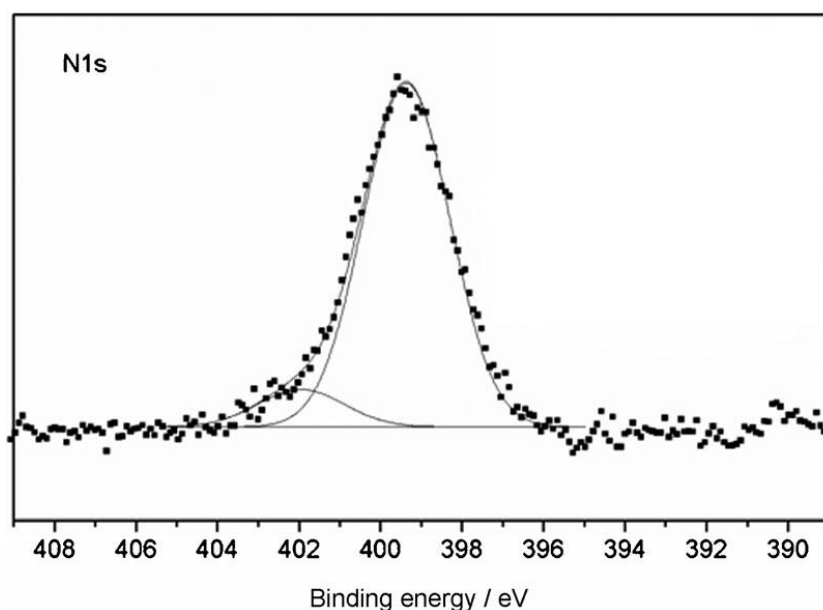
Previous studies with the obtained magnetic silica support ( $Fe_3O_4@SiO_2$ ) by Rossi *et al.* showed that these particles are highly stable and easily recoverable.<sup>247</sup> They exhibit superparamagnetism in a large range of temperatures. And any non magnetic material or molecules attached to the magnetic support in this system can be separated by applying a remote magnetic field and they are redispersed immediately after the field is removed. So, in order to strongly attach on the non magnetic materials such as the nanocatalysts, functionalization of the surface of the support with amino groups that are available to

coordinate to the MNPs is necessary to prevent leaching of the catalysts after several recycling experiments.

The reaction of the ( $\text{Fe}_3\text{O}_4@\text{SiO}_2$ ) support with 3-aminopropyltriethoxysilane in toluene provides an extra molecular silica layer enriched with pending  $\text{NH}_2$  groups (eq. 11).



Rossi *et al.* confirmed the presence of these functional groups by means of X-ray photoelectron spectroscopy (XPS).<sup>247</sup> In (Figure 2.64) the N 1s spectrum could be deconvoluted into two peaks at 399.4 and 401.9 eV, which can be attributed to the primary amino groups ( $\text{C}-\text{NH}_2$ ) and their protonated  $\text{C}-\text{NH}_3^+$  form, respectively.

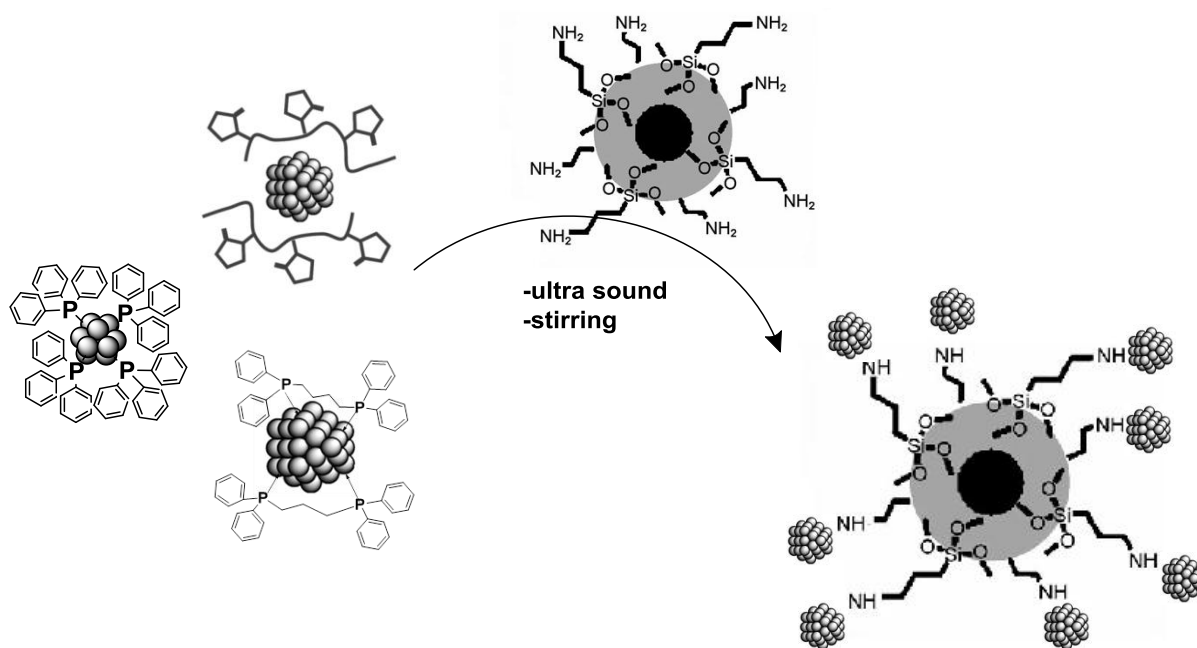


**Figure 2.64:** XPS spectrum of N 1s region of the amino-modified catalyst support ( $\text{Fe}_3\text{O}_4@\text{SiO}_2-\text{NH}_2$ ). (Adapted from reference<sup>247</sup>)



### II.9.3 Deposition of Rh NPs on the modified silica support

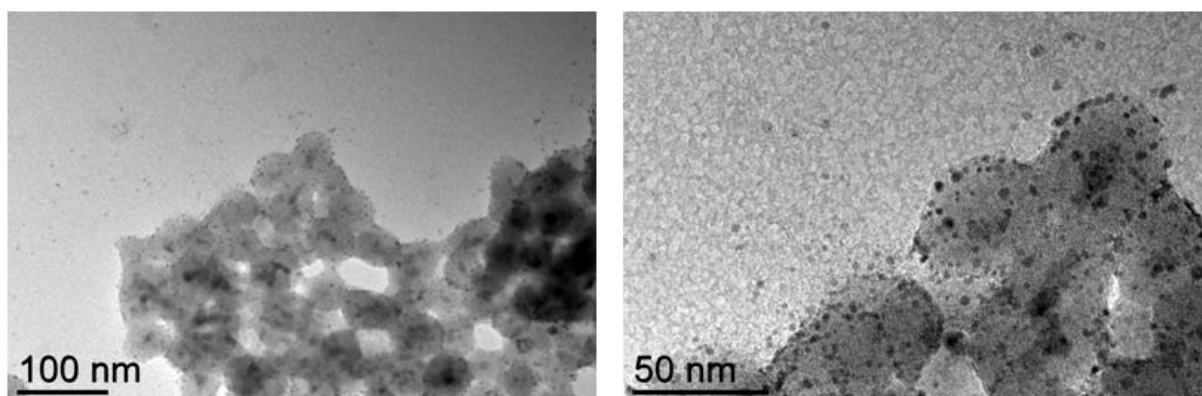
Previously synthesized and characterized Rh NPs including the  $\text{PPh}_3$ , dppb and the PVP-stabilized particles were deposited on the surface of the magnetic silica support according to Scheme 2.16. The deposition was performed at RT by mixing the support and the NPs in THF solution over 16 h. Reaction conditions were chosen to obtain final nanomaterials containing 2 mg of Rh metal for 100 mg of support. After 16 h of reaction, and washing with ethanol 3 times, ICP measurements indicated the presence of Rh at 1.145 %, 1.436 % and 2.316% in  $\text{RhPVP}@(\text{Fe}_3\text{O}_4@\text{SiO}_2\text{-NH}_2)$ ,  $\text{Rhdpbb}@(\text{Fe}_3\text{O}_4@\text{SiO}_2\text{-NH}_2)$  and  $\text{RhPPh}_3@(\text{Fe}_3\text{O}_4@\text{SiO}_2\text{-NH}_2)$  respectively.



**Scheme 2.16:** Deposition of Rh NPs on the amino modified silica support.

Figure 2.65 shows TEM images of the RhPVP NPs attached to the surface of the magnetic  $\text{Fe}_3\text{O}_4@\text{SiO}_2\text{-NH}_2$  support after dispersion in ethanol and dropping over a carbon coated copper TEM grid. High concentration of NPs present on the surface of the support is

visible that are tied to the surface amino groups. TEM images show also low leaching ratio, with a few free Rh particles over the grid.



**Figure 2.65:** TEM images of the RhPVP NPs attached to the surface of the magnetic silica support at two magnifications.

The supported nanoparticles were further used in different catalytic reactions (see chapter IV). Taking profit of the magnetic properties of the carrying support, recycling of the nanocatalysts was applicable leading to interesting results.

### II.10 Conclusion

Several systems of monometallic rhodium nanoparticles have been described in this chapter. They differ from each other according to the nature of the stabilizers used for their synthesis. A summary of their characteristics is given in table 2.5.

First, a polymer, PVP, allowed forming *ca.* 2.2 nm Rh NPs that are well-dispersed in the polymer matrix and present a narrow size distribution. Their crystalline structure is fcc. CO adsorption studies revealed a good accessibility of the metal surface with coordination of CO molecules in different modes and probably at different surface atoms (faces, edges, apexes).

The use of PPh<sub>3</sub> and dppb ligands in the synthesis of Rh NPs, which differ in the number of P coordinating atoms to the surface of the rhodium, evidenced that a starting ratio

of  $[P]/[Rh] = 0.6$  to 1 is necessary to achieve nanoparticles that are well-controlled and small in size. However, heating was essential to decompose the  $[Rh]$  complex when using the phosphines; this behavior is attributed to possible formation of *in situ* complexes as detected by NMR. The so-obtained particles display similar characteristics in terms of size ( $RhPPh_3=1.3$  nm,  $Rhddpb=1.7$  nm), dispersion and low crystalline structure ( $Mn\beta$  that is different than the fcc structure of the  $RhPVP$  NPs), as well as surface state. It is worth mentioning that  $Rh PPh_3$  NPs population shows a very narrow size distribution that indicates a very good control of the size in that case. CO adsorption studies revealed a good accessibility of the metal surface with coordination of CO molecules in different modes and probably at different Rh surface atoms..

PTA ligand resulted in well-dispersed and very small NPs (1.0 nm). The obtained particles showed a strong hydrophilic character, which allowed their easy transfer into water while maintaining their small mean size. Although, the results from CO adsorption studies were different than those obtained with previous systems. CO molecules coordinated in different modes revealing good accessibility of the metal surface.

The use of ferrocenyl phosphino ligands, which is a new family of ligands with no other example in literature allowed to obtain control on the formation of NPs resulting in very small particles with a size range between 1.1 and 1.7 nm. FT-IR investigations on L5 mono- and L2 bidentate ligands highlighted the effect of the hindrance at NPs surface on the coordination of CO on the surface of the particles.

A CXP calix[4]arene biphosphite ligand, was applied for the first time in the synthesis of MNPs. Well-controlled Rh particles were obtained with a mean size of 4 nm. These particles were used in catalytic hydroformylation reaction (see chapter V).

Employing a family of N-Heterocyclic carbenes in the synthesis of Rh NPs allowed forming well-controlled NPs that are soluble in both organic and aqueous solvents.

In addition to the RhNPs synthesis, we reported the synthesis of amino-modified silica support and the successful deposition of selected rhodium

nanoparticles systems on it, which was performed at the Laboratory of Nanomaterials and Catalysis (University of Sao Paulo, Brasil). As it will be described in chapter IV, this immobilization helps in the recovery of the catalyst.

**Table 2.5:** Summary of the characteristics of the prepared monometallic Rh NPs.

Stabilizer	Mean size (nm)	Rhodium content (%)	Number of Rh atoms	%Rh on surface	CO bridging	CO terminal	CO geminal	Structure
PVP	2.2	14.9	400	32.5	x	x	x	Fcc
PPh <sub>3</sub>	1.3	66.2	83	50.3	x	x	x	β-manganese
Dppb	1.7	45.6	185	40.5	x	x	x	β-manganese
PTA	0.9	42.5	27	56.7	x	(x)		oxidized
L1	1.5	22.7	127	44.9	x			fcc
L5	1.2	29.3	65	53.5	x	x	x	fcc
CXP	4.1	--	2591	18.5	--	--	--	--
PrIPr	2.9	--	917	25.4	--	--	--	--
PrIMes	1.7	--	185	40.5	--	--	--	--

---

# **Chapter III :**

# **Bimetallic**

# **Nanoparticles**

---

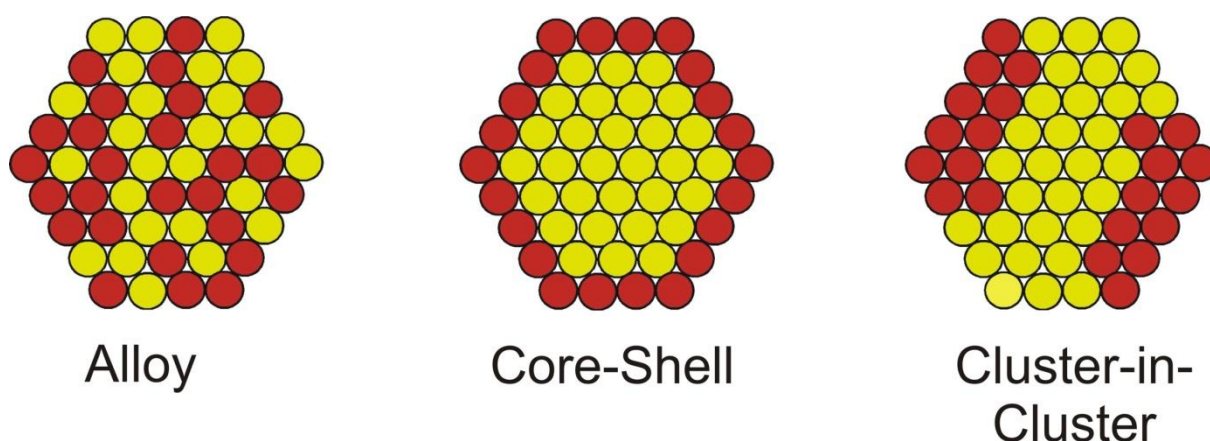


## III. Bimetallic Rhodium Nanoparticles

### III.1 Introduction

Bimetallic nanoparticles (BMNPs) are currently attracting a lot of interest due to their particular and promising properties which differ from those of their monometallic counterparts.<sup>248</sup> This high interest derives from the additional compositional degree of freedom which enables tuning of the physical and chemical properties of BMNPs, that also depend on their size, composition and structure.<sup>249</sup> In addition, they might present synergistic effect, resulting in a whole effect (in terms of activity and applications) of the combined elements superior than the sum of the individual effects of each element.

The addition of a second element makes the structures of bimetallic nanoparticles much more complex than those of their monometallic counterparts. In BMNPs, the two elements involved can be arranged following three main types of structures (Figure 3.66). In the alloy structure, the atoms are randomly adjusted.<sup>250</sup> The second possibility for BMNPs structures is the core-shell arrangement which consists of a core of one metal encapsulated by a layer of a second metal.<sup>251</sup> In the cluster-in-cluster formations, one element forms nanoclusters and the second element surrounds these nanoclusters and acts as a binder.



**Figure 3.66:** Main types of structures encountered for bimetallic nanoparticles.

Different strategies can be used for producing bimetallic nanoparticles, since these systems can overpass several limitations, combining the properties associated with the two

constituent metals. The preparation of bimetallic nanoparticles using metal complexes or metal salts, can be carried out following two main approaches that are co-reduction<sup>252-257</sup> or successive reduction<sup>258-259</sup> of the two metal precursors. Co-reduction is the simplest preparative method of bimetallic nanoparticles, being the same as for monometallic systems except the number of metal precursors which is equal to two. Successive reduction is usually applied to prepare “core-shell” structured bimetallic nanoparticles. Other methods exist but they are narrowly employed, such as the use of bimetallic complexes as metal source<sup>260</sup> and electrolysis of bulk metals.<sup>261</sup>

In most cases, there is a great enhancement in the specific physical and chemical properties of BMNPs owing to a synergistic effect. But, their precise characterization for a complete understanding in terms of structure, composition and behavior remains challenging. In the process of BMNPs characterization, besides the usual characteristics as the size, shape, and metal composition, the distribution and surface ordering of the two metals needs to be deeply investigated because it can affect the activity, selectivity and stability in catalysis. The use of a combination of different characterization techniques is thus necessary to determine the precise structure of the BMNPs, and even like this, sometimes some questions may remain.

Rhodium NPs are commonly used as catalysts for different catalytic reactions, mainly in hydrogenation of arenes and other substrates.<sup>112-113,167,262</sup> However, their use at an industrial scale is restricted by the limited reserves and high price of Rh. Therefore a potential solution to circumvent this obstacle is the partial replacement of Rh by a less expensive metal. In addition to the economic benefits of this substitution, the resulting bimetallic NPs do not only display a simple combination of the properties of each individual constituent. They may also show new properties and capabilities due to a synergy between the two metals.<sup>263</sup> This can be another motivation to associate a second metal to rhodium to prepare novel catalysts.

Rhodium is probably not the most used metal in the synthesis of bimetallic nanoparticles, but several examples in literature report the interest of RhM species mostly for catalytic applications. For instance, Li and coworkers<sup>263</sup> reported the synthesis of RhNi bimetallic NPs using a simple one-pot procedure, where the composition of the bimetallic



NPs can be tailored. They evaluated the catalytic performance of the obtained RhNi NPs of different compositions in the hydrogenation of arenes at room temperature, and found that they exhibit higher activity than pure Rh NPs (phenol hydrogenation conversion: RhNi 54.4%; Rh: 42.5%).

Nishihara *et al.*<sup>264</sup> published the synthesis of RhFe NPs inside the cavities of TPP-DPA G4 dendrimer (Porphyrin-core phenylazomethine dendrimer generation 4), by chemical reduction of FeCl<sub>3</sub> and RhCl<sub>3</sub> salts with NaBH<sub>4</sub>. The resulting particles (average size of 1.1 ± 0.2 nm) were tested in the catalytic hydrogenation of olefins and nitroarenes under mild conditions showing improved results in comparison to monometallic Rh NPs or Rh complex.

Lu *et al.*<sup>265</sup> published the synthesis of bimetallic RhRu NPs stabilized inside a fifth-generation poly(amidoamine) dendrimer (G5-Q). These BMNPs were synthesized by co-decomposition of the two different metal ions (RhCl<sub>3</sub> and RuCl<sub>3</sub>) using NaBH<sub>4</sub> in presence of the dendrimer. Resulted NPs varied in size between 1 and 5 nm depending on the metal ratios. All displayed a high efficiency for hydrosilylation regarding the regioselective synthesis of multifunctional hybrid poly(methylhydro)siloxanes. The bimetallic systems presented higher catalytic activity than physical mixtures of their monometallic counterparts, which was attributed by the authors to a synergistic electronic effect.

Su and coworkers<sup>266</sup> studied the effect of different [Rh]/[Co] metal ratios in RhCo bimetallic nanoparticles in the selective hydrogenation of unsaturated carbon-carbon bonds with hydrous hydrazine as hydrogen source. A ratio of 4/1 Rh to Co was found to be the most active composition with a 90% conversion of styrene into ethylbenzene which is a higher conversion than the obtained with monometallic Rh NPs.

Cheng *et al.*<sup>267</sup> used the chemical reduction method of Rh and Ni salts to synthesize bimetallic RhNi NPs deposited on ZIF-8 support (Zeolitic imidazolate framework). The obtained particles had a mean diameter of 1.2 ± 0.2 nm. These NPs were tested in the dehydrogenation of hydrazine in alkaline solution. They exhibited high catalytic activity reaching a turnover frequency value of 140 h<sup>-1</sup> and 100% hydrogen selectivity at 50 °C. More recently, the same group reported the synthesis and the deposition of RhNi BMNPs containing different [Rh]/[Ni] ratios on the same ZIF-8 support. Among all the tested

catalysts, Rh<sub>15</sub>Ni<sub>85</sub>@ZIF-8 exhibited the highest catalytic activity toward hydrolysis of ammonia borane, with a turnover frequency value of 58.8 mol H<sub>2</sub>.min<sup>-1</sup>.(mol catalyst)<sup>-1</sup> and 100% hydrogen selectivity at room temperature.<sup>268</sup>

Gonzalez and coworkers<sup>269</sup> reported on the catalytic ethanol oxidation reaction using carbon supported RhPdNPs/C supported on an electrode. They showed that PtRh/C catalysts enhanced the total ethanol oxidation with respect to pure Pt/C by driving the reaction *via* the CO<sub>2</sub> route. The faradic current efficiency for the oxidation of ethanol to CO<sub>2</sub> increased from 0.08 on pure Pt/C to 0.5 on the Pt<sub>47</sub>Rh<sub>53</sub>/C catalyst at 0.7 V vs. RHE (Reversible Hydrogen Electrode). It was concluded that electronic effects play a key role in the mechanism of ethanol oxidation on PtRhNPs/C electrodes.

Somorjai *et al.*<sup>270</sup> studied the effect of different compositions and sizes of PtRh bimetallic nanoparticles in the isomerization of *n*-hexane. PtRh alloys were synthesized in various metal compositions through colloidal technique. Pt(acac)<sub>2</sub> and Rh(acac)<sub>3</sub> were used as metal sources and the [Pt]/[Rh] metal ratio was varied with constant metal amount. The synthesis was performed in presence of triethylene glycol and PVP under constant temperature of 503 K for 1 h resulting in change of solution color into black indicating the formation of NPs with a mean size around 6.5 nm.

Tu *et al.*<sup>271</sup> published the synthesis of RhPt bimetallic nanoclusters with different metal compositions through chemical reduction method using H<sub>2</sub>PtCl<sub>6</sub> and RhCl<sub>3</sub> as metal sources and NaBH<sub>4</sub> as a reducing agent. They studied the effect of modifying the structure of the poly(vinylpyrrolidone) polymer on surface structures of the bimetallic species. Results showed that more Rh rich surfaces were typically obtained with PVP and more Pt rich surface upon employing microwaves in the synthesis.

Previous studies in the team have shown the interest of following the organometallic approach to get bimetallic nanoparticles. It is possible to take benefit of the kinetics of decomposition of organometallic or metal-organic complexes or of the influence of the stabilizer to orientate the synthesis towards the formation of alloy type or core-shell type bimetallic nanoparticles. This has been demonstrated for PtRu systems, and other bimetallic compositions.<sup>75</sup> For example, D. Ciuculescu and D. Zitoun used the organometallic approach

to synthesize in one pot procedure RhFe<sup>272</sup> and RhCo<sup>79</sup> bimetallic NPs, using [Rh( $\eta^3$ -C<sub>3</sub>H<sub>5</sub>)<sub>3</sub>] with Fe[N(SiMe<sub>3</sub>)<sub>2</sub>]<sub>2</sub> and [Rh(acetylacetonate)( $\eta^4$ -C<sub>8</sub>H<sub>12</sub>)] with [Co( $\eta^3$ -C<sub>8</sub>H<sub>13</sub>)( $\eta^4$ -C<sub>8</sub>H<sub>12</sub>)]. The aim of their work was the enhancement of the magnetic character on nanoscale, through the 3d/4d elements association and size reduction which cause 4d elements such as Rh to become ferromagnetic below a critical size.

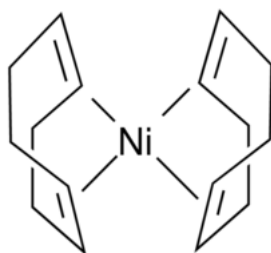
In the following parts, with the idea of application in catalysis we will present the organometallic synthesis of different RhM bimetallic NPs stabilized either with PVP polymer (steric stabilization) or hexadecylamine (HDA) (electrosteric stabilization). RhNi systems will be described in details. We will also explore briefly the synthesis of other bimetallic systems such as RhPd, RhPt, and RhRu which may offer new research opportunities in terms of characteristics and potential catalytic applications.

### III.2 RhNi Bimetallic Nanoparticles

Nickel was chosen to synthesize RhNi bimetallic nanoparticles, due to previous works in the team with this metal either for monometallic<sup>28-31</sup> or bimetallic NPs production.<sup>252</sup> Moreover, nickel might offer an additional advantage that is importing magnetic character to the obtained NPs. In catalysis, magnetic properties can be of interest for the recycling aspects of the catalysts.

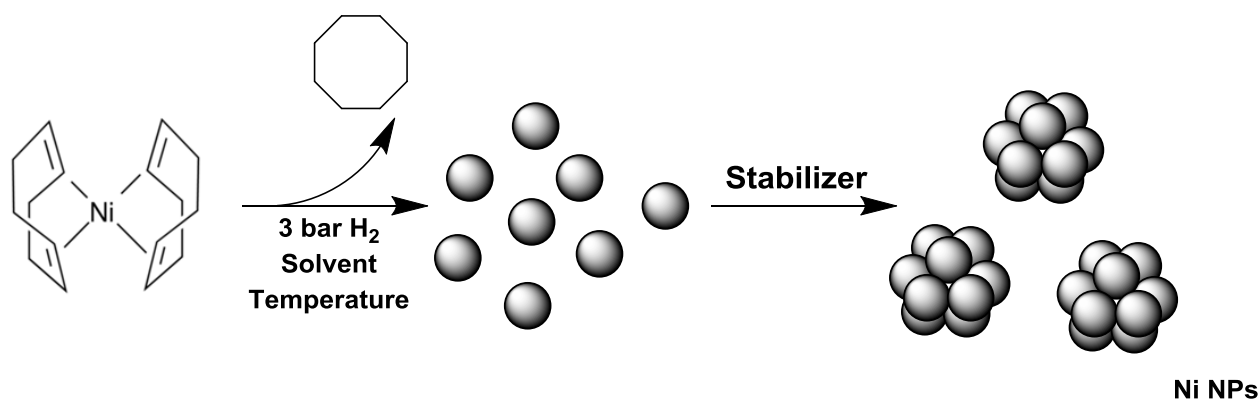
Nickel nanostructured materials are often considered to be difficult to prepare because they are easily oxidizable.<sup>273</sup> They display magnetic properties and good electrical conductivity. They can find a wide range of applications, mainly in catalysis, as for example electrodes of fuel cells, and in magnetic materials.<sup>274</sup>

Before investigating the synthesis of bimetallic RhNi NPs, we studied the decomposition of bis(cyclooctadiene)-nickel(0) [Ni(cod)<sub>2</sub>] complex (Scheme 3.17), as the metal source, to form monometallic NiNPs in reaction conditions similar as those previously applied for the elaboration of Rh NPs.



**Scheme 3.17:** Structure of bis(cyclooctadiene)-nickel(0)  $[Ni(cod)_2]$  complex.

The  $[Ni(cod)_2]$  complex was treated in solution under 3 bar of dihydrogen to allow reduction of the olefinic ligands and liberate the nickel atoms. Cyclooctane is the only product formed during the reaction. It is an inert molecule which does not interfere in the NP growth process, resulting in naked Ni atoms which assemble to form NPs whose growth is controlled with the help of specific stabilizers (Scheme 3.18). Decomposition of the nickel precursor could not be performed at room temperature; heating the reaction medium at 65 °C was crucial to obtain the Ni NPs. We also noticed that faster reactions (higher rate) occurred with higher nickel precursor concentration. This could be explained by an autocatalytic process since Ni materials are active in hydrogenation reaction.<sup>42</sup> In particular, Raney Ni is well-known as hydrogenation catalyst.<sup>275</sup>



**Scheme 3.18:** Decomposition of  $[Ni(cod)_2]$  precursor following the organometallic approach.

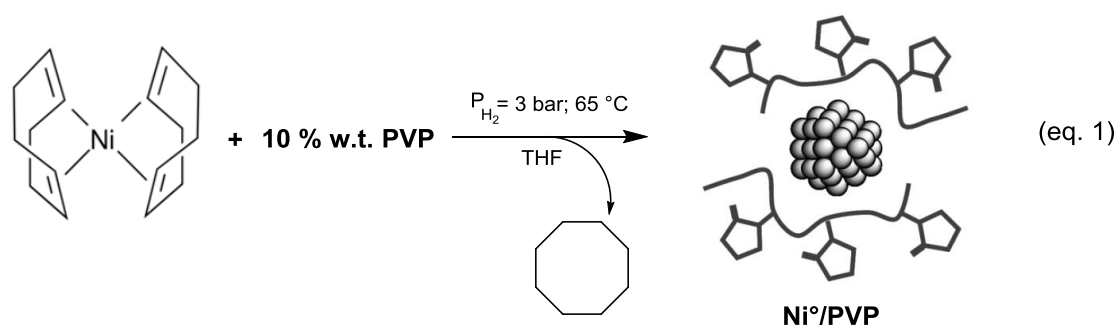
### III.2.1 Monometallic Systems

Polyvinylpyrrolidone polymer (PVP) and hexadecylamine ligand (HDA) were chosen to control the growth of RhNi bimetallic nanoparticles due to previous experience in the team with these two stabilizers. As already commented, PVP provides a steric stabilization due to an embedding of the particles in the polymer matrix while HDA coordinates at their metal surface through the amine function. The long alkyl chain of the amine probably helps protecting the particles through a steric effect. In order to study and compare the BMNPs formation, monometallic RhPVP, RhHDA, NiPVP and NiHDA NPs were needed as reference samples. The synthesis of Rh PVP NPs has been previously reported in chapter II. Syntheses of NiPVP, RhHDA and NiHDA NPs are described here after.

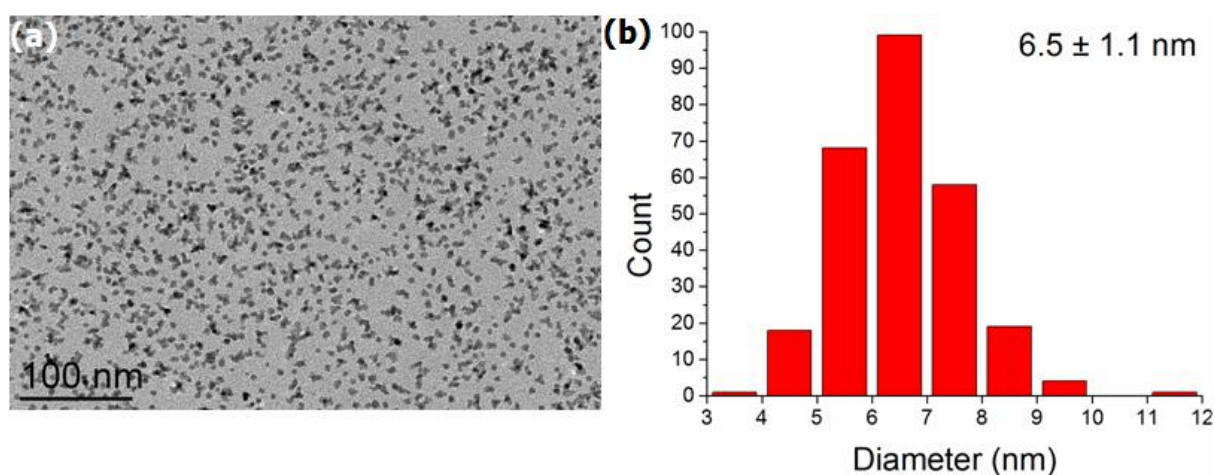
#### III.2.1.1 PVP-stabilized Ni NPs

Previously in the team, the synthesis of NiPVP NPs had been investigated under several conditions. Tayeb Oud Ely *et al.*<sup>4</sup> decomposed the  $[\text{Ni}(\text{cod})_2]$  precursor with PVP in  $\text{CH}_2\text{Cl}_2$  solution under dihydrogen pressure at 60 °C. The obtained particles resulted in ferromagnetic agglomerates of a mean size of 30 nm. Later, Nadège Cordente *et al.*<sup>276</sup> using the same approach could control the size of the particles by changing the solvent and controlling the water and dioxygen content of the reaction medium. Several systems were obtained and NiO NPs were also achieved.

Herein, PVP-stabilized monometallic Ni NPs were synthesized from the  $[\text{Ni}(\text{cod})_2]$  complex as the metal source with a ratio of  $[\text{Ni}]/[\text{PVP}] = 10$  wt. % in THF solution and under  $\text{H}_2$  pressure at 65 °C. (eq. 1)



The reaction mixture passed from light yellow to black color after 3h heating at 65 °C, indicating the formation of the Ni NPs. The reaction was stopped after 16h. Then, one drop of the crude colloidal solution was dispersed over a carbon coated copper grid for TEM analysis using a JOEL 1011 electron microscope. Obtained images showed well-dispersed NPs with non-homogeneous shapes (Figure 3.67a) unlike the spherical morphology obtained for RhPVP NPs. They display a mean size of  $6.5 \pm 1.1$  nm that was measured through manual counting for over 250 particles (Figure 3.67b).

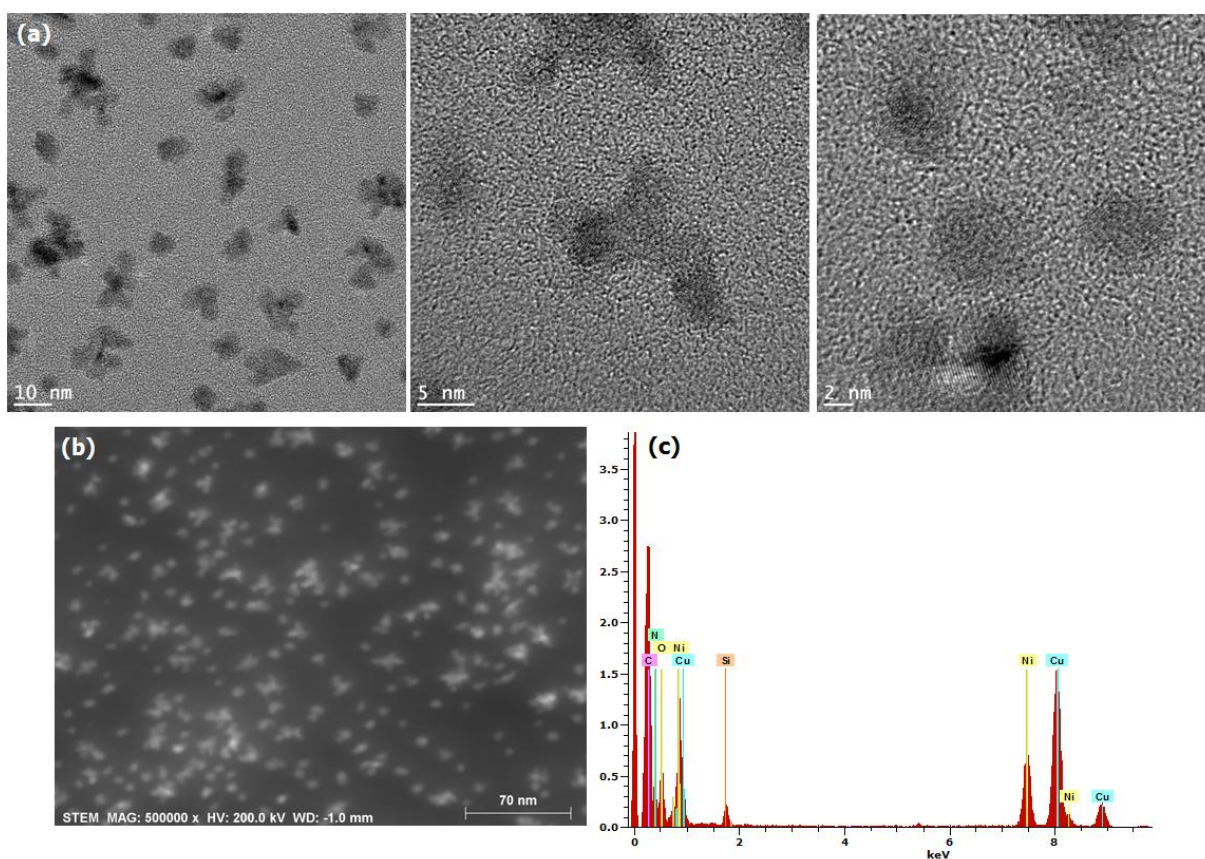


**Figure 3.67:** (a) TEM image of PVP-stabilized Ni NPs (b) corresponding size distribution histogram.

Further high resolution electron microscopy investigations (Figure 3.68a) confirmed the size and the form observed for these Ni NPs by regular TEM. In addition, it appeared that these NPs present both amorphous and crystalline domains. The presence of amorphous regions could be attributed to partially oxidized Ni particles as previously observed.<sup>276</sup> Such an oxidation process is very common with Ni NPs due to the high oxophilic character of this metal. Exposition to oxygen is expected to occur when handling the TEM grids for analysis, since the introduction to the microscope is performed in air.

STEM-HAADF was another analysis technique used to characterize the Ni NPs. This technique is highly sensitive to the Z number of elements. With this imaging mode, the signals of the organic polymeric matrix are lowered due to the great difference in Z number

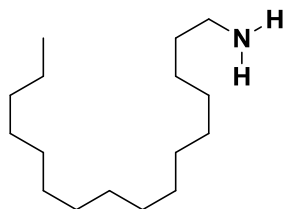
between the Ni atoms and the atoms of C, H, N and O elements contained in the polymer. This allows having more precise views of the Ni nanoparticles. The images thus obtained (Figure 3.68b) confirmed the good dispersion of the particles all over the grid, and the irregular shapes they display. EDX analysis was also performed on single particles to determine their elemental content (Figure 3.68c). EDX spectra revealed the presence of an intense nickel peak, in addition to peaks corresponding to the organic elements from the stabilizing PVP polymer.



**Figure 3.68:** (a) HRTEM images of Ni PVP NPs at different magnifications (b) STEM-HAADF image (c) EDX analysis spectrum.

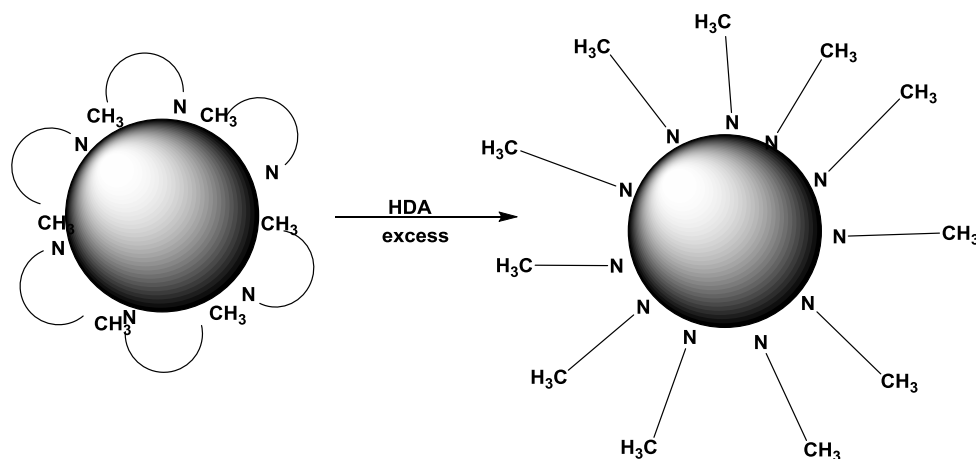
## III.2.1.2 HDA-stabilized Rh NPs

Hexadecylamine (HDA) (Scheme 3.19) is a C-16 alkylamine that weakly coordinates to the surface of metals. This ligand was chosen to stabilize Rh NPs after being successfully applied with different metals in the team.<sup>71,195,217,277-280</sup>



**Scheme 3.19:** Formula of hexadecylamine (HDA).

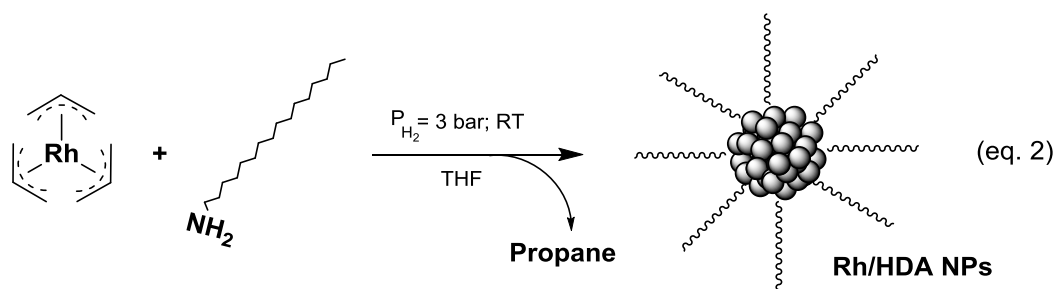
From a previous work in the group, it was shown by NMR studies that for a very low HDA content, the coverage of the surface of Ru NPs by the ligand is taking place through interaction of the methyl groups, probably under the form of agostic interactions, well-known in molecular chemistry. Addition of an extra amount of HDA resulted in the displacement of this weak interaction by an amino group as shown in Scheme 3.20.<sup>71</sup> The weak character of the coordination of HDA at metallic surface can be used to control the growth of MNPs toward shape-controlled particles.<sup>277,280-281</sup>



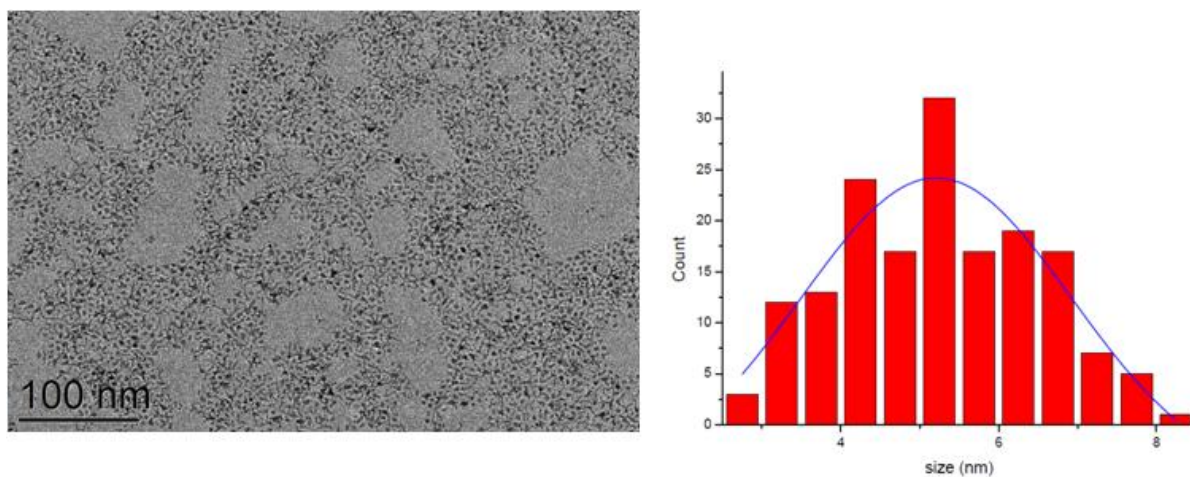
**Scheme 3.20:** Possible ways of coordination of hexadecylamine (HDA) on nanoparticles as a function of amine concentration.<sup>71</sup>



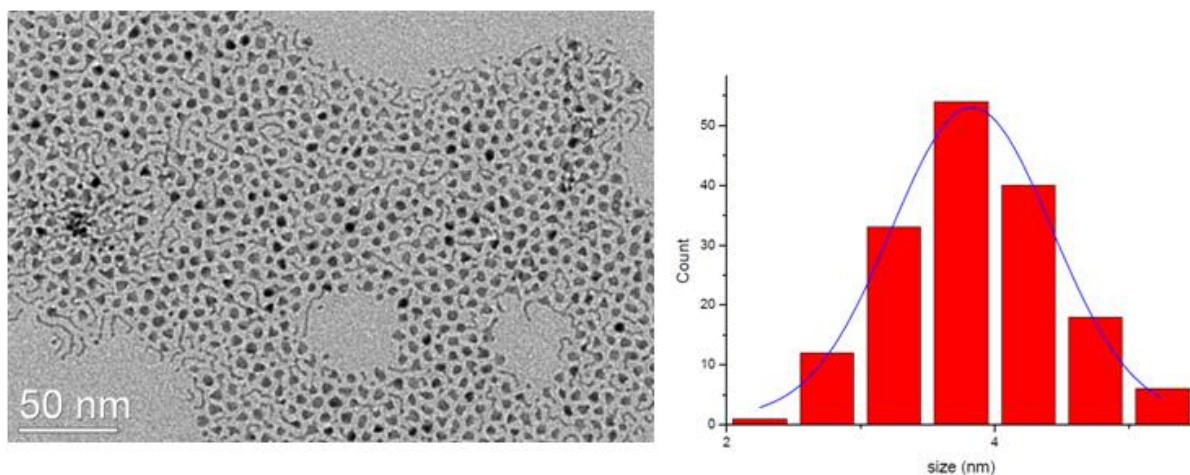
We intended to compare the effect of different [HDA]/[Rh] ratios on the characteristics of the obtained particles in terms of size and shape. Thus, the synthesis of HDA-stabilized Rh NPs in THF was performed in the presence of 1, 2 or 5 molar equivalents of the ligand to metal proportion according to the following reaction (eq. 2).



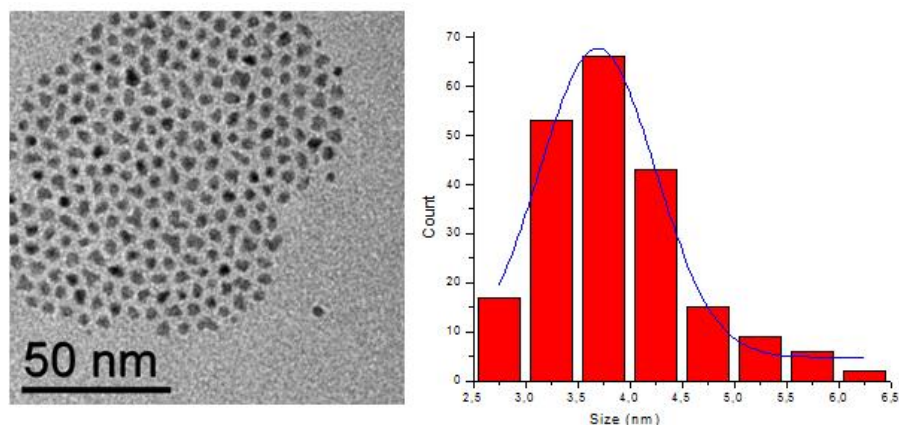
Reaction proceeded at room temperature. The change of color from yellow to black colloidal solution occurred within 15 minutes, but the reaction was left overnight to insure the total decomposition of the Rh precursor. TEM analysis of the crude colloidal solution revealed the presence of well-dispersed Rh NPs. Reaction with 1 molar equivalent of HDA led to particles with an average size of  $5.2 \pm 3.2$  nm and a large size distribution (Figure 3.69). It is in fact a mixture of small and large particles with no specific shape. When the reaction was performed with 2 equivalents of HDA, smaller particles were formed with an average size of  $3.8 \pm 1.1$  nm (Figure 3.70). They display both spherical and elongated morphologies. For the Rh NPs prepared with 5 equivalents of HDA (Figure 3.71), a mean size of  $3.7 \pm 1.1$  nm was measured, with better homogeneous shapes all over the grid. From these results we can conclude that higher quantity of stabilizer (comparison of 1 eq. and 2 eq. of HDA) increases the growth control by replacing weaker agostic interaction with more amine coordination, which leads to smaller particles till reaching a point of saturation where addition of extra stabilizing ligand (5 eq. HDA) does not change much the particle mean size but provides a better controlled population of NPs that display regular shapes and sizes.



**Figure 3.69:** TEM image of Rh NPs stabilized with 1 eq. of HDA ligand in THF, with the corresponding size distribution histogram.



**Figure 3.70:** TEM image of Rh NPs stabilized with 2 eq. of HDA ligand in THF, with the corresponding size distribution histogram.

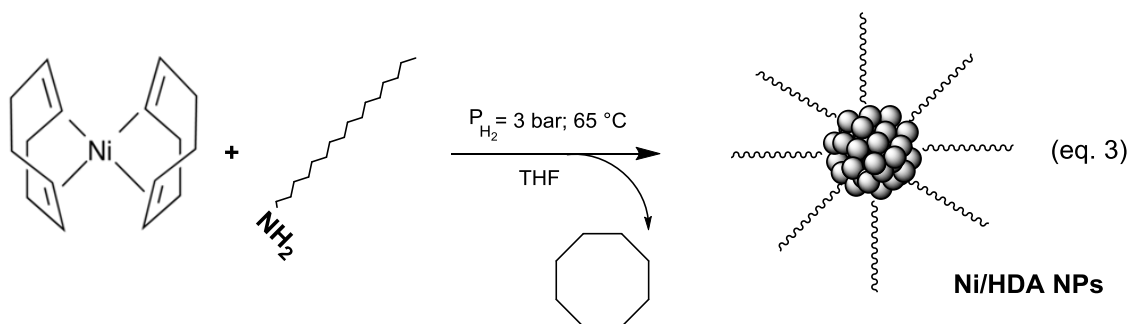


**Figure 3.71:** TEM image of Rh NPs stabilized with 5 eq. of HDA ligand in THF, with the corresponding size distribution histogram.

### III.2.1.3 HDA-stabilized Ni NPs

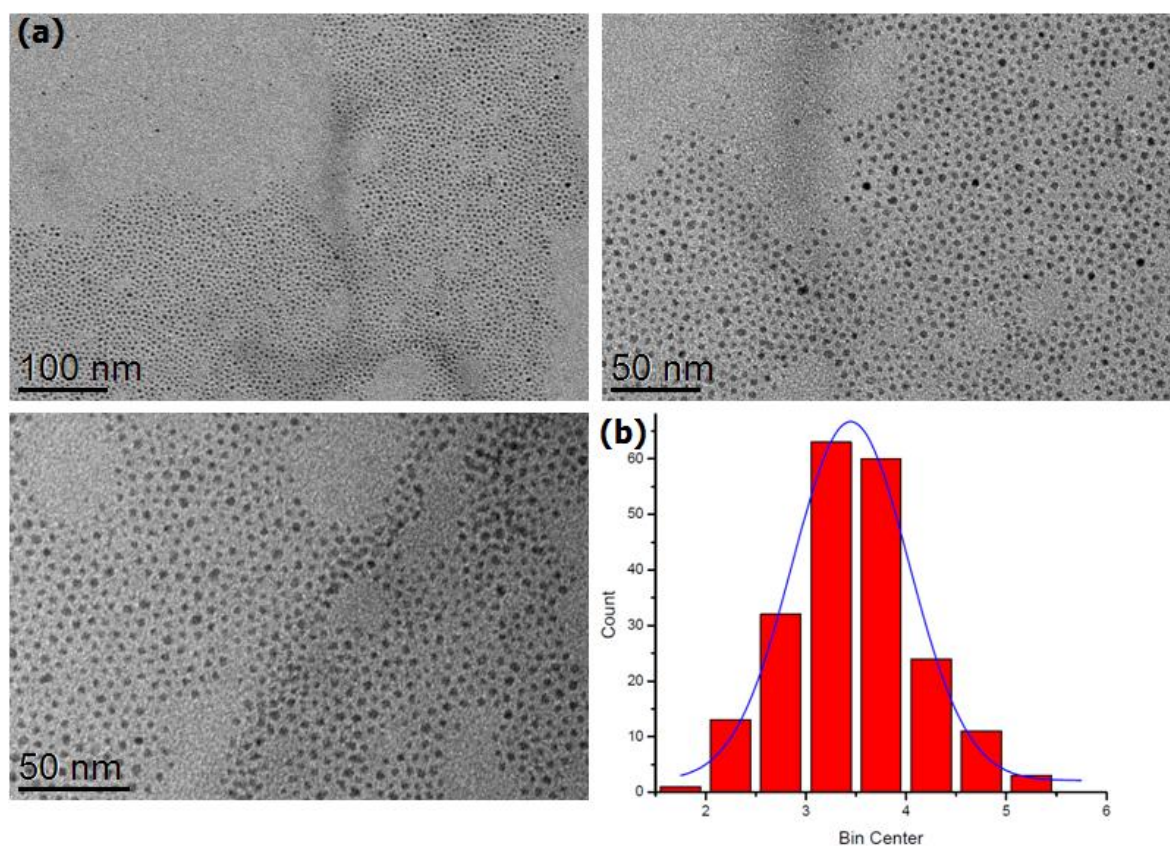
NiHDA NPs were previously obtained in the team through decomposition of the Ni(cod)<sub>2</sub> precursor under H<sub>2</sub> in the presence of 1 or 2 equivalents of HDA in THF solvent at 70 °C.<sup>277</sup> Ni nanorods were formed under these conditions.

After studying the effect of different ratios of HDA on Rh NPs synthesis, we focused on the use of 5 equivalents of this stabilizer to prepare Ni NPs because it resulted in well-dispersed Rh NPs with homogeneous size and uniform shape. Using the Ni(cod)<sub>2</sub> precursor we thus performed the synthesis of monometallic Ni NPs stabilized with 5 molar equivalents of HDA (eq. 3).



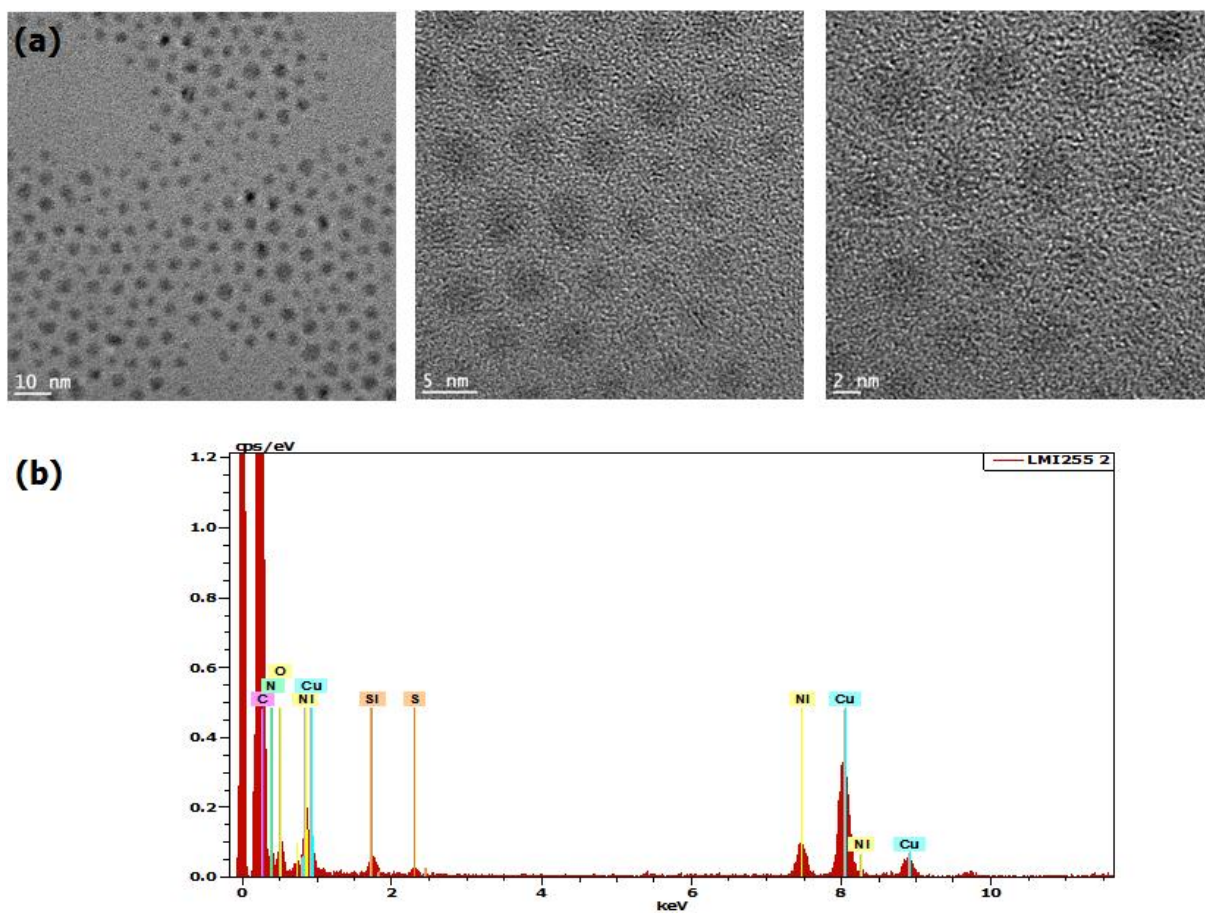
The yellow solution of Ni complex and HDA in THF became black after one night under 3 bar of dihydrogen at 65°C, indicating the formation of Ni NPs. A drop of the crude colloid solution was transferred onto a carbon covered copper grid for TEM analysis. The obtained images (Figure 3.72a) revealed the presence of very well-controlled NPs with

spherical and uniform shape unlike the nanorods form obtained previously in the team,<sup>277</sup> a homogeneous size distribution with a mean size of  $3.4 \pm 1.1$  nm. (Figure 3.72b)



**Figure 3.72:** (a) TEM images and (b) Size distribution histogram of HDA-stabilized Ni NPs (5 eq.).

High resolution TEM and EDX analysis were also performed for this Ni/HDA<sub>5</sub> system of nanoparticles (Figure 3.73a). HRTEM images confirmed the shape and the size of the obtained particles, but no information could be extracted about the crystalline structure. NPs showed amorphous structure which could be attributed to partial metal oxidation and/or to a high ligand proportion as the result of 5 eq. of HDA introduced for their synthesis. EDX spectrum highlighted the presence of elemental nickel metal, and confirmed the presence of nitrogen element coming from the amine ligand. It also revealed the presence of oxygen that could come from nickel oxide (Figure 3.73b).

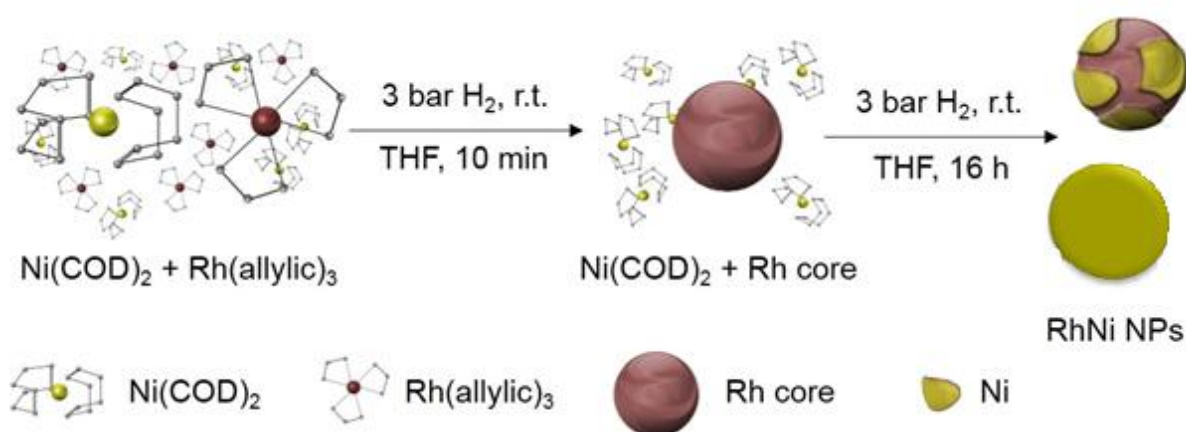


**Figure 3.73:** (a) HRTEM images and (b) EDX analysis spectrum of HDA-stabilized Ni NPs (5 eq.).

### III.2.2 Bimetallic RhNi Systems

RhNi bimetallic nanoparticles were prepared following a one step synthesis procedure under typical decomposition reaction conditions (3 bar of H<sub>2</sub>, r.t., overnight). [Rh( $\eta^3$ -C<sub>3</sub>H<sub>5</sub>)<sub>3</sub>] and [Ni(cod)<sub>2</sub>] complexes were used as metal sources in different metal ratios to explore different RhNi compositions. Size control of the particles was studied using either 10 % weight of PVP or 5 molar equivalents of HDA as stabilizers.

Interestingly, although the [Ni(cod)<sub>2</sub>] complex when exposed alone to 3 bar of dihydrogen in the presence of stabilizer presents resistance to decomposition at r.t., when mixing both [Rh( $\eta^3$ -C<sub>3</sub>H<sub>5</sub>)<sub>3</sub>] and [Ni(cod)<sub>2</sub>], we noticed that the nickel precursor could be decomposed at r.t. as later confirmed by ICP and EDX analysis. We attribute this behavior to a catalytic effect of Rh NPs that probably helps the decomposition of [Ni(cod)<sub>2</sub>] by acting as hydrogenation catalyst. Indeed, from our experience with the [Rh( $\eta^3$ -C<sub>3</sub>H<sub>5</sub>)<sub>3</sub>] complex, we know it is easily decomposed in the presence of PVP or HDA, yielding to Rh NPs that are active in hydrogenation reaction (see chapter IV). So, considering that the Rh NPs are instantaneously obtained after H<sub>2</sub> exposure, it is expected they can catalyze the hydrogenation of cyclooctadiene (cod) of the Ni precursor, leading to the liberation of Ni atoms. This may result in the formation of Ni layer around the pre-formed Rh NPs, or Ni islands at their surface depending on the quantity of nickel precursor introduced. This will be discussed in details in the following parts (Scheme 3.21).

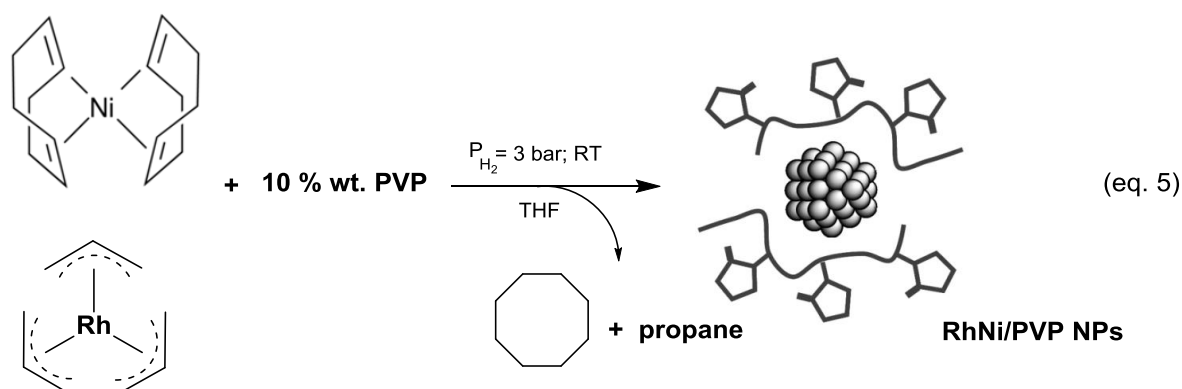


**Scheme 3.21:** Schematic presentation of the decomposition of [Rh( $\eta^3$ -C<sub>3</sub>H<sub>5</sub>)<sub>3</sub>] and [Ni(cod)<sub>2</sub>] complexes following the organometallic approach

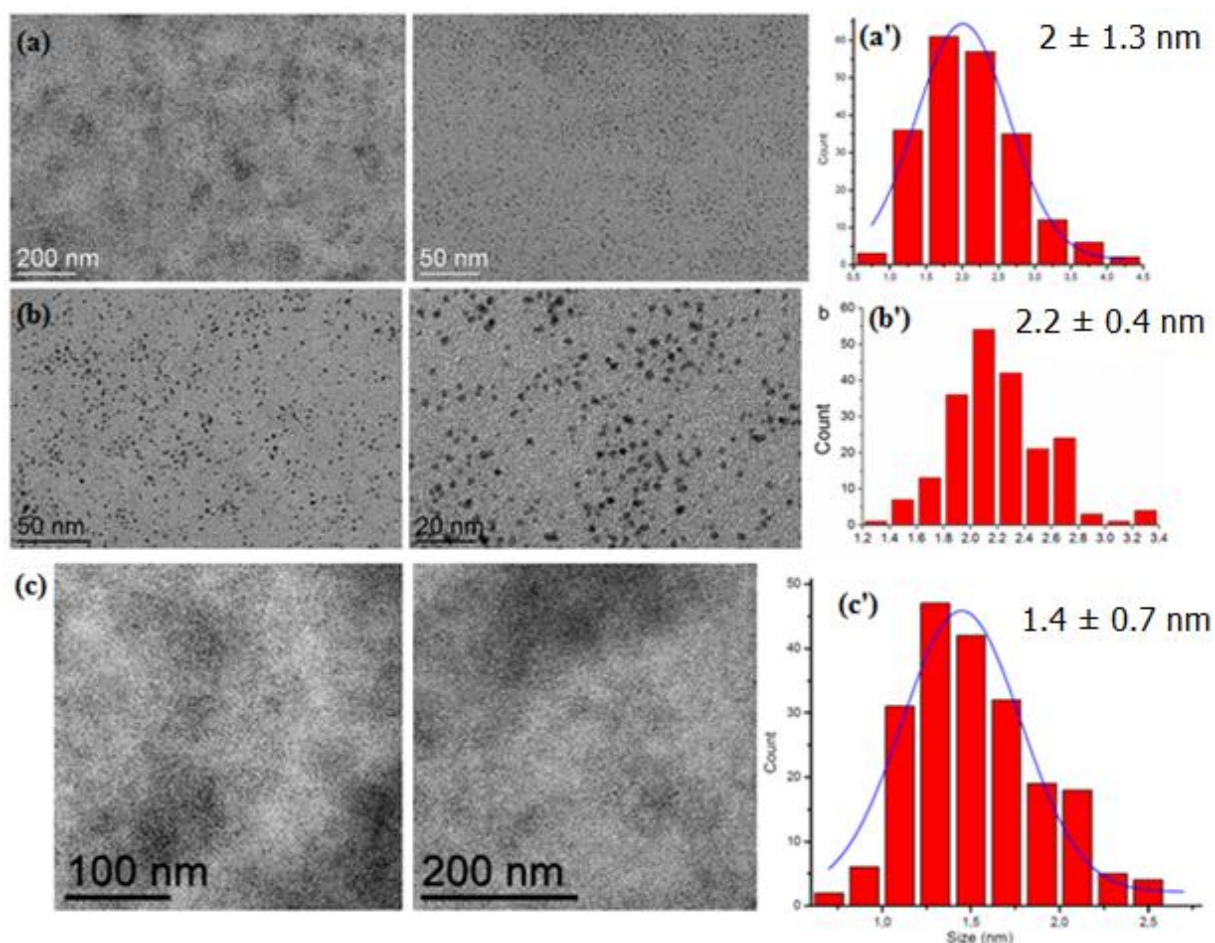
## III.2.2.1 PVP-stabilized RhNi NPs

Different [Rh]/[Ni] metal ratios were used to study the formation of RhNi bimetallic nanoparticles using in all cases 10 % weight of PVP to control the particle growth. The different [Rh:Ni] ratios tested varied from [2:8], [5:5] and [8:2] leading to Rh<sub>2</sub>Ni<sub>8</sub>, Rh<sub>5</sub>Ni<sub>5</sub>, and Rh<sub>8</sub>Ni<sub>2</sub> systems of particles as described hereafter.

The three syntheses were performed applying the same reaction conditions (eq. 5). A solution of PVP dissolved in THF was added into the Fischer Porter vessel that contained the two complexes and maintained at low temperature. This was followed by pressurizing the reactor with 3 bar of H<sub>2</sub> and leaving the reaction at r.t. overnight, to insure full decomposition of metal complexes. Fast change of color from yellow into black solution indicated the NPs formation. Faster reaction rates were observed with higher [Rh] ratios, confirming our expectation of the decomposition of the Ni precursor at r.t. when mixing with the Rh one.



TEM analysis realized from the crude colloidal solutions after depositing a drop on carbon grids revealed the presence of small NPs in a size range of 1.5 – 2.5 nm. No agglomerations were observed over the grids (Figure 3.74). ICP-AES analysis confirmed the presence of both Rh and Ni metals in the NPs formed, attesting of the decomposition of the two precursors.



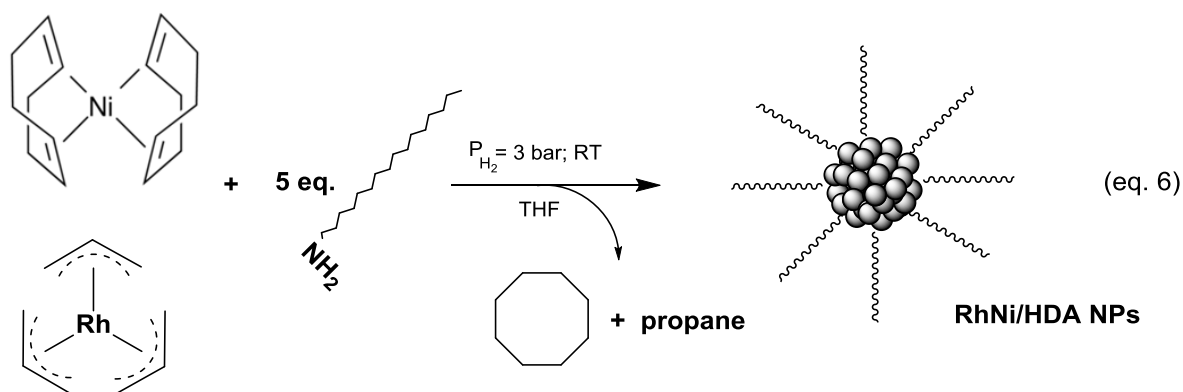
**Figure 3.74:** TEM images of PVP-stabilized (a)  $Rh_2Ni_8$  (b)  $Rh_5Ni_5$  (c)  $Rh_8Ni_2$ , with their corresponding size distribution histograms (a') (b') (c').

Mineralization of the PVP-stabilized nanoparticle samples for the ICP-AES analysis was performed in aqua regia at room temperature. A rapid dissolution of the NPs occurred with all the different samples. Results obtained were in total accordance with the calculated theoretical percentages, with a negligible 0.05 excess of Ni ratio in the  $Rh_8Ni_2$  sample (see Table 3.6).

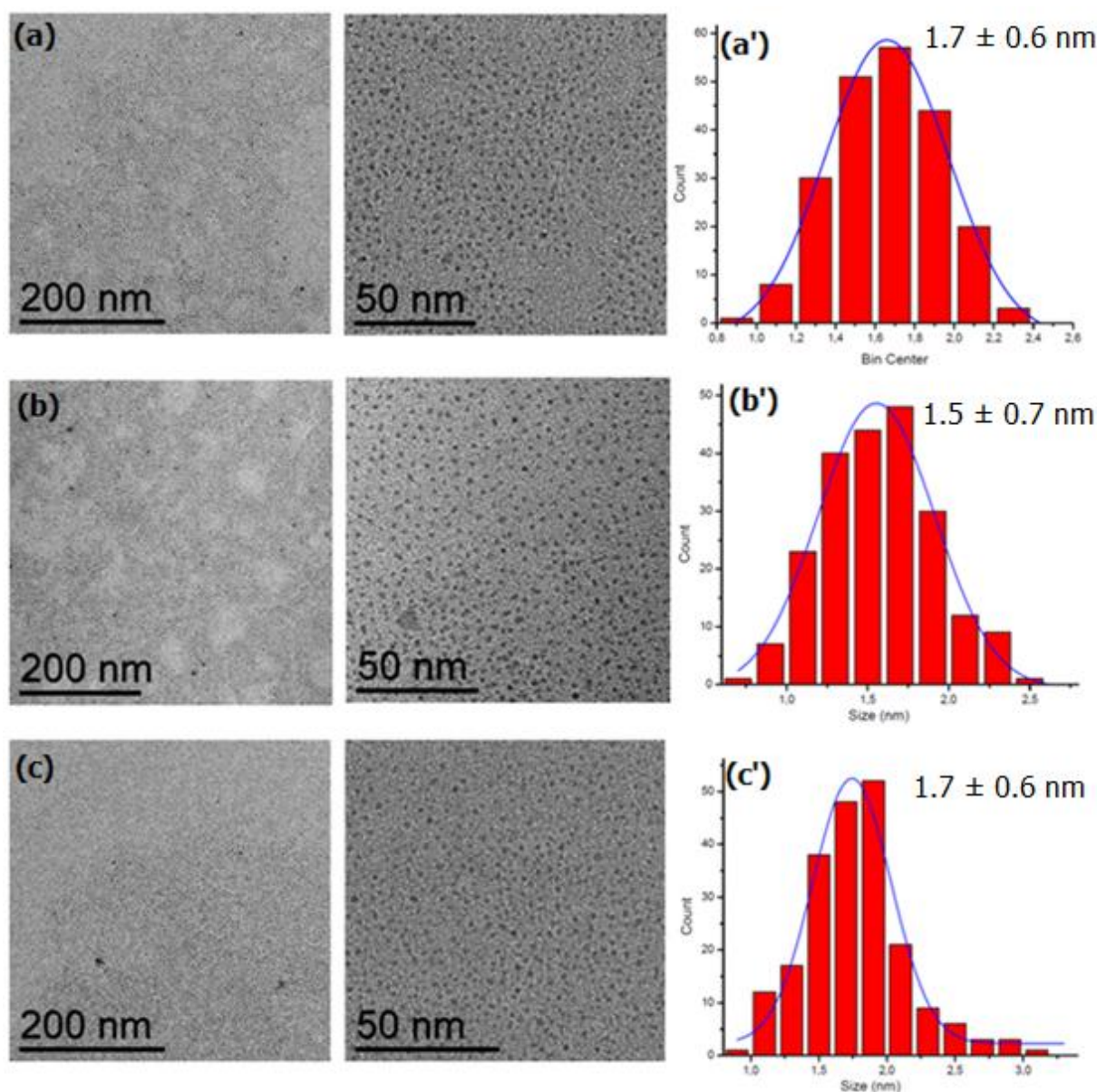
### III.2.2.2 HDA-stabilized RhNi NPs

Different  $[Rh]/[Ni]$  metal ratios were also used to study the formation of the bimetallic nanoparticles, in the presence of 5 molar equivalents of HDA to control the particle growth in all the cases. The different  $[Rh:Ni]$  ratios tested varied from [2:8], [5:5] and [8:2] giving rise to  $Rh_2Ni_8$ ,  $Rh_5Ni_5$ , and  $Rh_8Ni_2$  nanoparticle samples.





The three syntheses were performed applying the same reaction conditions (eq. 6). A THF solution of HDA was added into the Fischer Porter glassware that contained the two complexes dissolved in THF. The reactor was maintained at low temperature to prevent any intermediate complex formation, followed by pressurizing with 3 bar of  $H_2$  and the reaction was left under constant stirring at r.t. overnight, to insure full decomposition of metal complexes. TEM analysis from the crude colloidal solutions was then performed. Obtained images revealed the presence of ultra small NPs for the three syntheses having almost the same mean size in the range 1.5 – 1.7 nm (Figure 3.75).



**Figure 3.75:** TEM images of HDA-stabilized (a)  $Rh_2Ni_8$  (b)  $Rh_5Ni_5$  (c)  $Rh_8Ni_2$ , with their corresponding size distribution histograms (a') (b') (c').

Mineralization of the HDA-stabilized RhNi nanoparticles samples for the ICP-AES analysis performed in aqua regia at room temperature was not as simple as in the case of the PVP systems. Solid traces were always present in the acidic solution and heating of the acid up to 40°C was necessary to dissolve completely the NPs. Results obtained showed a good accordance with theoretical values, although slightly higher Ni ratios were obtained with the  $Rh_2Ni_8$  and  $Rh_8Ni_2$  samples with a difference ratio range of 0.08 and 0.1, respectively. This difference could be attributed to the difficulties in the mineralization step.

In Table 3.6, the mean size and metal contents obtained for all the NP samples of Rh, Ni and RhNi synthesized are summarized.

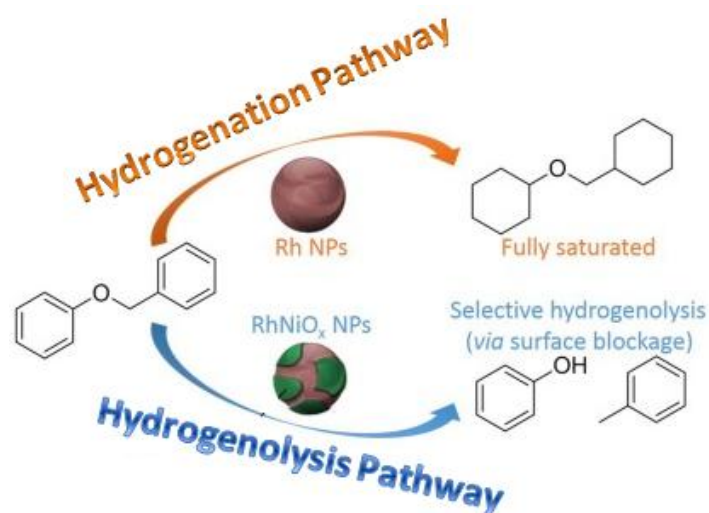
**Table 3.6:** Summary of synthesized Rh, Ni and RhNi NPs with their corresponding average sizes, and the Rh and Ni metal content in each system.

Nanoparticles	Stabilizer	Size (nm)	wt. % of Rh	wt. % of Ni	Rh/Ni (mol/mol)
Rh	PVP (10 wt.)	2.2 ± 0.9	14.9	---	1:0
Rh <sub>2</sub> Ni <sub>8</sub>	PVP (10 wt.)	2.0 ± 1.3	2.14	4.6	0.25:1
Rh <sub>5</sub> Ni <sub>5</sub>	PVP (10 wt.)	2.2 ± 0.4	7.71	4.4	0.99:1
Rh <sub>8</sub> Ni <sub>2</sub>	PVP (10 wt.)	1.4 ± 0.7	6.6	1.17	1:0.30
Ni	PVP (10 wt.)	6.5 ± 1.1	---	9.11	0:1
Rh	HDA (1 eq.)	5.2 ± 3.2	22.7	---	1:0
Rh	HDA (2 eq.)	3.8 ± 1.1	16.6	---	1:0
Rh	HDA (5 eq.)	3.6 ± 1.1	8.06	---	1:0
Ni	HDA (5 eq.)	3.4 ± 1.1	---	4.42	0:1
Rh <sub>2</sub> Ni <sub>8</sub>	HDA (5 eq.)	1.6 ± 0.6	1.2	3.72	0.17:1
Rh <sub>5</sub> Ni <sub>5</sub>	HDA (5 eq.)	1.5 ± 0.7	3.5	1.95	1:0.97
Rh <sub>8</sub> Ni <sub>2</sub>	HDA (5 eq.)	1.7 ± 0.6	4.9	0.96	1:0.35

### III.2.3 PVP-stabilized RhNiO<sub>x</sub> NPs

In the framework of a collaborative Merlion project with the team of Pr. Ning Yan at the National University of Singapore (NUS) we were interested in having in hands Rh-NiO<sub>x</sub> nanoparticles to evaluate their catalytic properties in the selective hydrogenolysis of model molecules to mimic lignin conversion into bio-fuel under dihydrogen treatment. For this reaction it was reported that Rh NPs partially covered by NiO<sub>x</sub> are interesting candidates.<sup>282-283</sup> In fact, since Rh NPs are highly active in hydrogenation reactions which overtake the hydrogenolysis reaction pathway, it is needed to partially cover their surface with a catalytically inactive part, which can be NiO<sub>x</sub> islands. The already synthesized RhNi NPs appeared thus as good candidates to provide nanocatalysts comprised of a core of Rh and a Ni coverage on the surface. For deactivating the Ni domains, we decided to oxidize the NPs under air. This could be easily performed since Ni is very sensitive to air. RhNiO<sub>x</sub> NPs

consisting of a Rh core partially covered with inactive  $\text{NiO}_x$  islands were produced by this way with the idea to overcome the hydrogenation pathway and favor the hydrogenolysis one in the treatment of 1-benzyloxy-2-methoxy-benzene under digydrogen (see chapter IV) (Figure 3.76).<sup>85</sup>



**Figure 3.76:** Selective hydrogenolysis of C–O bond over arene hydrogenation of 1-benzyloxy-2-methoxy-benzene.<sup>85</sup>

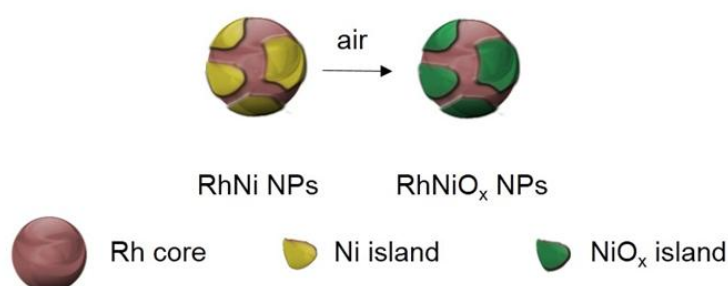
Among the bimetallic RhNi NPs previously synthesized, we decided to focus on the PVP stabilized RhNi systems. This choice was supported by two main reasons that are: 1) the PVP stabilizer offers a free surface that is easily accessible by the substrates in catalysis; 2) PVP transfers its hydrophilic character to the particles allowing their solubility in water and consequently to perform catalysis in aqueous phase.

The [Rh]/[Ni] 50/50 composition was selected allowing us to have in hands 2.2 nm PVP-stabilized  $\text{Rh}_5\text{Ni}_5$  NPs. First we made an estimation of the surface coverage of 2.2 nm Rh cores by nickel. For that purpose, we considered spherical NPs of 2.2 nm diameter with a close packed structure in which 74% of the volume is filled.<sup>284</sup> The number of metal atoms (N) to fill the NPs can be calculated following (eq. 6) where D represents the average mean diameter of spherical NPs, and d represents the diameter of Rh atom .

$$N = 0.74 D^3/d^3 \quad (\text{eq. 6})$$

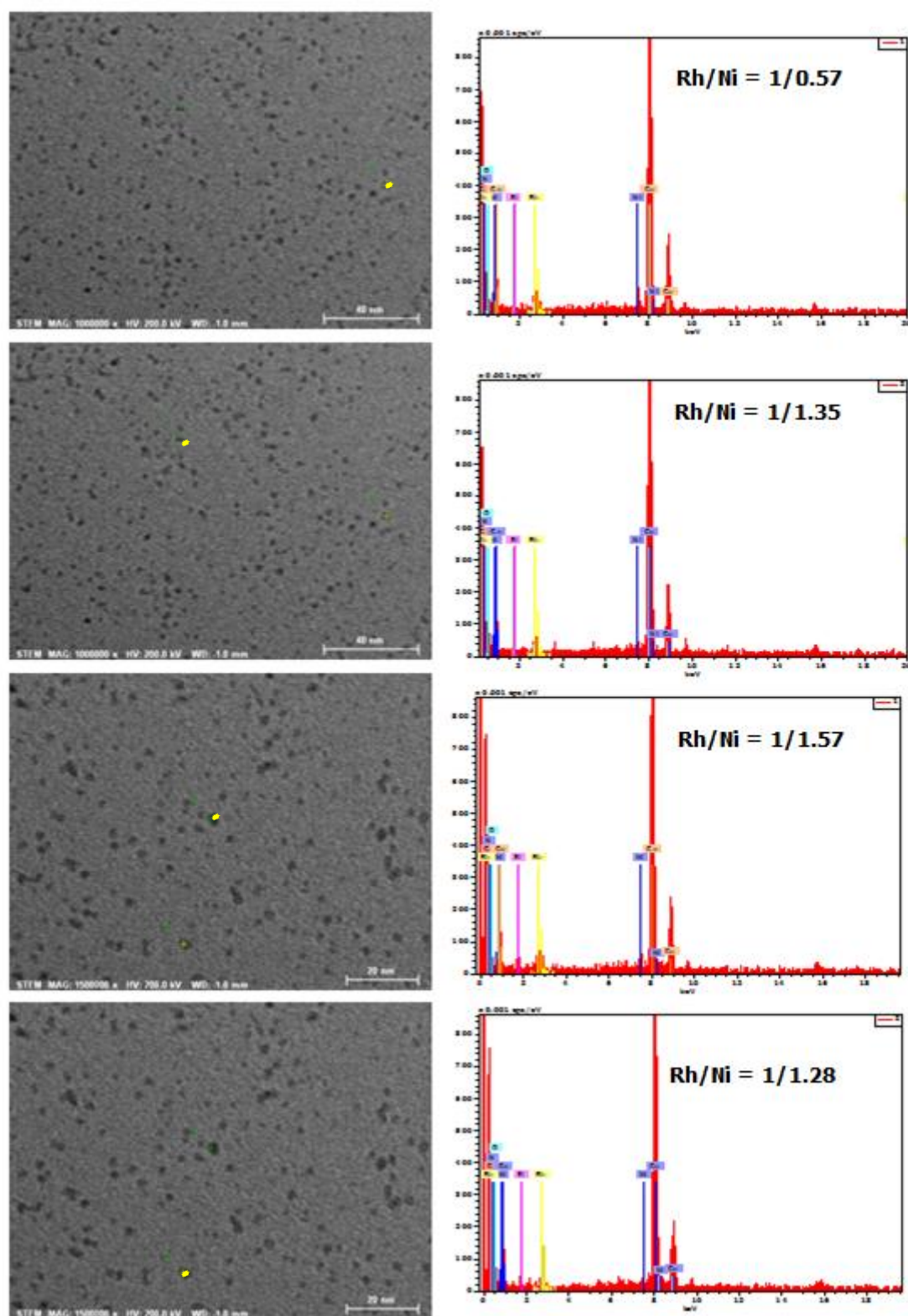
Considering 2.2 nm NPs and Rh as metal (Rh atom diameter = 0.276 nm), spherical particles thus consist of 400 close packed Rh atoms. To form a close packed monolayer around these 2.2 nm cores, higher number of Ni atoms are necessary. Since equal amount of Ni was used (compared to Rh) in the synthesis of the Rh<sub>5</sub>Ni<sub>5</sub>/PVP NPs, it was calculated that the Ni content is able to cover only 80% of Rh core. The surface Ni might thus segregate into small regions that we call hereafter islands, dividing Rh terraces into small domains.

Taking benefit of the highly oxophilic character of the nickel in Ni NPs, the Rh<sub>5</sub>Ni<sub>5</sub>/PVP NPs were exposed to air for 30 minutes to oxidize the Ni islands and obtain the desired Rh NPs with NiO<sub>x</sub> surface decoration (Figure 3.77).



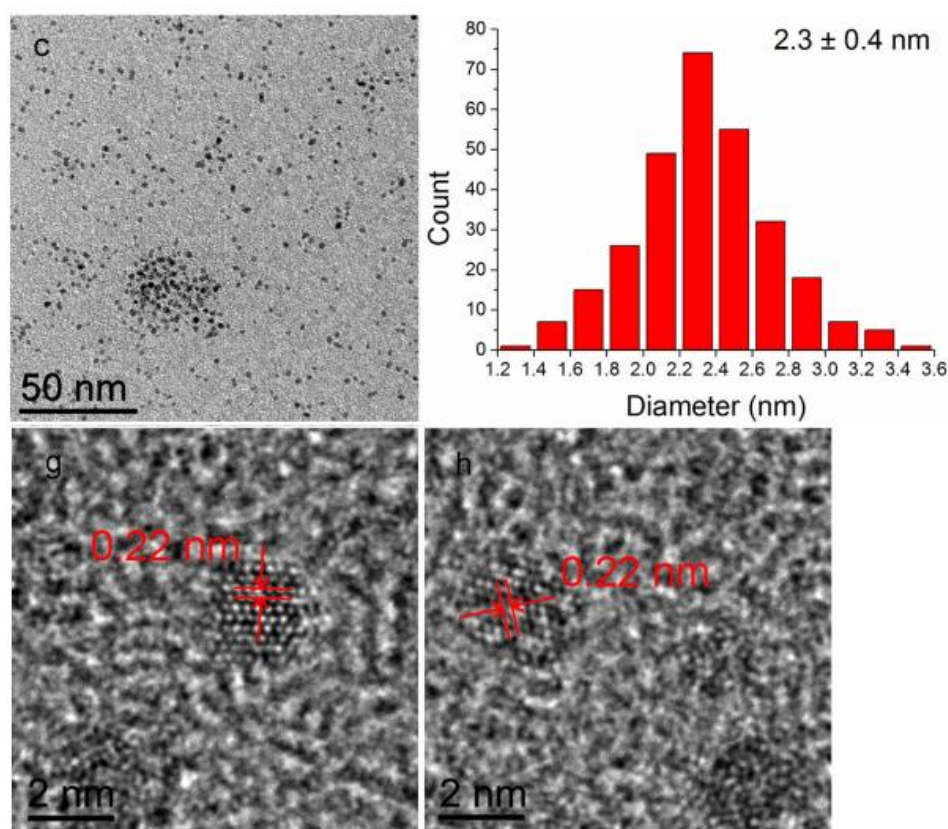
**Figure 3.77:** Oxidation of the PVP-stabilized Rh<sub>5</sub>Ni<sub>5</sub> NPs to obtain NiO<sub>x</sub> islands on Rh cores

The metal composition in Rh<sub>5</sub>Ni<sub>5</sub>/PVP NPs was first studied by elemental distribution analysis using STEM-EDX technique (Figure 3.78). Both Rh and Ni were found present in randomly selected individual NPs. Although the Rh/Ni ratio varied significantly in different particles (ranging from 1:0.57 to 2.35:1)<sup>85</sup> this result is a strong indication that the NPs are not a mixture of monometallic NPs and supports their bimetallic composition.



**Figure 3.78:** STEM images of  $\text{NiO}_x/\text{Rh}$  NPs with four randomly selected particles, and their corresponding EDX spectra, where Ni/Rh atomic ratios are shown.

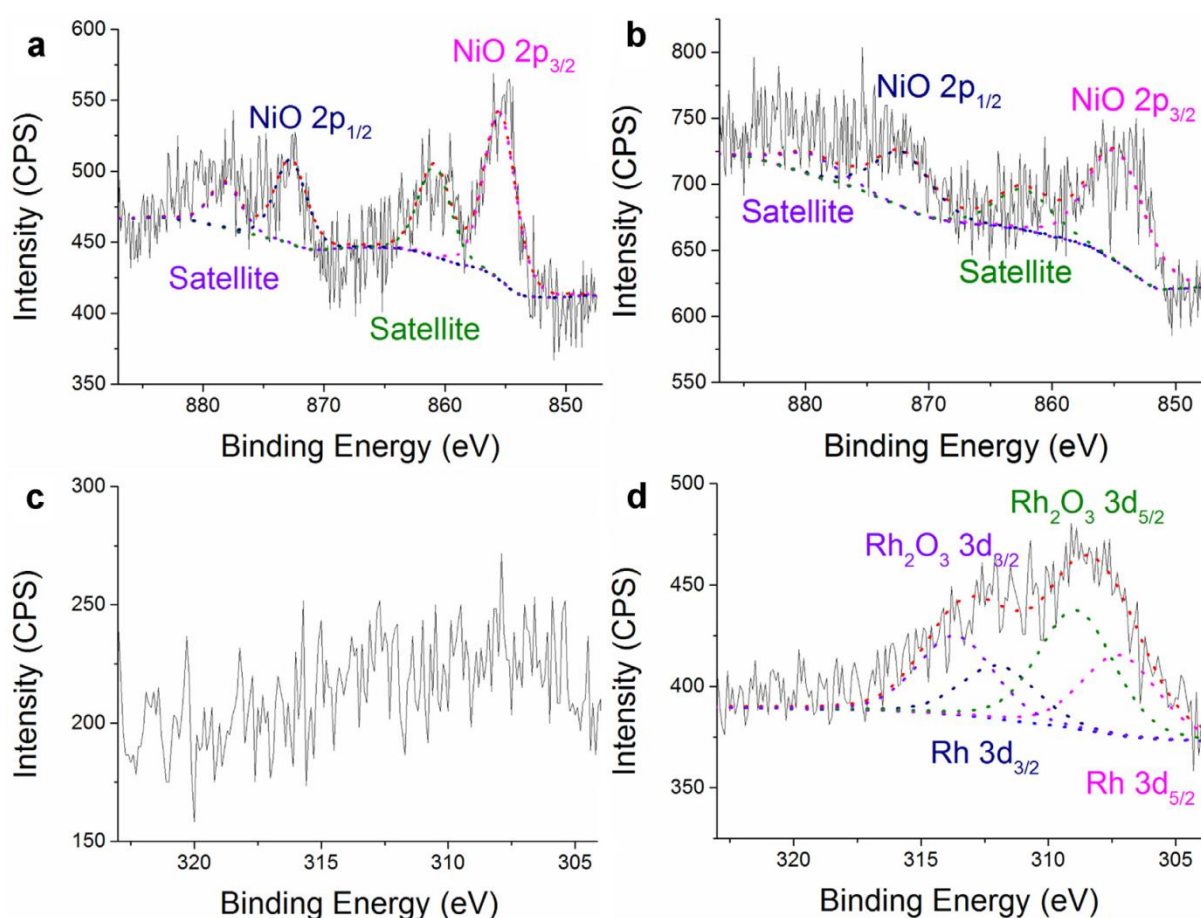
From the HRTEM images of oxidized Rh<sub>5</sub>Ni<sub>5</sub> NPs (Figure 3.79) it was clearly observed that the NPs are well-crystallized. Only an interplanar spacing of 0.22 nm was found, corresponding to (1 1 1) spacing of fcc Rh. Considering that at room temperature [Rh( $\eta^3$ -C<sub>3</sub>H<sub>5</sub>)<sub>3</sub>] is much more easily decomposed than [Ni(cod)<sub>2</sub>] and that the PVP-stabilized Rh<sub>5</sub>Ni<sub>5</sub> NP have a similar particle size ( $2.2 \pm 0.4$  nm, Figure 3.79) as RhPVP NPs ( $2.3 \pm 0.4$  nm, Chapter 2.1.1), it is plausible that during the synthesis of Rh<sub>5</sub>Ni<sub>5</sub> NPs, [Rh( $\eta^3$ -C<sub>3</sub>H<sub>5</sub>)<sub>3</sub>] underwent fast decomposition forming Rh NPs and then the Rh cores catalyzed the hydrogenation of cod into cyclooctane, inducing the decomposition of [Ni(cod)<sub>2</sub>] on the Rh cores surface. The co-decomposition procedure would have thus followed an *in situ* seed mediated growth mechanism, leading to the formation of Rh<sub>5</sub>Ni<sub>5</sub> NPs constituted of a core which is pure fcc Rh with a surface decorated with Ni. Such a structure makes the oxidation of nickel even easier when exposed to air, thus leading to RhNiO<sub>x</sub> NPs. NiO<sub>x</sub> islands could not be detected by HRTEM probably due to an amorphous structure.



**Figure 3.79:** TEM and HRTEM analysis of Rh/NiO<sub>x</sub> NPs with the corresponding size distribution histogram.

## III.2.3.1 XPS Analysis

X-ray Photoelectron Spectroscopy (XPS) was employed to investigate the electronic state and surface content of the NPs. The measurements were performed at Japan Synchrotron Radiation Research Institute, Hyogo, Japan, on a VG Escalab MKII spectrometer, using a mono Al  $K\alpha$  X-ray source ( $h\nu = 1486.71$  eV, 5 mA, 15 kV) and calibrated by setting the C 1s peak to 285.0 eV.



**Figure 3.80:** XPS spectra of (a) NiO<sub>x</sub>/Rh and (b) Ni NPs at Ni 2p region; (c) NiO<sub>x</sub>/Rh and (d) Rh NPs at Rh 3d region.

Figures 3.80a,b show the spectra for NiO<sub>x</sub>/Rh and Ni NPs for the Ni 2p region, the shift of the Ni 2p<sub>3/2</sub> peak to a higher energy of around 855 eV (compared with metallic Ni which has a binding energy of 852.7 eV) and the satellite peaks at around 862 eV are



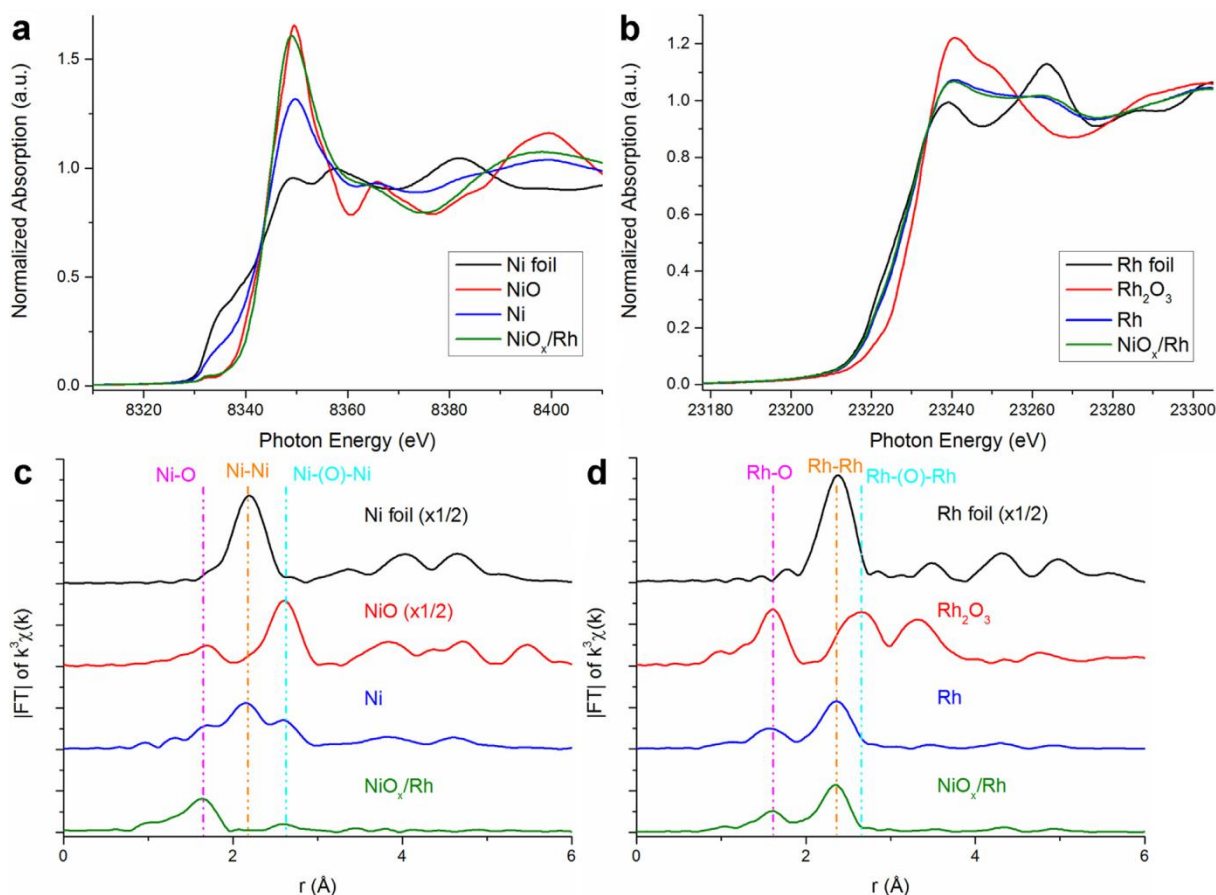
observed in both samples, indicating the oxidation of metallic Ni into NiO<sub>x</sub> as the result of NPs exposure to air.

Figures 3.80c,d show the original Rh 3d spectra for NiO<sub>x</sub>/Rh and Rh NPs, as well as the deconvolutions for Rh NPs. In addition to the peaks at 307.2 eV, assigned to the binding energy of 3d<sub>5/2</sub> for Rh(0), peaks at about 309 eV corresponding to Rh(III) can be seen in Rh NPs, indicating the existence of positively charged Rh. These peaks could belong to Rh atoms located on NP surface, which are commonly bearing certain positive charges.<sup>285</sup> Notably, the signal/noise ratio of the Rh spectrum for NiO<sub>x</sub>/Rh NPs was much lower than that of Rh NPs, which can be ascribed to the coverage of Rh core by Ni species in NiO<sub>x</sub>/Rh NPs.

By integration of the Ni 2p region and Rh 3d region spectra, a surface atoms ratio of Rh/Ni = 1/4 in NiO<sub>x</sub>/Rh NPs could be estimated, which is in good accordance with ca. 80% coverage from our model estimation.

### III.2.3.2 XAS Analysis

X-ray absorption spectroscopy was also used to study at atomic scale the electronic and geometric structure of the Rh-NiO<sub>x</sub> NPs in comparison with the pure Rh and Ni NPs. The Ni and Rh K-edge XAS measurements of NiO<sub>x</sub>/Rh, Ni NPs, Rh NPs and the reference samples (Ni foil, NiO, Rh foil, and Rh<sub>2</sub>O<sub>3</sub>) were recorded at the SPring-8 (Japan Synchrotron Radiation Research Institute, Hyogo, Japan) in the transmission mode at ambient temperature.



**Figure 3.81:** (a) Ni and (b) Rh K-edge XANES spectra of NiO<sub>x</sub>/Rh, Ni, and Rh NPs. Fourier transformed (c) Ni and (d) Rh K-edge EXAFS spectra of NiO<sub>x</sub>/Rh, Ni and Rh NPs. The spectra of Ni foil, Rh foil, NiO, and Rh<sub>2</sub>O<sub>3</sub> are included as references.

The Ni K-edge XANES spectra of NiO<sub>x</sub>/Rh and Ni NPs (Figure 3.81a) show that Ni in these NPs is mostly in oxidized form, in agreement with the XPS observation. The white line intensity of NiO<sub>x</sub>/Rh NPs is similar to the NiO reference, indicating that the Ni in NiO<sub>x</sub>/Rh NPs is almost fully oxidized. On the other hand, medium white line intensity is observed for Ni in pure Ni NPs, suggesting that pure Ni NPs contain a mixture of metallic Ni and nickel oxide. In NiO<sub>x</sub>/Rh NPs, the Ni on the surface of RhNi NPs could not form a multi-layered shell to prevent the oxidation of Ni in “inner layers”, therefore all Ni was oxidized. On the other hand, the core of monometallic Ni NPs was protected by the Ni oxide outer layer, and remained in the metallic state. The Rh K-edge spectra of NiO<sub>x</sub>/Rh and Rh NPs are compiled in Figure 3.81b. The absorption edge for Rh NPs is in between those of Rh foil and Rh<sub>2</sub>O<sub>3</sub>, indicating the existence of positive charged Rh, in accordance with the XPS analysis. Rh in NiO<sub>x</sub>/Rh is also partially oxidized, sharing an almost same XANES with Rh NPs. This again implies that the decoration of Rh NPs by NiO<sub>x</sub> did not substantially modify the electronic properties of Rh (Figure 3.81b).

Similar interpretation could be drawn according to the Fourier transformed EXAFS (Figure 3.81c,d). The main peak in the spectrum of Ni K-edge of NiO<sub>x</sub>/Rh NPs is at ca. 1.6 Å, corresponding well to Ni–O peak. Very limited contribution of Ni–Ni peak at 2.2 Å reveals that the surface Ni on Rh cores in NiO<sub>x</sub>/Rh NPs is fully oxidized. On the other hand, very similar EXAFS spectra in the spectra of Rh K-edge for Rh and RhNi NPs are observed, with similar portions of Rh–O peak at ca. 1.5 Å and Rh–Rh peak at ca. 2.3 Å. Furthermore, the EXAFS spectrum fitting was performed (check experimental part), and the derived structure parameters are compiled in (Table 3.7). For the Ni K-edge, the first shell for NiO<sub>x</sub>/Rh NPs, corresponding to Ni–O, showed a coordination number of 4.6, close to the bulk Ni–O standard, whereas the coordination number of the second shell dropped to only 3.7, which was much smaller as compared to bulk Ni–O standard, indicating the segments of NiO<sub>x</sub> on Rh core were in very small size. As compared to the bulk NiO standard, the NiO<sub>x</sub> species in NiO<sub>x</sub>/Rh NPs showed a shorter Ni–O distance (2.047 Å < 2.087 Å) and a longer Ni–(O)–Ni distance (3.020 Å > 2.952 Å). Moreover, the Debye Waller factor ( $\sigma^2$ ) for the fitting of the second shell Ni–Ni was quite large, meaning the structure was highly disordered. These results indicate that the surface NiO<sub>x</sub> might mostly exist as NiO<sub>6</sub> segments connected weakly by Ni–O–Ni connections. On the other side, the structure parameters for Ni NPs are in good accordance with the structure proposed before, where the Ni–Ni was origin from the metallic Ni core, and the Ni–O and Ni–(O)–Ni represented the oxidized surface. For both Rh and NiO<sub>x</sub>/Rh NPs at Rh K-edge, the data could be well-fitted with Rh–O Rh–Rh but without the Rh<sub>2</sub>O<sub>3</sub> characteristic Rh–Rh1 or Rh–Rh2, indicating metallic Rh cores for both samples and the oxygen atoms were only located on the surface (for Rh NPs) or the interface of NiO<sub>x</sub> and Rh core (for NiO<sub>x</sub>/Rh). Notably, the Rh–Ni was involved to get a better curve fitting for the NiO<sub>x</sub>/Rh sample, but the contribution was very low, with a coordination number of 0.6 only.

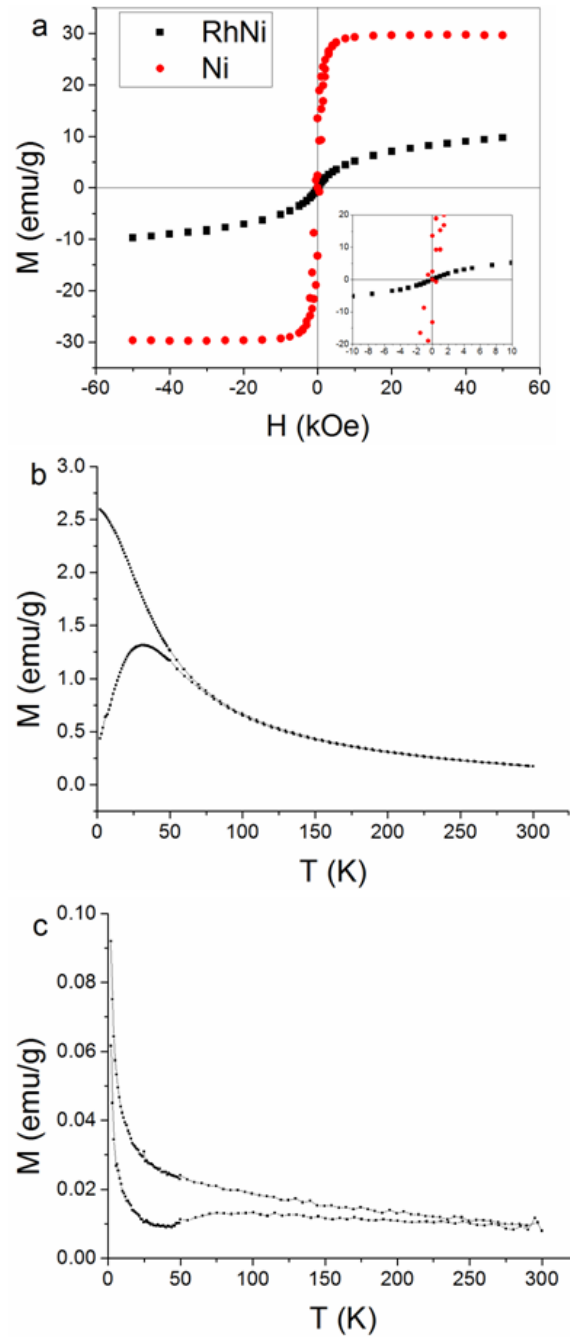
**Table 3.7:** Structure parameters by curve fitting of FT-EXAFS<sup>d</sup>.

			CN <sup>b</sup>	R (Å)	$\Delta E$ (eV)	$\sigma^2$ (Å <sup>2</sup> )	
Ni-K	NiO <sub>x</sub> /Rh NPs <sup>d</sup>	Ni–O	5.0 ± 0.3	2.047 ± 0.005	1.4 ± 0.9	0.0064 ± 0.0006	
		Ni–(O)–Ni	3.7 ± 2.1	3.020 ± 0.044	3.0 ± 5.1	0.0191 ± 0.0059	
	Ni NPs <sup>d</sup>	Ni–O	3.4 ± 0.6	2.046 ± 0.015	0.1 ± 1.8	0.0090 ± 0.0022	
		Ni–Ni	3.4 ± 0.6	2.468 ± 0.010	–3.3 ± 2.3	0.0068 ± 0.0010	
	Ni foil <sup>d</sup>	Ni–(O)–Ni	6.8 ± 1.2	2.957 ± 0.014	0.1 ± 1.8	0.0127 ± 0.0015	
		Ni–Ni	12 <sup>c</sup>	2.483 ± 0.002	–0.7 ± 0.0	0.0061 ± 0.0002	
		Ni–O	6 <sup>c</sup>	2.087 ± 0.002	1.5 ± 0.8	0.0061 ± 0.0009	
		Ni–(O)–Ni	12 <sup>c</sup>	2.952 ± 0.002	–	0.0062 ± 0.0004	
	Rh-K	NiO <sub>x</sub> /Rh NPs <sup>e</sup>	Rh–O	2.4 ± 0.4	2.021 ± 0.011	–3.1 ± 2.8	0.0047 ± 0.0011
			Rh–Ni	0.6 ± 0.3	2.576 ± 0.026	0.5 ± 5.2	0.0034 ± 0.0019
Rh NPs <sup>e</sup>		Rh–Rh	4.8 ± 0.9	2.655 ± 0.011	–5.0 ± 1.5	0.0080 ± 0.0011	
		Rh–O	2.5 ± 0.6	2.019 ± 0.015	–2.1 ± 3.6	0.0048 ± 0.0016	
Rh foil <sup>e</sup>		Rh–Rh	5.7 ± 0.6	2.677 ± 0.005	–5.0 ± 1.2	0.0075 ± 0.0006	
		Rh–Rh	12 <sup>c</sup>	2.688 ± 0.002	–4.1 ± 0.5	0.0042 ± 0.0002	
Rh <sub>2</sub> O <sub>3</sub> <sup>e</sup>		Rh–O	6 <sup>c</sup>	2.043 ± 0.015	1.0 ± 1.6	0.0030 ± 0.0007	
		Rh–Rh1	1 <sup>c</sup>	2.735 ± 0.020	–	0.0027 ± 0.0009	
		Rh–Rh2	3 <sup>c</sup>	3.010 ± 0.022	–	0.0033 ± 0.0005	

<sup>a</sup>Amplitude reduction factor of Ni and Rh were estimated from Ni foil, NiO, Rh foil and Rh<sub>2</sub>O<sub>3</sub> reference samples. <sup>b</sup>CN, coordination number. <sup>c</sup>Fixed when fitting. Curve fitting analyses were performed in the range 1.2–3.0d or 1.1–3.0e Å in R space.

### III.2.3.3 Magnetic Measurements

Since the obtained PVP-stabilized Ni and RhNi NPs showed magnetic properties upon exposure to exterior magnetic field, which could be of interest for catalyst recovering and recycling, we investigated the magnetic properties of the NiO<sub>x</sub>/Rh and Ni NPs by measuring by SQUID both the field dependent magnetization (M–H) and temperature dependent magnetization (ZFC-FC). This was performed at the LCC-Toulouse. In the magnetization curve M–H measured at 2 K (Figure 3.82a), Ni NPs exhibited ferromagnetic property, the magnetization of which increased sharply with increasing field, reaching saturation magnetization  $M_s$  of 30 emu/g at nearly 10 kOe. This is consistent with the reported Ni NPs prepared and measured under similar conditions.<sup>286</sup>



**Figure 3.82:** (a) Magnetization curve  $M$ – $H$  of  $\text{NiO}_x/\text{Rh}$  and Ni NPs measured at 2 K (inset: enlargement of low field). ZFC-FC curves for (b) Ni and (c)  $\text{NiO}_x/\text{Rh}$  NPs.

On the other hand,  $\text{NiO}_x/\text{Rh}$  NPs exhibited anti-ferromagnetic property, the magnetization of which did not reach saturation even when the field went up to 50 kOe, in good agreement with the reported NiO system.<sup>287-288</sup> For the ZFC-FC measurement, the samples were cooled to 2 K first, in the absence of magnetic field. Then a magnetic field of

10 Oe was induced, followed by measuring of the magnetization with increasing temperature to obtain the ZFC curves as shown in Figure 3.82b,c in the lower curves. Subsequently, the FC curves (Figure 3.82b,c, the upper curves) were obtained by cooling down the samples back to 2 K when keeping the external magnetic field. The two samples showed distinguished behaviors in the ZFC-FC measurements.

For Ni NPs (Figure 3.82b), the blocking temperature (TB) of about 31 K could be seen as the maximum point in ZFC curve, and a splitting temperature between ZFC and FC curves could be obtained at around 95 K, in good accordance with the reported observations on Ni NPs.<sup>289</sup> For NiO<sub>x</sub>/Rh NPs (Figure 3.82c), the low magnetization decreased with increasing temperature in both ZFC and FC curves, but no characteristic temperatures could be determined from the curves. This is believed to be due to the disordered and coordination unsaturated state of the NiO on the shell of NPs.<sup>288</sup>

#### III.2.3.4 Conclusion

Using the [Ni(cod)<sub>2</sub>] complex, several PVP and HDA-stabilized nickel nanoparticles samples were prepared under H<sub>2</sub> pressure at 65 °C. Obtained systems were well-controlled in size, and Ni NPs displayed magnetic properties consistent with the literature data. Next, syntheses of bimetallic RhNi nanoparticles were performed using the same stabilizers, with different metal ratios. Decomposition of both precursors occurred in a one pot synthesis at r.t. Profiting from the hydrogenating activity of Rh, the Ni precursor was easily decomposed without heating. We managed to obtain a range of different RhNi systems with different [Rh:Ni] ratios ([2:8], [5:5] and [8:2]). Small RhNi NPs with a size range between 1.5 and 2.2 nm were obtained with metal composition in good accordance with theoretical expected values as seen by TEM and EDX analysis, respectively.

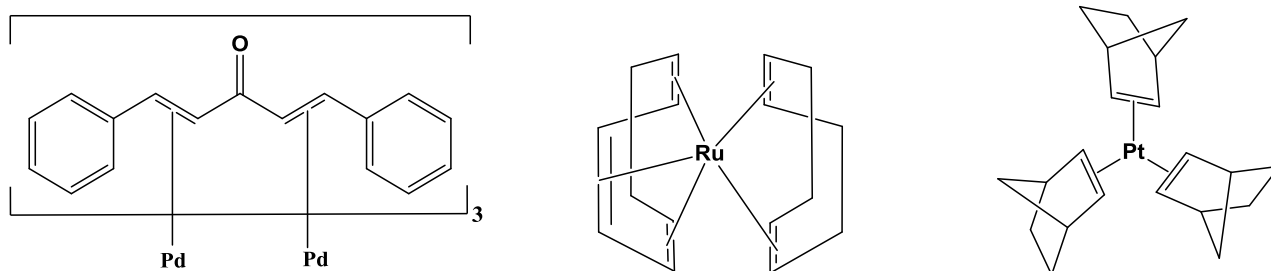
Given for our interest in synthesis of RhNiO<sub>x</sub> NPs, already synthesized PVP-stabilized RhNi BMNPs were exposed to air to oxidize the Ni islands on the NPs surface. TEM, HRTEM, ICP-OES, EDX, XPS, XAS and SQUID analysis results corroborated with each other, are a strong indication of the following key structural features for the obtained Rh, Ni and RhNiO<sub>x</sub> NPs stabilized by PVP: 1) Rh NPs are very small in size (2.3 nm), with surface being partially oxidized; 2) Ni NPs are considerably larger (6.5 nm) and display an oxidized surface; 3) RhNiO<sub>x</sub> NPs possess a Rh core (2.2 nm) with a similar mean size as pure Rh NPs.

A layer of highly disordered NiO<sub>x</sub> was evidenced on the Rh core, covering approximately 80% of surface sites and breaking up the terrace sites into small segments. The NiO<sub>x</sub> islands barely showed any electron interaction with the Rh core but purely as a modifier tuning surface geometric properties. As it will be seen hereafter, the catalytic data obtained in the hydrogenolysis of 1-benzyloxy-2-methoxy-benzene also support this proposed NiO<sub>x</sub>-decorated RhNPs structure, NiO<sub>x</sub>/Rh. (See Chapter IV)

### III.3 RhM Bimetallic Nanoparticles (M=Pd, Pt, Ru)

The association of Rh with another metal to form bimetallic NPs may result in different benefits. It is expected to obtain not a simple combination or enhancement of the properties associated with their monometallic counterparts, but many interesting new properties with a combination of multiple functions and broadened application fields. This may result from synergistic effects between the two metals since changing their components and morphologies may lead to relevant physical or chemical performances modified.<sup>290</sup> The particularity of noble metals in comparison to other elements is their profound electron structures, exhibiting irreplaceable advantages in the area of catalysis. Therefore it is of great interest to associate together noble metals to design new bimetallic noble nanostructures, and study their catalytic activities with the aim to determine the relationships between the properties and the sizes, compositions and structures of bimetallic NPs.

For this reason, and given successful results in the synthesis of RhNi BMNPs, we were interested in evaluate more the potential of the  $[\text{Rh}(\eta^3\text{-C}_3\text{H}_5)_3]$  complex in the synthesis of other bimetallic systems of nanoparticles. Previously used in the team, palladium, platinum and ruthenium organometallic complexes shown in Scheme 3.22 were selected to explore the formation of new bimetallic nano-systems. The main objective of this part of the PhD work was to probe synthesis tools for future projects in catalysis.



**Scheme 3.22:** Structures of  $[\text{Pd}_2(\text{dba})_3]$ ,  $[\text{Ru}(\text{cod})(\text{cot})]$  and  $[\text{Pt}(\text{nor})_3]$  complexes.

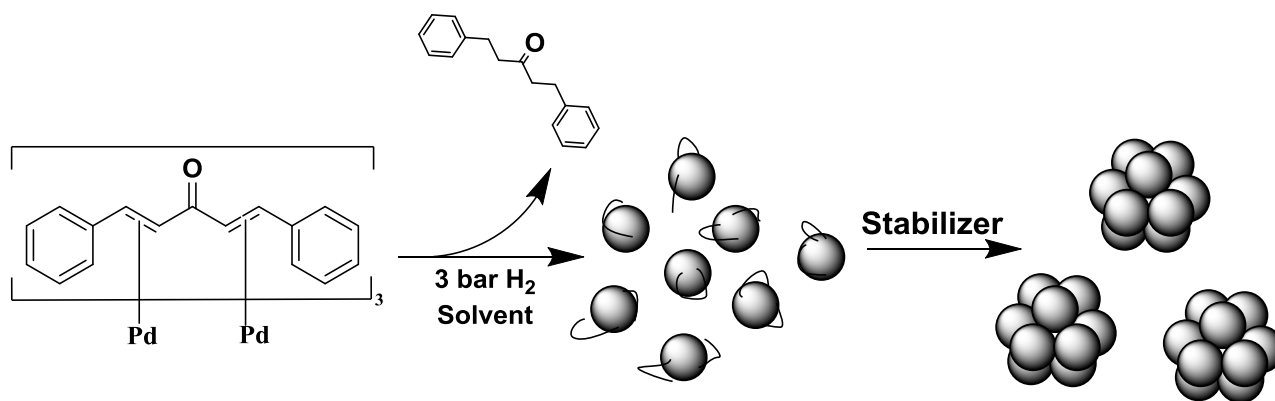


### III.3.1 RhPd System

Both palladium and rhodium are noble metals that are expected to crystallize in a face centered cubic (fcc) unit cell.<sup>291</sup> In literature, it has been reported that one of the main interests of RhPd alloy is that this material is capable of absorbing high levels of hydrogen upon pressure of gaseous dihydrogen,<sup>292-293</sup> which might be of great advantage for catalytic reactions of hydrogen capture.

Few examples in literature deal with the synthesis of bimetallic RhPd NPs. In the team, the synthesis of Pd NPs was previously investigated from the tris(dibenzylideneacetone)dipalladium(0)  $[\text{Pd}_2(\text{dba})_3]$  complex (Scheme 3.22) in the presence of several stabilizing agents like HDA,<sup>217</sup> PVP,<sup>294</sup> pyrazole ligands<sup>295</sup> ... for different catalytic applications.<sup>252,294-295</sup>

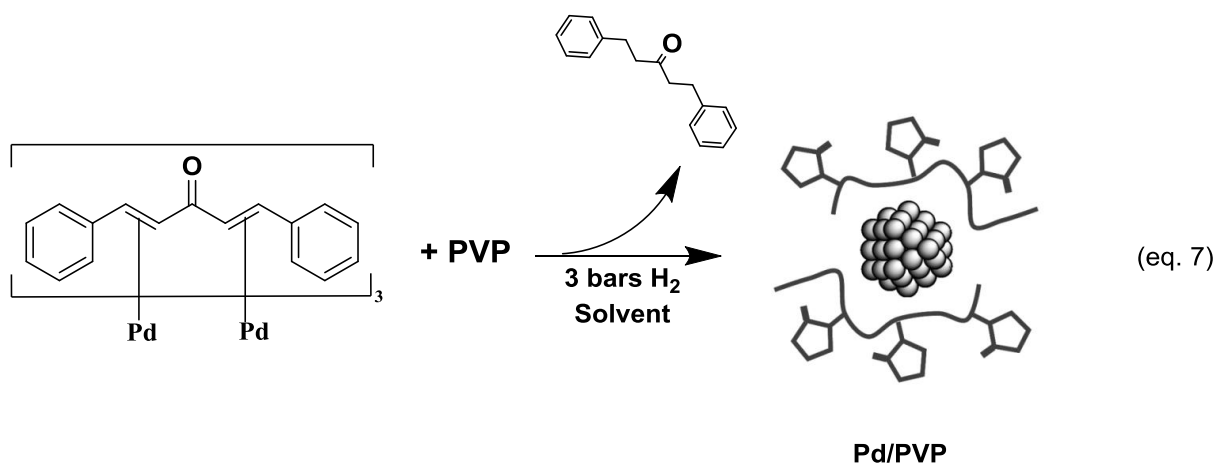
The  $[\text{Pd}_2(\text{dba})_3]$  complex is easily decomposed under dihydrogen pressure at room temperature, resulting in Pd NPs with different size range depending on the nature and the quantity of the stabilizer<sup>217</sup> (Scheme 3.23).



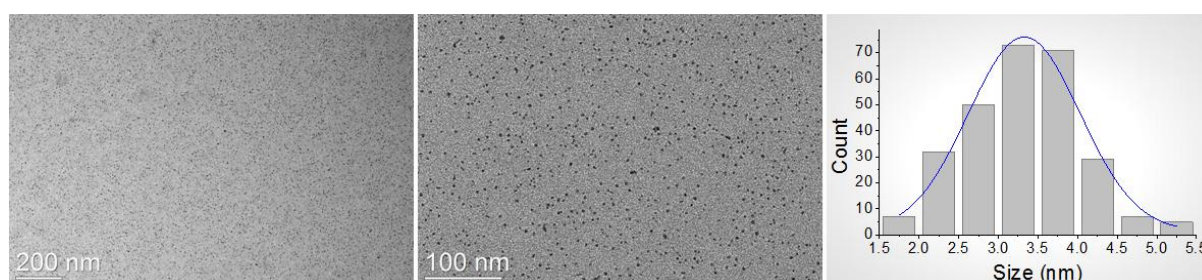
**Scheme 3.23:** Decomposition of tris(dibenzylideneacetone)dipalladium(0)  $[\text{Pd}_2(\text{dba})_3]$  complex following the organometallic approach.

## III.3.1.1 PVP-stabilized Pd NPs

Following our previous work with rhodium, investigation of the synthesis of PVP-stabilized Pd NPs was performed using 10 % wt. of the polymer compared to the metal (1/2 of the complex). Reaction proceeded at room temperature, and instantaneous change of color from dark red (red wine) to black occurred within a few minutes after applying 3 bar of H<sub>2</sub> (eq. 7). This change of color is an indication of the formation of Pd NPs.

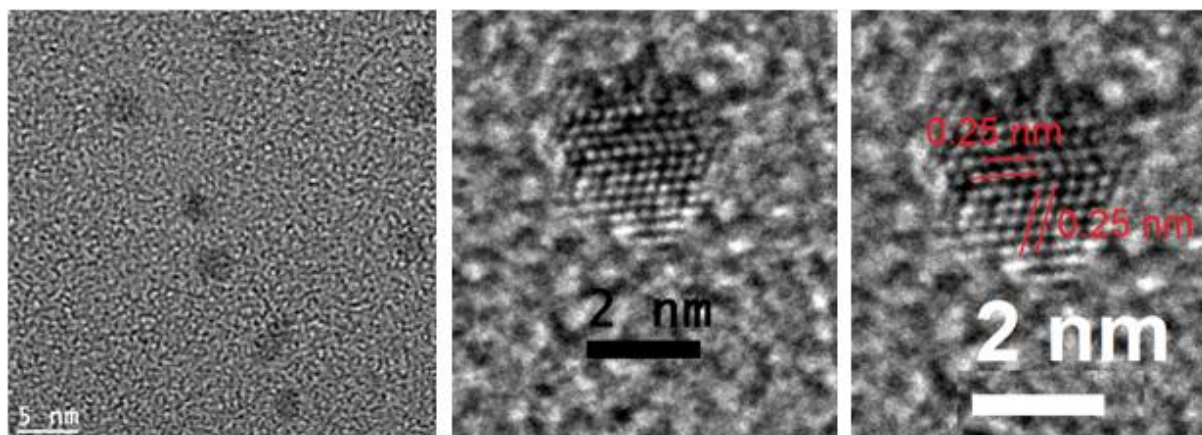


The black colloidal solution was found to be stable for several days, without precipitation or color change. Obtained NPs were analyzed by TEM showing the presence of well-controlled NPs with spherical shape, without any agglomeration (Figure 3.83). The calculated average size of the obtained NPs is around  $3.1 \pm 1.1$  nm.



**Figure 3.83:** TEM images of PVP-stabilized Pd NPs and their corresponding size distribution histogram.

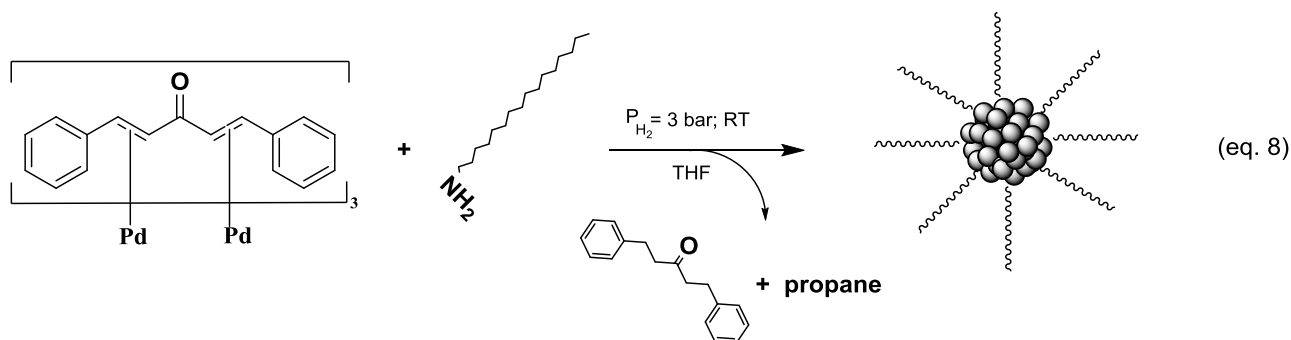
HRTEM analysis confirmed the size and the form of the particles and revealed that the Pd NPs are nicely crystalline, with one interplanar spacing of 0.25 nm that is in correspondence to fcc structure (Figure 3.84).

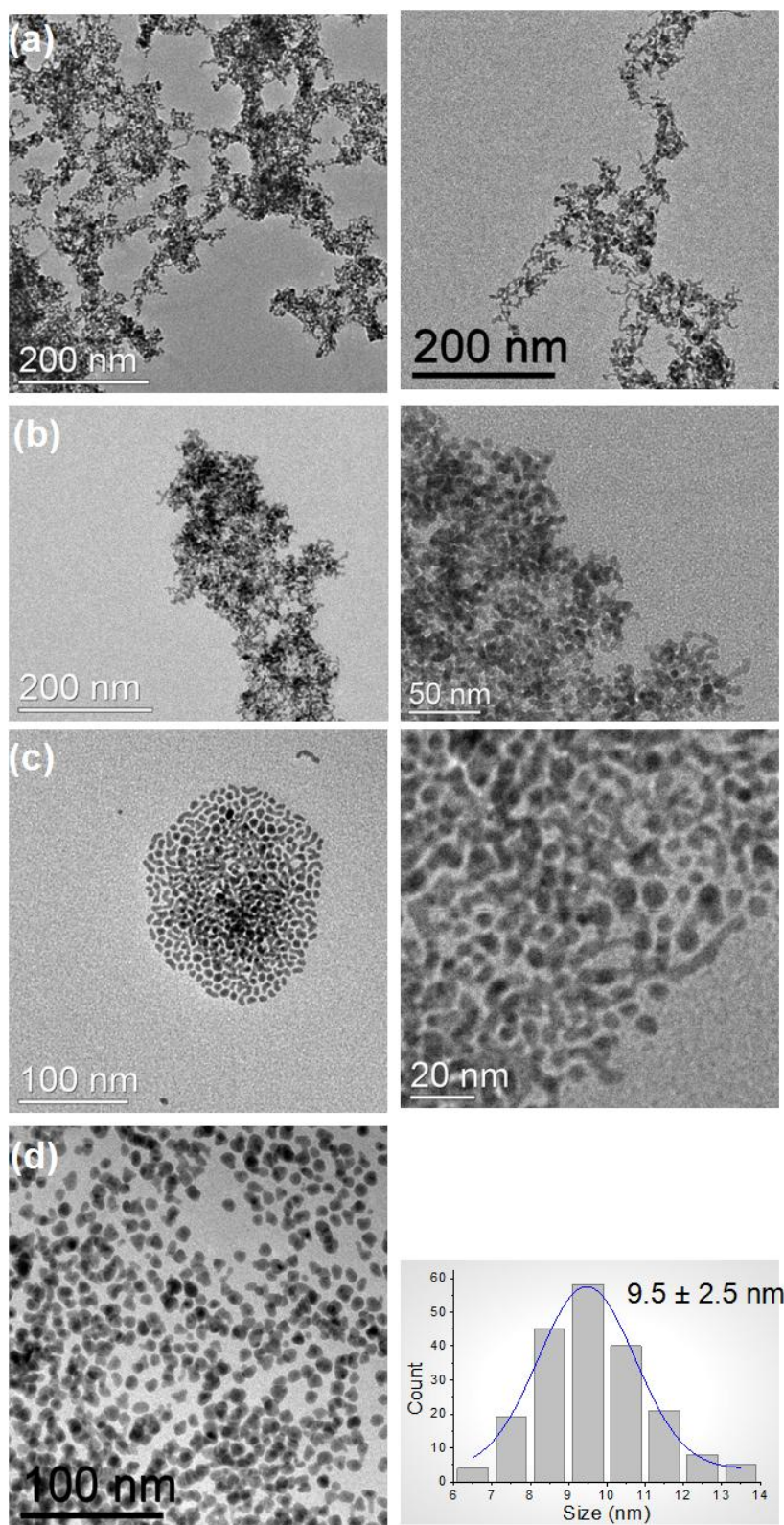


**Figure 3.84:** HRTEM images of PVP-stabilized Pd NPs.

### III.3.1.2 HDA-stabilized Pd NPs

Stabilization of Pd NPs with the weak coordinating ligand hexadecylamine (HDA) in THF was also performed (eq. 8). Different ratios of  $[M]/[L]$  resulted in different sizes of Pd NPs, where smaller and more dispersed particles were obtained with higher quantities of HDA. Synthesis with 1, 2, 5, and 10 molar equivalents of HDA were performed to achieve a series of different Pd particles as shown in Figure 3.85.



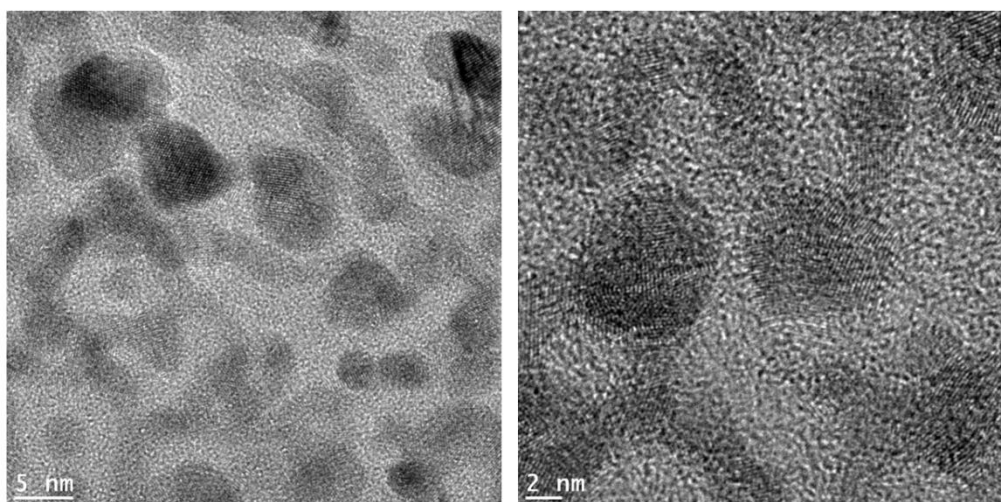


**Figure 3.85:** TEM images of Pd NPs stabilized with (a) 1, (b) 2, (c) 5, and (d) 10 molar equivalents of HDA.

Pd NPs stabilized with 1 and 2 equivalents of HDA (Figure 3.85a, b) are agglomerated all over the grid; although with 2 equivalents of HDA a pattern of smaller particles seems to form the large agglomerates. Raising the stabilizer agent quantity up to 5

equivalents results in more shape- and size-controlled particles (Figure 3.85c) with non homogeneous elongated forms that are organized in colonies. The use of 10 molar equivalents of HDA resulted in the formation of smaller and well-controlled Pd particles having a spherical shape and no agglomeration was observed all over the grid. The obtained particles have a mean size range of  $9.5 \pm 2.5$  nm.

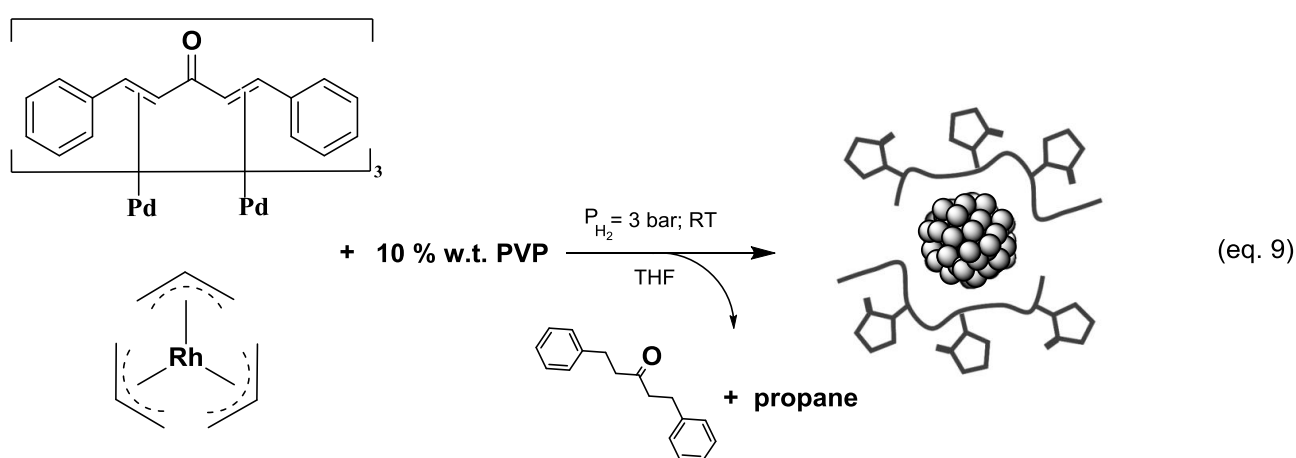
HRTEM analysis of Pd NPs stabilized with 5 molar equivalents of HDA was performed since this quantity of stabilizing agent was set to be the standard value in the synthesis of the bimetallic systems. Elongated in shape particles were found to be well-crystallized (Figure 3.86).



***Figure 3.86:*** HRTEM images of Pd NPs stabilized with 5 eq. of HDA.

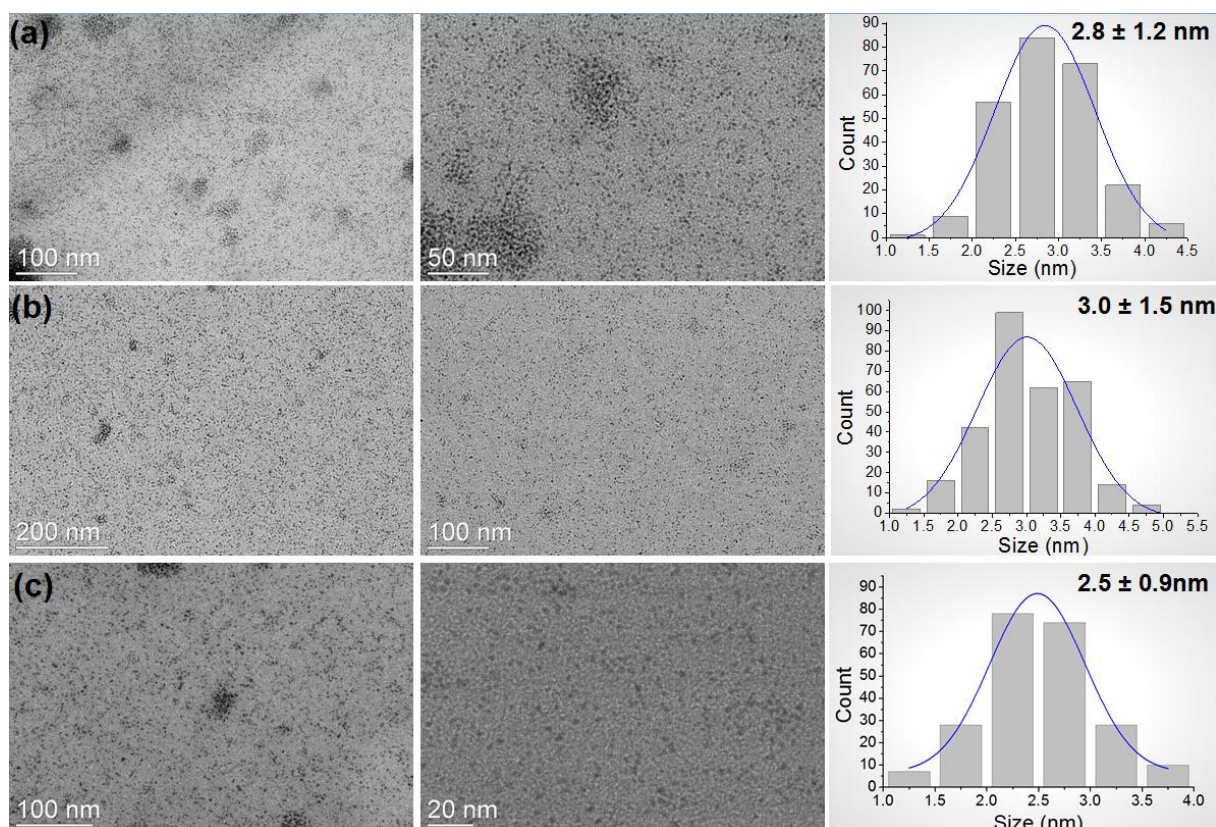
## III.3.1.3 PVP-stabilized RhPd NPs

The one pot synthesis of PVP-stabilized RhPd NPs was performed following the reaction conditions reported in eq. 9. 10 % weight to metal of the PVP polymer was dissolved in THF solution and added to a mixture of the two metal precursors. The reaction was pressurized with dihydrogen (3 bar) overnight at r.t. Different [Rh]/[Pd] ratios were studied as follows: Rh<sub>2</sub>Pd<sub>8</sub>, Rh<sub>5</sub>Pd<sub>5</sub>, and Rh<sub>8</sub>Pd<sub>2</sub>. Change of color in reactions was instantaneous and evidenced the formation of NPs. The presence of both metals in the formed nanoparticles was attested by ICP-AES and EDX analyses.



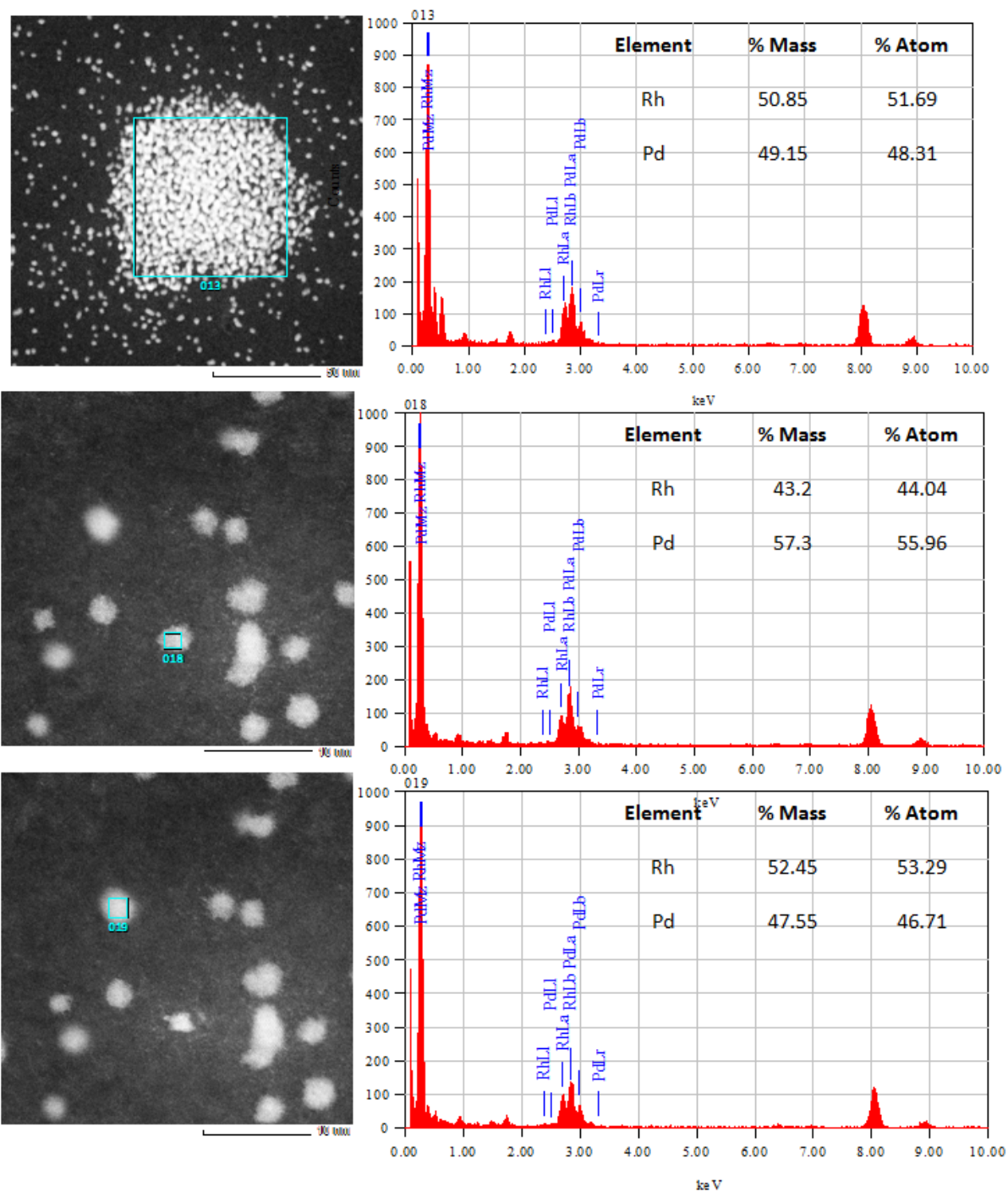
TEM analysis of the crude black colloidal solutions (Figure 3.87) showed well-controlled small NPs with a spherical shape. The mean size range for the three systems of NPs prepared varies from 2.5 to 3 nm.

ICP-AES analysis was performed to determine the resulting metal contents for the three systems or RhPd NPs, after their purification by precipitating with cold pentane and centrifuging. The results are presented in Table 3.8. Obtained values show very high accordance with a small error range when comparing experimental and theoretical data, which strongly supports that the applied reaction conditions allowed the full decomposition of the two metal precursors.



**Figure 3.87:** TEM images of PVP-stabilized (a)  $Rh_2Pd_8$ , (b)  $Rh_5Pd_5$ , and (c)  $Rh_8Pd_2$  with their corresponding size distribution histograms.

STEM-HAADF analysis was performed using a JEM-ARM200F transmission electron microscope which affords high resolution by atom imaging in addition to the atom-to-atom chemical mapping (Figure 3.88). Obtained images are accompanied with quantitative EDX analysis showing the present elements in addition to mass and atomic percentages of Rh and Pd metals. Analysis over both single and a group of PVP-stabilized  $Rh_5Pd_5$  NPs revealed the presence of both metals in a ratio very close to 50/50. This result is in accordance with the expected theoretical value which confirms the formation of RhPd NPs that have the target metal composition, mainly RhPd 50/50.

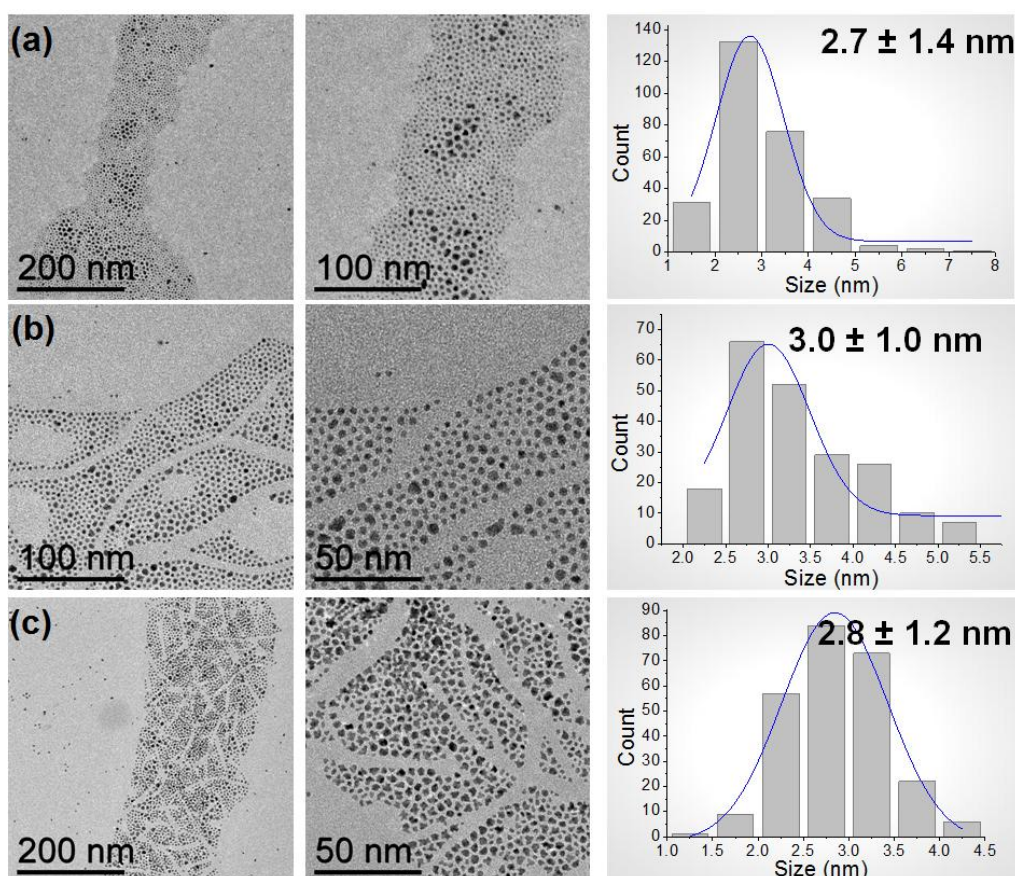


**Figure 3.88:** STEM-HAADF images, EDX and metal contents of PVP-stabilized  $Rh_5Pd_5$ .



## III.3.1.4 HDA-stabilized RhPd NPs

The synthesis of bimetallic RhPd NPs ( $\text{Rh}_2\text{Pd}_8$ ,  $\text{Rh}_5\text{Pd}_5$  and  $\text{Rh}_8\text{Pd}_2$ ) was carried out at r.t. under 3 bar  $\text{H}_2$  with 5 molar equivalents of HDA (eq. 8). Small NPs with a size range between 2.7 and 3 nm were observed by TEM (Figure 3.89). Although monometallic HDA-stabilized Pd NPs were not very well-controlled and molar equivalents up to 10 were needed to achieve better controlled but large 9.5 nm particles, and that monometallic Rh/HDA NPs also showed a size between 3.5 and 5.5 nm, the co-decomposition of  $[\text{Rh}(\eta^3\text{-C}_3\text{H}_5)_3]$  and  $[\text{Pd}_2(\text{dba})_3]$  resulted in the formation of smaller, more uniform and well-dispersed particles. ICP-AES analysis allowed to determine the metal composition of the particles after their purification by precipitation with cold pentane and centrifuging. Here again a relatively good accordance between expected theoretical values and experimental ones was observed. Thus, co-decomposition of  $[\text{Rh}(\eta^3\text{-C}_3\text{H}_5)_3]$  and  $[\text{Pd}_2(\text{dba})_3]$  complexes in the applied conditions leads easily to RhPd NPs of selected composition.



**Figure 3.89:** TEM images of HDA (5 eq.) stabilized (a)  $\text{Rh}_2\text{Pd}_8$ , (b)  $\text{Rh}_5\text{Pd}_5$ , and (c)  $\text{Rh}_8\text{Pd}_2$  with their corresponding size distribution histograms.

Table 3.8 provides a summary of the different RhPd NPs that were synthesized using PVP and HDA as stabilizers. Both mono- and bimetallic PVP-stabilized NPs were found to be well-dispersed with a small mean size between 2 and 3 nm, and their metal contents were

in coherence with the theoretical expected ones. For HDA-stabilized NPs, although the monometallic Rh and Pd particles are not of small size neither well-controlled, the combination of the two metals resulted in well-dispersed and well-controlled particles with a size range between 2.7 and 5 nm. Concerning the metal compositions measured by ICP-AES analysis, they indicate a good coherence between theoretical and experimental values. For both PVP- and HDA-stabilized NPs systems. The two metal precursors are well-decomposed under the applied reaction conditions and allow the formation of bimetallic NPs whose structure is not defined yet. More analytical work is necessary to complete this question.

**Table 3.8:** Summary of synthesized Rh, Pd and RhPd BMNPs with their corresponding average sizes, and the Rh and Pd metal content in each system.

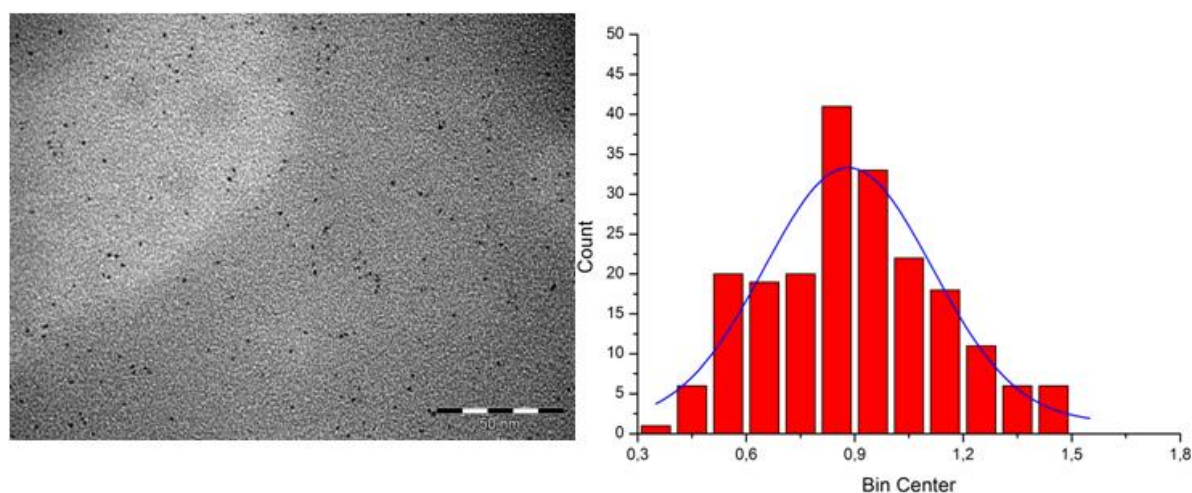
Nanoparticles	Stabilizer	Size (nm)	wt. % of Rh	wt. % of Pd	Rh/Pd (mol/mol)
Rh	PVP (10 eq.)	2.2 ± 0.9	14.9	---	1:0
Pd	PVP (10 eq.)	3.1 ± 1.1	---	6.22	0:1
Rh <sub>2</sub> Pd <sub>8</sub>	PVP (10 eq.)	2.8 ± 1.2	1.57	5.88	0.27:1
Rh <sub>5</sub> Pd <sub>5</sub>	PVP (10 eq.)	3.0 ± 1.5	3.84	4.28	0.95 :1
Rh <sub>8</sub> Pd <sub>2</sub>	PVP (10 eq.)	2.5 ± 0.9	5.95	1.69	1:0.27
Rh	HDA (1 eq.)	5.2 ± 3.2	22.7	---	1:0
Rh	HDA (2 eq.)	3.8 ± 1.1	16.6	---	1:0
Rh	HDA (5 eq.)	3.7 ± 1.1	8.06	---	1:0
Pd	HDA (1 eq.)	xx*	---	11.9	0:1
Pd	HDA (2 eq.)	xx*	---	9.2	0:1
Pd	HDA (5 eq.)	xx*	---	5.4	0:1
Pd	HDA (10 eq.)	9.5 ± 2.5	---	3.87	0:1
Rh <sub>2</sub> Pd <sub>8</sub>	HDA (5 eq.)	2.7 ± 1.4	0.95	4.66	0.21:1
Rh <sub>5</sub> Pd <sub>5</sub>	HDA (5 eq.)	3.0 ± 1	2.87	3.2	0.94:1
Rh <sub>8</sub> Pd <sub>2</sub>	HDA (5 eq.)	2.8 ± 1.2	5.74	1.41	1:0.18

\*agglomerated NPs with non-uniform shape.

Under the framework of a collaborative project with Dr. Esther Ramírez Meneses and Dr. Miguel Antonio Domínguez Crespo in Mexico, the series of PVP- and HDA-stabilized Rh, Ni, Pd and the bimetallic RhNi and RhPd ones are presently under evaluation as catalysts in fuel cells for the catalytic methanol oxidation reaction.

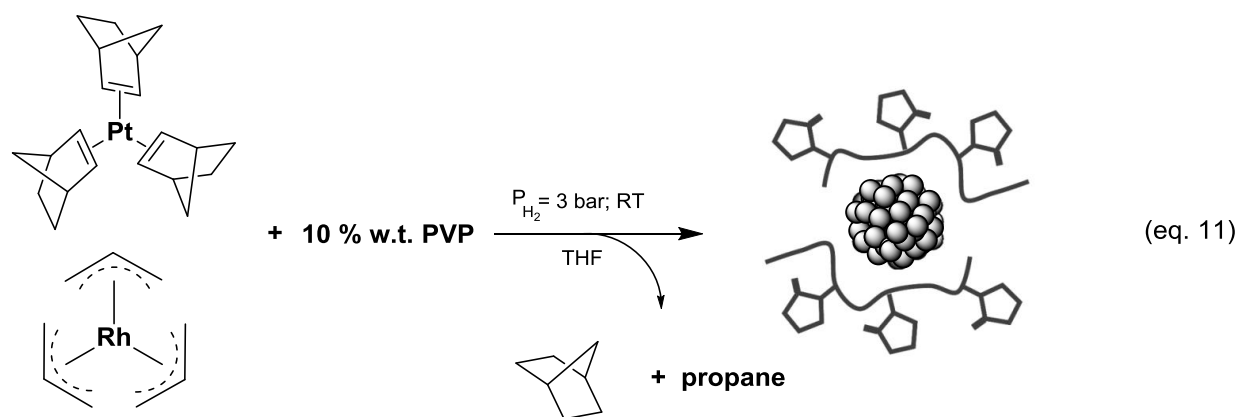
### III.3.2 RhPt System

In order to investigate the potential of the  $[\text{Rh}(\eta^3\text{-C}_3\text{H}_5)_3]$  precursor in synthesizing RhPt bimetallic nanoparticles, we tested the  $[\text{Pt}(\text{nor})_3]$  complex under dihydrogen decomposition conditions. This platinum complex is light sensitive. Under dihydrogen pressure releasing of naked Pt atoms and production of norbornane as a byproduct are expected. Mixing the  $[\text{Pt}(\text{nor})_3]$  complex with a THF solution of PVP, and pressurizing with 3 bar of  $\text{H}_2$  allowed the colorless solution to become black rapidly indicating the easy formation of NPs. From TEM analysis (Figure 3.90), the obtained Pt NPs are well-dispersed and small in size with a mean size of  $0.9 \pm 0.5$  nm.

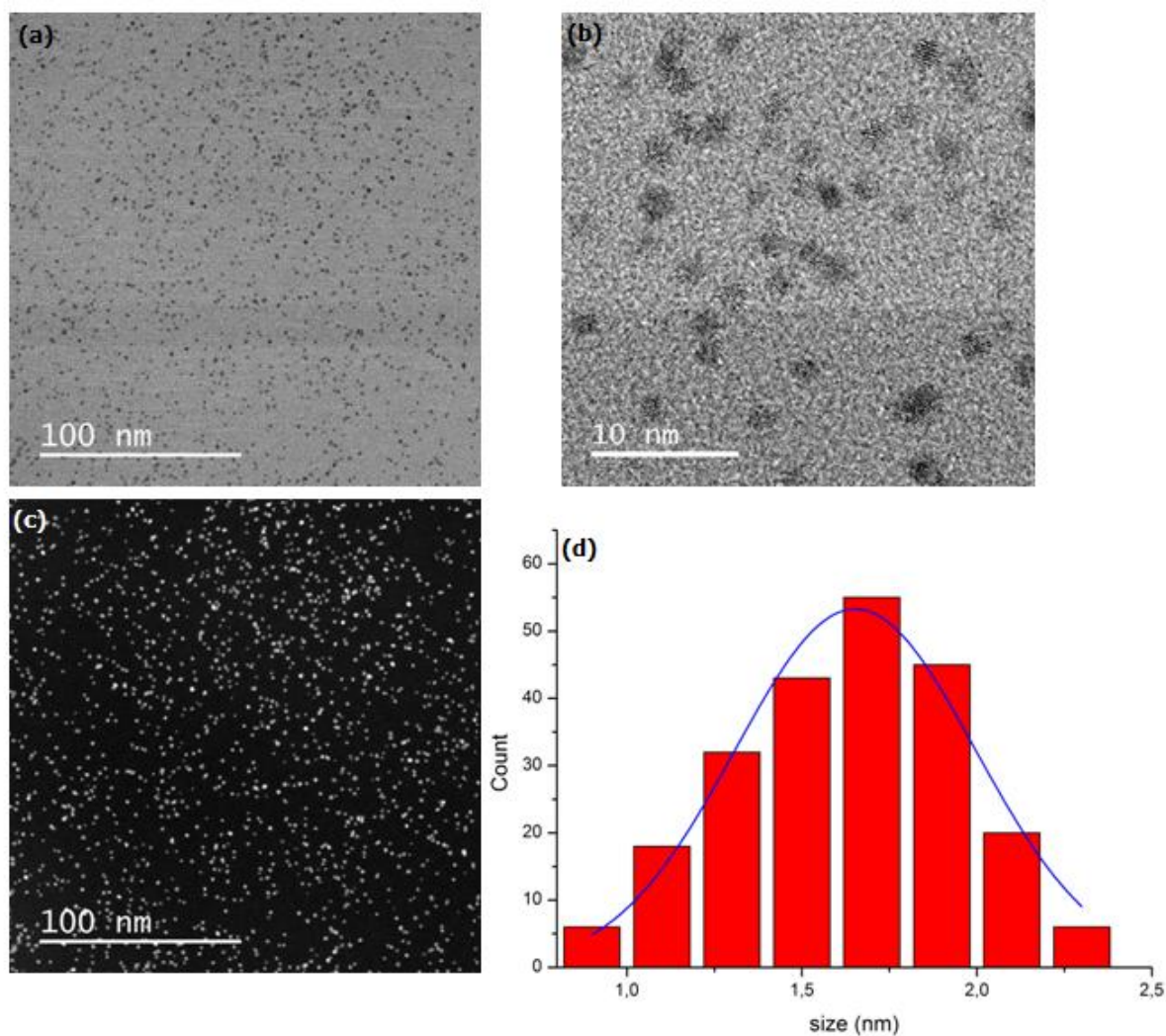


**Figure 3.90:** TEM image of PVP-stabilized Pt NPs with the corresponding size histogram.

Since both  $[\text{Pt}(\text{nor})_3]$  and  $[\text{Rh}(\eta^3\text{-C}_3\text{H}_5)_3]$  complexes result in small and well-controlled NPs with 10 % w.t. of PVP, we set to use the same stabilizer in same quantity to prepare PVP-stabilized RhPt NPs with a 50/50 metal ratio. The reaction was performed at r.t., where the two precursors were added to a Fischer Porter vessel and mixed with the THF solution of PVP. The glassware was pressurized with 3 bar of  $\text{H}_2$  which caused the pale yellow solution become black in less than 10 minutes (eq. 11), indicating the rapid formation of NPs. To insure full decomposition of both precursors the reaction was kept under the same conditions for 16h.



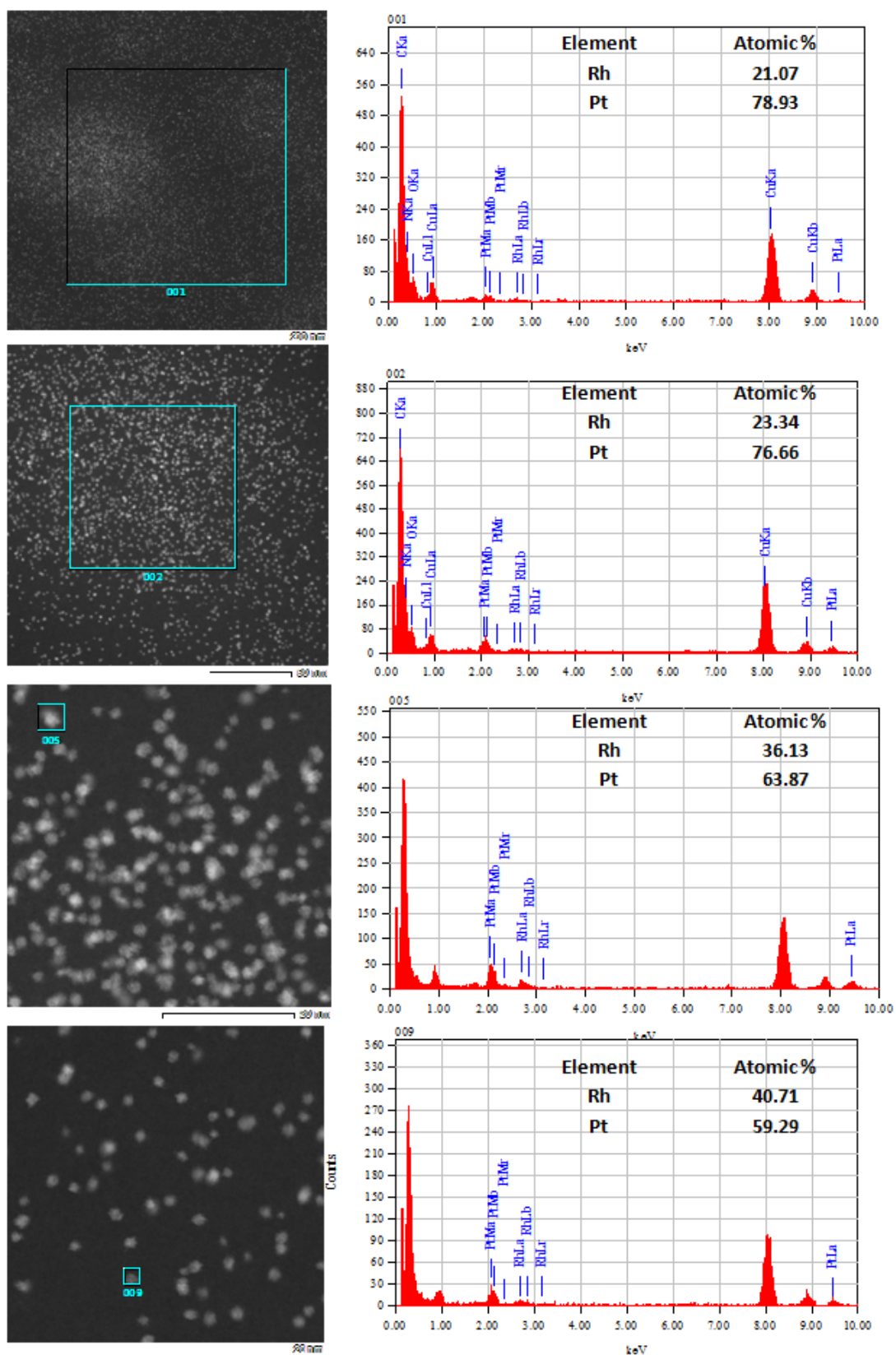
A drop of the colloidal solution was then dispersed over a carbon grid and introduced into a JEM-ARM200F transmission electron microscope which affords high resolution by atom imaging in addition to the atom-to-atom chemical mapping. STEM-HAADF analysis was also employed to overcome the polymer matrix effect; the chemical contrast allows the distinguishing of elements with higher Z number (Figure 3.91c). Obtained images reveal the presence of spherical, small, and well-dispersed NPs with a mean size of  $1.7 \pm 0.7$  nm. Although crystalline domains were visible through the high resolution TEM images, exact evaluation of the crystallinity of the particles was difficult to identify due to the important influence of the polymer.



**Figure 3.91:** (a) TEM, (b) HRTEM, (c) and HAADF-STEM images of PVP-stabilized  $Rh_{50}Pt_{50}$  NPs with (d) the corresponding size histogram.

EDX analysis technique that is associated with the JEM-ARM200F transmission electron microscope was also used for chemical characterization of the particles. Targeting large areas on the grid allowed to evaluate the decomposition of both of the metal precursors, and targeting individual particles confirmed the presence of either bimetallic or two monometallic systems. Also, profiting from the quantitative elemental analysis we could acquire information on the metal ratios in the sample. Analysis on large areas of the copper grid revealed the presence of both Rh and Pt metals with a ratio of Pt/Rh around 3/1 (Figure 3.92). Targeting over 15 individual particles revealed that in all the cases, the particles contain both Rh and Pt metals thus indicating the success in synthesizing bimetallic PVP-stabilized RhPt NPs. Nevertheless, the ratio of the two metals is not as expected, with a

dominant percentage of Pt over the Rh. The percentage of Rh indeed varied from 20 to 40%. These results indicate that  $[\text{Rh}(\eta^3\text{-C}_3\text{H}_5)_3]$  and  $[\text{Pt}(\text{nor})_3]$  complexes can be used to prepare RhPt bimetallic NPs. The discrepancy observed in the  $[\text{Rh}]/[\text{Pt}]$  metal ratio compared to expected theoretical values, evidences that the reaction conditions probably need some adjustments to get precisely a target composition as 50/50 for example. The  $[\text{Pt}(\text{nor})_3]$  complex is decomposed more rapidly than the  $[\text{Rh}(\eta^3\text{-C}_3\text{H}_5)_3]$  one which may explain the higher ratio of Pt in the obtained RhPt NPs. A door is opened but more work is necessary to find better reaction conditions in order to get RhPt NPs having a desired metal composition.

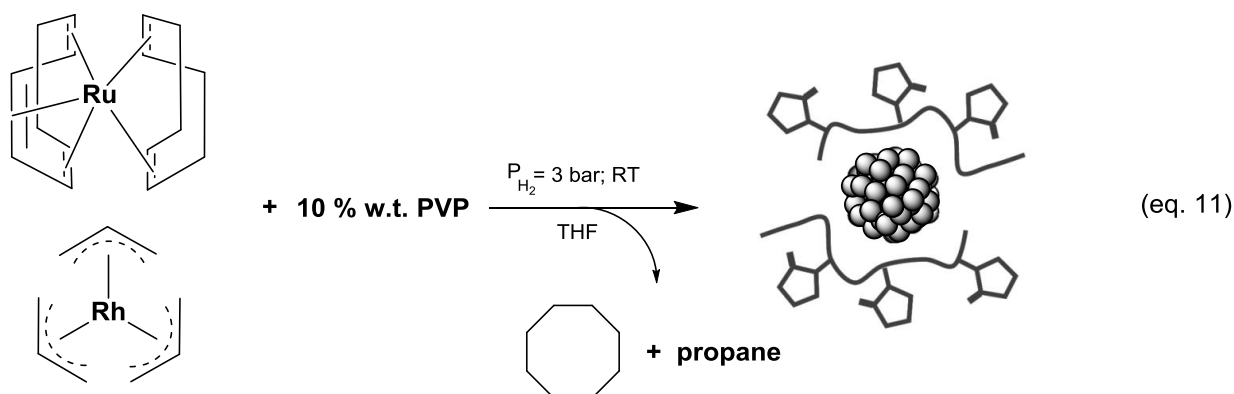


**Figure 3.92:** EDX analysis of PVP-stabilized Rh<sub>50</sub>Pt<sub>50</sub> NPs with quantitative metal ratios.

### III.3.3 RhRu System

For the same objective of widening the RhM bimetallic nanoparticles library, we studied the integration of ruthenium metal with the rhodium following the organometallic approach by using the  $[\text{Ru}(\text{cod})(\text{cot})]$  complex with the  $[\text{Rh}(\eta^3\text{-C}_3\text{H}_5)_3]$ . This ruthenium precursor is widely used in the team for developing mono- and bimetallic Ru NPs.<sup>71,216,226,258,296-297</sup> It decomposes easily under dihydrogen pressure at r.t.. Ideally each molecule of the complex releases one naked Ru atom and two cyclooctane molecules which are inert toward the metal surface.

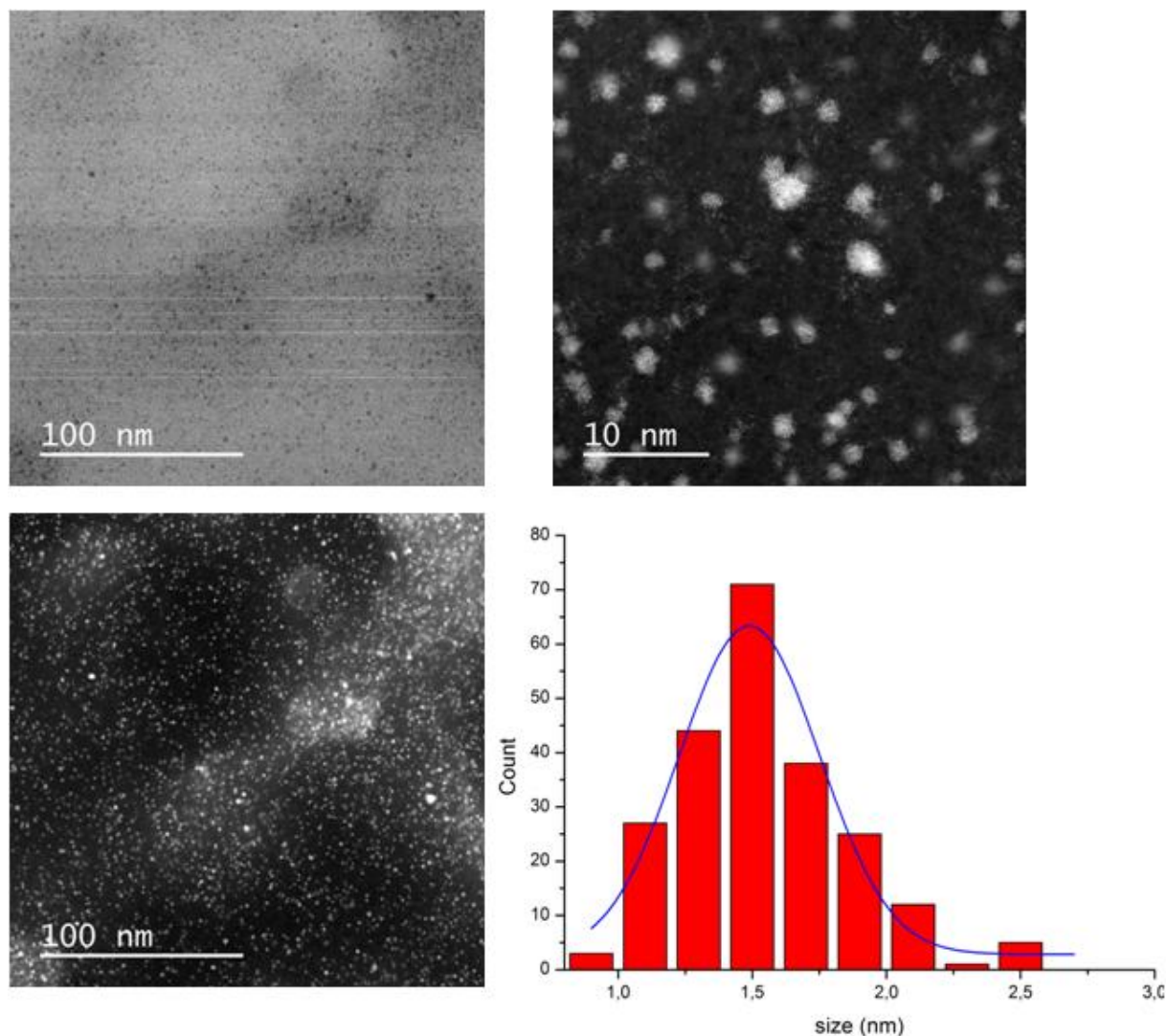
The synthesis of pure PVP-stabilized Ru NPs<sup>71,297</sup> revealed that at room temperature and 3 bar of  $\text{H}_2$ ,  $[\text{Ru}(\text{cod})(\text{cot})]$  complex decomposes to give small well crystalline NPs with a mean size of  $1.3 \pm 0.2$  nm. Therefore, for the synthesis of a bimetallic system of RhRu NPs, we employed 10 % wt. of PVP as a stabilizer and a 50/50 metal ratio. Synthesis was performed at r.t. under 3 bar of dihydrogen according to eq. 11. Formation of nanoparticles was confirmed by the rapid change of color from yellow to black within a couple of minutes, but the reaction was kept for 16 h to insure complete decomposition of the precursors.



Transmission electron microscopy of the crude solution revealed the formation of spherical, well-dispersed particles with a mean size of  $1.5 \pm 0.5$  nm (Figure 3.93). Although crystalline domains were visible with some individual particles at high resolution mode, we could not retrieve detailed information about the crystalline structure of the obtained nanoparticles due to the effect of the polymer. Indeed, it was clearly visible that the particles are strongly embedded inside a thick matrix, which caused difficulties in focusing the microscope. Again STEM-HAADF technique helped to circumvent the polymer effect, and



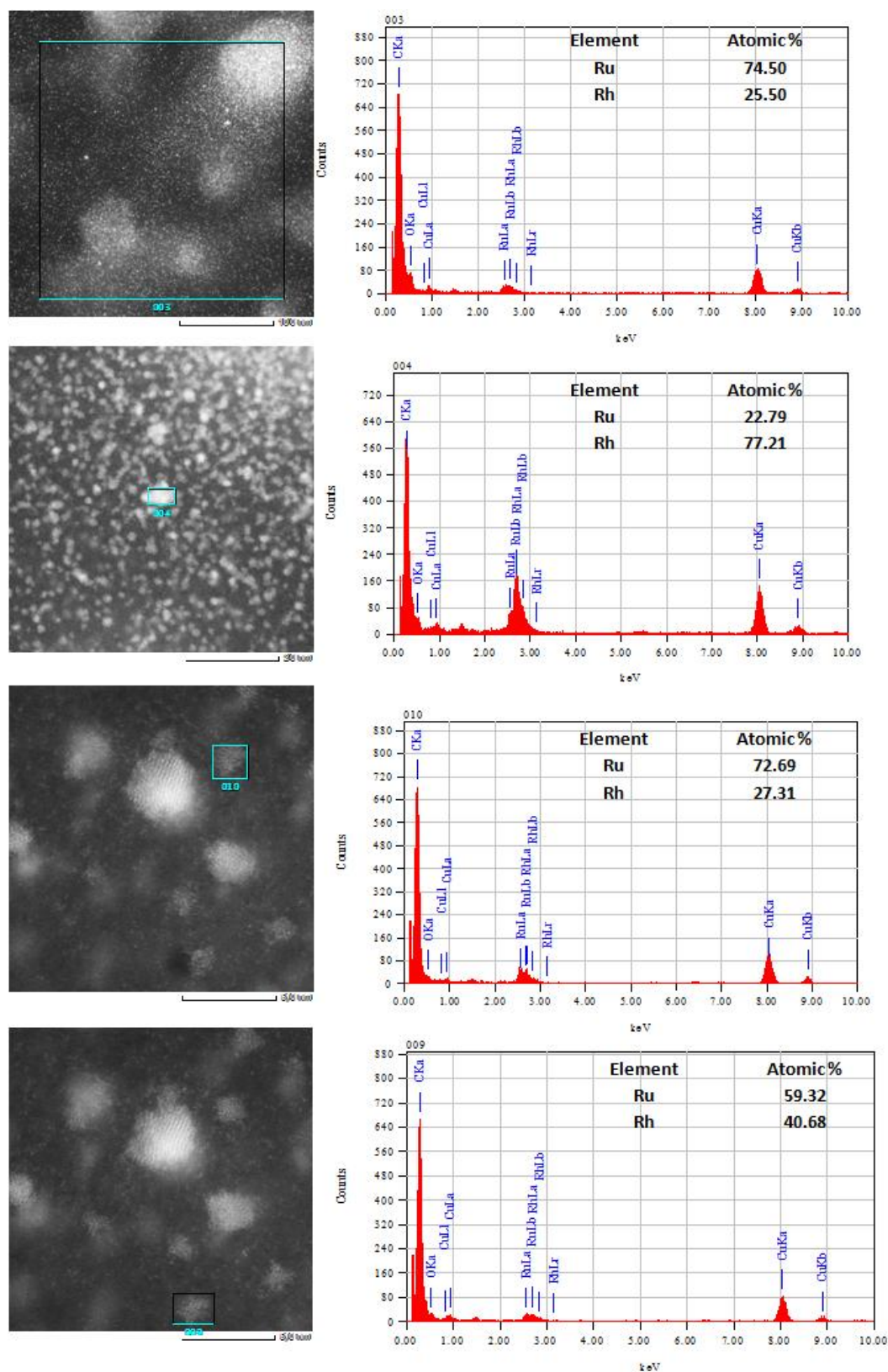
highlighted the chemical contrast of the metal content which facilitated sighting and counting of the particles.



**Figure 3.93:** TEM, and HRTEM HAADF-STEM images of PVP-stabilized  $Rh_{50}Ru_{50}$  NPs with the corresponding size histogram.

EDX analysis was applied to evaluate the composition of the nanoparticles through quantitative elemental analysis (Figure 3.94). Targeting a large area of the TEM grid revealed the presence of both rhodium and ruthenium with a ratio around 3/1 of Ru/Rh, a value being far from the expected 1/1 theoretical ratio. But, when targeting several individual particles,

Rh content was found to be dominant in larger particles and Ru in smaller ones. In few cases, a ratio close to the theoretical one was found. Results obtained with EDX confirmed that bimetallic Rh/Ru NPs were obtained. However, the metal ratio between the two metals is not uniform within the particles individually, a random behavior was found which can be attributed mainly to the low miscibility<sup>298</sup> of rhodium and ruthenium metals. Here also, complementary synthesis experiments and characterization are needed to be able to get better defined and resolved in structure RhRu NPs.



**Figure 3.94:** EDX analysis of PVP-stabilized  $Rh_{50}Ru_{50}$  NPs with quantitative metal ratios.

### III.4 Conclusion and Perspective

In this chapter we investigated the synthesis of bimetallic RhM NPs following the organometallic approach. It appears that the  $[\text{Rh}(\eta^3\text{-C}_3\text{H}_5)_3]$  complex is a good precursor to synthesize various RhM bimetallic systems. With  $[\text{Ni}(\text{cod})_2]$  and  $[\text{Pd}_2(\text{dba})_3]$  precursors. PVP- and HDA-stabilized RhNi and RhPd systems were obtained with different metal ratios. PVP-stabilized  $\text{RhNiO}_x$  system was investigated in catalytic reactions (see chapter IV). We took profit from the destructive synergetic effect between the Rh and the oxidized Ni layer to overcome catalytic limits in the selective hydrogenolysis of 1-benzoxy-2-methoxy-benzene which is critical in lignin conversion for syntheses of biofuel.<sup>85</sup> RhPd systems are presently being evaluated as catalysts in fuel cells for the catalytic methanol oxidation reaction in Mexico.

Apart from  $[\text{Ni}(\text{cod})_2]$  and  $[\text{Pd}_2(\text{dba})_3]$  complexes other different noble metal organometallic complexes including  $[\text{Pt}(\text{nor})_3]$  and  $[\text{Ru}(\text{cod})(\text{cot})]$  were also successfully applied with the  $[\text{Rh}(\eta^3\text{-C}_3\text{H}_5)_3]$  in the synthesis of PVP-stabilized noble BMNPs. Small RhPt and RhRu bimetallic NPs were obtained. Although complete characterization of the obtained systems is not yet performed, the preliminary results obtained open the door for future investigations and new applications.

---

# **Chapter IV :**

# **Application in**

# **Catalysis**

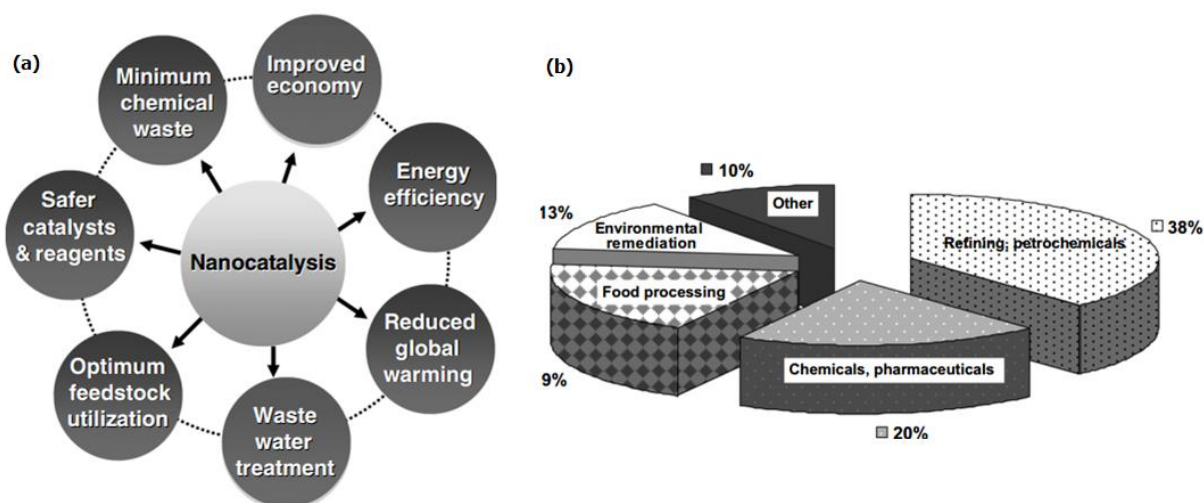
---



## IV: Application in Catalysis

### IV.I Introduction

Catalysis is a process of high importance in chemistry since many reactions that are common in the chemical industry would not be possible without the help of catalysts. Approximately 85–90 % of the products of chemical industry are achieved by catalytic processes (Figure 4.95b),<sup>9</sup> which are divided in three main categories: heterogeneous, homogeneous and enzymatic catalysis. Although homogeneous and heterogeneous catalysis are considered to be different domains, where in a heterogeneous reaction, the catalyst is in a different phase from the reactants, and in a homogeneous reaction, the catalyst is in the same phase as the reactants, both have the same objective of finding better catalytic performance.<sup>2</sup>



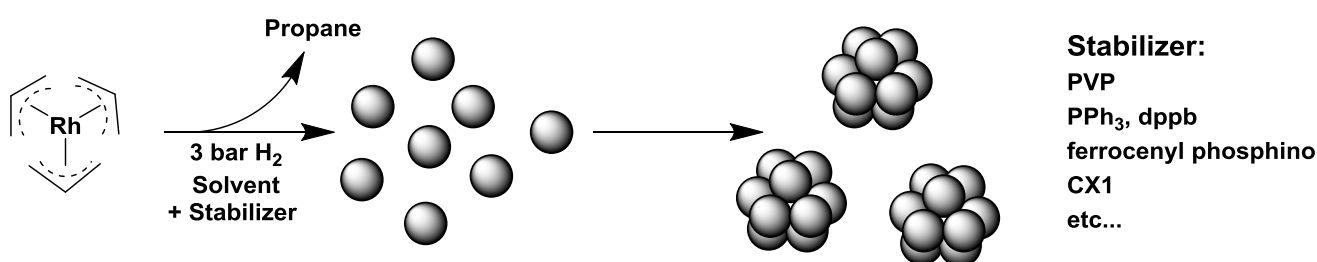
**Figure 4.95:** (a) Expected benefits of nanocatalysis; and (b) catalyst market by end-use.<sup>2</sup>

Both heterogeneous and homogeneous catalysis have different advantages and disadvantages over each other. For instance, heterogeneous catalysis benefits from easy removal of catalytic materials and possible use of high temperatures, but it suffers from lack of selectivity and understanding of the mechanistic aspects that are indispensable for parameter improvements. Whereas, homogeneous catalysis that overcomes the obstacle of selectivity and high efficiency, suffers from the difficulty or the impossibility of recovering the catalysts from the reaction media and most often the catalysts have limited thermal stability. That is why metal nanoparticles (NPs) from colloidal synthesis are advantageous in

fundamental catalysis research because of their ability to bridge the gap of differences between homogeneous and heterogeneous catalysis, given its frontier position.<sup>8</sup> Several benefits are expected from nanocatalysis as illustrated in Figure 4.95a.

The effect of size in nanocatalysis has been early observed with the catalytic research development through studies of ultrafine particles and single-site catalysts. Increased catalytic activity obtained with smaller catalyst particles is traditionally thought to result from the increased proportion of active species on the surface when the size decreases. But the development of nanoscience has led to awareness that in addition to the increase in surface area and heterogeneity of atomic structure, NPs exhibit quantum size effects in their electronic nature.<sup>299</sup> Therefore, the marriage between nanoscience/nanotechnology and catalysis brings huge opportunities for the development of nanocatalysts owing to their unique large surface-to-volume ratios, electronic behavior, and quantum-size effects.

Rhodium nanoparticles previously described in this thesis work were synthesized in solution from the  $[\text{Rh}(\eta^3\text{-C}_3\text{H}_5)_3]$  complex under dihydrogen pressure (Scheme 4.24). Several types of stabilizers were used under different reaction conditions with the aim to obtain small and well-dispersed Rh NPs with a narrow size distribution. In addition to the precise control of size that the organometallic approach offers for the synthesis of nanomaterials, it is also a good way to achieve “clean” NPs with specific desired species on their surface that can orientate their surface properties and consequently their performance in catalysis.



**Scheme 4.24:** Synthesis of Rh NPs following the organometallic approach using  $[\text{Rh}(\eta^3\text{-C}_3\text{H}_5)_3]$  complex.

Thus, after reporting the synthesis and characterization of different Rh NPs systems we will present now the results obtained using mono-, bi-metallic and supported Rh particles as nanocatalysts. Several catalytic reactions that are common with rhodium have been explored including mainly: hydrogenation, hydroformylation and hydrogenolysis reactions.



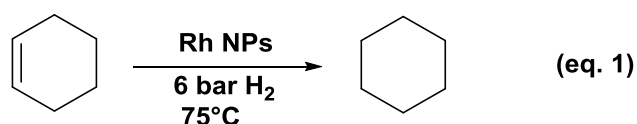
## IV.2 Hydrogenation Reaction

Rhodium is very well-known for being a highly active catalyst in hydrogenation reaction. It has been shown that in both heterogeneous and homogeneous catalytic reactions it has superior activity in hydrogenation of unsaturated substrates including alkenes, alkynes, aromatics, nitriles, pyridines... This part will rely with the evaluation of different RhNPs systems either in colloidal solution, or supported on silica in hydrogenation of cyclohexene and aromatic derivatives as model catalytic reactions. Hydrogenation studies with levulinic acid, benzoic acid, their derivatives and styrene will be also presented.

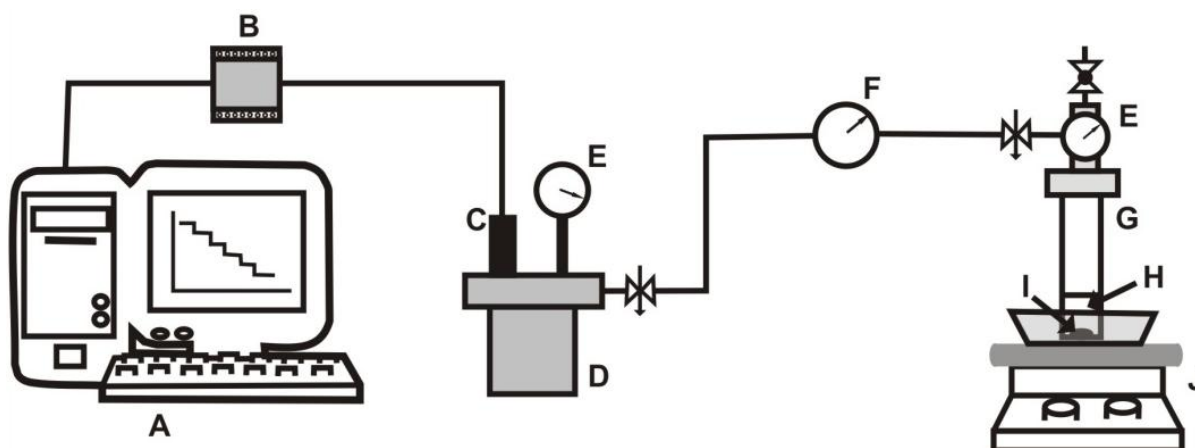
### IV.2.1 Non-Supported and Supported Rh NPs in Hydrogenation Reaction

Under the framework of a CAPES-COFECUB project (N°695/10), I had the opportunity to pass one month in the group of Liane Rossi (Laboratory of Nanomaterials and Catalysis at the University of São Paulo, Brazil) to evaluate myself the interest of RhNPs in hydrogenation catalysis. For that purpose, we chose RhPVP, RhPPh<sub>3</sub> and Rhdpbb systems of NPs and investigated their activity in hydrogenation of simple alkenes and arenes. These three systems of RhNPs were chosen because they displayed a close mean size range (1.3-2.2) nm, and they offered the possibility to study the stabilizer effect on the catalytic behavior; the PVP polymer affords a steric stabilization without direct coordination to the metallic surface of the NPs unlike the coordination of the phosphine ligands PPh<sub>3</sub> and dpbb. Therefore, studies with non-supported Rh NPs were first performed to provide fundamental understanding of the effect of the ligands on both activity and stability of the nanocatalysts, also to serve as a basis for the development of the supported analogues. The supported systems served the comparison in terms of activity, as well as to study the benefit of recycling and reusing of the nanocatalysts upon depositing the Rh NPs on a magnetic amino-modified iron core silica (FFSiNH<sub>2</sub>) as a support.

Hydrogenation reactions of cyclohexene, a well-known model substrate, were performed under fixed temperature of 75°C and fixed pressure of 6 bar in the presence of the RhNPs without any added solvent. (eq. 1)



During the hydrogenation tests, the reaction pressure was maintained constant (6 bar) through connection of the reactor with a dihydrogen gas supply tank (Scheme 4.25). The consumption of dihydrogen in the external tank was monitored and expressed in a pressure consumption curve with respect to time until reaction completion (full conversion).



**Scheme 4.25:** Schematic presentation of the hydrogenation monitoring system.

The final conversion was confirmed by gas chromatography (GC) and the turnover numbers (TONs), expressed in mol of substrate transformed per mol of rhodium, were determined. From each dihydrogen consumption curve the following parameters could be extracted:

- The period of time with no consumption of dihydrogen before the reaction started, also called activation time.
- The period of time for reaction completion determined as the time where the consumption of dihydrogen stopped.
- The turnover frequencies (TOF) determined by linearization of the hydrogen consumption curves at initial reaction time (< 20% conversion).

Considering that 1 mol of substrate is converted per each mol of dihydrogen, the TOF is given as mol of substrate converted per mol of rhodium per hour.

### IV.2.1.1 Hydrogenation of Cyclohexene with Non-Supported Rh NPs

A first set of hydrogenation catalytic tests was performed using isolated RhPVP, RhPPh<sub>3</sub> and Rhdppb NPs and the cyclohexene. The obtained results are summarized in Table 4.9. Considering that the fraction of exposed Rh atoms (surface atoms) present in each catalyst will be different, TOFs were corrected by the fraction of surface metal atoms as given in Table 4.9. These corrected TOFs were obtained by dividing the TOFs values by the approximate dispersion (D: the fraction of exposed Rh) values of ca. 0.52, 0.76 and 0.62 for RhPVP, RhPPh<sub>3</sub> and Rhdppb, respectively, calculated by considering the formation of full-shell clusters of rhodium.<sup>300</sup>

**Table 4.9:** Hydrogenation of cyclohexene with non-supported RhNPs.<sup>a</sup>

Catalyst	TON <sup>b</sup>	Activation time (h) <sup>c</sup>	Time (h) <sup>d</sup>	TOF (h <sup>-1</sup> ) <sup>e</sup>
RhPVP	4040	0.31	2.55	3960 (7550)
RhPPh <sub>3</sub>	3838	0.07	1.67	3720 (4875)
Rhdppb	3838	0.05	2.14	2715 (4340)

<sup>a</sup> Reaction conditions (solventless): Cyclohexene, catalyst, 75°C, 6 atm of H<sub>2</sub>.

<sup>b</sup> Turnover number (TON) expressed as moles of the substrate transformed per moles of catalyst.

<sup>c</sup> Time interval without consumption of dihydrogen.

<sup>d</sup> Time interval required for each cycle reaction completion estimated by H<sub>2</sub> consumption curves (>99% conversion as determined by GC).

<sup>e</sup> Turnover frequency (TOF) expressed as moles of the substrate transformed per moles of catalyst per h. In parenthesis, TOF corrected per mol of surface Rh atoms.

PVP-stabilized Rh NPs were found to be the most active catalyst for the hydrogenation of cyclohexene, which suggests a more accessible metallic surface. In fact, PVP can be considered to have no or only weak interaction with a metallic surface in comparison with a stronger phosphine Rh-P interaction, which limits the catalytic activity of the phosphine-stabilized RhNPs. Moreover, the PVP-stabilized Rh NPs exhibited a ca. 5 times longer activation time when compared to the phosphine-stabilized catalysts, which may be an indication of surface restructuring, eventually reduction of surface metal atoms, before the reaction starts. The phosphine-stabilized Rh NPs exhibited a very short activation time, which is an indication of a surface readily available for hydrogen chemisorption. This statement is supported by previous studies on the surface state of RuPVP and Rudppb NPs, showing that under oxidation conditions the Ru core of the RuPVP NPs was fully oxidized and the Ru core of the Rudppb was less sensitive to oxidation.<sup>301</sup> The activity (TOFs) corrected for exposed metal atoms of RhPPh<sub>3</sub> and Rhdppb catalysts is lower than that of

RhPVP one, which suggests the phosphine ligands are coordinating strongly to the metal surface (as observed by NMR studies, chapter II), blocking active sites. The difference between the two phosphines is not significant.

#### IV.2.1.2 Hydrogenation of Cyclohexene with Supported Rh NPs

The supported Rh NPs were studied in the same catalysis conditions and the results obtained are summarized in Table 4.10. The supported catalysts have the great advantage of being easily separated magnetically by placing a magnet on the reactor walls. The organic phase is easily recovered with a syringe for analysis by gas chromatography, while the catalyst can be reused. Compared with non-supported systems, the Rh@FFSiNH<sub>2</sub> catalysts were tested at 10 times higher substrate to catalyst molar ratio and all of them reached full conversion, with TONs of 36500. Moreover, the same amount of substrate was converted in a shorter period of time resulting in better catalytic performances, which are also corroborated by increased TOFs. Considering that each catalyst has different sizes of RhNPs, the TOFs were corrected for exposed metal atoms, for comparison. The RhPVP NPs were the most active after immobilization on the amino-functionalized silica-coated magnetite support and the phosphine ligands (PPh<sub>3</sub> and dppb) were still coordinating strongly to the metal surface, which reflected in lower TOFs of Rh dppb@FFSiNH<sub>2</sub> and RhPPh<sub>3</sub>@FFSiNH<sub>2</sub> and, in this case, also longer activation times. Again, the difference between the two phosphines is not significant.

**Table 4.10:** Hydrogenation of cyclohexene with supported Rh NPs.<sup>a</sup>

Catalyst	TON <sup>b</sup>	Activation time (h) <sup>c</sup>	Time (h) <sup>d</sup>	TOF (h <sup>-1</sup> ) <sup>e</sup>
RhPVP@FFSiNH <sub>2</sub>	36500	0.05	0.58	105,700 (203,270)
RhPPh <sub>3</sub> @FFSiNH <sub>2</sub>	36500	0.15	1.50	23,650 (31,120)
Rh dppb@FFSiNH <sub>2</sub>	36500	0.23	1.80	24,850 (40,080)

<sup>a</sup> Reaction conditions (solventless): Cyclohexene(14.6 mmol), Rh catalyst (0.0004 mmol), 75°C, 6 atm of H<sub>2</sub>.

<sup>b</sup> Turnover number (TON) expressed as moles of the substrate transformed per moles of catalyst.

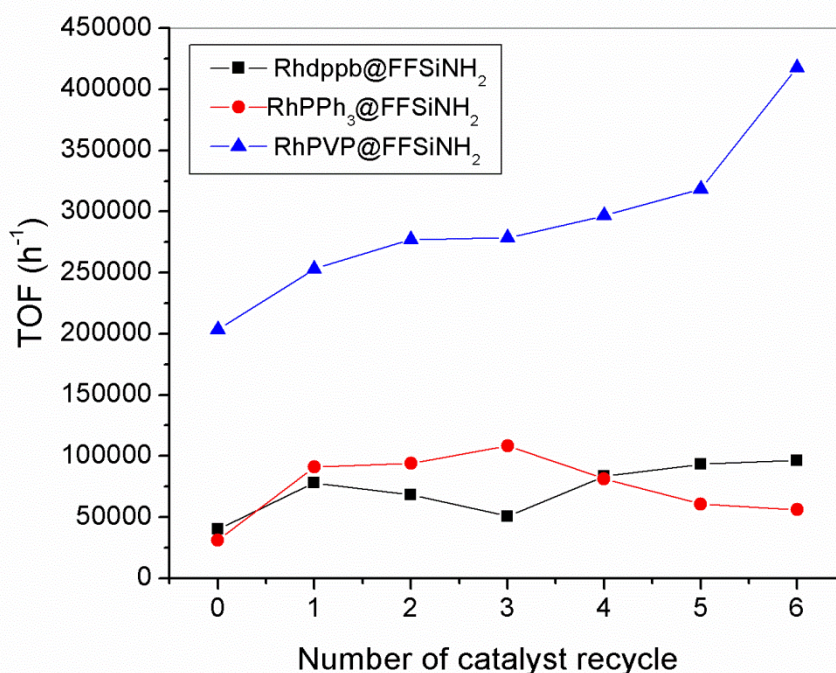
<sup>c</sup> Time interval without consumption of dihydrogen.

<sup>d</sup> Time interval required for each cycle reaction completion estimated by H<sub>2</sub> consumption curves (>99% conversion as determined by GC).

<sup>e</sup> Turnover frequency (TOF) expressed as moles of the substrate transformed per moles of catalyst per h. In parenthesis, TOF corrected per mol of surface Rh atoms.

Taking benefit of the magnetic properties of the support, the catalysts were reused in successive hydrogenation cycles performed by simply applying a magnet on the walls of the

reactor. After removing the products and drying the recovered catalyst under vacuum, a new quantity of cyclohexene was added in the reactor to pursue the catalysis. Results obtained for seven successive runs are given in Figure 4.96. The initial activity of RhPVP@FFSiNH<sub>2</sub> at ca. 200,000 h<sup>-1</sup> steadily increased until the 6<sup>th</sup> recycle, reaching ca. 400,000 h<sup>-1</sup>. An increase of the activity can be explained by a more active surface after the successive reactions probably due to the washing out of PVP stabilizer from the nanoparticle surface. Examples showing activity recovering after removal of stabilizer have been reported before for polymer-stabilized supported metal nanoparticle catalysts.<sup>143,302</sup> The immobilization of polymer-stabilized RhNPs appears thus as an excellent strategy to retain the high activity of the colloidal NPs but more importantly, it provides a way to improve their catalytic performance as the stabilizer can be removed without compromising their stability. The initial activity of Rhdppb@FFSiNH<sub>2</sub> and RhPPh<sub>3</sub>@FFSiNH<sub>2</sub> at ca. 40,000 h<sup>-1</sup> and 30,000 h<sup>-1</sup>, respectively, increased to 80,000 and 90,000 h<sup>-1</sup> in the 1<sup>st</sup> recycle and thus were maintained in this range (50,000 to 100,000 h<sup>-1</sup>) until the 6<sup>th</sup> recycle. These results corroborate the previous results found with the colloidal RhNPs, which suggests that the phosphine ligands are coordinating strongly to the metal surface and, moreover, they are not being displaced during the recycling experiments.

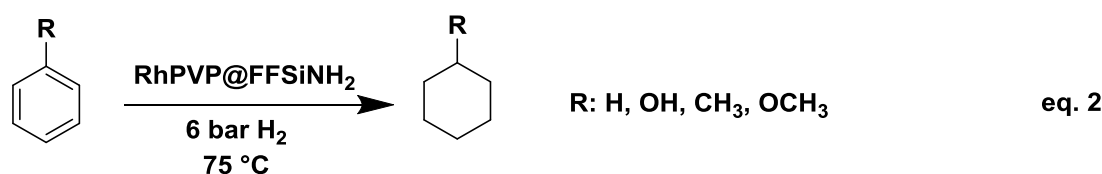


**Figure 4.96:** Catalyst recycling test expressed as TOF ( $h^{-1}$ , corrected for exposed Rh atoms) of Rhdpbb@FFSiNH<sub>2</sub> (square), RhPPh<sub>3</sub>@FFSiNH<sub>2</sub> (circle) and RhPVP @FFSiNH<sub>2</sub> (triangle) for successive hydrogenations of cyclohexene.

This work has been just submitted for a publication at *Applied Catalysis A: general journal*.<sup>303</sup>

### IV.2.1.3 Hydrogenation of Arenes with Supported Rh NPs

After the interesting results they provided in hydrogenation of cyclohexene, we decided to evaluate the supported RhPVP NPs in more challenging arene hydrogenation reactions. Using the same reaction conditions (solventless, 6 atm H<sub>2</sub>, 75 °C), a set of arenes including benzene, phenol, toluene and anisole were tested (eq. 2), and the hydrogen consumption was monitored during the reaction to identify reaction completion time and to determine the TOF values. The results are presented in Table 4.11.



**Table 4.11:** Hydrogenation of arenes with RhPVP@FFSiNH<sub>2</sub> NPs.<sup>a</sup>

Substrate	TON <sup>b</sup>	Activation time (h) <sup>c</sup>	Time (h) <sup>d</sup>	TOF (h <sup>-1</sup> ) <sup>e</sup>
Benzene	1000	0.2	7	737.5 (1418.2)
Toluene	1000	0.2	16	189 (363.4)
Anisole	1000	2.4	20	163.3 (315.5)
Phenol*	1000	0.1	18	412.5 (797)

<sup>a</sup> Reaction conditions (solventless): Cyclohexene(14.6 mmol), Rh catalyst (0.0004 mmol), 75°C, 6 atm of H<sub>2</sub>.

<sup>b</sup> Turnover number (TON) expressed as moles of the substrate transformed per moles of catalyst.

<sup>c</sup> Time interval without consumption of dihydrogen.

<sup>d</sup> Time interval required for each cycle reaction completion estimated by H<sub>2</sub> consumption curves (>99% conversion as determined by GC).

<sup>e</sup> Turnover frequency (TOF) expressed as moles of the substrate transformed (TOF) per moles of catalyst per h. In parenthesis, TOF corrected per mol of surface Rh atoms.

\*single product of cyclohexanone obtained.

It is important to note that the hydrogenation of arenes usually requires harsher conditions while using our RhPVP@FFSiNH<sub>2</sub> catalyst full hydrogenation was achieved in mild conditions with all the selected substrates at a fixed TON of 1000. Results in Table 4.11 reveal that complete hydrogenation of simple benzene was the fastest with a 7h reaction time achieving a TOF of 1418.2 (TOF corrected per mol of surface Rh atoms). Other substrates including toluene, anisole and phenol, needed longer reaction times (16-20 h) to achieve full conversion, consequently causing lower TOFs. This behavior might be attributed to the electronic contribution caused by the extra groups these substrates have and the bulkiness they add to the structure which may prevent the approach through the face of the arene which is important for their hydrogenation. This can be particularly important given the small size of the RhPVP NPs (2.2 nm).

### IV.2.2 PVP-Stabilized Rh NPs in Hydrogenation of Benzoic acid, its Derivatives and Levulinic acid

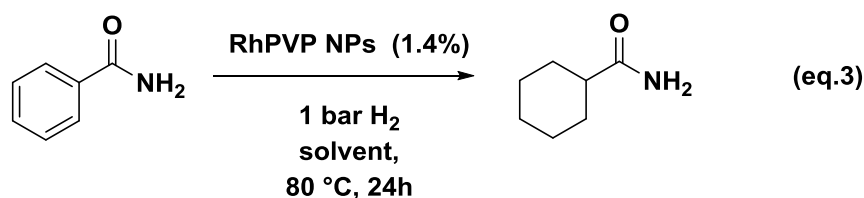
The chemoselective aromatic ring (C=C) hydrogenation of benzoic acid (BA) to cyclohexane carboxylic acid (CCA) is one of the most important steps in both petrochemical industry for cleaning diesel fuel, and the pharmaceutical industry for safe drug synthesis. The choice of Polyvinylpyrrolidone (PVP) as a stabilizer, with its three dimensional network, allowed to control the RhNPs growth with a uniform metal nanoparticle dispersion and a clean surface. Moreover, thanks to its hydrophilic character, it makes it possible to perform catalytic reactions in water. That is why RhPVP NPs were chosen as catalyst for the following part of this chapter dedicated to catalysis

The studies were performed in collaboration with Eduardo J. García-Suárez and coworkers at the “Centre for Catalysis and Sustainable Chemistry” at the Technical University of Denmark. We were interested in studying the aqueous phase hydrogenation of benzoic acid (BA) and its derivative Benzamide (BM) to cyclohexane carboxylic acid (CCA) and cyclohexane carboxamide (CCM) over PVP-stabilized RhNPs using water as a green and eco-friendly solvent at room temperature and 1 atmosphere of H<sub>2</sub> pressure. Furthermore, RhNPs were tested as catalyst in a multi-step reaction called “ketone hydrogenation followed by cyclization” where fuel additive,  $\gamma$ -valerolactone (GVL) is the desired product from levulinic acid (LA) and its methyl ester (MLA) hydrogenation.

## IV.2.2.1 Optimization of Reaction Parameters

In order to find the best reaction conditions, the hydrogenation of Benzamide (BM) to cyclohexane carboxamide (CCM) was chosen as a standard reaction to optimize the reaction parameters (solvent, temperature and time), since it is cheaper and more stable towards hydrogenation (therefore more selective) than benzoic acid (BA).

Furthermore, a control experiment with no catalyst was performed to investigate the indispensability of the catalyst for BM hydrogenation to CCM. As expected no reaction product was achieved under our given reaction conditions.



First, three different solvents namely hexane, methanol and water were chosen to run BM hydrogenation at 80 °C under the pressure of 1 bar of dihydrogen according to eq. 3. After 24 h, reactions were stopped. Structures of the products formed were identified using gas chromatography coupled with Mass spectrometry (GC-MS) analysis. Results obtained are presented in Table 4.12.

**Table 4.12:** Solvent effect on the BM hydrogenation to CCM over Rh@PVP NPs.

Entry	Catalyst	Solvent	Conversion (%)	Yield (%)
1	Rh@PVP	n-hexane	39	39
2	Rh@PVP	Methanol	71	70
3	Rh@PVP	Water	100	>99
4*	Rh@PVP	Water	100	>99

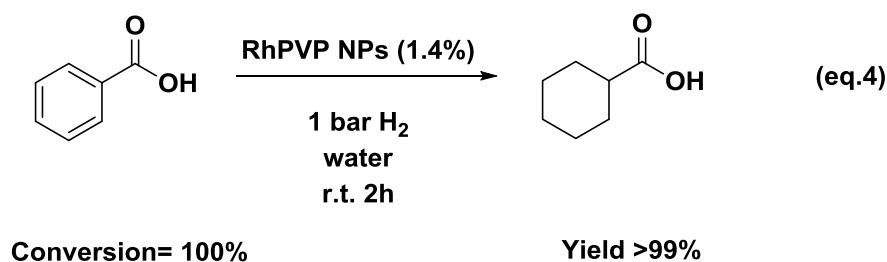
(Reaction conditions, Rh/substrate: 1.4%, 1 bar H<sub>2</sub>, 80 °C, 320 rpm, solvent 50 mL, reaction time 24 h, \* r.t., 2h)

Performing the reaction in hexane resulted in a conversion of 39% (Table 4.12. Entry 1), low percentage in comparison with the more polar methanol solvent that gave a 71%



conversion under the same reaction conditions (Table 4.12 Entry 2). However, full conversion of the substrate into CCM was achieved in water (Table 4.12 Entry 3). This result was desired and expected due the high solubility of the PVP polymer in water and protic solvents, hydrophilic character that is transferred from the polymer to the embedded Rh NPs inside its matrix. Moreover, performing the reaction in water in milder condition at room temperature over 2 h resulted in the same results with full conversion of the BM into CCM (Table 4.12 Entry 4).

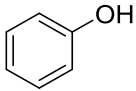
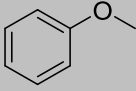
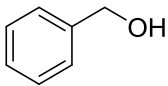
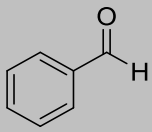
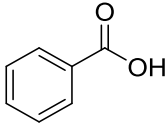
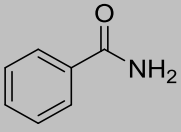
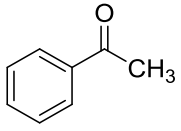
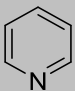
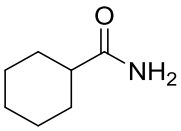
Therefore, standard reaction parameters were set to 1 bar of dihydrogen, reaction time of 2h at room temperature. The hydrogenation of benzoic acid under these conditions performed (eq. 4) and resulted in full conversion into the cyclohexane carboxylic acid product.



The overwhelming activity of Rh@PVP in the selective hydrogenation of arenes at room temperature in short reaction time enticed us to investigate a scope of substrates under the same conditions. Results are presented in Table 4.13.

**Table 4.13:** Substrates scope on the hydrogenation of aromatics with RhPVPNPs.

Entry	Substrate	Conversion (%)	Yield (%)	Selectivity (%)
1		100	>99	>99

2		100	>99	>99
3		100	>99	>99
4		93	>92	>99
5		75	73	>98
6		100	>99	>99
7		100	97	97
8		100	20	20
9		86	>85	>98
10		0	--	--

(Reaction conditions, Rh/substrate: 1.4%, 1 bar H<sub>2</sub>, 320 rpm, H<sub>2</sub>O 50 mL, r.t., 2h)

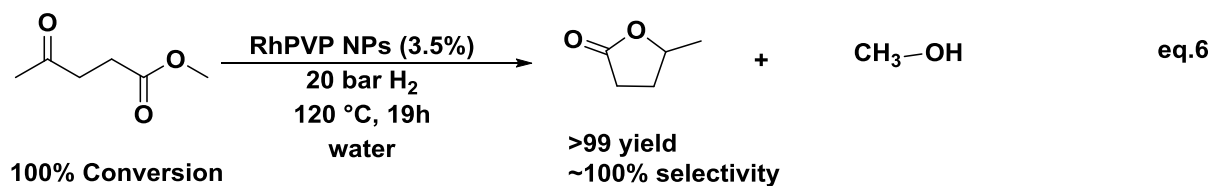
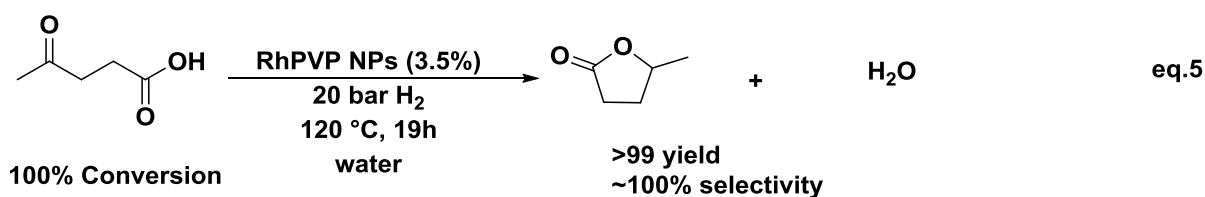
Results obtained revealed the high activity of our PVP-stabilized Rh NPs in the hydrogenation of arenes. Full conversion was obtained with almost all the substrates used, with high selectivity towards the arene group, and no hydrogenation of the carbonyl group when present.

## IV.2.2.2 Hydrogenation of Levulinic Acid (LA) and its Methyl Ester Derivative.

Biomass feedstocks are invaluable as an immediate and relatively cheap resource to provide the initial feedstock in the development of large biobased chemical products such as reducing sugars, furfural, various carboxylic acids including levulinic acid, succinic acids and lactic acids, etc. Levulinic acid (LA) in particular is a well-known product of hexose acid hydrolysis and it is inexpensively obtained by the decomposition of cellulose feedstock of glucose. Consequently, it is an attractive starting material for the production of many useful C5 based compounds such as  $\gamma$ -valerolactone (GVL), 2-methyltetrahydrofuran (MTHF) and other derivatives.<sup>304</sup>

The high activity of the PVP-stabilized RhNPs in hydrogenation prompted us to evaluate their activity in the levulinic acid (LA) and its methyl ester derivative hydrogenation which is a multi-step reaction called “ketone hydrogenation followed by cyclization”. Reactions were performed under 20 bar of dihydrogen at 120 °C in water. 3.5% of Rh NPs were utilized to catalyze the substrates which represent 1.8% of surface rhodium atoms by considering the 0.52 fraction of surface metal atom.

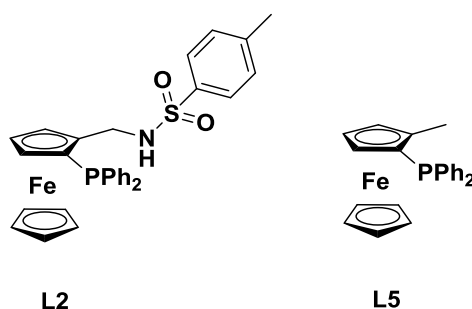
After 19 h, GC and GC-MS revealed full conversion of the LA and the MLA substrates, and the presence of the desired GVL molecule as a single product in both reactions (eq.5 and eq.6). Reactions found to be quantitative with >99% yield and full selectivity toward the GVL product.



All these results obtained in collaboration with E.J. García-Suárez *et al.* will be submitted for publication. The manuscript is presently under preparation.

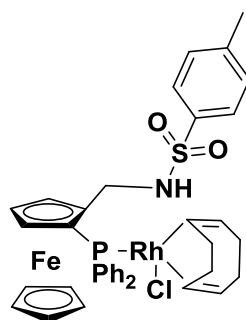
### IV.2.3 Hydrogenation of Styrene with Ferrocenyl Phosphine-stabilized Rh NPs

In chapter II, we described the synthesis of Rh NPs using a family of ferrocenyl phosphino ligands that resulted in well-controlled NPs with a small size range between 1.1 and 1.7 nm. To our best of knowledge, the use of such a type of ligands is a first for stabilizing MNPs. Consequently, it was motivating to investigate their interest in hydrogenation catalysis. This study was carried in collaboration with E. Dedier, E. Manoury and R. Poli at LCC-Toulouse.



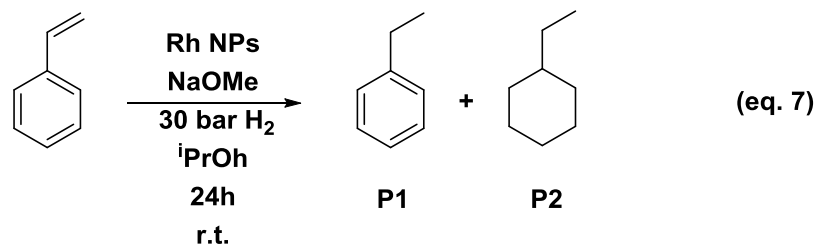
**Scheme 4.26:** Ferrocenyl phosphine ligands used for the synthesis of Rh NPs for styrene hydrogenation reaction.

Rhodium nanoparticles stabilized with ligand L2 and L5 were chosen to serve in catalytic hydrogenation of styrene in order to study the effect of the mono and the bidentate coordinating ligands in the reaction (Scheme 4.26). Moreover, the activity of L2- stabilized Rh NPs could be compared with that of a Rh complex bearing the same ligand used by our collaborators (Scheme 4.27).



**Scheme 4.27:** Rh complex with the L2 ligand.

Hydrogenation of styrene was performed at r.t. under 30 bar of dihydrogen pressure in autoclave over 24 h in iso-propanol solution (eq. 7). Same reaction conditions were applied for both L2- and L5-stabilized Rh NPs. The influence of the presence and the absence of a base (NaOMe) was explored. Results obtained are summarized in Table 4.14.



**Table 4.14:** Styrene and ethyl-benzene hydrogenation using L2- and L5-stabilized Rh NPs. Reaction conditions: iso-propanol solvent, 30 bar  $H_2$ , r.t., 24h

Entry	Catalyst	Substrate	$n_{\text{Substrate}}$	S/C	Catalyst (%)	$n_{\text{base}}/n_{\text{Rh}}$	Styrene (%)	P1 (%)	P2 (%)	TON
1	L2 Rh NPs	Styrene	0.0005	146	0.7	0	0	92.5	7.5	146
2		Styrene	0.0015	439	0.2	0	0	97.6	2.3	439
3		Styrene	0.0005	146	0.7	7	0	99.7	0.3	146
4		Styrene	0.0015	439	0.2	8	0	99.8	0.2	439
5		Ethyl-benzene	0.00049	144	0.7	0	--	93.9	6.1	144
6		Ethyl-benzene	0.00049	144	0.7	7	--	99.6	0.4	144
7	L5 Rh NPs	Styrene	0.0005	252	0.4	0	0	90	10	252
8		Styrene	0.0015	756	0.1	0	0	97	3	756
9		Styrene	0.0005	252	0.4	14	0	98.3	1.7	252
10		Styrene	0.0015	756	0.1	16	0	>99	<1	756
11		Ethyl-benzene	0.00049	247	0.4	0	--	81	19	247
12		Ethyl-benzene	0.00049	247	0.4	15	--	98.8	1.2	247

All reactions performed showed full conversion of the styrene starting material after 24h under the applied conditions. Entries 1 and 2 show the activity of 0.7% and 0.2% of L2-stabilized Rh NPs in absence of the NaOMe base. Ethylbenzene (P1) is the main product formed, but the complete hydrogenation of the arene and the ethylene group leading to ethylcyclohexane (P2) was also observed representing 7.5% of the products in case of higher catalyst percentage (0.7%); almost three times higher than in the case of 0.2% of NPs. Entries 3 and 4 represent the same reactions while adding the NaOMe base. The influence of the base appeared directly in the products formed favoring the selectivity toward the ethylbenzene (P1) with very low P2 percentage (0.2-0.3%), NaOMe thus prevents arene hydrogenation regardless of the catalyst amount.

With L5-stabilized Rh NPs a similar behavior was observed. Entries 7 and 8 with 0.4% and 0.1% Rh percentages, respectively resulted in 10% and 3% of the fully hydrogenated product P2 and 90% and 97% of the ethylbenzene product (P1). Entries 9 and 10 which correspond to the same reactions with added base again show evolution of the reaction toward higher quantity of ethylbenzene product (P1) with only 1.2% of P2 in the case of 0.4% of Rh NPs.

Then, commercial ethylbenzene was introduced as substrate in the same reactions condition with 0.7% of L2-stabilized Rh NPs without (Entry 5) and with additional base (Entry 6), and with 0.4% of L5-stabilized Rh NPs without (Entry 11) and with additional base (Entry 12). Hydrogenation toward P2 occurs with 6.1% conversion with the L2Rh NPs system and 19% with the L5Rh NPs system. However, upon performing the reactions in presence of the base, hydrogenation of the arene moiety is almost prohibited in both cases.

Although rhodium is well-known in hydrogenation of aromatics, when using L2- and L5-stabilized Rh NPs, we found that hydrogenation of the arene moiety is very low, according to a previous report published by Graydon *et al.*<sup>305</sup> Rh NPs with a mean size of 1.4 nm and less do not exhibit activity in benzene ring hydrogenation reactions. The Rh NPs used in this study have a mean size of  $1.5 \pm 0.6$  nm and  $1.2 \pm 0.6$  nm for L2- and L5-stabilized Rh NPs, respectively. We can thus attribute the low aromatics hydrogenation to a plausible surface blocking of the NPs caused by the ferrocenyl group. A lack of accessibility of the rhodium surface may indeed result from the coordination of the ligand onto NP surface and leading to

high steric hindrance. This blockage of the metal surface induced by the coordination of a ligand may open the way towards selective hydrogenation reactions. These catalytic results will be joined to the NPs synthesis and characterization data described in chapter II to prepare a publication manuscript.

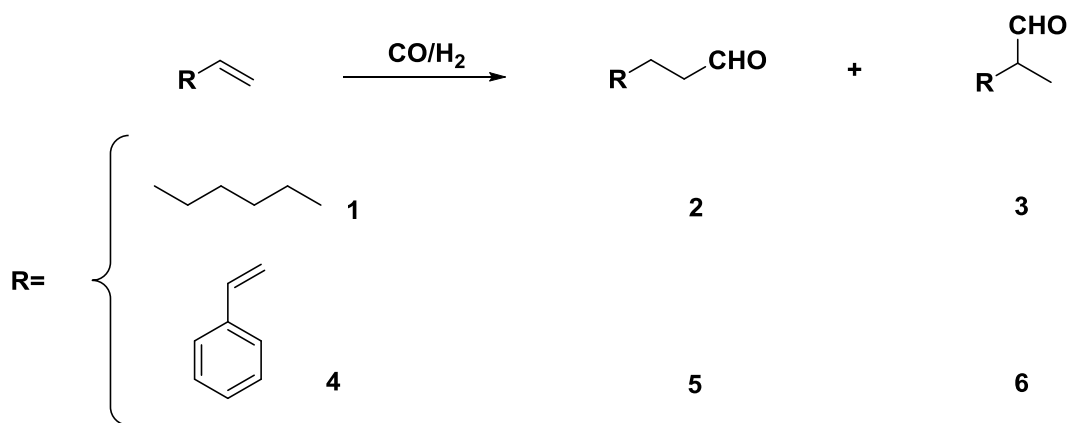
### **IV.3 Hydroformylation Reaction**

Hydroformylation, the conversion of olefins into aldehydes through the addition of syngas (CO and H<sub>2</sub>) is an important industrial reaction that employs catalysis by transition metals. Initially, cobalt complexes were used for this reaction but later, rhodium complexes have been implemented due to their higher activity under milder reaction conditions. Concerning Rh NPs, it appears that only a few papers deal with rhodium metal nanoparticles for investigation in this reaction, although it is well-known as highly active metal in the reaction in homogeneous conditions as mentioned before. Especially, that in most of the reported systems, leaching of the NPs systems and formation of intermolecular complexes or clusters happens under the harsh conditions.<sup>149</sup>

#### **IV.3.1 Hydroformylation of Oct-1-ene and Styrene with PPh<sub>3</sub>- and TOAB-stabilized Rh NPs.**

Under the framework of a CAPES-COFECUB project (N°695/10), with the group of Liane Rossi (Laboratory of Nanomaterials and Catalysis) at the university of São Paulo, Brazil, hydroformylation reaction was studied using two different systems of Rh NPs synthesized through two different methods. PPh<sub>3</sub>-stabilized Rh NPs synthesized following the organometallic approach and tetraoctylammonium bromide (TOAB)-stabilized Rh NPs synthesized through chemical reduction of the RhCl<sub>3</sub>.xH<sub>2</sub>O salt using NaBH<sub>4</sub><sup>143</sup> were selected for a comparative study.

The aim of this study was to compare the catalytic activity in hydroformylation reactions of RhPPh<sub>3</sub> NPs which display at their surface coordinated PPh<sub>3</sub> because it is used as stabilizer and RhTOAB NPs (original and modified by addition of external monophosphines; PPh<sub>3</sub>, (CH<sub>3</sub>)<sub>2</sub>PPh, ClPPh<sub>2</sub>, HPPh<sub>2</sub>). For that purpose, two model substrates were chosen namely, oct-1-ene and styrene (Scheme 4.28).



**Scheme 4.28:** Hydroformylation of oct-1-ene (1) and styrene (4) and the corresponding linear (2, 5) and branched (3, 6) aldehyde products, respectively.

One of the difficulties in the hydroformylation reaction lies with the mixture of isomeric products (linear and branched), which, unless the substrate is ethylene, is subsequently formed. Indeed, an isomerization of the olefinic bonds may take place before hydroformylation giving rise to different branched aldehydes. Furthermore, hydrogenation of the olefinic bonds is also a competing reaction, mostly because of the similarity of the catalysts used in both hydroformylation and hydrogenation reactions as well as of the reaction conditions

Hydroformylation of oct-1-ene and styrene substrate was performed after dissolution of  $\text{PPh}_3$ -stabilized Rh NPs in toluene, under 50 bar of Syngas ( $\text{H}_2:\text{CO} = 1:1$ ) in a stainless steel autoclave for 3h. Results obtained are summarized in Table 4.15. Products presented in the table as other aldehydes and alcohols were attributed to unidentified aldehydes and alcohols due to characteristic GC retention times and the presence of characteristic peaks in their mass spectra.

**Table 4.15:** Hydroformylation of oct-1-ene and styrene catalyzed by Rh- $\text{PPh}_3$ .<sup>a</sup>

Entry	Substrate	P/Rh	Temperature (°C)	Conversion (%)	Selectivity (%)				
					Aldehydes			Alcohols	
					I	b	Others		Isomers/ Hydrogenated
1	Oct-1-	-	80	72	25	45	-	4	25/1



	ene								
<b>2</b>	Oct-1-	-	120	100	34	41	18	4	2/1
	ene								
<b>3</b>	Styrene	-	120	100	38	61	-	-	0/1
<b>4</b>	Oct-1-	20	120	91	49	25	18	4	0/0
	ene								

<sup>a</sup>Reaction conditions: 20 mL of toluene, oct-1-ene or styrene (7.6 mmol), catalyst (5.1  $\mu$ mol of Rh), 50 bar of H<sub>2</sub>:CO – 1:1, [substrate]/[catalyst]= 1500, 3 h.

In the case of oct-1-ene, after 3 h at 80°C, the RhPPh<sub>3</sub> NPs present an activity reaching 72% of conversion (Table 4.15, entry 1), with a selectivity of 25% of the linear product and 45% of the branched product. In addition, 25% of isomers and 1% of hydrogenated products were detected. Increasing the temperature to 120 °C (Table 4.15, entry 2) allowed to achieve full conversion of the oct-1-ene, and improved the selectivity to the linear product to 34% and the selectivity to the branched product decreased to 41%. However, 18% of other aldehydes, 2% of isomers and 1% of hydrogenated products were observed. It appears that with the temperature increase, isomerization took place and hydroformylation of internal product was possible (others). When styrene was used as reagent (Table 4.15, entry 3), 38% of the selectivity was found for the linear aldehyde, 61% for the branched, and only 1% for the hydrogenated product, with high activity (100% of conversion in 3 h). Addition of free PPh<sub>3</sub> to the RhPPh<sub>3</sub> NPs (P/Rh = 20) in the hydroformylation of oct-1-ene (Entry 4) increased selectivity to the linear product (49%), decreased the selectivity to branched aldehyde (25%) and 18% of other products with a slight decrease of conversion in 3 h (91%). These differences in selectivities can be explained by the amount of PPh<sub>3</sub> used as stabilizer . The addition of more PPh<sub>3</sub> limits the formation of branched products and hydrogenated products.

For comparison purpose the TOAB-stabilized Rh NPs synthesized through chemical reduction of the RhCl<sub>3</sub>.xH<sub>2</sub>O by NaBH<sub>4</sub><sup>143</sup> were also used in hydroformylation reactions under similar conditions. In this case the effect of the addition of external PPh<sub>3</sub> ligands was studied. Obtained results are summarized in Table 4.16.

**Table 4.16:** Hydroformylation of oct-1-ene and styrene by RhTOAB NPs with and without addition of an external PPh<sub>3</sub>.<sup>a</sup>

Entry	Substrate	Ligands	P/R	Temperature (°C)	Time (h)	Conversion	Selectivity (%)			
							Aldehydes	Alcohols/ hydrogenated	Other	
1	Oct-1-ene	-	-	80	24	5	30	70	-	-
2	Oct-1-ene	-	-	120	24	100	35	36	26	3/0
3	Styrene	-	-	120	22	100	33	67	-	-
4	Oct-1-ene	PPh <sub>3</sub>	1	120	24	100	37	33	27	3/0
5	Oct-1-ene	PPh <sub>3</sub>	20	120	10	80	51	26	19	4/0
6	Oct-1-ene	PPh <sub>3</sub>	20	80	10	32	70	30	-	-
7	Styrene	PPh <sub>3</sub>	20	120	10	82	51	48	-	0/1

<sup>a</sup>Reaction conditions: 20 mL of toluene, oct-1-ene or styrene (7.6 mmol), catalyst (5.1 μmol of Rh), 50 bar of H<sub>2</sub>:CO – 1:1, [substrate]/[catalyst]=1500.

The as-prepared RhTOAB NPs poorly converted oct-1-ene with 5% conversion (table 4.16, entry 1) at 80°C which resulted completely into hydroformylation products, i.e., aldehydes 2 (linear) and 3 (branched), with predominance of the branched product (70%). At 120°C (entry 2), the reaction was faster, reaching 100% of conversion in 24 h. Although the selectivity to branched products has changed (36%) and to linear products slightly increased (35%), it is worth mentioning that there was 3% alcohol formation, i.e., a reduction of part of the aldehydes occurred, and 26% of products were other aldehydes which indicate extensive isomerization of 1 and subsequent hydroformylation of the internal isomers. Clearly, a pronounced induction time takes place considering that in 6 h no conversion was obtained; however, it is important to state that no appreciable substrate hydrogenation occurred. This behavior seemed to us quite interesting because the competition between hydrogenation and hydroformylation reaction is one of the reasons for the observed decreased of selectivity to aldehydes in many molecular catalytic systems. Then, RhTOAB NPs were used to hydroformylate styrene (Entry 3). In 22 h at 120°C, 100% of conversion was obtained with 67% of selectivity for the branched aldehyde.

The comparison between the activities of RhPPh<sub>3</sub> NPs and the RhTOAB ones prompted us to add free triphenylphosphine (PPh<sub>3</sub>) to the latter system, to try to improve the catalytic performance. Indeed, this strategy is known with molecular catalysts to decrease the induction time and improve the selectivity.

At P/Rh = 1, the hydroformylation of oct-1-ene with PPh<sub>3</sub> occurs very slowly, 100% of conversion was observed for 24 h at 120°C and 50 bar of CO:H<sub>2</sub> (Table 4.16, entry 4). The selectivities obtained are similar to that observed for the RhTOAB NPs without PPh<sub>3</sub>. This indicates that the chosen phosphine proportion was not sufficient to improve neither the activity nor the selectivity of the catalytic system. However, At P/Rh = 20 (Table 4.16, entry 5) for 10 h, the conversion increased for 80%. The selectivities barely changed. A decrease of temperature to 80°C led to a high increase in the selectivity of the linear aldehyde (70%) and no other aldehydes formation, but with just 32% of conversion (Table 4.16, entry 6).

The hydroformylation of styrene with RhTOAB/PPh<sub>3</sub> NPs (20 eq.) presented 82% of conversion and one increase of selectivity to the linear product (Table 4.16, entry 7). The

linear aldehyde reached 51%, the branched 48% and the molecule has no option for isomerization, presenting 1% of ethylbenzene, the hydrogenated product.

From these results, we can conclude that the addition of a phosphine in the reaction mixture with the RhTOAB NPs helped in increasing the reaction rate; however a value of 20 equivalents was essential to promote this effect. With the PPh<sub>3</sub>-stabilized Rh NPs prepared through the organometallic approach, faster reaction rates were obtained (3h, 100% conversion) without any additional ligands. These RhPPh<sub>3</sub> NPs form a catalytic system very selective to aldehydes and present a much higher activity compared to RhTOAB NPs. The difference in activity between the two systems studied can be explained by different surface states owing to the way of preparation of the particles. In RhPPh<sub>3</sub> NPs, the PPh<sub>3</sub> is used as the stabilizer and is thus expected to be coordinated at the metallic surface and thus to influence NP surface properties.<sup>158</sup> In the case of RhTOAB NPs, the addition of free phosphine has a positive influence of their catalytic behavior, but one concern is the nature of the interaction with the metal surface if any exists.

Another concern is the nature of the real active species in the catalytic hydroformylation reaction. From our results it appears clearly that a direct coordination of the PPh<sub>3</sub> at metal surface has a positive effect on the catalytic performance. Nevertheless, we do not know if the catalytic way is the same starting from Rh PPh<sub>3</sub> NPs or RhTOAB + PPh<sub>3</sub> NPs. During the catalytic study, both colloidal solutions of RhTOAB/PPh<sub>3</sub> and RhPPh<sub>3</sub> NPs in toluene presented a dark colour before catalysis. However, in both cases, the solution turned light brown after the reaction that could correspond to the formation of molecular species. Moreover, previous results from the group evidenced the formation of a molecular complex, namely [RhH(CO)<sub>2</sub>], during the catalysis,<sup>77</sup> which was shown by NMR. Consequently, this work could be completed by NMR characterization of the reaction mixture under catalysis conditions to try to understand the catalysis act. Another complement is the realization of poisoning tests by addition of CS<sub>2</sub> to have indication of catalysis blockage if any.

A series of poisoning tests (Table 4.17) were already carried out. CS<sub>2</sub> poisoning tests may poison both homogeneous and heterogeneous catalysts under certain conditions. Usually, less than 1 equivalent of CS<sub>2</sub> is used to evaluate heterogeneous catalysts and 1-2 equivalents

are used to assess homogeneous catalysts. Therefore the poisoning tests were performed by adding 0.5 or 1.5 equivalent of CS<sub>2</sub>.

**Table 4.17:** CS<sub>2</sub> addition at the beginning of the oct-1-ene hydroformylation reaction for RhTOAB and RhPPh<sub>3</sub> NPs.<sup>a</sup>

Entry	Catalyst	CS <sub>2</sub> ratio	Time	Conversion	Selectivity (%)				
					Aldehydes			alcohols	
					l	b	Others	Isomers/ Hydrogenated	
1	RhTOAB <sup>b</sup>	0.5	24	23	69	31	-	-	0/0
2	Rh-PPh <sub>3</sub> <sup>b</sup>	0.5	24	90	25	45	-	4	25/1
3	RhTOAB <sup>c</sup>	0.5	24	20	70	30	-	-	0/0
4	Rh-PPh <sub>3</sub> <sup>c</sup>	0.5	24	74	26	46	-	4	23/1
5	RhTOAB <sup>c</sup>	1.5	24	5	70	30	-	-	0/0
6	Rh-PPh <sub>3</sub> <sup>c</sup>	1.5	24	90	25	45	-	3	24/1

<sup>a</sup>Reaction conditions: 20 mL of toluene, oct-1-ene or styrene (7.6 mmol), catalyst (5.1 μmol of Rh), 80 °C, 50 bar of H<sub>2</sub>:CO – 1:1, [substrate]/[catalyst]= 1500. <sup>b</sup>addition of CS<sub>2</sub> before reaction starting. <sup>c</sup>addition of CS<sub>2</sub> after 1.5 hour of the reaction starting.

In all the experiments, we did not observe any significant change in the selectivity between the poisoned and non-poisoned systems. However, the experiments performed with the poison before and after the reaction clearly slowed the reactions. In addition, concentration of CS<sub>2</sub> of 1.5 equivalents presented lower activities when sub-stoichiometric conditions were used. The same results were obtained when sub-stoichiometric equivalents were changed to 0.3 and 0.7. One limitation with CS<sub>2</sub> test is that it is preferable to perform it at a temperature lower than 50 °C to avoid CS<sub>2</sub> dissociation from heterogeneous catalysts that can take place at T >50 °C. In the present case, the experiments were performed at 80°C due to the inactivity of the catalysts at lower temperature. Therefore these poisoning tests are not conclusive. We cannot exclude the possibility that the hydroformylation reaction occurs at the NP surface; however data including induction time for RhTOAB NPs and the alteration of the solution

color at the end of the catalysis are indicative of NPs degradation under the reaction conditions, maybe towards the formation of a molecular complex.

All these results indicate that RhPPh<sub>3</sub> NPs form a catalytic system very selective to aldehydes and present a much higher activity compared to RhTOAB NPs even in presence of added PPh<sub>3</sub>. The difference in activity between the two systems studied can be explained by different surface states owing to the way of preparation of the particles. In RhPPh<sub>3</sub> NPs, the PPh<sub>3</sub> is used as the stabilizer and is thus coordinated at the metallic surface and thus to influence NP surface properties.<sup>158</sup> In the case of RhTOAB NPs, the addition of free phosphine has a positive influence of their catalytic behavior, but one concern is the nature of the interaction with the metal surface if any exists. Moreover, another question in this catalysis is the nature of the real active species. Is it a nanoparticle or a molecular complex? This question remains opened and complementary work is needed to find out an answer.

### IV.3.1 Hydroformylation of Styrene with CXP-stabilized Rh NPs.

To the best of our knowledge, the use of CXP ligand to stabilize Rh NPs is a first and the obtained NPs are small in size and well-dispersed. In collaboration with David Semeril at the “Laboratoire de Chimie Inorganique Moléculaire et Catalyse, Institut de Chimie UMR, Université de Strasbourg” who provided the macrocyclic calix[4]arene ligand, we could evaluate the activity of the obtained NPs in the hydroformylation of styrene. Comparison with the PVP-stabilized Rh NPs system was performed and effect of the addition of extra CXP ligand was also studied.

Typical reaction procedure was performed in a glass-lined, stainless steel autoclave containing a magnetic stirring bar. The autoclave was charged under nitrogen with Rh NPs (0.003 g, 0.03 mmol) and toluene (10 mL). Once closed, the autoclave was flushed twice with syngas (CO/H<sub>2</sub>=1:1), pressurized with a CO/H<sub>2</sub> mixture and heated at 80 °C. After 16 h, the autoclave was depressurized, styrene (0.66 mL, 5.7 mmol) and internal standard (decane ; 0.25 mL) were added to the reaction mixture. The autoclave was then heated and pressurized. The progress of the reaction was checked by monitoring the pressure decrease. During the

experiments, several samples were taken and analyzed by GC or  $^1\text{H}$  NMR spectroscopy. Obtained results are reported in Table 4.18.

**Table 4.18:** Hydrogenation of Styrene with RhCXP and RhPVP NPs.<sup>a</sup>

Entry	Catalyst	Temperature (C)	Time (h)	P(CO/H <sub>2</sub> ) (bar)	Conversion (%)	Selectivity	
						Linear (%)	Branched (%)
1	RhCXP NPs	100	24	30 (CO/H <sub>2</sub> 1:1)	97	18	82
2	RhCXP NPs	80	24	30 (CO/H <sub>2</sub> 1:1)	89	26	74
3	RhCXP NPs	80	3	30 (CO/H <sub>2</sub> 1:1)	16	42	58
4	RhCXP NPs <sup>b</sup>	80	14	30 (CO/H <sub>2</sub> 1:1)	70	53	47
5	RhCXP NPs	50	24	30 (CO/H <sub>2</sub> 1:2)	33	89	11
6	RhPVP NPs	50	24	30 (CO/H <sub>2</sub> 1:2)	traces	0	traces
7	RhPVP NPs <sup>c</sup>	50	24	30 (CO/H <sub>2</sub> 1:2)	3	64	36

<sup>a</sup> Reactions conditions (Rh cat 0.5%, 50 bar syngas). <sup>b</sup> 8 equivalents of excess CXP ligand. <sup>c</sup> 4 equivalents of excess CXP ligand.

Hydroformylation of styrene using the CXP-stabilized Rh NPs was performed under a constant pressure of 50 bar of syngas. Reaction at 100 °C (table 4.18, Entry 1) resulted in 97% conversion of the starting material after 24 h ; 82% of the products correspond to the branched aldehyde, and 18% to the linear one. Repeating the same reaction at 80 °C (Entry 2) gave a slightly lower conversion of 89%, and maintained the favouring of the branched aldehyde with a l/b ratio of 26/74. Entry 3 represents the reaction under the same reaction condition of entry 2 but with a shorter reaction time of 3 h, not surprisingly, the conversion is low with 16%, however, l/b ratio is 42/58 increasing the linear product percentage. Whereas, the

reaction upon adding extra 8 equivalents of the free CXP ligand, after 14 h resulted in 70% conversion and small enhancement in the l/b ratio of 53/47. According to literature, to overcome the selectivity issue, decreasing the reaction temperature and altering the CO:H<sub>2</sub> ratio is a key solution.<sup>306</sup> Entry 5 represents the use of 1:2 ration of CO:H<sub>2</sub> and a temperature of 50 °C, despite that the conversion decreased to 33% after 24 h, but linear product was highly favored with a l/b ration of 89/11. For comparison purpose with the RhCXP system of NPs, RhPVP NPs were also evaluated, at 50 °C with a 30 bar of syngas (CO/H<sub>2</sub> 1:2) (Entry 6). traces of reacted substrates were detected that correspond to the branched aldehyde product. Upon repeating the same reaction while adding 4 equivalents of the free CX, conversion reached 3% but with linear higher ration of linear products than branched (l/b= 64/36). These preliminary results indicate that RhPVP NPs are not active at 50 °C and that the addition of free calixarene may improve their catalytic performance. This may be explained by an interaction between Rh metal surface and the calixarene as it may exist in the CXP-stabilized Rh NPs that were found to be higher active and selective. Here again, more work is necessary to complete these results and get more information about this catalytic system.

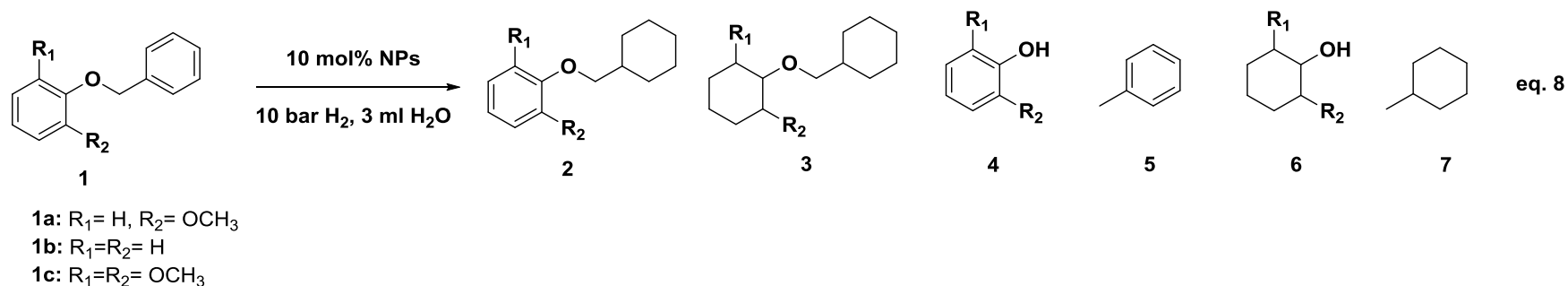


## IV.4 Hydrogenolysis Reaction

Lignin is a highly functionalized polymer that is enriched with aromatic rings and C–O bonds. In recent years, hydrogenolysis of C–O bonds in lignin has been widely recognized as a promising strategy to break it down into monomeric compounds and oligomers, but the competitive hydrogenation of the aromatic rings is always a problem.<sup>307-309</sup> Indeed, the undesired hydrogenation reaction leads to extra consumption of dihydrogen, and generation of saturated products that are normally of lower value.

In lignin hydrogenolysis using nanocatalysts, the undesired hydrogenation of aromatics requires the adsorption of benzene rings on a NP terrace whereas this is not necessary for C–O bond hydrogenolysis. As such, in collaboration with the team of Pr. Ning Yan at the National University of Singapore (NUS) we envisaged a strategy where an inert metal oxide is deposited on a metal NP surface to segregate terrace zones, thereby preventing benzene ring coordination and hydrogenation. Along this line, we focused on the surface decoration of Rh NPs by NiO<sub>x</sub> *via* the organometallic approach. As described in chapters II and III the olefinic complexes [Rh( $\eta^3$ -C<sub>3</sub>H<sub>5</sub>)<sub>3</sub>] and [Ni( $\eta^4$ -C<sub>8</sub>H<sub>12</sub>)<sub>2</sub>] and PVP were employed for preparing Rh, Ni and RhNi NPs to evaluate their catalytic performance in hydrogenolysis reaction. Since the contamination effects of ligands from the precursors and reducing agents are eliminated, this way of NP synthesis sounds suitable for the exploration of the surface structure-reactivity relationships in nanocatalysis.<sup>252,310-311</sup>

Rh is well-known for its excellent benzene ring hydrogenation property. On the other hand, its activity in C–O bond hydrogenolysis is typically low. In order to explore the surface site blockage effect on the selective hindering of benzene ring hydrogenation without compromising C–O bond hydrogenolysis, several compounds that imitate the lignin compounds 1a–c were selected to react with 10 bar H<sub>2</sub> in water over 10% of Rh, NiO<sub>x</sub> and NiO<sub>x</sub>/Rh NPs (Table 4.19)



**Table 4.19:** Hydrogenolysis of 1-benzyloxy-2-methoxybenzene compounds using NiO<sub>x</sub>/Rh, Rh, and Ni NPs stabilized by PVP as catalysts.

Entry	Substrate	Catalyst	Temp	Time	Conversion	Yield			
						2	3	4+5	6+7
1	1a	Rh	60	1	100	0	33	0	67
2	1a	Ni	60	1	6	0	0	6	0
3	1a	NiO <sub>x</sub> /Rh	60	1	61	1	0	60	0
4	1a	Rh	25	2	68	1	21	0	42
5	1a	NiO <sub>x</sub> /Rh	25	2	18	0	0	17	1
6	1a	NiO <sub>x</sub> /Rh	25	5	91	1	0	88	2
7	1a	NiO <sub>x</sub> /Rh	25	40	100	0	0	88	12
8	1b	Rh	60	1	100	0	31	0	69
9	1b	Ni	60	1	10	0	0	10	0
10	1b	NiO <sub>x</sub> /Rh	60	1	66	0	0	65	1
11	1c	Rh	60	1	100	0	48	0	50
12	1c	Ni	60	1	3	0	0	3	0
13	1c	NiO <sub>x</sub> /Rh	60	1	50	0	0	50	0

As shown in Table 4.19 entry 1 monometallic Rh NPs showed high activity with 1a, achieving 100% conversion at 60 °C within 1h. However, all the benzene rings in the products were saturated as a consequence of the high activity of Rh towards hydrogenation of benzene. 33% product was fully hydrogenated without C–O bond cleavage (compound 3). Not surprisingly, Ni NPs (Table 4.19, entry 2) displayed a very low activity (6% conversion) despite a high selectivity towards hydrogenolysis. Under identical reaction conditions, NiO<sub>x</sub>/Rh NPs (entry 3) selectively catalyzed hydrogenolysis of 1a with a moderate activity, yielding 61% aromatic products (4 + 5) with negligible hydrogenation product (1% of 2). As well-known in literature, a certain size of segment is required for the hydrogenation of benzene ring over heterogeneous catalysts. It was suggested that Rh NPs under 1.4 nm exhibited no activity in benzene ring hydrogenation.<sup>305</sup> The size of Rh and NiO<sub>x</sub>/Rh NPs (2.3 nm) is slightly larger than the critical size (1.4 nm) required for benzene ring hydrogenation, which explains the good hydrogenation activity of benzene rings over pure Rh NPs. At the same time, our strategy of using NiO<sub>x</sub> for the surface partial blockage appears to be highly successful in further reducing the terrace size of the Rh domains below its critical size, so that these NPs become inactive in benzene ring hydrogenation. Further, the reaction was conducted at r.t. to obtain more information on kinetics (entry 4–7). Reaching a conversion of 64%, the products over pure Rh NPs were almost fully hydrogenated after merely 2 h, revealing fast hydrogenation of benzene rings, which could not be avoided by reducing the reaction temperature. Under the same conditions, 18% conversion was achieved over NiO<sub>x</sub>-decorated Rh NPs, with only less than 1% of hydrogenated products. Because the Rh content in NiO<sub>x</sub>/Rh NPs was 50% as compared to that in monometallic Rh NPs, and that ca. 80% surface in NiO<sub>x</sub>/Rh NPs was blocked by Ni, NiO<sub>x</sub>/Rh NPs had approximately 10% of surface Rh sites as compared to same amount of RhNPs. Therefore, although NiO<sub>x</sub>/Rh NPs produced less hydrogenolysis products than Rh NPs (18:42), the TOF for the hydrogenolysis reaction, with respect to every exposed Rh sites, was much higher (180:42). Although the effect of different sites (kinks/steps vs. terraces) in the hydrogenolysis of the C–O bond of the substrate we used for this study has not been reported, hydrogenolysis reaction is well known to be structure sensitive. For instance, several works<sup>312-315</sup> reported that the kink/step sites are more active for hydrogenolysis of C–C bond, while terraces favour the hydrogenation/dehydrogenation reactions. Since no electronic modification was observed, the enhanced TOF in hydrogenolysis is probably likely due to the blocking of terraces which favour the hydrogenation reaction. Prolonging the reaction time to 5 h over NiO<sub>x</sub>/Rh NPs increased the yield of hydrogenolysis products to 88%, with negligible increase in

hydrogenated products. Notably, the reaction was conducted with a very long duration of 40 h, but 88% of products remained unhydrogenated. These results demonstrate very effective inhibition of the hydrogenation by site blockage effect over the entire reaction period. Finally, additional substrates, including 1b, bearing no methoxyl substitution (entry 8–10) and 1c with one more methoxyl substitution (entry 11–13), were tested over the three NP samples. Despite the generally higher yields with 1b and lower yields with 1c ascribed to their difference in steric hindrance, similar trends were observed: Rh NPs showed 100% conversion with all the benzene rings hydrogenated; Ni NPs showed high selectivity but very low activity; NiO<sub>x</sub>/Rh exhibited moderate conversion but always with excellent inhibition of the benzene ring hydrogenation due to NiO<sub>x</sub> blockage.

This catalysis work was done during two one-month stays in the lab of Pr. Ning Yan in 2014 and 2015. It has been accepted for a publication at *J. Mol. catal A: Chemical*, **2016** which is presently in press.<sup>85</sup>

### IV.5 Conclusion

In this chapter, we presented the investigation of different systems of Rh-based NPs whose synthesis and characterization were described in chapter II and III in catalytic applications including hydrogenation, hydroformylation and hydrogenolysis reactions.

Hydrogenation using RhPVP, Rh-dppb and RhPPh<sub>3</sub> NPs in colloidal and supported conditions was performed in the Laboratory of Nanomaterials and Catalysis headed by L. Rossi at the University of São Paulo, Brazil. Obtained results (submitted to a publication)<sup>303</sup> revealed that these Rh NPs systems are very active in hydrogenation of alkenes. Moreover, and profiting from the magnetic property of the support, recycling and reusing were easily achieved with high TOFs. Hydrogenation of different arenes was also performed leading to full conversions. The chemoselective hydrogenation of benzoic acid, levulinic acid, and their derivatives using PVP-Stabilized Rh NPs in water was also achieved giving rise to very interesting results in mild conditions. In addition, “ketone hydrogenation followed by cyclization” reaction was performed in the presence of RhPVP NPs to synthesize  $\gamma$ -valerolactone with also promising results. This work was performed in collaboration with E.J. Garcia-Suarez at the technical university of Denmark.

A novel system of Rh NPs stabilized with ferrocenyl phosphino ligands (from the colleagues at LCC; E. Deydier, E. Manoury and R. Poli) was evaluated in the hydrogenation reaction of styrene. The effect of the presence or absence of base on the selectivity of the reaction was studied as well. It appeared clearly that the ferrocenyl phosphino ligand stabilized Rh NPs favor the formation of ethylbenzene over ethylcyclohexane. These results are attributed to a blockage of the rhodium surface due to size limitations and ligand coordination. They thus open the door towards selective hydrogenation of compounds by using Rh NPs that have a limited accessibility of their surface by a careful choice of their stabilizers. More work in this direction would be of interest to develop more selective nanocatalysts.

In the second part of this chapter, hydroformylation reaction was studied, firstly through a comparison between the RhPPh<sub>3</sub> system synthesized *via* the organometallic approach and another system of RhTOAB NPs synthesized by reduction of metal salts. Obtained results showed that the RhPPh<sub>3</sub> system surpass the RhTOAB one in terms of activity and selectivity even after adding 20 equivalents of extra monophosphines for the RhTOAB one (a publication is presently in preparation). Secondly, novel CXP-stabilized RhNPs were utilized in the hydroformylation of styrene. They presented high activity, and selectivity but these preliminary results need to be completed to confirm the interest of these NPs in this reaction and to compare with the activity of molecular complexes stabilized with the same calixarene. This part was realized with D. Semeril in Strasbourg.

In the third part, bimetallic PVP-stabilized RhNiO<sub>x</sub> NPs were applied in the hydrogenolysis reaction of several substrates that imitate the lignin structure. The decoration of the surface of the Rh NPs with NiO<sub>x</sub> regions served to overcome the hydrogenation pathway and to obtain desired aromatic products with high yields. These results obtained in collaboration with the group of N. Yan from Singapore (Merlion project) were submitted to *J. Mol. Catal. A: Chem.* and accepted for publication in 2016, presently in press.

All these catalysis studies evidence the interest of having in hands metal nanoparticles, in the present case of rhodium but it is true for any other metal, that are well-controlled in size and surface state for a better understanding of the relationships between the structure of the particles and their catalytic performances. The organometallic approach

developed in the team may offer efficient synthesis tool and nice NP systems to perform such studies which are key point to be able to develop more active and more efficient nanocatalysts.

**Chapter V :**

**General**

**Conclusion and**

**Perspectives**

---





## V. General Conclusion and Perspectives

In this PhD manuscript, the synthesis, characterization and application in catalysis of rhodium based mono- and bimetallic nanoparticles are reported. Rhodium has been chosen as the core metal of this thesis work given its well-known ability to catalyze an array of synthetic transformations, with quite often unique selectivity, especially in the hydrogenation and hydroformylation reactions.

The main objective of the work was the development of synthesis tools to achieve small and well-defined rhodium nanoparticles in the presence of various stabilizers including a polymer and different coordinating ligands. The second objective was to investigate the obtained nanoparticles in the catalysis to study the influence of the stabilizing agent on their surface properties. This research project has been developed thanks to a MESR fellowship and CNRS funding. It included several collaborations at the national and international levels. During the thesis course, three one-month stays were performed overseas. A first stage was done in the group of Pr. Liane M. Rossi at the “*Laboratory of Nanomaterials and Catalysis*” (University of Sao Paulo, Brasil) under the framework of a CAPES-COFECUB project. Two others took place in the group of Pr. Ning Yan at the “*Laboratory of Green Catalysis*” (NUS, Singapore) under the framework of a MERLION project. These short stays allowed to develop catalysis applications.

Monometallic rhodium nanoparticles were synthesized following the organometallic approach by decomposition of the  $[\text{Rh}(\eta^3\text{-C}_3\text{H}_5)_3]$  complex in solution under mild dihydrogen pressure (3 bar) and in the presence of a specific stabilizer from the beginning of the procedure. Bimetallic rhodium containing nanoparticles were synthesized following the same procedure in one step by co-decomposition of the  $[\text{Rh}(\eta^3\text{-C}_3\text{H}_5)_3]$  complex with another organometallic precursor ( $[\text{Ni}(\text{cod})_2]$ ,  $[\text{Pd}_2(\text{dba})_3]$ ,  $[\text{Ru}(\text{cod})(\text{cot})]$  and  $[\text{Pt}(\text{nor})_3]$ ). The preparation of well-controlled particles that are small in size could be achieved in a reproducible manner. The characterization of the so-obtained nanoparticles performed using different techniques including: TEM, HRTEM, EDX, WAXS, XPS, EXAFS, XANES, NMR, IR, ICP... among other techniques. Various types of stabilizers were used in the synthesis of the nanoparticles, showing difference in their ability to control the NPs growth. This is the result of different behaviors regarding the formation of nuclei and interaction with metal

surface; some ligands coordinate strongly to the rhodium surface (carbenes, phosphines), and others weakly (HDA), while PVP polymer allows steric stabilization without direct coordination.

The synthesis of PVP-stabilized rhodium nanoparticles offered nanoparticles with a free surface that allowed us to compare their reactivity in catalysis with that of nanoparticles stabilized with coordinating ligands. Indeed, it is generally considered that the polyvinylpyrrolidone polymer (PVP) blocks the growth of the metal nanoparticles by a confinement effect inside the cavities of the polymeric matrix while ligands coordinate at the surface. Using a percentage of 10% w.t. of PVP to rhodium, the formation of particles was fast at room temperature, and resulted in small, spherical and well-controlled NPs with a mean size of  $2.2 \pm 0.9$  nm. These particles presented a high activity in the catalytic hydrogenation of alkenes and arenes under mild reaction conditions in comparison with other systems of particles that is attributed to the ability of the clean and free metallic surface to host the substrates. However, in hydroformylation reaction, RhPVP nanoparticles were not active, which can be explained by the absence of ligands notably phosphine ones, as it is well-known that phosphines are needed for rhodium to catalyze this reaction.

For the decomposition of the  $[\text{Rh}(\eta^3\text{-C}_3\text{H}_5)_3]$  precursor in the presence of strong coordinating ligands, including phosphines and carbenes, it was noticed that heating the system was essential to prepare NPs. In order to understand the reason behind this, NMR study was done in the case of triphenylphosphine as a ligand by performing the synthesis of the particles inside a NMR tube under dihydrogen pressure, that revealed the formation of a Rh-phosphine specie in solution, which disappeared after formation of NPs.

The use of triphenylphosphine ( $\text{PPh}_3$ ) and (diphenylphosphino)butane (dppb) ligands in the synthesis of Rh NPs, which differ in the number of P coordinating atoms to the rhodium surface, evidenced that a starting ratio of  $[\text{P}]/[\text{Rh}] = 0.6$  to 1 is necessary to achieve nanoparticles that are well-controlled and small in size. The so-obtained particles display similar characteristics in terms of size, dispersion and low crystallinity, as well as surface state. However, their behavior in the hydrogenation of alkenes in colloidal solution and after their immobilization on silica-coated magnetic particles as a support was almost identical.  $\text{PPh}_3$ -stabilized rhodium nanoparticles were also tested in the hydroformylation of styrene

and octene, resulting in high catalytic activity when comparing with other rhodium nano systems that were synthesized from  $\text{RhCl}_3 \cdot 3\text{H}_2\text{O}$  as metal source (with TOAB as stabilizer) even in the presence of added phosphines.

The synthesis of water-soluble Rh NPs using 1,3,5-triaza-7-phosphaadamantane (PTA) as ligand, similarly to the  $\text{PPh}_3$  and dppb ligands, needed heating and a [P]/[Rh] ratio of 0.8 to achieve well-controlled NPs. These obtained particles showed a very small size and strong hydrophilic character, which allowed their easy transfer into water while maintaining their small size. This study allows to have in hands synthesis tools towards aqueous colloidal solutions of ultra-small RhNPs that may be of high interest in catalysis.

In collaboration with the group of Prof. R. Poli and Dr. E. Manoury at the LCC-Toulouse, we investigated the use of ferrocenyl phosphino ligands. They exhibited strong control upon using 0.2 equivalents of the ligands resulting in very small particles with a size range between 1.1 and 1.7 nm. Up to our knowledge, this type of ligands had never been used in the synthesis of metal nanoparticles before. Catalytic studies with chosen systems in the selective hydrogenation of styrene showed promising results.

Another novel ligand used in the synthesis of rhodium nanoparticles is the CXP macromolecule, which is a calix[4]arene biphosphite macrocycle through a collaboration with Dr. David Sémeril at the "*Laboratoire de Chimie Inorganique Moléculaire et Catalyse*" in Strasbourg. Obtained NPs were applied in the hydroformylation of styrene, resulting in high activity and selectivity which is challenging in nanocatalysts.

Another class of ligands, namely N-heterocyclic carbenes were also tested in the synthesis of rhodium nanoparticles. The formation of the free carbenes was performed instantaneously in the same vessel while synthesizing the NPs, upon heating and using the right quantities of base and ligand. Nice rhodium NPs could be achieved in this conditions that are also water-soluble thanks to the sulfonate groups the ligand bear. More work is needed to develop this part of the PhD but it opens new perspective.

In addition to the RhNPs synthesis, we also explored the deposition of selected particles on amino-modified silica support. This part was performed at the “*Laboratory of Nanomaterials and Catalysis*” (University of Sao Paulo, Brasil headed by L. Rossi). Supported rhodium nanoparticles were evaluated in the hydrogenation of alkenes showing increased activity in comparison with the colloidal ones. In addition, thanks to the magnetic character of the support, recycling and reuse of the catalysts could be easily performed improving the interest of these supported nanocatalysts.

The preparation of bimetallic nanoparticles, was performed using the  $[\text{Rh}(\eta^3\text{-C}_3\text{H}_5)_3]$  precursor with other organometallic complexes in one pot procedure. These complexes include  $[\text{Ni}(\text{cod})_2]$ ,  $[\text{Pd}_2(\text{dba})_3]$ ,  $[\text{Ru}(\text{cod})(\text{cot})]$  and  $[\text{Pt}(\text{nor})_3]$ . The stabilization of the bimetallic systems was performed either with PVP or HDA, leading to well-controlled systems. Some of the described systems require further characterization to better understand their composition and surface state, in addition of studying their interest in catalysis or other fields of applications. Nevertheless, the results obtained open the door for the development of future research. Whereas, another system has been fully-characterized and engineered towards a precise aim, such as the PVP-stabilized  $\text{RhNiO}_x$  system. This system was carefully tailored to synthesize small well-controlled rhodium cores decorated with nickel islands on the surface by using exact metal amounts. Later, the nickel regions were oxidized to inhibit their reactivity. This was achieved to overcome the high activity of rhodium in hydrogenation of arenes by reducing the active site areas preventing the substrate approachment through the face. This inhibition helped in favoring hydrogenolysis C-O bond cleavage reaction, which is useful in the lignin transformation to biofuel by giving rise to desired hydrocarbons. This system was characterized with several techniques including EXAFS, EXANES, magnetic measurements and else. It was performed in close collaboration with the group of N. Yan at the “*Laboratory of Green Catalysis*” (NUS, Singapore).

This thesis work thus offers a library of different rhodium-based mono and bimetallic nanoparticles that are easily synthesized from the  $[\text{Rh}(\eta^3\text{-C}_3\text{H}_5)_3]$  precursor in mild reaction conditions including low dihydrogen pressure. The so-obtained nanoparticles are well-controlled and display a metallic surface available for chemical transformations. The rhodium surface could be functionalized by a careful choice of the stabilizer with the aim to tune their surface properties. We also reported the successful use of novel ligands that gave rise to well-

controlled particles with very interesting catalytic performance, notably in the terms of regioselectivity which is a challenging part of nanocatalysis. The rhodium nanoparticles prepared presented high activity in hydrogenation, hydroformylation and hydrogenolysis. Obtained results show the effect of the stabilizers on the behavior of the catalysts, allowing to provide fundamental conclusions. Also, the reported surface decoration approach followed for RhNiO<sub>x</sub> system may help in orientating the activity of other nanocatalysts, and our results in the hydrogenolysis catalysis is a good objective evidence of the power of the organometallic way to achieve successfully.

In this thesis, we investigated the synthesis, characterization and the surface properties of rhodium based mono- and bimetallic nanoparticles using the concept of coordination chemistry. The originality of this work lies with the large variety of stabilizing agents used to design monometallic Rh NPs in one hand, and in a second hand the preparation of bimetallic Rh NPs. We could obtain nice results in this field, thanks to the effectiveness of the organometallic approach. Some of the obtained nanoparticles systems were successfully applied in catalysis, thus showing the interest of solution modern nanochemistry. Some results of this work are not complete, and need more efforts to totally understand the studied systems and profit from them, and will be kept as open doors for future research.

## References

- (1) Philippot, K.; Chaudret, B. *Comptes Rendus Chimie* **2003**, *6*, 1019.
- (2) Philippot, K.; Serp, P. In *Nanomaterials in Catalysis*; Wiley-VCH Verlag GmbH & Co. KGaA: 2013, p 1.
- (3) Salata, O. *Journal of Nanobiotechnology* **2004**, *2*, 3.
- (4) Ely, T. O.; Amiens, C.; Chaudret, B.; Snoeck, E.; Verelst, M.; Respaud, M.; Broto, J.-M. *Chemistry of Materials* **1999**, *11*, 526.
- (5) Yi, D. K.; Lee, S. S.; Ying, J. Y. *Chemistry of Materials* **2006**, *18*, 2459.
- (6) Riley, D. J. *Current Opinion in Colloid & Interface Science* **2002**, *7*, 186.
- (7) Denicourt-Nowicki, A.; Roucoux, A. In *Nanomaterials in Catalysis*; Wiley-VCH Verlag GmbH & Co. KGaA: 2013, p 55.
- (8) Astruc, D. In *Nanoparticles and Catalysis*; Wiley-VCH Verlag GmbH & Co. KGaA: 2008, p 1.
- (9) Chorkendorff, I.; Niemantsverdriet, J. W. In *Concepts of Modern Catalysis and Kinetics*; Wiley-VCH Verlag GmbH & Co. KGaA: 2005, p 1.
- (10) Allhoff, F.; Lin, P.; Moore, D.; Wiley- Blackwell: Malden, MA, 2010.
- (11) In *Comptes Rendus de la 11e CGPM (1960)* 1961, p 87.
- (12) Taniguchi, N. In *Intl. Conf. Prod. Eng. Tokyo, Part II, Japan Society of Precision Engineering*, 1974.
- (13) Feynman, R. In *American Physical Society meeting at the California Institute of Technology (CalTech)* California, 1959.
- (14) Appenzeller, T. I. M. *Science* **1991**, *254*, 1300.
- (15) Angelini, I. *Journal of Archaeological Science*, **2004**, *31*, 1175.
- (16) Ashby *Nanomaterials, nanotechnologies and design : an introduction for engineers and architects* Burlington, Mass : Butterworth-Heinemann, 2009.
- (17) Heiligtag, F. J.; Niederberger, M. *Materials Today* **2013**, *16*, 262.
- (18) Wood, N. *Chinese glazes, their origins, chemistry and recreation*, University of Pennsylvania Press Philadelphia, USA. , 1999.
- (19) Hunt, L. B. *Gold Bull* **1976**, *9*, 134.
- (20) Faraday, M. *Philosophical Transactions of the Royal Society of London* **1857**, *147*, 145.

- (21) Graham, T. *Philosophical Transactions of the Royal Society of London* **1861**, 151, 183.
- (22) Wood, R. W. *Philosophical Magazine Series 6* **1902**, 4, 396.
- (23) Wood, R. W. *Philosophical Magazine Series 6* **1912**, 24, 316.
- (24) Mie, G. *Annalen der Physik* **1908**, 330, 377.
- (25) Rickerby, D. G. *Impact of Electron and Scanning Probe Microscopy on Materials Research*; Springer Netherlands, 1999; Vol. 364.
- (26) von Ardenne, M. *Z. Physik* **1938**, 109, 553.
- (27) Endo, M.; Kroto, H. W. *The Journal of Physical Chemistry* **1992**, 96, 6941.
- (28) Oberlin, A.; Endo, M.; Koyama, T. *Journal of Crystal Growth* **1976**, 32, 335.
- (29) Carlson, D. E.; Wronski, C. R. *Applied Physics Letters* **1976**, 28, 671.
- (30) Klitzing, K. v.; Dorda, G.; Pepper, M. *Physical Review Letters* **1980**, 45, 494.
- (31) Binnig, G.; Rohrer, H. *IBM Journal of Research and Development* **1986**, 30, 355.
- (32) Binnig, G.; Quate, C. F.; Gerber, C. *Physical Review Letters* **1986**, 56, 930.
- (33) Haruta, M.; Kobayashi, T.; Sano, H.; Yamada, N. *Chemistry Letters* **1987**, 16, 405.
- (34) Thompson, D. T. *Nano Today* **2007**, 2, 40.
- (35) Iijima, S. *Nature* **1991**, 354, 56.
- (36) Jang, B.; Huang, W.; Nanotek Instruments, Inc.: United States, 2002; Vol. 36613711.
- (37) Mirkin, C. A. *Small* **2005**, 1, 14.
- (38) Prieto, G.; Zečević, J.; Friedrich, H.; de Jong, K. P.; de Jongh, P. E. *Nat Mater* **2013**, 12, 34.
- (39) Hartland, G.; Okamoto, H.; Orrit, M.; Zijlstra, P. *Physical Chemistry Chemical Physics* **2013**, 15, 4090.
- (40) Nitta, N.; Wu, F.; Lee, J. T.; Yushin, G. *Materials Today* **2015**, 18, 252.
- (41) Tee, B. C. K.; Wang, C.; Allen, R.; Bao, Z. *Nat Nano* **2012**, 7, 825.
- (42) Aiken Iii, J. D.; Finke, R. G. *Journal of Molecular Catalysis A: Chemical* **1999**, 145, 1.
- (43) Paul, D. B.; Jason, J. D. In *Dekker Encyclopedia of Nanoscience and Nanotechnology, Second Edition*; Taylor & Francis: 2009; Vol. null, p 2898.
- (44) McCaffrey, R.; Long, H.; Jin, Y.; Sanders, A.; Park, W.; Zhang, W. *Journal of the American Chemical Society* **2014**, 136, 1782.

- (45) Jin, R.; Cao, Y.; Mirkin, C. A.; Kelly, K. L.; Schatz, G. C.; Zheng, J. G. *Science* **2001**, *294*, 1901.
- (46) Schmid, G. *Chemical Reviews* **1992**, *92*, 1709.
- (47) Horikoshi, S.; Serpone, N. In *Microwaves in Nanoparticle Synthesis*; Wiley-VCH Verlag GmbH & Co. KGaA: 2013, p 1.
- (48) Sakthivel, S.; Krishnan, V. V.; Pitchumani, B. *Particuology* **2008**, *6*, 120.
- (49) Brust, M.; Walker, M.; Bethell, D.; Schiffrin, D. J.; Whyman, R. *Journal of the Chemical Society, Chemical Communications* **1994**, 801.
- (50) Guari, Y.; Thieuleux, C.; Mehdi, A.; Reye, C.; Corriu, R. J. P.; Gomez-Gallardo, S.; Philippot, K.; Chaudret, B.; Dutartre, R. *Chemical Communications* **2001**, 1374.
- (51) Yonezawa, T.; Yasui, K.; Kimizuka, N. *Langmuir* **2001**, *17*, 271.
- (52) Douglas, F. J.; MacLaren, D. A.; Murrie, M. *RSC Advances* **2012**, *2*, 8027.
- (53) Link, S.; El-Sayed, M. A. *The Journal of Physical Chemistry B* **1999**, *103*, 4212.
- (54) Turkevich, J.; Kim, G. *Science* **1970**, *169*, 873.
- (55) Maase, M.; Verlag Mainz: Aachen, 1999.
- (56) Oxtoby, D. W. *Nature* **2000**, *406*, 464.
- (57) LEISNER, T.; ROSCHE, C.; WOLF, S.; GRANZER, F.; WÖSTE, L. *Surface Review and Letters* **1996**, *03*, 1105.
- (58) Bönnemann, H.; Richards, Ryan M. *European Journal of Inorganic Chemistry* **2001**, *2001*, 2455.
- (59) Cavicchioli, M.; Varanda, L. C.; Massabni, A. C.; Melnikov, P. *Materials Letters* **2005**, *59*, 3585.
- (60) Eustis, S.; Hsu, H.-Y.; El-Sayed, M. A. *The Journal of Physical Chemistry B* **2005**, *109*, 4811.
- (61) Lee, S. W.; Kumpfer, J. R.; Lin, P. A.; Li, G.; Gao, X. P. A.; Rowan, S. J.; Sankaran, R. M. *Macromolecules* **2012**, *45*, 8201.
- (62) Ernst, A. Z.; Sun, L.; Wiaderek, K.; Kolary, A.; Zoladek, S.; Kulesza, P. J.; Cox, J. A. *Electroanalysis* **2007**, *19*, 2103.
- (63) Ponce, A. A.; Klabunde, K. J. *Journal of Molecular Catalysis A: Chemical* **2005**, *225*, 1.
- (64) Sperling, R. A.; Parak, W. J. *Philosophical Transactions of the Royal Society of London A: Mathematical, Physical and Engineering Sciences* **2010**, *368*, 1333.
- (65) Sun, Q.; Li, Z.; Li, S.; Jiang, L.; Wang, J.; Wang, P. *Energy & Fuels* **2014**, *28*, 2384.



- (66) In *Metallopolymer Nanocomposites*; Springer Berlin Heidelberg: 2005; Vol. 81, p 65.
- (67) Ratheesh Kumar, V. K.; Gopidas, K. R. *Tetrahedron Letters* **2011**, 52, 3102.
- (68) Luska, K. L.; Migowski, P.; Leitner, W. *Green Chemistry* **2015**, 17, 3195.
- (69) Roucoux, A.; Schulz, J.; Patin, H. *Chemical Reviews* **2002**, 102, 3757.
- (70) Ling, D.; Hackett, M. J.; Hyeon, T. *Nano Today* **2014**, 9, 457.
- (71) Pan, C.; Pelzer, K.; Philippot, K.; Chaudret, B.; Dassenoy, F.; Lecante, P.; Casanove, M.-J. *Journal of the American Chemical Society* **2001**, 123, 7584.
- (72) Dassenoy, F.; Philippot, K.; Ould Ely, T.; Amiens, C.; Lecante, P.; Snoeck, E.; Mosset, A.; Casanove, M.-J.; Chaudret, B. *New Journal of Chemistry* **1998**, 22, 703.
- (73) Kinayyigit, S.; Lara, P.; Lecante, P.; Philippot, K.; Chaudret, B. *Nanoscale* **2014**, 6, 539.
- (74) Scott, R. W. J.; Wilson, O. M.; Crooks, R. M. *The Journal of Physical Chemistry B* **2005**, 109, 692.
- (75) Amiens, C.; Chaudret, B.; Ciuculescu-Pradines, D.; Colliere, V.; Fajerweg, K.; Fau, P.; Kahn, M.; Maisonnat, A.; Soulantica, K.; Philippot, K. *New Journal of Chemistry* **2013**, 37, 3374.
- (76) McCabe, R. W. *Synthesis and Reactivity in Inorganic and Metal-Organic Chemistry* **1987**, 17, 455.
- (77) Axet, M. R.; Castellón, S.; Claver, C.; Philippot, K.; Lecante, P.; Chaudret, B. *European Journal of Inorganic Chemistry* **2008**, 2008, 3460.
- (78) Ayval, T.; Lecante, P.; Fazzini, P.-F.; Gillet, A.; Philippot, K.; Chaudret, B. *Chemical Communications* **2014**, 50, 10809.
- (79) Zitoun, D.; Respaud, M.; Fromen, M.-C.; Casanove, M. J.; Lecante, P.; Amiens, C.; Chaudret, B. *Physical Review Letters* **2002**, 89, 037203.
- (80) de Caro, D.; Wally, H.; Amines, C.; Chaudret, B. *Journal of the Chemical Society, Chemical Communications* **1994**, 1891.
- (81) Redel, E.; Krämer, J.; Thomann, R.; Janiak, C. *Journal of Organometallic Chemistry* **2009**, 694, 1069.
- (82) Amiens, C.; de Caro, D.; Chaudret, B.; Bradley, J. S.; Mazel, R.; Roucau, C. *Journal of the American Chemical Society* **1993**, 115, 11638.
- (83) GERD H. WOEHRLER; JAMES E. HUTCHISON; SAİM ÖZKAR; FINKE, R. G. *Turk J Chem* **2006**, 30, 1.
- (84) Podorov, S. G.; Faleev, N. N.; Pavlov, K. M.; Paganin, D. M.; Stepanov, S. A.; Förster, E. *Journal of Applied Crystallography* **2006**, 39, 652.

- (85) Zhang, J.; Ibrahim, M.; Collière, V.; Asakura, H.; Tanaka, T.; Teramura, K.; Philippot, K.; Yan, N. *Journal of Molecular Catalysis A: Chemical* **2016**.
- (86) Marbella, L. E.; Millstone, J. E. *Chemistry of Materials* **2015**, *27*, 2721.
- (87) Pastawski, H. M.; Gascón, J. A. *Physical Review B* **1997**, *56*, 4887.
- (88) Gaur, A.; Shrivastava, B. D. *Ref. J. Chem.* **2015**, *5*, 361.
- (89) Henderson, G. S.; de Groot, F. M. F.; Moulton, B. J. A. *Reviews in Mineralogy and Geochemistry* **2014**, *78*, 75.
- (90) Melancon, M.; Lu, W.; Li, C. *Materials research bulletin* **2009**, *34*, 415.
- (91) Guo, D.; Zhu, L.; Huang, Z.; Zhou, H.; Ge, Y.; Ma, W.; Wu, J.; Zhang, X.; Zhou, X.; Zhang, Y.; Zhao, Y.; Gu, N. *Biomaterials* **2013**, *34*, 7884.
- (92) Mohammadi, H.; Abedi, A.; Akbarzadeh, A.; Mokhtari, M. J.; Shahmabadi, H. E.; Mehrabi, M. R.; Javadian, S.; Chiani, M. *International Nano Letters* **2013**, *3*, 28.
- (93) Selvan, S. T.; Tan, T. T. Y.; Yi, D. K.; Jana, N. R. *Langmuir* **2010**, *26*, 11631.
- (94) Hirsch, L. R.; Stafford, R. J.; Bankson, J. A.; Sershen, S. R.; Rivera, B.; Price, R. E.; Hazle, J. D.; Halas, N. J.; West, J. L. *Proceedings of the National Academy of Sciences* **2003**, *100*, 13549.
- (95) Walkey, C.; Das, S.; Seal, S.; Erlichman, J.; Heckman, K.; Ghibelli, L.; Traversa, E.; McGinnis, J. F.; Self, W. T. *Environmental Science: Nano* **2015**, *2*, 33.
- (96) Rai, M.; Yadav, A.; Gade, A. *Biotechnology Advances* **2009**, *27*, 76.
- (97) Weir, A.; Westerhoff, P.; Fabricius, L.; Hristovski, K.; von Goetz, N. *Environmental Science & Technology* **2012**, *46*, 2242.
- (98) Chung, J.; Ko, S.; Bieri, N. R.; Grigoropoulos, C. P.; Poulikakos, D. *Applied Physics Letters* **2004**, *84*, 801.
- (99) Chung, J.; Bieri, N. R.; Ko, S.; Grigoropoulos, C. P.; Poulikakos, D. *Appl Phys A* **2004**, *79*, 1259.
- (100) Tang, B.; Li, J.; Hou, X.; Afrin, T.; Sun, L.; Wang, X. *Industrial & Engineering Chemistry Research* **2013**, *52*, 4556.
- (101) Becheri, A.; Dürr, M.; Lo Nostro, P.; Baglioni, P. *J Nanopart Res* **2008**, *10*, 679.
- (102) Sanchez, F.; Sobolev, K. *Construction and Building Materials* **2010**, *24*, 2060.
- (103) Cedillo-González, E. I.; Riccò, R.; Montorsi, M.; Montorsi, M.; Falcaro, P.; Siligardi, C. *Building and Environment* **2014**, *71*, 7.
- (104) Nowack, B.; Bucheli, T. D. *Environmental Pollution* **2007**, *150*, 5.
- (105) Zhang, W.-x. *J Nanopart Res* **2003**, *5*, 323.
- (106) Sinha, A. K.; Suzuki, K.; Takahara, M.; Azuma, H.; Nonaka, T.; Fukumoto, K. *Angewandte Chemie International Edition* **2007**, *46*, 2891.

- (107) Zhang, J.; Teo, J.; Chen, X.; Asakura, H.; Tanaka, T.; Teramura, K.; Yan, N. *ACS Catalysis* **2014**, *4*, 1574.
- (108) Yan, N.; Zhao, C.; Luo, C.; Dyson, P. J.; Liu, H.; Kou, Y. *Journal of the American Chemical Society* **2006**, *128*, 8714.
- (109) Xia, Y.; Xiong, Y.; Lim, B.; Skrabalak, S. E. *Angewandte Chemie International Edition* **2009**, *48*, 60.
- (110) Wollaston, W. H. *Philosophical Transactions of the Royal Society of London* **1804**, *94*, 419.
- (111) Nomura, K. *Journal of Molecular Catalysis A: Chemical* **1998**, *130*, 1.
- (112) Guerrero, M.; Chau, N. T. T.; Noel, S.; Denicourt-Nowicki, A.; Hapiot, F.; Roucoux, A.; Monflier, E.; Philippot, K. *Current Organic Chemistry* **2013**, *17*, 364.
- (113) Roucoux, A.; Nowicki, A.; Philippot, K. In *Nanoparticles and Catalysis*; Wiley-VCH Verlag GmbH & Co. KGaA: 2008, p 349.
- (114) Rossen, K. *Angewandte Chemie International Edition* **2001**, *40*, 4611.
- (115) Wang, Q.; Liu, H.; Han, M.; Li, X.; Jiang, D. *Journal of Molecular Catalysis A: Chemical* **1997**, *118*, 145.
- (116) Moreno-Mañas, M.; Pleixats, R. *Accounts of Chemical Research* **2003**, *36*, 638.
- (117) Guha, N. R.; Reddy, C. B.; Aggarwal, N.; Sharma, D.; Shil, A. K.; Bandna, Das, P. *Advanced Synthesis & Catalysis* **2012**, *354*, 2911.
- (118) Kanuru, V. K.; Humphrey, S. M.; Kyffin, J. M. W.; Jefferson, D. A.; Burton, J. W.; Armbruster, M.; Lambert, R. M. *Dalton Transactions* **2009**, 7602.
- (119) Li, L.; Tian, C.; Yang, J.; Zhang, X.; Chen, J. *International Journal of Hydrogen Energy* **2015**, *40*, 14866.
- (120) Donck, S.; Gravel, E.; Li, A.; Prakash, P.; Shah, N.; Leroy, J.; Li, H.; Namboothiri, I. N. N.; Doris, E. *Catalysis Science & Technology* **2015**, *5*, 4542.
- (121) Rico Pérez, V.; Ángeles Velasco Beltrán, M.; He, Q.; Wang, Q.; Salinas Martínez de Lecea, C.; Bueno López, A. *Catalysis Communications* **2013**, *33*, 47.
- (122) Li, F.; Qian, Q.; Yan, F.; Yuan, G. *Materials Chemistry and Physics* **2008**, *107*, 310.
- (123) Park, J. H.; Kim, E.; Chung, Y. K. *Organic Letters* **2008**, *10*, 4719.
- (124) Zhang, Y.; Ligthart, D. A. J. M.; Quek, X.-Y.; Gao, L.; Hensen, E. J. M. *International Journal of Hydrogen Energy* **2014**, *39*, 11537.
- (125) Ikeda, T.; Xiong, A.; Yoshinaga, T.; Maeda, K.; Domen, K.; Teranishi, T. *The Journal of Physical Chemistry C* **2013**, *117*, 2467.

- (126) Maeda, K.; Teramura, K.; Masuda, H.; Takata, T.; Saito, N.; Inoue, Y.; Domen, K. *The Journal of Physical Chemistry B* **2006**, *110*, 13107.
- (127) Chandra, S.; Lokesh, K. S.; Nicolai, A.; Lang, H. *Analytica Chimica Acta* **2009**, *632*, 63.
- (128) Song, Z.; Chang, H.; Zhu, W.; Xu, C.; Feng, X. *Scientific Reports* **2015**, *5*, 7792.
- (129) Cantane, D. A.; Ambrosio, W. F.; Chatenet, M.; Lima, F. H. B. *Journal of Electroanalytical Chemistry* **2012**, *681*, 56.
- (130) Becher, P. *Journal of Dispersion Science and Technology* **1988**, *9*, 425.
- (131) Dautzenberg, H. *Acta Polymerica* **1985**, *36*, 457.
- (132) Hirai, H. *Journal of Macromolecular Science: Part A - Chemistry* **1979**, *13*, 633.
- (133) Borsla, A.; Wilhelm, A. M.; Delmas, H. *Catalysis Today* **2001**, *66*, 389.
- (134) Pellegatta, J.-L.; Blandy, C.; Collière, V.; Choukroun, R.; Chaudret, B.; Cheng, P.; Philippot, K. *Journal of Molecular Catalysis A: Chemical* **2002**, *178*, 55.
- (135) Ohde, H.; Ohde, M.; Wai, C. M. *Chemical Communications* **2004**, 930.
- (136) Mu, X.-d.; Evans, D.; Kou, Y. *Catal Lett* **2004**, *97*, 151.
- (137) Harada, T.; Ikeda, S.; Ng, Y. H.; Sakata, T.; Mori, H.; Torimoto, T.; Matsumura, M. *Advanced Functional Materials* **2008**, *18*, 2190.
- (138) Yang, X.; Yan, N.; Fei, Z.; Crespo-Quesada, R. M.; Laurenczy, G.; Kiwi-Minsker, L.; Kou, Y.; Li, Y.; Dyson, P. J. *Inorganic Chemistry* **2008**, *47*, 7444.
- (139) Huang, Y.; Xu, S.; Lin, V. S. Y. *ChemCatChem* **2011**, *3*, 690.
- (140) Quek, X.-Y.; Guan, Y.; Hensen, E. J. M. *Catalysis Today* **2012**, *183*, 72.
- (141) Yan, N.; Yuan, Y.; Dyson, P. J. *Chemical Communications* **2011**, *47*, 2529.
- (142) Bhorali, N.; Ganguli, J. *Catal Lett* **2013**, *143*, 276.
- (143) Rossi, L.; Vono, L. R.; Garcia, M. S.; Faria, T. T.; Lopez-Sanchez, J. *Top Catal* **2013**, *56*, 1228.
- (144) Moreno-Marrodan, C.; Liguori, F.; Mercade, E.; Godard, C.; Claver, C.; Barbaro, P. *Catalysis Science & Technology* **2015**, *5*, 3762.
- (145) Denicourt-Nowicki, A.; Roucoux, A. *Current Organic Chemistry* **2010**, *14*, 1266.
- (146) Komiyama, M.; Hirai, H. *Bulletin of the Chemical Society of Japan* **1983**, *56*, 2833.
- (147) Noel, S.; Leger, B.; Herbois, R.; Ponchel, A.; Tilloy, S.; Wenz, G.; Monflier, E. *Dalton Transactions* **2012**, *41*, 13359.

- (148) Kuklin, S.; Maximov, A.; Zolotukhina, A.; Karakhanov, E. *Catalysis Communications* **2016**, *73*, 63.
- (149) Guerrero, M.; Chau, N. T. T.; Noel, S.; Denicourt-Nowicki, A.; Hapiot, F.; Roucoux, A.; Monflier, E.; Philippot, K. *Current Organic Chemistry* **2013**, *17*, 364
- (150) Landre, P. D.; Richard, D.; Draye, M.; Gallezot, P.; Lemaire, M. *Journal of Catalysis* **1994**, *147*, 214.
- (151) Gual, A.; Godard, C.; Philippot, K.; Chaudret, B.; Denicourt-Nowicki, A.; Roucoux, A.; Castellón, S.; Claver, C. *ChemSusChem* **2009**, *2*, 769.
- (152) Escárcega-Bobadilla, M. V.; Tortosa, C.; Teuma, E.; Pradel, C.; Orejón, A.; Gómez, M.; Masdeu-Bultó, A. M. *Catalysis Today* **2009**, *148*, 398.
- (153) Buil, M. L.; Esteruelas, M. A.; Niembro, S.; Oliván, M.; Orzechowski, L.; Pelayo, C.; Vallribera, A. *Organometallics* **2010**, *29*, 4375.
- (154) Larpent, C.; Menn, F. B.-L.; Patin, H. *Journal of Molecular Catalysis* **1991**, *65*, L35.
- (155) Arzoumanian, H.; Nuel, D. *Comptes Rendus de l'Académie des Sciences - Series IIC - Chemistry* **1999**, *2*, 289.
- (156) Glöckler, J.; Klütze, S.; Meyer-Zaika, W.; Reller, A.; García-García, F. J.; Strehblow, H.-H.; Keller, P.; Rentschler, E.; Kläui, W. *Angewandte Chemie International Edition* **2007**, *46*, 1164.
- (157) Snelders, D. J. M.; Yan, N.; Gan, W.; Laurency, G.; Dyson, P. J. *ACS Catalysis* **2012**, *2*, 201.
- (158) Llop Castelbou, J.; Bresó-Femenia, E.; Blondeau, P.; Chaudret, B.; Castellón, S.; Claver, C.; Godard, C. *ChemCatChem* **2014**, *6*, 3160.
- (159) Denicourt-Nowicki, A.; Roucoux, A. In *Metal Nanoparticles for Catalysis: Advances and Applications*; The Royal Society of Chemistry: 2014, p 99.
- (160) Schulz, J.; Roucoux, A.; Patin, H. *Chemistry – A European Journal* **2000**, *6*, 618.
- (161) Schulz, J.; Levigne, S.; Roucoux, A.; Patin, H. *Advanced Synthesis & Catalysis* **2002**, *344*, 266.
- (162) Roucoux, A.; Schulz, J.; Patin, H. *Advanced Synthesis & Catalysis* **2003**, *345*, 222.
- (163) Mevellec, V.; Nowicki, A.; Roucoux, A.; Dujardin, C.; Granger, P.; Payen, E.; Philippot, K. *New Journal of Chemistry* **2006**, *30*, 1214.
- (164) Péliesson, C.-H.; Vono, L. L. R.; Hubert, C.; Denicourt-Nowicki, A.; Rossi, L. M.; Roucoux, A. *Catalysis Today* **2012**, *183*, 124.

- (165) Guyonnet Bilé, E.; Denicourt-Nowicki, A.; Sassine, R.; Beaunier, P.; Launay, F.; Roucoux, A. *ChemSusChem* **2010**, *3*, 1276.
- (166) Guyonnet Bilé, E.; Cortelazzo-Polisini, E.; Denicourt-Nowicki, A.; Sassine, R.; Launay, F.; Roucoux, A. *ChemSusChem* **2012**, *5*, 91.
- (167) Barthe, L.; Denicourt-Nowicki, A.; Roucoux, A.; Philippot, K.; Chaudret, B.; Hemati, M. *Catalysis Communications* **2009**, *10*, 1235.
- (168) Adkins, H.; Krsek, G. *Journal of the American Chemical Society* **1949**, *71*, 3051.
- (169) Garcia, M. A. S.; Oliveira, K. C. B.; Costa, J. C. S.; Corio, P.; Gusevskaya, E. V.; dos Santos, E. N.; Rossi, L. M. *ChemCatChem* **2015**, *7*, 1566.
- (170) Smith, T. W.; Google Patents: 1981.
- (171) Tuchbreiter, L.; Mecking, S. *Macromolecular Chemistry and Physics* **2007**, *208*, 1688.
- (172) Antonietti, L.; Aymonier, C.; Schlotterbeck, U.; Garamus, V. M.; Maksimova, T.; Richtering, W.; Mecking, S. *Macromolecules* **2005**, *38*, 5914.
- (173) Dupont, J.; Fonseca, G. S.; Umpierre, A. P.; Fichtner, P. F. P.; Teixeira, S. R. *Journal of the American Chemical Society* **2002**, *124*, 4228.
- (174) Bruss, A. J.; Gelesky, M. A.; Machado, G.; Dupont, J. *Journal of Molecular Catalysis A: Chemical* **2006**, *252*, 212.
- (175) Uson, R.; Oro, L. A.; Cabeza, J. A.; Bryndza, H. E.; Stepro, M. P. In *Inorganic Syntheses*; John Wiley & Sons, Inc.: 2007, p 126.
- (176) Han, D.; Li, X.; Zhang, H.; Liu, Z.; Hu, G.; Li, C. *Journal of Molecular Catalysis A: Chemical* **2008**, *283*, 15.
- (177) Li, K.; Wang, Y.; Jiang, J.; Jin, Z. *Catalysis Communications* **2010**, *11*, 542.
- (178) Li, K.; Wang, Y.; Jiang, J.; Jin, Z. *Chinese Journal of Catalysis* **2010**, *31*, 1191.
- (179) Behr, A.; Brunsch, Y.; Lux, A. *Tetrahedron Letters* **2012**, *53*, 2680.
- (180) Shaharun, M. S.; Dutta, B. K.; Mukhtar, H.; Maitra, S. *Chemical Engineering Science* **2010**, *65*, 273.
- (181) Zeng, Y.; Wang, Y.; Xu, Y.; Song, Y.; Zhao, J.; Jiang, J.; Jin, Z. *Chinese Journal of Catalysis* **2012**, *33*, 402.
- (182) Xu, Y.; Wang, Y.; Zeng, Y.; Jiang, J.; Jin, Z. *Catal Lett* **2012**, *142*, 914.
- (183) Lyubimov, S. E.; Rastorguev, E. A.; Lubentsova, K. I.; Korlyukov, A. A.; Davankov, V. A. *Tetrahedron Letters* **2013**, *54*, 1116.
- (184) Ioni, Y. V.; Lyubimov, S. E.; Davankov, V. A.; Gubina, S. P. *Russ Chem Bull* **2014**, *63*, 2243.

- (185) Tan, M.; Yang, G.; Wang, T.; Vitidsant, T.; Li, J.; Wei, Q.; Ai, P.; Wu, M.; Zheng, J.; Tsubaki, N. *Catalysis Science & Technology* **2015**.
- (186) Jacinto, M. J.; Kiyohara, P. K.; Masunaga, S. H.; Jardim, R. F.; Rossi, L. M. *Applied Catalysis A: General* **2008**, 338, 52.
- (187) de Silva, R. M.; Palshin, V.; Fronczek, F. R.; Hormes, J.; Kumar, C. S. S. R. *The Journal of Physical Chemistry C* **2007**, 111, 10320.
- (188) Amiens, C.; Ciuculescu-Pradines, D.; Philippot, K. *Coordination Chemistry Reviews* **2016**, 308, Part 2, 409.
- (189) Lagunas, A.; Jimeno, C.; Font, D.; Solà, L.; Pericàs, M. A. *Langmuir* **2006**, 22, 3823.
- (190) Cormary, B.; Dumestre, F.; Liakakos, N.; Soulantica, K.; Chaudret, B. *Dalton Transactions* **2013**, 42, 12546.
- (191) Liakakos, N.; Cormary, B.; Li, X.; Lecante, P.; Respaud, M.; Maron, L.; Falqui, A.; Genovese, A.; Vendier, L.; Koïnis, S.; Chaudret, B.; Soulantica, K. *Journal of the American Chemical Society* **2012**, 134, 17922.
- (192) Kwon, S. G.; Hyeon, T. *Accounts of Chemical Research* **2008**, 41, 1696.
- (193) He, M.; Protesescu, L.; Caputo, R.; Krumeich, F.; Kovalenko, M. V. *Chemistry of Materials* **2015**, 27, 635.
- (194) Barry, S. T. *Coordination Chemistry Reviews* **2013**, 257, 3192.
- (195) Ramirez-Meneses, E. PhD Thesis, Université Paul Sabatier, 2004.
- (196) Powell, J.; Shaw, B. L. *Chemical Communications (London)* **1966**, 236.
- (197) Powell, J.; Shaw, B. L. *Chemical Communications (London)* **1966**, 323.
- (198) Beconsall, J. K.; O'Brien, S. *Chemical Communications (London)* **1966**, 720.
- (199) Beconsall, J. K.; Job, B. E.; O'Brien, S. *Journal of the Chemical Society A: Inorganic, Physical, Theoretical* **1967**, 423.
- (200) Koczur, K. M.; Mourdikoudis, S.; Polavarapu, L.; Skrabalak, S. E. *Dalton Transactions* **2015**, 44, 17883.
- (201) BARLOW, W. *Nature* **1883**, 29, 186.
- (202) Barr, T. L. *The Journal of Physical Chemistry* **1978**, 82, 1801.
- (203) Peuckert, M. *Surface Science* **1984**, 141, 500.
- (204) de Caro, D.; S. Bradley, J. *New Journal of Chemistry* **1998**, 22, 1267.
- (205) Duncan, T. M.; Zilm, K. W.; Hamilton, D. M.; Root, T. W. *The Journal of Physical Chemistry* **1989**, 93, 2583.
- (206) Bradley, J. S.; Millar, J. M.; Hill, E. W.; Behal, S. *Journal of Catalysis* **1991**, 129, 530.

- (207) Bradley, J. S.; Hill, E. W.; Behal, S.; Klein, C.; Duteil, A.; Chaudret, B. *Chemistry of Materials* **1992**, *4*, 1234.
- (208) McMillan, J. W.; Fischer, H. E.; Schwartz, J. *Journal of the American Chemical Society* **1991**, *113*, 4014.
- (209) Martinez-Prieto, L. M.; Urbaneja, C.; Palma, P.; Campora, J.; Philippot, K.; Chaudret, B. *Chemical Communications* **2015**, *51*, 4647.
- (210) Basile, F.; Bersani, I.; Del Gallo, P.; Fiorilli, S.; Fornasari, G.; Gary, D.; Mortera, R.; Onida, B.; Vaccari, A. *International Journal of Spectroscopy* **2011**, *2011*, 8.
- (211) Castelbo, J. PhD Thesis, Rovira i Virgili University, 2014.
- (212) Wey, J. P.; Neely, W. C.; Worley, S. D. *The Journal of Physical Chemistry* **1991**, *95*, 8879.
- (213) Lara, P.; Philippot, K.; Chaudret, B. *ChemCatChem* **2013**, *5*, 28.
- (214) Son, S. U.; Jang, Y.; Yoon, K. Y.; Kang, E.; Hyeon, T. *Nano Letters* **2004**, *4*, 1147.
- (215) Bresó-Femenia, E.; Godard, C.; Claver, C.; Chaudret, B.; Castillon, S. *Chemical Communications* **2015**, *51*, 16342.
- (216) Gutmann, T.; Bonnefille, E.; Breitzke, H.; Debouttiere, P.-J.; Philippot, K.; Poteau, R.; Buntkowsky, G.; Chaudret, B. *Physical Chemistry Chemical Physics* **2013**, *15*, 17383.
- (217) Ramirez, E.; Jansat, S.; Philippot, K.; Lecante, P.; Gomez, M.; Masdeu-Bultó, A. M.; Chaudret, B. *Journal of Organometallic Chemistry* **2004**, *689*, 4601.
- (218) Heaton, B. T.; Iggo, J. A.; Jacob, C.; Nadarajah, J.; Fontaine, M. A.; Messere, R.; Noels, A. F. *Journal of the Chemical Society, Dalton Transactions* **1994**, 2875.
- (219) Kim, M.-S.; Song, H.-S.; Park, H. J.; Hwang, S.-J. *Chemical and Pharmaceutical Bulletin* **2012**, *60*, 543.
- (220) Grubbs, R. B. *Nat Mater* **2007**, *6*, 553.
- (221) Mayer, M.; Meyer, B. *Angewandte Chemie International Edition* **1999**, *38*, 1784.
- (222) Dassenoy, F.; Casanove, M.-J.; Lecante, P.; Verelst, M.; Snoeck, E.; Mosset, A.; Ely, T. O.; Amiens, C.; Chaudret, B. *The Journal of Chemical Physics* **2000**, *112*, 8137.
- (223) Choukroun, R.; de Caro, D.; Chaudret, B.; Lecante, P.; Snoeck, E. *New Journal of Chemistry* **2001**, *25*, 525.
- (224) Daigle, D. J.; Pepperman, A. B.; Vail, S. L. *Journal of Heterocyclic Chemistry* **1974**, *11*, 407.
- (225) Debouttiere, P.-J.; Martinez, V.; Philippot, K.; Chaudret, B. *Dalton Transactions* **2009**, 10172.



- (226) Debouttière, P.-J.; Coppel, Y.; Denicourt-Nowicki, A.; Roucoux, A.; Chaudret, B.; Philippot, K. *European Journal of Inorganic Chemistry* **2012**, 2012, 1229.
- (227) Chahdoura, F.; Favier, I.; Pradel, C.; Mallet-Ladeira, S.; Gómez, M. *Catalysis Communications* **2015**, 63, 47.
- (228) Cloete, J.; Mapolie, S. F.; Malgas-Enus, R. *Polyhedron* **2015**, 102, 469.
- (229) Sawamura, M.; Nakayama, Y.; Kato, T.; Ito, Y. *The Journal of Organic Chemistry* **1995**, 60, 1727.
- (230) McManus, H. A.; Guiry, P. J. *Chemical Reviews* **2004**, 104, 4151.
- (231) Cabrera, S.; Arrayás, R. G.; Martín-Matute, B.; Cossío, F. P.; Carretero, J. C. *Tetrahedron* **2007**, 63, 6587.
- (232) Mateus, N.; Routaboul, L.; Daran, J.-C.; Manoury, E. *Journal of Organometallic Chemistry* **2006**, 691, 2297.
- (233) Riener, K.; Haslinger, S.; Raba, A.; Högerl, M. P.; Cokoja, M.; Herrmann, W. A.; Kühn, F. E. *Chemical Reviews* **2014**, 114, 5215.
- (234) Waters, J. B.; Goicoechea, J. M. *Coordination Chemistry Reviews* **2015**, 293–294, 80.
- (235) Crudden, C. M.; Allen, D. P. *Coordination Chemistry Reviews* **2004**, 248, 2247.
- (236) Wang, Z.; Jiang, L.; Mohamed, D. K. B.; Zhao, J.; Hor, T. S. A. *Coordination Chemistry Reviews* **2015**, 293–294, 292.
- (237) Sommer, W. J.; Weck, M. *Coordination Chemistry Reviews* **2007**, 251, 860.
- (238) Youngs, W. J.; Knapp, A. R.; Wagers, P. O.; Tessier, C. A. *Dalton Transactions* **2012**, 41, 327.
- (239) Lara, P.; Suárez, A.; Collière, V.; Philippot, K.; Chaudret, B. *ChemCatChem* **2014**, 6, 87.
- (240) Tandukar, S.; Sen, A. *Journal of Molecular Catalysis A: Chemical* **2007**, 268, 112.
- (241) Hurst, E. C.; Wilson, K.; Fairlamb, I. J. S.; Chechik, V. *New Journal of Chemistry* **2009**, 33, 1837.
- (242) Gonzalez-Galvez, D.; Lara, P.; Rivada-Wheelaghan, O.; Conejero, S.; Chaudret, B.; Philippot, K.; van Leeuwen, P. W. N. M. *Catalysis Science & Technology* **2013**, 3, 99.
- (243) Baquero, E. A.; Tricard, S.; Flores, J. C.; de Jesús, E.; Chaudret, B. *Angewandte Chemie International Edition* **2014**, 53, 13220.
- (244) Astruc, D.; Lu, F.; Aranzaes, J. R. *Angewandte Chemie International Edition* **2005**, 44, 7852.

- (245) Rossi, L. M.; Silva, F. P.; Vono, L. L. R.; Kiyohara, P. K.; Duarte, E. L.; Itri, R.; Landers, R.; Machado, G. *Green Chemistry* **2007**, *9*, 379.
- (246) Philipse, A. P.; van Bruggen, M. P. B.; Pathmamanoharan, C. *Langmuir* **1994**, *10*, 92.
- (247) Jacinto, M. J.; Silva, F. P.; Kiyohara, P. K.; Landers, R.; Rossi, L. M. *ChemCatChem* **2012**, *4*, 698.
- (248) Peng, L.; Ringe, E.; Van Duyne, R. P.; Marks, L. D. *Physical Chemistry Chemical Physics* **2015**, *17*, 27940.
- (249) McNamara, K.; Tofail, S. A. M. *Physical Chemistry Chemical Physics* **2015**, *17*, 27981.
- (250) Shah, A.; Rahman, L.; Qureshi, R.; Z, R. *Rev. Adv. Mater. Sci.* **2012**, *30*, 133.
- (251) Wang, H.; Chen, L.; Feng, Y.; Chen, H. *Accounts of Chemical Research* **2013**, *46*, 1636.
- (252) Costa, N. J. S.; Guerrero, M.; Collière, V.; Teixeira-Neto, É.; Landers, R.; Philippot, K.; Rossi, L. M. *ACS Catal.* **2014**, *4*, 1735.
- (253) Mattei, J. G.; Pelletier, F.; Ciuculescu, D.; Lecante, P.; Dupin, J. C.; Yaacoub, N.; Allouche, J.; Greneche, J. M.; Gonbeau, D.; Amiens, C.; Casanove, M. J. *The Journal of Physical Chemistry C* **2013**, *117*, 1477.
- (254) Kim, K.; Kim, K. L.; Shin, K. S. *The Journal of Physical Chemistry C* **2011**, *115*, 14844.
- (255) Zhang, H.; Okuni, J.; Toshima, N. *Journal of Colloid and Interface Science* **2011**, *354*, 131.
- (256) Wu, W.; Lei, M.; Yang, S.; Zhou, L.; Liu, L.; Xiao, X.; Jiang, C.; Roy, V. A. L. *Journal of Materials Chemistry A* **2015**, *3*, 3450.
- (257) Jeyabharathi, C.; Venkateshkumar, P.; Mathiyarasu, J.; Phani, K. L. N. *Electrochimica Acta* **2008**, *54*, 448.
- (258) Qi, X.; Axet, M. R.; Philippot, K.; Lecante, P.; Serp, P. *Dalton Transactions* **2014**, *43*, 9283.
- (259) Gawande, M. B.; Goswami, A.; Asefa, T.; Guo, H.; Biradar, A. V.; Peng, D.-L.; Zboril, R.; Varma, R. S. *Chemical Society Reviews* **2015**, *44*, 7540.
- (260) Kahani, S. A.; Shahrokh, M. *New Journal of Chemistry* **2015**, *39*, 7916.
- (261) Sharma, M. K.; Buchner, R. D.; Scharmach, W. J.; Papavassiliou, V.; Swihart, M. T. *Aerosol Science and Technology* **2013**, *47*, 858.
- (262) Gniewek, A.; Trzeciak, A. M. *Top Catal* **2013**, *56*, 1239.
- (263) Duan, H.; Wang, D.; Kou, Y.; Li, Y. *Chemical Communications* **2013**, *49*, 303.

- (264) Nakamura, I.; Yamanoi, Y.; Imaoka, T.; Yamamoto, K.; Nishihara, H. *Angewandte Chemie International Edition* **2011**, *50*, 5830.
- (265) Peng, X.; Pan, Q.; Lu, X. *Journal of Applied Polymer Science* **2011**, *122*, 334.
- (266) Lin, J.; Chen, J.; Su, W. *Advanced Synthesis & Catalysis* **2013**, 355, 41.
- (267) Xia, B.; Cao, N.; Dai, H.; Su, J.; Wu, X.; Luo, W.; Cheng, G. *ChemCatChem* **2014**, *6*, 2549.
- (268) Xia, B.; Liu, C.; Wu, H.; Luo, W.; Cheng, G. *International Journal of Hydrogen Energy* **2015**, *40*, 16391.
- (269) Bergamaski, K.; Gonzalez, E. R.; Nart, F. C. *Electrochimica Acta* **2008**, *53*, 4396.
- (270) Musselwhite, N.; Alayoglu, S.; Melaet, G.; Pushkarev, V. V.; Lindeman, A. E.; An, K.; Somorjai, G. A. *Catal Lett* **2013**, *143*, 907.
- (271) Tu, W.; Hou, T.; Qi, K.; Chen, D.; Cao, S. *Colloids and Surfaces A: Physicochemical and Engineering Aspects* **2013**, *428*, 47.
- (272) Ciuculescu, D.; Amiens, C.; Respaud, M.; Falqui, A.; Lecante, P.; Benfield, R. E.; Jiang, L.; Fauth, K.; Chaudret, B. *Chemistry of Materials* **2007**, *19*, 4624.
- (273) Chandra, S.; Kumar, A.; Tomar, P. K. *Journal of Saudi Chemical Society* **2014**, *18*, 437.
- (274) Wu, S.-H.; Chen, D.-H. *Journal of Colloid and Interface Science* **2003**, *259*, 282.
- (275) Mozingo, R.; Spencer, C.; Folkers, K. *Journal of the American Chemical Society* **1944**, *66*, 1859.
- (276) Cordente, N.; Toustou, B.; Collière, V.; Amiens, C.; Chaudret, B.; Verelst, M.; Respaud, M.; Broto, J.-M. *Comptes Rendus de l'Académie des Sciences - Series IIC - Chemistry* **2001**, *4*, 143.
- (277) Cordente, N.; Respaud, M.; Senocq, F.; Casanove, M.-J.; Amiens, C.; Chaudret, B. *Nano Letters* **2001**, *1*, 565.
- (278) Salas, G.; Santini, C. C.; Philippot, K.; Colliere, V.; Chaudret, B.; Fenet, B.; Fazzini, P. F. *Dalton Transactions* **2011**, *40*, 4660.
- (279) Pelzer, K. PhD Thesis, Université Paul Sabatier, 2003.
- (280) Ramirez, E.; Eradès, L.; Philippot, K.; Lecante, P.; Chaudret, B. *Advanced Functional Materials* **2007**, *17*, 2219.
- (281) Garcia-Martinez, J. C.; Scott, R. W. J.; Crooks, R. M. *Journal of the American Chemical Society* **2003**, *125*, 11190.
- (282) Song, Q.; Wang, F.; Cai, J.; Wang, Y.; Zhang, J.; Yu, W.; Xu, J. *Energy & Environmental Science* **2013**, *6*, 994.

- (283) Sergeev, A. G.; Webb, J. D.; Hartwig, J. F. *Journal of the American Chemical Society* **2012**, *134*, 20226.
- (284) Torquato, S.; Stillinger, F. H. *Journal of Applied Physics* **2007**, *102*, 093511.
- (285) Baghbanian, S. M.; Farhang, M.; Vahdat, S. M.; Tajbakhsh, M. *Journal of Molecular Catalysis A: Chemical* **2015**, *407*, 128.
- (286) Yuanzhi, C.; Dong-Liang, P.; Dongxing, L.; Xiaohua, L. *Nanotechnology* **2007**, *18*, 505703.
- (287) Karimi, M.; Avci, P.; Mobasser, R.; Hamblin, M. R.; Naderi-Manesh, H. *Journal of nanoparticle research : an interdisciplinary forum for nanoscale science and technology* **2013**, *15*, 1651.
- (288) Rinaldi-Montes, N.; Gorria, P.; Martinez-Blanco, D.; Fuertes, A. B.; Fernandez Barquin, L.; Rodriguez Fernandez, J.; de Pedro, I.; Fdez-Gubieda, M. L.; Alonso, J.; Olivi, L.; Aquilanti, G.; Blanco, J. A. *Nanoscale* **2014**, *6*, 457.
- (289) Ramírez-Meneses, E.; Betancourt, I.; Morales, F.; Montiel-Palma, V.; Villanueva-Alvarado, C. C.; Hernández-Rojas, M. E. *J Nanopart Res* **2010**, *13*, 365.
- (290) Duan, S.; Wang, R. *Progress in Natural Science: Materials International* **2013**, *23*, 113.
- (291) Ugalde, M.; Chavira, E.; Ochoa-Lara, M. T.; Figueroa, I. A.; Quintanar, C.; Tejada, A. *Journal of Nanotechnology* **2013**, *2013*, 9.
- (292) Flanagan, T. B.; Baranowski, B.; Majchrzak, S. *The Journal of Physical Chemistry* **1970**, *74*, 4299.
- (293) Artman, D.; Flanagan, T. B. *The Journal of Physical Chemistry* **1973**, *77*, 2804.
- (294) Eduardo, J. G.-S.; Patricia, L.; Ana, B. G.; Karine, P. *Recent Patents on Nanotechnology* **2013**, *7*, 247.
- (295) Peral, D.; Gomez-Villarraga, F.; Sala, X.; Pons, J.; Carles Bayon, J.; Ros, J.; Guerrero, M.; Vendier, L.; Lecante, P.; Garcia-Anton, J.; Philippot, K. *Catalysis Science & Technology* **2013**, *3*, 475.
- (296) Bonnefille, E.; Novio, F.; Gutmann, T.; Poteau, R.; Lecante, P.; Jumas, J.-C.; Philippot, K.; Chaudret, B. *Nanoscale* **2014**, *6*, 9806.
- (297) Pelzer, K.; Vidoni, O.; Philippot, K.; Chaudret, B.; Collière, V. *Advanced Functional Materials* **2003**, *13*, 118.
- (298) McCarley, R. E. In *Metal-Metal Bonds and Clusters in Chemistry and Catalysis*; Fackler, J. P., Ed.; Springer US: Boston, MA, 1990, p 91.
- (299) Yang, F.; Deng, D.; Pan, X.; Fu, Q.; Bao, X. *Natl Sci Rev* **2015**, *2*, 183.
- (300) Umpierre, A. P.; de Jesús, E.; Dupont, J. *ChemCatChem* **2011**, *3*, 1413.

- (301) Novio, F.; Monahan, D.; Coppel, Y.; Antorrena, G.; Lecante, P.; Philippot, K.; Chaudret, B. *Chemistry – A European Journal* **2014**, *20*, 1287.
- (302) Lopez-Sanchez, J. A.; Dimitratos, N.; Hammond, C.; Brett, G. L.; Kesavan, L.; White, S.; Miedziak, P.; Tiruvalam, R.; Jenkins, R. L.; Carley, A. F.; Knight, D.; Kiely, C. J.; Hutchings, G. J. *Nat Chem* **2011**, *3*, 551.
- (303) Ibrahim, M.; Garcia, M. A. S.; Vono, L. L. R.; Lecante, P.; Rossi, L. M.; Philippot, K. *Catal. Sci. Tech.* **2016**, *submitted*.
- (304) Upare, P. P.; Lee, J.-M.; Hwang, D. W.; Halligudi, S. B.; Hwang, Y. K.; Chang, J.-S. *Journal of Industrial and Engineering Chemistry* **2011**, *17*, 287.
- (305) Graydon, W. F.; Langan, M. D. *Journal of Catalysis* **1981**, *69*, 180.
- (306) Guerrero, M.; T. Than Chau, N.; Noel, S.; Denicourt-Nowicki, A.; Hapiot, F.; Roucoux, A.; Monflier, E.; Philippot, K. *Current Organic Chemistry* **2013**, *17*, 364.
- (307) Zhang, J.; Teo, J.; Chen, X.; Asakura, H.; Tanaka, T.; Teramura, K.; Yan, N. *ACS Catal.* **2014**, *4*, 1574.
- (308) Pierson, Y.; Chen, X.; Bobbink, F. D.; Zhang, J.; Yan, N. *ACS Sustainable Chem. Eng.* **2014**, *2*, 2081.
- (309) Zhang, J.; Asakura, H.; Rijn, J. v.; Yang, J.; Duchesne, P.; Zhang, B.; Chen, X.; Zhang, P.; Saeys, M.; Yan, N. *Green Chem.* **2014**, *16*, 2432.
- (310) Lara, P.; Philippot, K.; Lacroix, L.-M.; Lachaize, S.; Liakakos, N.; Soulantica, K.; Chaudret, B. In *Advances in Organometallic Chemistry and Catalysis*; John Wiley & Sons, Inc.: 2013, p 421.
- (311) Domínguez-Crespo, M. A.; Ramírez-Meneses, E.; Torres-Huerta, A. M.; Garibay-Febles, V.; Philippot, K. *Int. J. Hydrogen Energy* **2012**, *37*, 4798.
- (312) Rovik, A. K.; Klitgaard, S. K.; Dahl, S.; Christensen, C. H.; Chorkendorff, I. *Applied Catalysis A: General* **2009**, *358*, 269.
- (313) Sinfelt, J. H. *Science* **1977**, *195*, 641.
- (314) Vang, R. T.; Honkala, K.; Dahl, S.; Vestergaard, E. K.; Schnadt, J.; Laegsgaard, E.; Clausen, B. S.; Nørskov, J. K.; Besenbacher, F. *Nat Mater* **2005**, *4*, 160.
- (315) Jones, G.; Jakobsen, J. G.; Shim, S. S.; Kleis, J.; Andersson, M. P.; Rossmeisl, J.; Abild-Pedersen, F.; Bligaard, T.; Helveg, S.; Hinnemann, B.; Rostrup-Nielsen, J. R.; Chorkendorff, I.; Sehested, J.; Nørskov, J. K. *Journal of Catalysis* **2008**, *259*, 147.



---

# **Chapter VI :**

# **Experimental**

# **Part**

---





## VI Experimental Part

### VI.1 Generals and Materials

All operations were carried out using Standard Schlenk tube, Fischer-Porter glassware techniques and vacuum lines techniques or in a glove-box (Braun) under argon atmosphere. Pentane, toluene, tetrahydrofurane and dichloromethane were dehydrated through filtration on a column in a purification apparatus (Braun). Solvents were purified then degassed by freeze-pumping method. Polyvinylpyrrolidone 40000 (PVP40, Sigma-Aldrich) was dried over  $P_2O_5$  (Sigma-Aldrich) and kept inside the glovebox before usage. Other Chemicals are listed below and were used as received unless otherwise specified.

- $[RhCl_3 \cdot 3H_2O]$  (99.9%, ABCR)
- $[Ru(cod)(cot)]$  (>97%, Nanomeps)
- $[[Ni(cod)_2]$  (Sigma-Aldrich)
- $[Pd_2(dba)_3]$  (Sigma-Aldrich)
- $[Pt(nor)_3]$  (Synthesized by Edwin Baquero Velasco)
- Allylmagnesium chloride solution ( 2.0 M in THF, Sigma-Aldrich)
- Polyvinylpyrrolidone 40000 (PVP40, Sigma-Aldrich)
- Triphenylphosphine  $PPh_3$  (99%, Sigma-Aldrich)
- 1,4-Bis(diphenylphosphino)butane dppb (98%, Sigma-Aldrich)
- 1,3,5-triaza-7-phosphaadamantane PTA (97%, Sigma-Aldrich)
- Hexadecylamine HDA (97%, Sigma-Aldrich)
- Potassium tert-butoxide (99.99%, Sigma-Aldrich)
- Tetrahydrofurane THF (99.9%, Carlo Erba)
- Toluene (99.8%, Carlo Erba)
- Dichloromethane (99.8%, Carlo Erba)
- Pentane (99%, Carlo Erba)
- Argon (Alphagaz Smartop)
- Carbon monoxide (Alphagaz Smartop)
- $^{13}C$ -Carbon monoxide ( $^{13}C$ , 99.14%, Eurisotp)
- Dihydrogen (Alphagaz Smartop)

## VI.2 Characterization Techniques

### VI.2.1 Transmission Electron Microscopy

Samples for electron microscopy analysis were prepared by slow evaporation of a drop of crude colloidal solution deposited onto holey carbon-covered copper grids under argon (in glove-box) for THF solutions and under air for aqueous solutions. Transmission Electron Microscopy at low (TEM) and high resolution (HRTEM) analyses were performed at the “UMS 3623 - Centre de microcaractérisation Raimond Castaing”, “TEMSCAN” previously. TEM images were obtained using either MET JEOL 1100 electron microscope operating at 100 kV with resolution point of 4.5°A or MET JEOL JEM 1400 operating at 120 kV. HRTEM observations were carried out with a JEOL JEM 2010 electron microscope working at 200 kV with a resolution point of 2.5°A and equipped with X-ray analysis PGT (light elements detection, resolution 135 eV). The size distributions were determined through a manual analysis of enlarged micrographs with ImageJ software to obtain a statistical size distribution and a mean diameter. FFT treatments have been carried out with Digital Micrograph Software (Version 1.80.70).

For each system of NPs, the mean size was calculated by assuming spherical form. Size distributions are quoted as the mean diameter  $\pm$  the **double** of the standard deviation ( $\sigma$ ) which corresponds to **95%** of error range. In all size distributions, over than 200 non-touching particles were counted.

### VI.2.2 Wide Angle X-ray Scattering

Wide Angle X-ray Scattering (WAXS) measurements were performed at CEMES-Toulouse by Pierre Lecante. Data collection was done on small amounts of powder (obtained after purification and drying) sealed in 1, 1.5, or 2.5 mm diameter Lindemann glass capillaries after filling in a glovebox. Measurements of the X-ray intensity scattered by the samples irradiated with graphite monochromatized molybdenum KR (0.071069 nm) radiation were performed using a dedicated two-axis diffractometer. Time for data collection was typically 20 h for a set of 457 measurements collected at room temperature in the range  $0^\circ < \theta < 65^\circ$  for equidistant  $s$  values ( $s = 4\pi(\sin \theta/\lambda)\dagger$ ). The raw intensity was corrected for contributions generated by other components (polymer, empty capillary) attenuated by sample absorption. Air scattering background was low enough to be neglected. Polarization

and self-absorption corrections were also applied. Data were reduced in order to extract the structure-related component of WAXS, the so-called reduced intensity function, normalized to a number of atoms corresponding to the size of the particles, and Fourier transformed allowing for radial distribution function (RDF) analysis, using:

$$F(r) = \frac{2r}{\pi} \int_{s_{min}}^{s_{max}} s \cdot i(s) \cdot \sin(r \cdot s) \cdot ds$$

Where  $F(r)$  is actually a reduced RDF whose maximum for a given  $r$  value indicates that at least two atoms in an elementary volume are separated by the distance  $r$ . Analysis of the experimental results provided an approximate measurement of the metal-metal bond length and of the order extent inside the particles. To further investigate the structure, different models were defined in order to compute theoretical functions for intensity and radial distribution via the Debye formula:

$$i_D(s) = 2 \sum_{i=1}^{N-1} \sum_{j=i+1}^N f_i(s) \cdot f_j(s) \cdot \frac{\sin(s \cdot r_{ij})}{s \cdot r_{ij}} \cdot \exp(-b_{ij} \cdot s^2)$$

Where  $N$  is the total number of atoms in the model,  $f_i$  the atomic scattering factor for atom  $i$ ,  $r_{ij}$  the distance between atoms  $i$  and  $j$ , and  $b_{ij}$  a dispersion factor affecting the  $i$ - $j$  interaction). The best values of the parameters defining the models were estimated from the agreement reached between experimental and computed RDF, both normalized to one atom, but also between the related reduced intensity functions.

### VI.2.3 Infrared Spectroscopy

Fourier Transform Infrared (FT-IR) spectra were recorded in the range 4000-400  $\text{cm}^{-1}$  under argon atmosphere using a Perkin-Elmer GX2000 spectrometer installed inside a glovebox of the team “*Ingénierie des Nanoparticules Métalliques*” at LCC-Toulouse.

**VI.2.4 Elemental Analysis**

ICP-AES analyses were performed on Leeman ICP-MS system at the “Service d’analyse élémentaire” at LCC-Toulouse, after mineralization of the samples in aqua regia under reflux.

**VI.2.5 Nuclear Magnetic Resonance Spectroscopy**

Nuclear Magnetic Resonance (NMR) experiments were carried out at the “Service RMN” in LCC-CNRS, Toulouse. The solution NMR experiments were performed on a Bruker (400 MHz or 500 MHz) spectrometer. Solution NMR experiments under dihydrogen pressure were performed by Christian Bijani. Solid State Nuclear Magnetic Resonance at Magic Angle Spinning (MAS-NMR) with and without  $^1\text{H}$ - $^{13}\text{C}$  cross coupling (CP) were performed by Yannick Coppel on a Bruker Avance 400WB instrument equipped with a 3.2 mm probe with a sample frequency being set at 16 kHz, using a 3.2 mm  $\text{ZrO}_2$  rotor.

**VI.2.6 X-Ray Absorption Spectroscopy**

X-ray absorption spectra (XAS) of the NiOx/Rh and Ni NPs and reference samples (Ni foil, and NiO) were recorded at the BL01B1 beamline at the SPring-8 (Japan Synchrotron Radiation Research Institute, Hyogo, Japan) in the transmission mode at ambient temperature. A Si(1 1 1) double crystal monochromator was used to obtain a monochromatic X-ray beam. The monochromator was calibrated at the shoulder peak of the absorption edge of an X-ray absorption near edge structure (XANES) spectrum of Cu foil. Rh K-edge XAS of the NiOx/Rh and Rh NPs and reference samples (Rh foil, and  $\text{Rh}_2\text{O}_3$ ) were also recorded in the same manner except for the use of a Si(3 1 1) double crystal monochromator. The monochromator was calibrated at the inflection point of the XANES spectrum of the Rh foil. In both cases, higher harmonics were removed by changing glancing angles of collimation and focusing mirrors. Data reduction was carried out with Athena and Artemis included in the Ifeffit and Demeter package. For curve-fitting analysis on extended X-ray absorption fine structure (EXAFS) spectra, each theoretical scattering path was generated with FEFF6.0L, and amplitude reduction factors were estimated by curve-fitting on the reference samples. The  $k^2$ -weighted EXAFS oscillation in the range of 3.0–15  $\text{Å}^{-1}$  was Fourier transformed, and curve-fitting analyses were performed in the appropriate range in R space as described in the following section.

**VI.2.7 Magnetic Properties Analysis**

SQUID measurements were performed on a SQUID magnetometer (MPMS Quantum Design) at the LCC-CNRS, Toulouse. The temperature was varied between 2 and 300 K according to a classical zero-field-cooling/field cooling (ZFC/FC) procedure in the presence of a very weak applied magnetic field (10 Oe). The field dependent magnetization was obtained at different temperatures in a magnetic field varying from +50 kOe to -50 kOe.

**VI.2.8 X-Ray Photoelectron Spectroscopy**

XPS measurements of RhPVP sample was acquired with a ThermoScientific system at room temperature using Al-K $\alpha$  radiation (1484.6 eV) as the excitation X-ray source. During analysis the pressure in the analysis chamber was maintained at  $2 \cdot 10^{-10}$  mbar. The XPS measurements were then performed in the electron binding energy ranges corresponding to 3d excitations of Rhodium, and 1s excitations of carbon, nitrogen and oxygen. All samples were measured twice and the reported values are the average of two scans. Analysis were performed at Technical University of Denmark.

XPS measurements of NiOx/Rh and Ni NPs were performed on a VG Escalab MKII spectrometer, using a mono Al K $\alpha$ X-ray source ( $h\nu = 1486.71$  eV, 5 mA, 15 kV) and calibrated by setting the C 1s peak to 285.0 eV, at Japan Synchrotron Radiation Research Institute, Hyogo, Japan.

**VI.3 Synthesis Procedures****VI.3.1 [Rh( $\eta^3$ -C<sub>3</sub>H<sub>5</sub>)<sub>3</sub>] complex**

Rh trisallyl (III) complex was synthesized according to the procedure described in “Synthetic Methods of Organometallics and Inorganic Chemistry” (Beckhaus 2000).

In a 500ml Schlenk tube, 1.5g of RhCl<sub>3</sub>·H<sub>2</sub>O (7.16 mmol) was added and dissolved in 140 ml of purified THF resulting in a dark red suspension. The solution was cooled down at -10°C under agitation and 36 ml (71.6 mmol) of allylmagnesiumchloride, (2M) in THF were added slowly using a syringe under argon. The solution progressively started getting yellow color. After complete addition of the allylmagnesiumchloride reagent, the solution was kept

under agitation for 1h at  $-10^{\circ}\text{C}$  and then for 16h at  $10^{\circ}\text{C}$ . Later, the THF was evaporated, and the obtained solid was dried under dynamic vacuum. 200 ml of pentane were added twice and the yellow solution was purified over a celite column. Then the pentane was evaporated and the resulting yellow solid introduced into a sublimator. Yellow crystals were collected on the walls of the cooled finger at  $40^{\circ}\text{C}$  under dynamic vacuum. 660 mg of yellow crystals were obtained and conserved under argon in the fridge of the glove box.

$^1\text{H}$  NMR ( $\text{CDCl}_3$ ): 1.63 ppm, *dd*,  $4\text{H}^{\text{a}}$ ,  $J_{\text{HH}}=11\text{Hz}$ ,  $J^{\text{ab}}=0.8\text{Hz}$ ,  $\text{CH}_2^{\text{ab}}$ ,  $(\text{CH}_2\text{CHCH}_2)_2$ ; 2.62 ppm, *dd*,  $2\text{H}^{\text{a}}$ ,  $J_{\text{HH}}=11.7\text{Hz}$ ,  $J_{\text{ab}}=1.32\text{Hz}$ ,  $\text{CH}_2^{\text{ab}}$ ,  $\text{CH}_2\text{CHCH}_2$ ; 2.77 ppm, *d*,  $4\text{H}^{\text{a}}$ ,  $J_{\text{HH}}=6.62\text{ Hz}$ ,  $\text{CH}_2^{\text{ab}}$ ,  $(\text{CH}_2\text{CHCH}_2)_2$ ; 2.99 ppm, *d*,  $2\text{H}^{\text{b}}$ ,  $J_{\text{HH}}=6.65\text{ Hz}$ ,  $\text{CH}_2^{\text{ab}}$ ,  $\text{CH}_2\text{CHCH}_2$ ; 3.96 ppm, *m*,  $2\text{H}$ ,  $\text{CH}$ ,  $(\text{CH}_2\text{CHCH}_2)_2$ ; 5.35 ppm,  $1\text{H}$ ,  $\text{CH}$ ,  $\text{CH}_2\text{CHCH}_2$ .

Microanalysis data experimental (theoretical) %C: 48.05 (47.8); %H: 6.7 (6.7).

### VI.3.2 PVP-stabilized Rh NPs

150 mg of  $[\text{Rh}(\eta^3\text{-C}_3\text{H}_5)_3]$  (0.66 mmol) were introduced under argon atmosphere in a Fischer-Porter reactor. After 0.5 h under vacuum at r.t. and cooling to 193 K, a THF solution (150 mL) of PVP (680 mg; Rh/PVP=10% wt) was transferred under argon by canula. Then the reaction medium was let to warm up to r.t. before adding dihydrogen (3 bar). The reaction mixture was left under vigorous stirring at r.t. It turned from pale yellow to black color in a few minutes. After a reaction time of 16 h, a homogeneous black colloidal solution was obtained. Remaining dihydrogen was evacuated and the volume of the solution was reduced to approximately 10 mL under vacuum before its transfer onto a solution of deoxygenated cold pentane (100 mL). A black precipitate formed which was filtered and dried under vacuum giving rise to the Rh NPs embedded in PVP as a fine black powder (622.5 mg). These Rh PVP NPs were found to be stable with time when kept argon atmosphere.

ICP AES analysis: Rh = 14.9 wt%.

### VI.3.3 $\text{PPh}_3$ -stabilized Rh NPs

150 mg of  $[\text{Rh}(\eta^3\text{-C}_3\text{H}_5)_3]$  (0.66 mmol) were introduced under argon atmosphere in a Fischer-Porter reactor. After 0.5 h under vacuum at r.t. and cooling to 193 K, a THF solution

(150 mL) containing 174 mg of  $\text{PPh}_3$  (0.66 mmol,  $[\text{PPh}_3]/[\text{Rh}] = 1$ ) was added. Then the reaction medium was let to warm up to r.t. before adding dihydrogen (3 bar) and then put in an oil bath previously heated at 338 K. The reaction mixture was left at 338 K under vigorous stirring during 18 h. After this reaction time, a homogeneous black colloidal solution was obtained. After cooling at r.t., remaining dihydrogen was evacuated and the volume of the solution was reduced to approximately 10 mL under vacuum before its transfer onto a solution of deoxygenated cold pentane (100 mL). A black precipitate formed which was filtered and dried under vacuum leading to the  $\text{PPh}_3$ -stabilized Rh NPs as a black powder (97.5 mg).  $\text{RhPPh}_3$  NPs were found to be stable with time when kept under argon atmosphere.

ICP AES analysis: Rh = 66.2 wt%.

#### **VI.3.4 dppb-stabilized Rh NPs**

150 mg of  $[\text{Rh}(\eta^3\text{-C}_3\text{H}_5)_3]$  (0.66 mmol) were introduced under argon atmosphere in a Fischer-Porter reactor. After 0.5 h under vacuum at r.t. and cooling to 193 K, a THF solution (150 mL) containing 84.75 mg of dppb (0.20 mmol,  $[\text{dppb}]/[\text{Rh}] = 0.3$ ) was added. Then the reaction medium was let to warm up to r.t. before adding dihydrogen (3 bar) and then put in an oil bath previously heated at 338 K. After cooling at r.t., remaining dihydrogen was evacuated and the volume of the solution was reduced to approximately 10 mL under vacuum before its transfer onto a solution of deoxygenated cold pentane (100 mL). A black precipitate formed leading to the dppb-stabilized Rh NPs as a black powder (66 mg).  $\text{Rh dppb}$  NPs were found to be stable with time when kept under argon atmosphere.

ICP AES analysis: Rh = 45.6 wt%.

#### **VI.3.5 PTA-stabilized Rh NPs**

150 mg of  $[\text{Rh}(\eta^3\text{-C}_3\text{H}_5)_3]$  (0.66 mmol) were introduced under argon atmosphere in a Fischer-Porter reactor. After 0.5 h under vacuum at r.t. and cooling to 193 K, a THF solution (150 mL) containing 83.39 mg of PTA (0.20 mmol,  $[\text{PTA}]/[\text{Rh}] = 0.8$ ) was added. Then the reaction medium was let to warm up to r.t. before adding dihydrogen (3 bar) and then put in an oil bath previously heated at 338 K. After cooling at r.t., remaining dihydrogen was

evacuated and the volume of the solution was reduced to approximately 10 mL under vacuum before its transfer onto a solution of deoxygenated cold pentane (100 mL). A black precipitate formed leading to the PPh<sub>3</sub>-stabilized Rh NPs as a black powder (85 mg). Rhdpbb NPs were found to be stable with time when kept under argon atmosphere.

ICP AES analysis: Rh = 41.6 wt%.

### **VI.3.6 Phosphine Ferrocene ligands-stabilized Rh NPs**

150 mg of [Rh( $\eta^3$ -C<sub>3</sub>H<sub>5</sub>)<sub>3</sub>] (0.66 mmol) were introduced under argon atmosphere in a Fischer-Porter reactor. After 0.5 h under vacuum at r.t. and cooling to 193 K, a CDCl<sub>2</sub> solution (150 mL) containing 0.2 molar equivalent of the chosen ligand (L1, L2, L3 or L4) or 0.4 molar equivalent of L5 was added. Then the reaction medium was let to warm up to r.t. before adding dihydrogen (3 bar) and then put in an oil bath previously heated at 313 K. After cooling at r.t., remaining dihydrogen was evacuated and the volume of the solution was reduced to approximately 10 mL under vacuum before its transfer onto a solution of deoxygenated cold pentane (100 mL). A black precipitate formed leading to the phosphine ferrocene-stabilized Rh NPs as a black powder.

ICP AES analysis L2-stabilized RhNPs : Rh: 29.3 wt%.

ICP AES analysis L5-stabilized RhNPs: Rh: 22.7 wt%.

### **VI.3.7 CXP-stabilized Rh NPs**

150 mg of [Rh( $\eta^3$ -C<sub>3</sub>H<sub>5</sub>)<sub>3</sub>] (0.66 mmol) were introduced under argon atmosphere in a Fischer-Porter reactor. After 0.5 h under vacuum at r.t. and cooling to 193 K, a CDCl<sub>2</sub> solution (150 mL) containing 0.2 molar equivalent of ligand CXP was added. Then the reaction medium was let to warm up to r.t. before adding dihydrogen (3 bar) and then put in an oil bath previously heated at 338 K. After cooling at r.t., remaining dihydrogen was evacuated and the volume of the solution was reduced to approximately 10 mL under vacuum before its transfer onto a solution of deoxygenated cold pentane (100 mL). A black precipitate formed leading to the phosphine CXP-stabilized Rh NPs as a black powder.



### VI.3.8 N-Heterocyclic Carbene-stabilized Rh NPs

150 mg of  $[\text{Rh}(\eta^3\text{-C}_3\text{H}_5)_3]$  (0.66 mmol) were introduced under argon atmosphere in a Fischer-Porter reactor. After 0.5 h under vacuum at r.t. and cooling to 193 K, a THF solution (150 mL) containing 0.2 molar equivalent of the chosen carbene (MPr-H, PrIMes-H or PrIPr-H) mixed with 1 molar equivalents (to the ligand) of ter-butoxide base was added. Then the reaction medium was let to warm up to r.t. before adding dihydrogen (3 bar) and then put in an oil bath previously heated at 338 K. After cooling at r.t., remaining dihydrogen was evacuated and the THF was evaporated. Then water was added and the solution was transferred into a dialysis bag for purification in water over 2 h. Later, water was evaporated resulting in a black precipitate.

### VI.3.2.9 Bimetallic NPs

The syntheses of the BMNPs were performed in one pot conditions under the same procedures as for the monometallic NPs while introducing simultaneously the two metal precursors into a Fisher–Porter bottle. The mixture was left under vacuum for 0.5 h, solution of THF containing PVP or HDA, was then introduced into the reactor under freezing temperature. The Fisher–Porter bottle was set to r.t. and then pressurized with dihydrogen gas (3 bar). Reactions were kept over 16 h typically till a black colloidal solution was obtained. Later, after releasing pressure, the volume of the solution was reduced to approximately 10 mL by solvent evaporation before its transfer into a solution of deoxygenated pentane to precipitate, and washing any residues in the system. Later, the obtained precipitate was filtered and dried under vacuum to give the nanoparticles as a solid dark powder.

### VI.3.10 of magnetic silica support

The magnetic support comprised of silica-coated magnetite NPs (FFSi) was prepared by reverse microemulsion method and functionalized with amino groups (FFSiNH<sub>2</sub>), as previously reported. (Rossi *et al. Applied Catalysis A: General* **2008**, 338, 52)

### VI.3.11 Deposition NPs onto silica support

As a general procedure, a THF solution (40 mL) containing the Rh NPs (27 mg RhPVP NPs; 7.3 mg RhPPh<sub>3</sub> NPs or 5.6 mg Rhdppb NPs) was added to 100 mg of the FFSiNH<sub>2</sub> support. The suspension was left under vigorous stirring overnight at r.t. Stirring

was stopped and the solid was recovered by applying a magnet to the reaction flask walls. The solvent was drained off completely and the solid was then washed with ethanol before drying under vacuum leading to RhPVP@FFSiNH<sub>2</sub>, RhPPh<sub>3</sub>@FFSiNH<sub>2</sub> and Rhdppb@FFSiNH<sub>2</sub> samples. This deposition protocol was performed with 2 mg of rhodium metal for 100 mg of silica support. ICP AES measurement allowed determining the metal content on the silica support after deposition of the nanoparticles as follows: RhPVP@FFSiNH<sub>2</sub> NPs: 1.14 wt% Rh,

RhPPh<sub>3</sub>@FFSiNH<sub>2</sub> NPs: 2.32 wt% Rh,

Rhdppb@FFSiNH<sub>2</sub> NPs: 1.44 wt% Rh.

## **VI.4 Catalytic Reactions**

### **VI.4.1 Hydrogenation of cyclohexene with Supported and Non-Supported Rh NPs:**

Hydrogenation reactions of cyclohexene were carried out at the University of Sao Paulo, Brazil, in a modified Fischer–Porter 100-mL glass reactor, which was loaded with the catalyst (non-supported or supported Rh NPs) and substrate under inert atmosphere (substrate-to-catalyst mol ratio are given in tables). The reactor was connected to a pressurized H<sub>2</sub> tank *via* a gas regulator, which was set to the required working pressure (6 atm). The pressure inside the reactor was maintained constant for the entire course of the reaction by leaving the reactor open to the H<sub>2</sub> supply tank. The temperature was maintained using an oil bath and a hot-stirring plate connected to a digital controller. The reactions were conducted under magnetic stirring (700 rpm) for the desired time. H<sub>2</sub> pressure fall in the H<sub>2</sub> supply tank was monitored with a pressure transducer interfaced through a Novus field logger converter to a computer. The pressure *versus* time data were collected by the Field Chart Novus software. After each reaction was complete (hydrogen consumption ceased), the products were collected and analyzed by GC. From the hydrogen consumption curves, was obtained, for each reaction, the time required for the complete conversion (> 99 %, confirmed by GC). The catalytic activity was expressed in turnover frequency (TOF) determined using the data from the hydrogenation curves transformed into conversions and then into turnover numbers (mole of substrate converted per mole of catalyst). From the slope of the turnover numbers *versus* time curves at initial rates (typically <20 % conversion), the initial TOF, in h<sup>-1</sup> was obtained. In recycling experiments, the magnetically recovered catalyst was dried in

vacuum at room temperature before the addition of a new portion of substrate under inert atmosphere. The reactor was connected again to the H<sub>2</sub> gas supply tank and successive hydrogenation reactions were performed.

#### **VI.4.2 Hydrogenation of benzoic acid and derivatives with Rh PVP NPs**

Chemoselective aromatic and levulinic acid (LA) hydrogenations were conducted in a 100 mL stainless steel high pressure reactor equipped with an electrically heated jacket, a turbine stirrer with a variable speed magnetic driver, and a liquid sampling line. In a typical reaction, the reactor was loaded with substrate (0.5 mmol), water (50 mL), and catalyst (10 mg). Then the reactor was filled with H<sub>2</sub> to 0.5 MPa three times followed by evacuation to displace residual air in the reactor. The autoclave was then pressurized with H<sub>2</sub> to 1.0 MPa and heated to 353 K and stirring at 320 rpm upon reaching the reaction temperature.

After allowing the reaction to proceed for 2 h (unless otherwise mentioned), the autoclave was then cooled down to the room temperature and aliquot of the reaction was submitted to gas chromatography (GC-FID, Agilent, 6890N) equipped with an HP-5 capillary column (Agilent, J&W, 30.0m x 320 μm) using N<sub>2</sub> as the carrier gas. The structures of the products were identified using gas chromatography coupled with Mass spectrometry (GC-MS) on Agilent 6850N spectrometer.

#### **VI.4.3 Hydrogenation of styrene with Ferrocenyl Phosphine-stabilized Rh NPs**

The hydrogenation of styrene reactions were carried out in a stainless steel reactor at room temperature, and 30 bar H<sub>2</sub>, under magnetic stirring. In a typical reaction, the solvent (toluene, 20.0 mL), the substrate (oct-1-ene or styrene; 4 mmol) and the internal standard (undecane; 2 mmol) were added in the reactor. For the Rh-TOAB catalyst, a toluene solution of Rh NPs and the chosen phosphine ligand were added to the reactor at a molar ratio of [P]/[Rh] = 20. For the Rh-PPh<sub>3</sub> catalyst, the dried solid was placed as isolated in the reactor and dissolved with toluene (20.0 mL). In all the catalytic reactions, the ratio of [substrate]/[Rh] was fixed at 1500. The catalytic reactions were prepared in air. The reactor was purged three times with the gas mixture CO/H<sub>2</sub> and then pressurized to start the catalytic reaction. The evolution of catalysis was followed by gas chromatography (GC-2010 Shimadzu) by sampling the liquid phase through a valve dip tube. Conversion and selectivity

were determined using calibration curves built with commercially available expected products of the reaction. The GC mass balance was based on the substrate consumption using undecane as an internal standard.

#### **VI.4.4 Hydroformylation of 1-octene and styrene with Rh-PPh<sub>3</sub> and Rh-TOAB NPs**

The hydroformylation reactions were carried out at the University of Sao Paulo, in a stainless steel reactor at 120°C, using an oil bath and a hot-stirring plate connected to a digital controller (ETS-D4 IKA), and 50 bar of syngas (CO/H<sub>2</sub> = 1), under magnetic stirring (700 rpm). In a typical reaction, the solvent (toluene, 20.0 mL), the substrate (oct-1-ene or styrene; 4 mmol) and the internal standard (undecane; 2 mmol) were added in the reactor. For the Rh-TOAB catalyst, a toluene solution of Rh NPs and the chosen phosphine ligand were added to the reactor at a molar ratio of [P]/[Rh] = 20. For the Rh-PPh<sub>3</sub> catalyst, the dried solid was placed as isolated in the reactor and dissolved with toluene (20.0 mL). In all the catalytic reactions, the ratio of [substrate]/[Rh] was fixed at 1500. The catalytic reactions were prepared in air. The reactor was purged three times with the gas mixture CO/H<sub>2</sub> and then pressurized to start the catalytic reaction. The evolution of catalysis was followed by gas chromatography (GC-2010 Shimadzu) by sampling the liquid phase through a valve dip tube. Conversion and selectivity were determined using calibration curves built with commercially available expected products of the reaction. The GC mass balance was based on the substrate consumption using undecane as an internal standard.

#### **VI.4.5 Hydroformylation of styrene with CXP-stabilized Rh NPs.**

Typical reaction procedure was performed in a glass-lined, stainless steel autoclave containing a magnetic stirring bar. The autoclave was charged under nitrogen with Rh NPs (0.003 g, 0.03 mmol) and toluene (10 mL). Once closed, the autoclave was flushed twice with syngas (CO/H<sub>2</sub>=1:1), pressurized with a CO/H<sub>2</sub> mixture and heated at 80 °C. After 16 h, the autoclave was depressurized, styrene (0.66 mL, 5.7 mmol) and internal standard (decane ; 0.25 mL) were added to the reaction mixture. The autoclave was then heated and pressurized. The progress of the reaction was checked by monitoring the pressure decrease. During the experiments, several samples were taken and analyzed by GC or <sup>1</sup>H NMR spectroscopy.

### VI.4.6 Hydrogenolysis of 1-benzoxy-2-methoxy benzene.

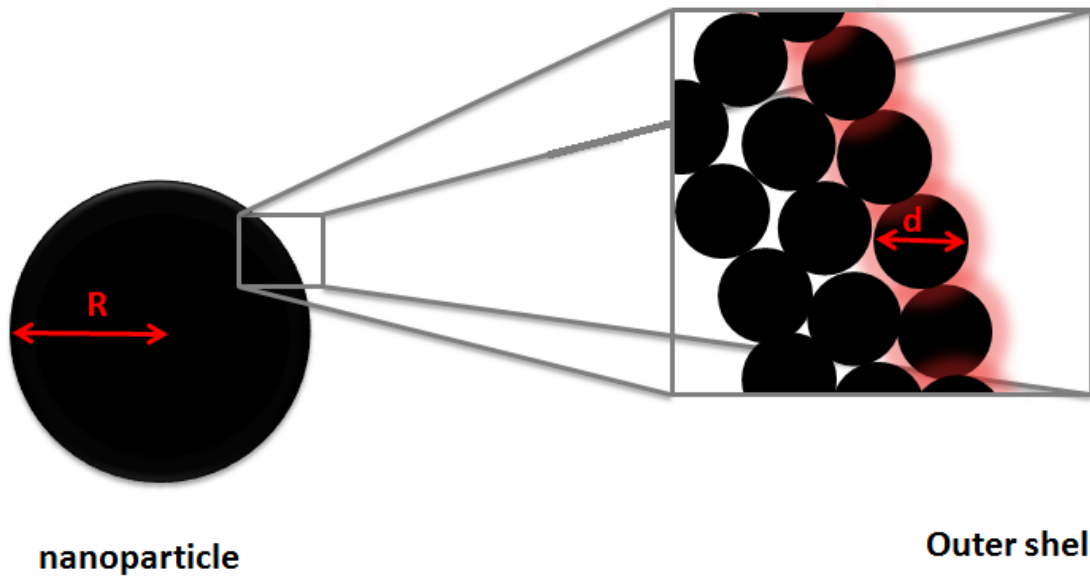
In a typical experiment, the substrate (0.1 mmol), catalyst (0.01 mmol based on metal), 3 mL of water and a magnetic stirrer were charged into a high pressure reactor (20 mL). After flushing with H<sub>2</sub> for 5 times, the reactor was charged with 10 bar H<sub>2</sub>, and put into a preheated oil bath with a stirring speed of 1000 rpm. After the reaction, the reactor was quenched to ambient temperature using cooling water, and the organic products were extracted using ethyl acetate (6 mL) and analyzed by gas chromatography (GC) and GC–mass spectroscopy (GC–MS) on an Agilent 7890A gas chromatograph with flame ionization detector (FID) and an Agilent 7890A-5975GC–MS instrument, both equipped with HP-5 capillary columns (30 m × μ250 m). The peak area was calibrated by FID effective carbon number (ECN) of the representing compound. Conversion is defined as the amount of rings in products divided by the total amount of rings found on GC-FID, multiplied by 100%. Yield is defined as the amount of rings in individual product divided by the total amount of rings found on GC-FID, multiplied by 100%. Selectivity is defined as the amount of rings in individual product divided by the amount of rings found in products on GC-FID:

$$\text{Conversion}(\%) = \left( 1 - \frac{2 \times \text{Area}_{sub} / \text{ECN}_{sub}}{\sum (\text{Area}_i / \text{ECN}_i) + 2 \times \sum (\text{Area}_j / \text{ECN}_j) + 2 \times \text{Area}_{sub} / \text{ECN}_{sub}} \right) \times 100\%$$

$$\text{Yield}_x(\%) = \frac{n \times \text{Area}_x / \text{ECN}_x}{\sum (\text{Area}_i / \text{ECN}_i) + 2 \times \sum (\text{Area}_j / \text{ECN}_j) + 2 \times \text{Area}_{sub} / \text{ECN}_{sub}} \times 100\%$$

Where n is the number of ring(s) in molecule, e.; i is subscript for monomers, while j is subscript for dimers.

## VI.5 Calculations on NPs



## VI.5.1 Number of Atoms

The calculation of total number of Rh atoms was obtained considering spherical NPs having closed packing structure (fcc) which uses approximately 74% of the volume.

- The diameter of Rh atom is  $d = 0.27$  nm.
- The mean diameter of the NPs is  $D$  (nm). And the radius  $R = D/2$
- sphere's volume is:  $V_{\text{sphere}} = (4/3)\pi R^3$

Thus the total number of Rh atoms ( $N$ ) in a closed packing  $d$  nm sphere particle was calculated as follows:

$$0.74 \times V_{\text{sphere}} / V_{\text{single Rh}} =$$

$$= 0.74 \times [(4/3)\pi(D/2)^3] / [(4/3)\pi(d/2)^3]$$

$$\mathbf{N = 0.74 \times D^3/d^3}$$

### VI.5.2 Percentage of Surface Atoms

The percentage of surface rhodium atoms in NPs was estimated as follows, considering that:

- "d" is the diameter of a one rhodium atom.
- "R" is the radius of the NPs (spherical NPs).
- Surface atoms form a spherical shell of thickness "d".
- The whole sphere's volume is:  $V_{\text{sphere}} = (4/3)\pi R^3$
- Shell's outer radius is R, and its inner radius is (R-d).
- the shell volume is therefore:  $V_{\text{shell}} = (4/3)\pi R^3 - (4/3)\pi(R-d)^3 = (4/3)\pi(R^3 - (R-d)^3)$

The whole sphere's volume is:  $V_{\text{sphere}} = (4/3)\pi R^3$

The percentage of surface atoms is in the same proportion as the shell's volume to the sphere's volume:

$$\begin{aligned} V_{\text{shell}}/V_{\text{sphere}} &= (4/3)\pi(R^3 - (R-d)^3) / ((4/3)\pi R^3) \\ &= (R^3 - (R-d)^3) / R^3 \end{aligned}$$





---

# Résumé de la Thèse

---



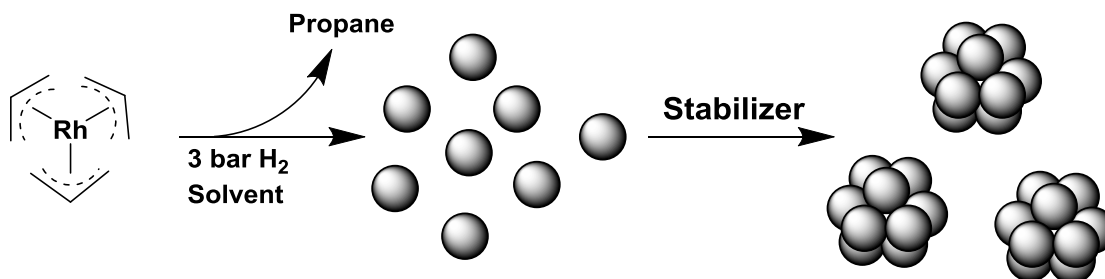
Au cours des 25 dernières années, le domaine des nanoparticules métalliques a été témoin de l'évolution croissante de l'intérêt de la communauté scientifique. Cela s'est illustré par des études extensives sur la synthèse, la caractérisation et l'évaluation du potentiel de ces nanoparticules pour des applications différentes.

Cet intérêt porté aux nanoparticules métalliques découle des propriétés inhabituelles qu'elles possèdent, en raison de leur position à la frontière entre les métaux à l'état moléculaire et ceux à l'état massif. Les applications des nanoparticules métalliques couvrent un large éventail de domaines, dont la santé, la médecine, le magnétisme, l'électrochimie, l'énergie, etc.

Une application particulière des nanoparticules métalliques est la catalyse, où celles-ci peuvent contribuer à combler l'écart des différences entre catalyse homogène et hétérogène. Cependant, la performance catalytique est fortement dépendante des propriétés physiques et chimiques des nanoparticules, raison pour laquelle le développement de méthodes de synthèses innovantes est essentiel pour manipuler et mieux comprendre leur comportement catalytique.

Ce manuscrit de thèse porte sur la préparation de nanoparticules mono- et bimétalliques à base de rhodium (Rh NPs), leur caractérisation et leur application en nanocatalyse. La méthode utilisée pour synthétiser les particules est l'approche organométallique. Le principal avantage de ce procédé est qu'il ne nécessite pas de conditions de réaction difficiles et permet d'obtenir des nanoparticules bien définies, en présence de stabilisants choisis qui peuvent être des polymères ou des ligands de coordination. En outre, on peut éviter la contamination de surface par un choix judicieux du précurseur métallique, cela étant un facteur essentiel pour étudier précisément les propriétés de leur surface et leur activité catalytique. Le complexe organométallique  $[\text{Rh}(\eta^3\text{-C}_3\text{H}_5)_3]$  a été utilisé comme source de rhodium en association avec un agent stabilisant approprié.

Ce précurseur est très intéressant pour l'élaboration de Rh NPs, car il se décompose facilement sous faible pression de dihydrogène dans les solvants organiques, conduisant à la libération d'atomes de rhodium, et le propane comme le seul sous-produit. Il en résulte de très petites nanoparticules, bien contrôlées en termes de taille, de morphologie et de dispersion, ainsi qu'une surface métallique propre qui peut être fonctionnalisée par un ligand.



Divers agents stabilisants ont été utilisés tout au long de ce travail afin d'étudier leur capacité à stabiliser les Rh NPs et leur influence sur les propriétés catalytiques des nanoparticules qui se sont révélées actives vis-à-vis de différentes réactions (*vide supra*). Des nanoparticules bimétalliques ont également été préparées en utilisant des outils de synthèse analogues grâce à une synthèse en une étape, à savoir la co-décomposition du  $[\text{Rh}(\eta^3\text{-C}_3\text{H}_5)_3]$  avec un autre précurseur organométallique, en présence d'un stabilisateur spécifique.

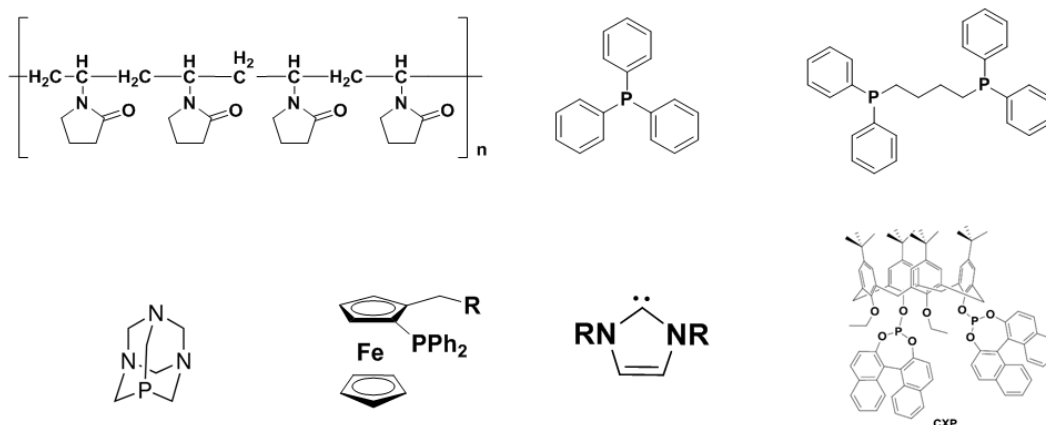
Ce travail a été réalisé au "Laboratoire de Chimie de Coordination du CNRS" à Toulouse, en France, dans l'équipe «Ingénierie des Nanoparticules Métalliques», sous la supervision du Dr Karine Philippot. Il a été financé par une bourse du MESR et par le CNRS. Au cours de la thèse, trois séjours d'un mois ont été effectués à l'étranger; le premier au "Laboratoire de Nanomatériaux et Catalyse" (Université de Sao Paulo, Brésil) dans le cadre d'un projet CAPES-COFECUB avec le groupe du Pr. Liane M. Rossi, et les deux autres au «Laboratoire de Green Catalysis" (NUS, Singapour) dans le cadre d'un projet MERLION avec le groupe du Pr. Ning Yan.

En plus de l'introduction et de la conclusion générale et de la partie expérimentale, ces travaux de thèse sont présentés en six chapitres distincts, comme suit:

Le chapitre I fournit des informations générales et des données bibliographiques sur le thème des nanoparticules métalliques. Il décrit la chronologie de l'histoire des nanoparticules métalliques et leur développement, ainsi que les principaux domaines de leurs applications. Ensuite, une partie est consacrée à montrer ce qui fait des nanoparticules métalliques des matériaux spéciaux et intéressants. Les principales méthodes de synthèse portant sur les voies chimiques en solution et en particulier l'approche organométallique, et une sélection appropriée de méthodes de caractérisation de MNP est également reportée. La dernière partie de ce chapitre clarifie plus particulièrement la synthèse des NPs de rhodium et leurs applications dans les réactions catalytiques d'hydrogénation et d'hydroformylation.

Dans le chapitre II, nous rapportons la synthèse de nanoparticules de rhodium monométalliques et leur caractérisation. Une variété de ligands a été utilisée en tant que stabilisants afin d'étudier leur influence sur les caractéristiques des particules. Pour des fins de comparaison, nous avons également procédé à la synthèse de Rh NPs en présence d'un polymère, la polyvinylpyrrolidone (PVP), considérant que les nanoparticules se développent dans la matrice polymère 3D sans interaction directe entre la PVP et la surface du métal. Dans le cas contraire, avec des ligands, nous nous attendons à la coordination sur la surface du métal et des effets différents en fonction de leur composition. Une variété de ligands phosphorés a été testée, notamment des phosphines (PPh<sub>3</sub>, dppb et PTA), calix [4] arène et un ligand de type phosphine ferrocène. Des carbènes solubles dans l'eau ont également été utilisés dans le but d'obtenir des solutions colloïdales aqueuses de rhodium. La dernière partie de ce chapitre est consacrée au dépôt de NPs Rh sélectionnées sur une silice magnétique amino-modifiée en tant que support.

Plusieurs systèmes de nanoparticules de rhodium monométalliques sont décrits dans ce chapitre. Ils se distinguent les uns des autres en fonction de la nature des stabilisants utilisés pour leur synthèse. Un résumé de leurs caractéristiques est donné dans le tableau suivant.



Stabilizer	Mean size (nm)	Rhodium content (%)	Number of Rh atoms	%Rh atoms on surface	CO bridging	CO terminal	CO geminal	Structure
<b>PVP</b>	2.2	14.9	303	32	x	x	x	Fcc
<b>PPh<sub>3</sub></b>	1.3	66.2	43	50	x	x	x	β-manganese
<b>Dppb</b>	1.7	45.6	114	40	x	x	x	β-manganese
<b>PTA</b>	0.9	42.5	10	65	x	(x)		oxidized
<b>L1</b>	1.5	22.7	82	44	x			fcc
<b>L5</b>	1.2	29.3	47	53	x	x	x	fcc
<b>CXP</b>	4.1	--	2190	18	--	--	--	--
<b>PrIPr</b>	2.9	--	709	25	--	--	--	--
<b>PrIMes</b>	1.7	--	114	40	--	--	--	--

Dans un premier temps, le polymère PVP a permis la formation de Rh NPs de ca 2.2 nm qui sont bien dispersées dans la matrice de polymère et présentent une distribution de tailles étroite. Leur structure cristalline est fcc. Des études d'adsorption de CO ont révélé une bonne accessibilité de la surface du métal avec la coordination de molécules de monoxyde de carbone.

L'utilisation des ligands PPh<sub>3</sub> et dppb pour la synthèse de nanoparticules de rhodium, qui diffèrent par le nombre d'atomes de phosphore susceptibles de se coordiner à la surface du rhodium, met en évidence qu'un rapport de départ de [P] / [Rh] = 0,6 à 1 est nécessaire pour obtenir des nanoparticules bien contrôlées et de petite taille. Cependant, un apport d'énergie (65°C) s'est avéré essentiel pour décomposer le complexe [Rh ( $\eta^3$ -C<sub>3</sub>H<sub>5</sub>)<sub>3</sub>] lors de l'utilisation de phosphines; ce comportement est attribué à la formation de complexes de rhodium à ligands phosphines insitu qui ont été détectés par des études RMN. Les particules ainsi

obtenues présentent des caractéristiques similaires en termes de taille ( $\text{RhPPH}_3 = 1,3 \text{ nm}$ ,  $\text{Rhddpb} = 1,7 \text{ nm}$ ), la dispersion et une faible cristallinité, ainsi que l'état de surface. Des études d'adsorption de CO ont révélé une bonne accessibilité de la surface du métal avec la coordination des molécules de monoxyde de carbone dans les différents modes.

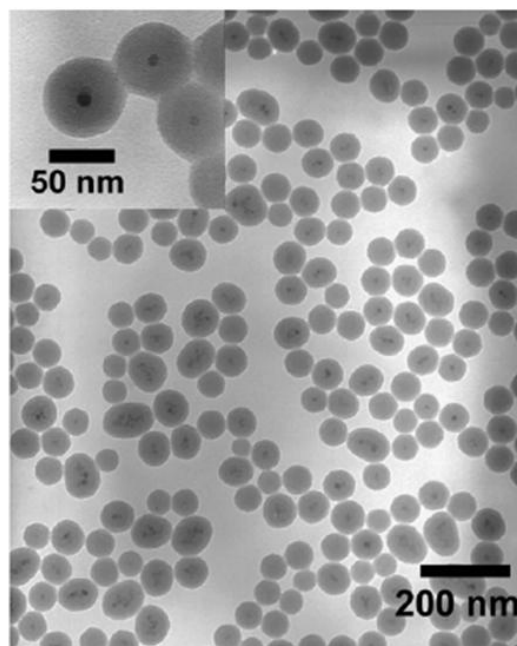
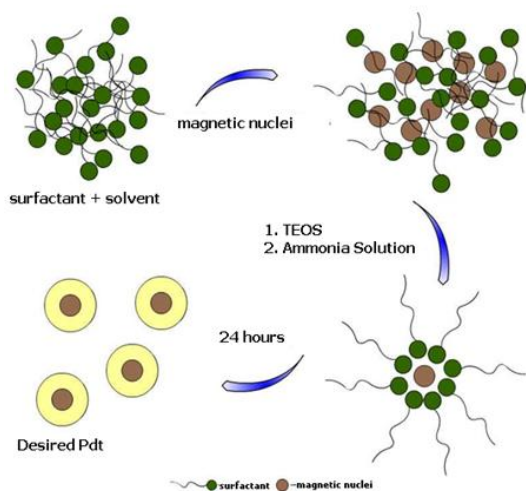
Le ligand PTA a donné lieu à des nanoparticules bien dispersées et très petites (ca 1,0 nm). Les particules obtenues ont montré un fort caractère hydrophile, ce qui a facilité leur transfert dans l'eau tout en maintenant leur petite taille moyenne. Bien que les études d'adsorption de CO ont conduit à des résultats différents et plus difficiles à interpréter par rapport aux systèmes précédents, il s'avère que les molécules de CO peuvent se coordonner dans des modes différents ce qui révèle une bonne accessibilité de la surface métallique.

Les ligands phosphine ferrocényle, une nouvelle famille de ligands non encore utilisés pour la synthèse de Rh NPs ont permis un fort contrôle de la formation de nanoparticules résultant en de très petites particules de tailles comprises entre 1,1 et 1,7 nm. Des investigations FT-IR sur les systèmes de particules stabilisées avec les ligands bidentés L5 mono- et L2 ont mis en évidence l'effet de l'entrave à la coordination de CO sur la surface des particules.

Un ligand calix CXP [4] arene bisphosphite, ont été utilisé pour la première fois dans la synthèse de nanoparticules métalliques. Des particules bien contrôlées ont été obtenues avec une taille moyenne de 4 nm. Ces particules ont été utilisées dans la réaction d'hydroformylation catalytique.

Enfin, l'utilisation d'une famille de carbènes N-hétérocycliques amphiphiles a permis la formation de NPs bien contrôlées qui sont solubles dans les solvants organiques et dans l'eau.

En plus de la synthèse RhNPs, nous reportons dans ce manuscrit la synthèse d'une silice magnétique amino-modifié utilisée ensuite avec succès comme support pour le dépôt d'une sélection de nanoparticules de rhodium par simple réaction d'imprégnation. Ce travail a été réalisé au Laboratoire de Nanomatériaux et Catalyse (Université de Sao Paulo, Brésil). Comme il sera décrit dans le chapitre IV, cette immobilisation contribuera à une récupération aisée du catalyseur.



Les synthèses de nanoparticules bimétalliques RhM NPs sont décrites dans le chapitre III. Dans ce chapitre, nous avons étudié la synthèse de nanoparticules bimétalliques à base de rhodium suivant l'approche organométallique comme préalablement appliquée pour les systèmes monométalliques. Le complexe  $[\text{Rh}(\eta^3\text{-C}_3\text{H}_5)_3]$  s'est avéré également un bon précurseur pour synthétiser différents systèmes de nanoparticules bimétalliques RhM.

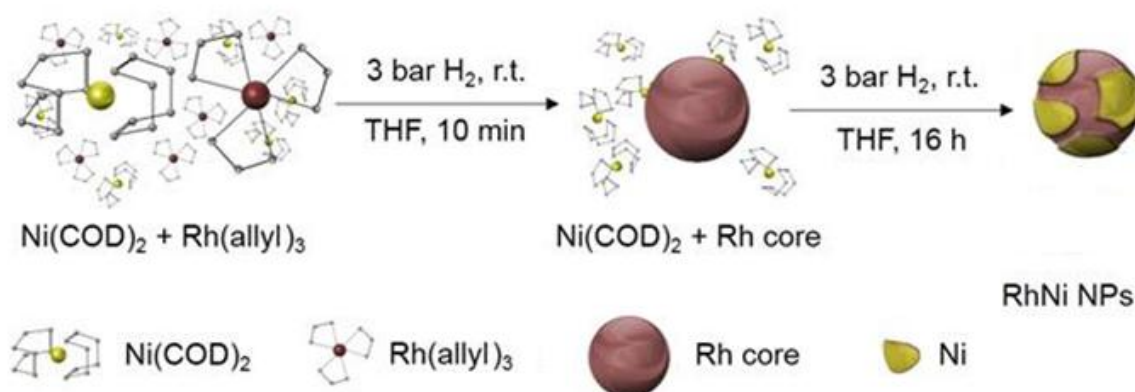
Des systèmes RhNi and RhPd stabilisés par la PVP et l'hexadécylamine (HDA) ont tout d'abord été synthétisés et caractérisés en utilisant des ratios de métaux différents. Des nanoparticules RhNiOx NPs ont ensuite été préparées en raison de leur intérêt en tant que catalyseur d'hydrogénolyse sélective de liaisons C-O. Les conditions de synthèse ainsi développées ont ultérieurement été appliquées pour l'élaboration de nanoparticules bimétalliques RhPt and RhRu en présence de PVP.

Avec les précurseurs  $[\text{Ni}(\text{cod})_2]$  et  $[\text{Pd}_2(\text{dba})_3]$ .

Pour ce qui concerne les systèmes RhNi et RhPd préparés en présence de PVP- et d'hexadécylamine, différents rapports métalliques ont été testés. Le système PVP- RhNiOx a été plus particulièrement étudié en catalyse : la présence d'ilôts d'oxyde de nickel à la surface du rhodium a été mise à profit pour surmonter les limites catalytiques dans l'hydrogénolyse sélective du 1-benzoxy-2-méthoxy-benzène, élément essentiel dans la conversion de lignine pour la synthèse de biocarburants. Les systèmes RhPd sont actuellement en cours



d'évaluation en tant que catalyseurs dans des piles à combustible pour la réaction d'oxydation catalytique du méthanol au Mexique (Collaboration E. Ramirez Meneses).



En plus des complexes  $[\text{Ni(cod)}_2]$  et  $[\text{Pd}_2(\text{dba})_3]$ , d'autres complexes organométalliques de métaux nobles incluant  $[\text{Pt}(\text{nor})_3]$  et  $[\text{Ru}(\text{cod})(\text{cot})]$ , ont également été utilisés avec succès, conduisant par co-décomposition avec le  $[\text{Rh}(\eta^3\text{-C}_3\text{H}_5)_3]$  à la formation nanoparticules RhPt et RhPd dans la PVP. Des NPs RhPt et RhRu de très petites tailles ont été obtenues. Bien que la caractérisation complète des systèmes obtenus n'ait pas encore été effectuée, les résultats préliminaires ouvrent un nouveau champ d'investigations pour accéder à des systèmes bimétalliques et d'intérêt en catalyse.

Le chapitre IV présente les résultats obtenus en catalyse en utilisant des nanoparticules à base de rhodium mono- et bimétalliques, préparés au cours de la thèse incluant les réactions d'hydrogénation, d'hydroformylation et d'hydrogénolyse. L'application en catalyse a concerné principalement la réaction d'hydrogénation, en utilisant les nanoparticules RhPVP, RhPPh<sub>3</sub>, Rhdpbb et Rh phosphino Ferrocene comme catalyseurs. Les nanoparticules RhPPh<sub>3</sub> et Rh calix [4] arène ont été par ailleurs évaluées dans la réaction d'hydroformylation. Enfin, les NPs bimétalliques RhNiOx ont catalysé l'hydrogénolyse du 1-benzyloxy-2-méthoxy-benzène, un substrat modèle de la lignine, en comparaison aux systèmes monométalliques RhPVP et NiPVP.

La catalyse d'hydrogénation d'alcènes et d'aromatiques a été réalisée au Laboratoire de Nanomatériaux et Catalyse à l'Université de São Paulo, Brésil. en utilisant les NPs RhPVP, Rh-dppb et RhPPh<sub>3</sub> NPs comme catalyseurs en conditions colloïdales et supportées. Les

résultats obtenus (soumis pour publication) en utilisant le cyclohexène comme substrat modèle ont révélé que ces systèmes de Rh NPs sont très actifs dans l'hydrogénation de cet alcène simple. En outre, grâce aux propriétés magnétiques du support silicié utilisé pour le dépôt des NPs de rhodium, le recyclage et la réutilisation des nanocatalyseurs ont été facilement réalisés par simple application d'un aimant sur les parois du réacteur entraînant la séparation du catalyseur du produit de réaction. Les réactivités obtenues (rendements ; fréquences de rotation - TOFs) se sont avérés élevés et constants dans les conditions de catalyse étudiées et ceci jusqu'à une dizaine de recyclages successifs. L'hydrogénation de différents arènes a également conduit à des résultats intéressants dans des conditions douces. Par ailleurs, l'hydrogénation chimiosélective dans l'eau des acides benzoïque et lévulinique et leurs dérivés en utilisant comme catalyseur les NPs Rh PVP, a également donné lieu à des résultats très intéressants là-encore dans des conditions douces. De même, la synthèse de la  $\gamma$ -valérolactone à partir de l'acide lévulinique ou de son ester méthylique par une réaction multi-étape d'hydrogénation-cyclisation catalysée par les NPs RhPVP a conduit à des résultats prometteurs.

Des NPs stabilisées par les ligands ferrocenyl phosphorés ont été évaluées dans la réaction d'hydrogénation du styrène. L'effet de la présence ou de l'absence d'une base sur la sélectivité de la réaction a également été étudié. Il est apparu clairement que la formation de l'éthylbenzène au détriment de l'éthylcyclohexane. Ces résultats sont attribués à un blocage de l'accessibilité de la surface des NPs rhodium probablement en raison de l'encombrement stérique du ligand. Ces résultats ouvrent des perspectives en termes de catalyse d'hydrogénation sélective. En effet, il serait intéressant d'explorer plus avant la réactivité de NPs de rhodium (ou autre métal) ayant une accessibilité limitée de leur surface par un choix judicieux de leurs stabilisants dans le but de développer plus de nanocatalyseurs sélectifs.

La réaction d'hydroformylation a fait l'objet de la deuxième partie de ce chapitre dédié à la catalyse. D'une part une comparaison entre le système de NPs RhPPh<sub>3</sub> synthétisées *via* l'approche organométallique et un autre système de NPs, RhTOAB, synthétisées par réduction du sel métallique RhCl<sub>3</sub>.3H<sub>2</sub>O a été menée. Les résultats obtenus ont montré que la réactivité du système RhPPh<sub>3</sub> a dépassé celle du système RhTOAB en termes d'activité et de sélectivité, et ceci même lors de l'ajout de vingt équivalents de monophosphine au nanocatalyseur RhTOAB. L'addition de phosphine aux NPs RhTOAB a entraîné une réactivité supérieure du système catalytique mais néanmoins inférieure à celle des NPs

RhPP<sub>3</sub>, possédant la phosphine coordonnée à leur surface Ces travaux ont mis en évidence le rôle de la phosphine sur les propriétés catalytiques des NPs de rhodium et au-delà l'intérêt d'intégrer la phosphine stabilisante dès l'étape de synthèse des NPs afin d'accroître son effet. Une publication rassemblant ces résultats est actuellement en préparation. D'autre part, les RhNPs stabilisées par le ligand calixarène ont également été testées dans l'hydroformylation du styrène, présentant une activité élevée et une sélectivité intéressante, mais ces résultats préliminaires nécessitent d'être complétés pour confirmer l'intérêt de ces NPs dans cette réaction.

Dans la troisième partie, les nanoparticules bimétalliques RhNiOx stabilisées par la PVP ont été évaluées dans la réaction d'hydrogénolyse de plusieurs substrats mimant la structure de la lignine. La présence d'îlots d'oxyde de nickel à la surface des NPs de rhodium a permis de limiter la réaction d'hydrogénation et d'obtenir les produits aromatiques désirés avec des rendements élevés. Ces résultats ont été acceptés pour publication à *J. Mol. Catal. A: Chem* en 2016, et sont actuellement sous presse.

En résumé, ce travail de thèse reporte une collection de nanoparticules à base de rhodium (mono- et bimétalliques) qui ont été facilement synthétisées à partir du précurseur  $[\text{Rh}(\text{C}_3\text{H}_5)_3]$  dans des conditions douces de réaction et en présence d'une grande variété de stabilisants, ainsi que leur caractérisation par une combinaison de différentes techniques de caractérisation et leur application en catalyse en solution colloïdale ou supportées. Les nanoparticules obtenues se sont avérées bien contrôlées en taille et en dispersion tout en présentant une surface disponible pour des transformations chimiques. Les études de caractérisation menées ont mis en évidence que la surface métallique peut être fonctionnalisée par le choix du stabilisant qui peut influencer leurs propriétés de surface, avec la possibilité de les orienter en fonction d'une application cible. En catalyse, les nanoparticules de rhodium préparées ont présenté une forte activité dans les réactions d'hydrogénation, d'hydroformylation et d'hydrogénolyse. Les résultats obtenus ont mis en évidence l'effet des stabilisants sur le comportement des catalyseurs, ce qui permet d'aboutir à des conclusions fondamentales. Par ailleurs, l'utilisation réussie de nouveaux ligands stabilisants (ligands ferrocényl phosphorés et calixarène bisphosphite) a donné lieu à des nanoparticules monométalliques bien contrôlées avec des performances catalytiques prometteuses, qui laissent entrevoir des perspectives intéressantes en catalyse d'hydrogénation régiosélective qui demeure un objectif difficile en nanocatalyse. En outre,

les résultats obtenus en hydrogénolyse de molécules modèles de la lignine catalysées par les systèmes RhNiOx ont montré que la décoration de la surface de nanoparticules préformées par adjonction d'un autre métal ou oxyde métallique judicieusement choisi est une approche pertinente pour orienter la réactivité des nanocatalyseurs, et ce qui ouvre de nouvelles perspectives de recherche.

En résumé, ces travaux de thèse comprennent la synthèse, la caractérisation et l'étude des propriétés de surface de nanoparticules mono- et bimétalliques à base de rhodium en utilisant les concepts de la chimie de coordination. L'originalité de ce travail réside dans la grande variété des agents de stabilisation utilisés pour concevoir des nanoparticules monométalliques de rhodium dans un premier temps, et la préparation de nanoparticules bimétalliques en associant d'autres métaux (tels que le Pd, le Ni, le Pt et le Ru) dans un second temps. Les résultats obtenus mettent en évidence l'efficacité et la versatilité de l'approche organométallique suivie. Certains des systèmes de nanoparticules obtenues ont été appliqués avec succès en catalyse, montrant ainsi l'intérêt de la nanochimie en solution pour l'élaboration de catalyseurs actifs en conditions colloïdales ou après dépôt sur support. Certains de ces travaux ne sont pas complets et nécessitent d'autres efforts de recherche pour mieux comprendre les systèmes étudiés et leurs bénéfices, et pourront faire l'objet de travaux de recherche dans le futur.

Pour conclure, l'ensemble de ces travaux de doctorat prouvent l'intérêt de disposer de nanoparticules métalliques (dans le cas présent de rhodium, mais cela est valable pour les autres métaux) qui sont bien contrôlées en taille et en état de surface pour une meilleure compréhension des relations entre la structure des particules et leurs performances catalytiques. L'approche organométallique développée dans l'équipe « Ingénierie des Nanoparticules Métalliques » du LCC-Toulouse, offre des outils de synthèse efficaces pour l'obtention de systèmes de NPs reproductibles, permettant d'accéder à des études fines, étape essentielle pour le développement de nanocatalyseurs plus actifs et plus efficaces.

## Personal Information

---

**NAME** Mahmoud IBRAHIM  
**Address** 5 rue cujas , appt 10, 31000, Toulouse, FRANCE  
**Mobile** (0033) 07 78 32 70 73  
**Email Address:** mah.ibrahim@hotmail.com  
**DATE OF BIRTH:** 7 October 1989 / Lebanon

## Academic Qualification

---

**2007-2010** Bachelor's Degree (BSC) in Chemistry, Beirut, Lebanon  
**2010-2011** MASTER's Degree (M1): Molecular Chemistry, Beirut, Lebanon  
**2011-2012** MASTER's Degree (M2): International Masters of Catalysis,  
 Organometallics and Green Chemistry, Rennes, France  
**2012-present** Ph.D in Organometallic Chemistry and Coordination, Toulouse,  
 France

## Research Experience

---

**August 2015** Hydrogenolysis of Lignin Derivatives. National Univeristy of Singapore.  
**October 2014** Evolution of Energy from Biomass. National University of Singapore.  
**Nov 2013** Performing Catalytic Tests of Colloidal and Supported Metal Nanoparticles. University of Sao Paulo, Brazil.  
**Oct 2012-present** Ph.D. Rhodium Based Mono- and Bi-Metallic Nanoparticles: Synthesis, Characterization and Application in Catalysis. LCC, Toulouse.  
**Nov 2011-Jun 2012** Masters Thesis. "Metal-catalyzed dehydrogenation of alcohols using Ru and Ir complexes, for polymer formation. University of Rennes 1  
**(2010-2011)** Research Project: Analysis of Al-Quraun Lake water. National Lebanese Atomic Community, Lebanese University, Beirut, Lebanon.  
**(2010-2011)** NANOTEchnology in Environmental Improvement.

**Publications:**

---

1. “Water Transfer of Hydrophobic Nanoparticles: Principles and Methods”  
Branca, M.; **Ibrahim, M.**;\* Ciuculescu, D.; Philippot, K.; Amiens, C.\* In *Handbook of Nanoparticles*; Aliofkhazraei, M., Ed.; Springer International Publishing: **2016**, p 1.
2. “Rh nanoparticles with NiOx surface decoration for selective hydrogenolysis of CO bond over arene hydrogenation”  
Zhang, J.;\* **Ibrahim, M.**;\* Collière, V.; Asakura, H.; Tanaka, T.; Teramura, K.; Philippot, K.; Yan, N. *Journal of Molecular Catalysis A: Chemical* **2016**.
3. “Polymer *versus* phosphine stabilized Rh nanoparticles as components of supported catalysts: implication in the hydrogenation of cyclohexene model molecule”  
**Ibrahim, M.**; Garcia, M. A. S.; Vono, L. L. R.; Lecante, P.; Rossi, L. M.; Philippot, K. *Catal. Sci. Tech.* **2016**, *Submitted*.
4. “Triphenylphosphine-stabilized Rh(0) nanoparticles as an efficient hydroformylation (pre)catalyst”  
Garcia, M. A. S.; **Ibrahim, M.**; Costa, C. S.; Lecante, P.; Korio, P.; Philippot, K.; Rossi, L. M. *Journal of Colloid and Interface Science.* **2016**, *in preparation*.
5. “Chemoselective Hydrogenation of Levulinic acid, Benzoic acid and its Derivatives over Rh nanoparticles Supported on PVP”  
**Ibrahim, M.**; Garcia-Suarez, E.; Philippot, K. *in preparation*.
6. “Electrochemical Study of Alcohol-stabilized Rh NPs in Fuel Cells”  
**Ibrahim, M.**; Ramirez, E.; Philippot, K. *in preparation*

**Mahmoud IBRAHIM**

*Rhodium Based Mono- and Bi-Metallic Nanoparticles: Synthesis, Characterization and Application in Catalysis*

Under the Supervision of Dr. Karine PHILIPPOT

## **ABSTRACT**

In this thesis, synthesis, characterization and catalytic applications of mono- and bi-metallic rhodium-based nanoparticles are reported. Rhodium has been chosen as a primary metal given its high interest in catalysis, mainly in hydrogenation and hydroformylation reactions.

The synthesis of mono-metallic rhodium nanoparticles (NPs) is the core of this work. It was performed by decomposition of the organometallic complex  $[\text{Rh}(\text{C}_3\text{H}_5)_3]$  in solution under dihydrogen pressure and in the presence of different stabilizers including ligands and polymers to control the growth of the particles. Selected nanoparticles were deposited on the surface of amino-functionalized magnetic silica as a support for recovery and recycling concerns in catalysis.

Diverse bi-metallic nanoparticles have been also prepared in one-pot conditions by co-decomposition of the  $[\text{Rh}(\text{C}_3\text{H}_5)_3]$  with other organometallic precursors including  $[\text{Ni}(\text{cod})_2]$ ,  $[\text{Ru}(\text{cod})(\text{cot})]$ ,  $[\text{Pt}(\text{nor})_3]$  and  $[\text{Pd}(\text{dba})_2]_2$ . Tuning of the metal ratios between  $[\text{Rh}]$  and the second metal  $[\text{M}]$ , or of the nature and the amount of the stabilizer used for the synthesis allowed to obtain nanoparticles of different sizes and chemical compositions.

The characterization of the obtained nanoparticles was performed by using a combination of state-of-art techniques (TEM, HRTEM, STEM-EDX, ICP, WAXS, EXAFS, Xanes, XPS, NMR...). Surface studies were carried out in some cases, by adsorbing CO on the surface of the particles which was followed by spectroscopic techniques (FT-IR, NMR) to probe their surface state.

Some of these nanoparticles were investigated in catalytic reactions, mainly hydrogenation with Rh NPs and hydrogenolysis for  $\text{RhNiO}_x$  NPs. Both colloidal and supported catalytic studies were carried out in the case of hydrogenation catalysis.

The originality of this work lies in the development of simple synthesis tools inspired from organometallic chemistry to get well-controlled rhodium-based nanoparticles in terms of size, size distribution, composition and surface state, all these parameters being important whatever the target application. The interest of the obtained nanoparticles in catalysis has been also evidenced in different reactions. This PhD work may open new opportunities of research both in nanochemistry and catalysis.

**KEYWORDS:** Rhodium, Bimetallic, Nanoparticles, Catalysis, Hydrogenation, Hydroformylation, Hydrogenolysis

**Laboratoire de Chimie de Coordination**

205 Route de Narbonne

31077 Toulouse Cedex 4

**Mahmoud IBRAHIM**

*Nanoparticules Mono- et Bi-Métalliques à Base de Rhodium: Synthèse, Caractérisation and Application en Catalyse*

Sous la direction de Dr. Karine PHILIPPOT

**RÉSUMÉ**

Dans cette thèse, la synthèse, la caractérisation et les applications en catalyse de nanoparticules mono- et bimétalliques à base de rhodium sont décrites. Le rhodium a été choisi comme métal central de cette étude en raison de son intérêt reconnu en catalyse, principalement pour les réactions d'hydrogénation et d'hydroformylation.

La synthèse de nanoparticules de rhodium monométalliques constitue le cœur de ce travail. Elle a été réalisée par décomposition du complexe organométallique  $[\text{Rh}(\text{C}_3\text{H}_5)_3]$  en solution, sous pression de dihydrogène et en présence de différents stabilisants tels que des ligands et des polymères pour contrôler la croissance des particules. Certaines nanoparticules ont été déposées sur la surface d'une silice magnétique fonctionnalisée par des groupements amines utilisée comme support, dans un objectif de récupération plus aisée pour le recyclage des catalyseurs.

Diverses nanoparticules bimétalliques ont également été préparées par co-décomposition du complexe  $[\text{Rh}(\text{C}_3\text{H}_5)_3]$  avec d'autres précurseurs organométalliques, incluant  $[\text{Ni}(\text{cod})_2]$ ,  $[\text{Ru}(\text{cod})(\text{cot})]$ ,  $[\text{Pt}(\text{nor})_3]$  et  $[\text{Pd}(\text{dba})_2]_2$ . En modulant les ratios de métaux entre  $[\text{Rh}]$  et le second métal  $[\text{M}]$ , ainsi que la nature et la quantité de stabilisant utilisé pour la synthèse, des nanoparticules de tailles et de compositions chimiques différentes ont pu être obtenues.

La caractérisation des nanoparticules ainsi préparées a été menée en utilisant une combinaison de techniques de l'état de l'art (TEM, HRTEM, STEM-EDX, ICP, WAXS, EXAFS, XANES, XPS, RMN ...). Pour certaines nanoparticules de rhodium, des études de surface ont été réalisées, par adsorption du CO sur la surface des particules et un suivi par des techniques spectroscopiques (FT-IR, RMN) pour sonder leur état de surface.

Un autre aspect de ce travail a concerné l'évaluation des nanoparticules synthétisées dans des réactions catalytiques, en particulier réactions d'hydrogénation avec des particules monométalliques de Rh et réaction d'hydrogénolyse avec des nanoparticules bimétalliques RhNiOx. Dans le cas de la catalyse d'hydrogénation, des études en conditions colloïdales et supportées ont été réalisées.

L'originalité de ce travail réside dans le développement d'outils de synthèse simples inspirés de la chimie organométallique pour obtenir des nanoparticules à base de rhodium bien contrôlées en termes de taille, distribution en taille, composition et état de surface, tous ces paramètres étant importants quelle que soit l'application visée. L'intérêt des nanoparticules obtenues en catalyse a également été mis en évidence dans différentes réactions. Ce travail de thèse offre de nouvelles opportunités de recherche, tant en nanochimie qu'en catalyse.

**MOT-CLÉS:** Rhodium, Bimétalliques, Nanoparticules, Catalyse, Hydrogénation, Hydroformylation, Hydrogénolyse

**Laboratoire de Chimie de Coordination**

205 Route de Narbonne

31077 Toulouse Cedex 4